Microneedles for Theranostics

Natasha Rajendran

Submitted to Swansea University in fulfilment of the requirements for the degree of Doctor of Philosophy

Swansea University 2022

DECLARATION

This work has not previously been accepted in substance for any degree and is not being concurrently submitted in candidature for any degree.

Signed ……. (candidate)

Date 09-Dec-2022

STATEMENT 1

This thesis is the result of my own investigations, expect where otherwise stated. Other sources are acknowledged by footnotes giving explicit references. A bibliography is appended.

Signed ……. (candidate)

Date 09-Dec-2022

STATEMENT 2

I hereby give consent for my thesis, if accepted, to be available for photocopying and for inter-library loan **after expiry of a bar on access approved by Swansea University.**

Signed ……. (candidate)

Date 09-Dec-2022

Ysgoloriaeth Sgiliau Economi Gwybodaeth (KESS) yn Gymru gyfan sgiliau lefel uwch yn fenter a arweinir gan Brifysgol Bangor ar ran y sector AU yng Nghymru. Fe'i cyllidir yn rhannol gan Gronfeydd Cymdeithasol Ewropeaidd (ESF) cydgyfeirio ar gyfer Gorllewin Cymru a'r Cymoedd.

Knowledge Economy Skills Scholarships (KESS) is a pan-Wales higher level skills initiative led by Bangor University on behalf of the HE sector in Wales. It is part funded by the Welsh Government's European Social Fund (ESF) convergence programme for West Wales and the Valleys.

This work is part funded by the Welsh Government's European Social Fund (ESF) convergence programme for West Wales and the Valleys.

Acknowledgments

Firstly, I would like to thank my Supervisors, **Dr Sanjiv Sharma,** and **Professor Owen Guy** for giving me the opportunity to carry out a PhD and for believing in my ability before I believed in myself. They were always there for guidance and allowed me to pursue my ideas with their support.

Next, I would like to thank my funding body KESS II, for providing the funding opportunities to fulfil my experimental ideas and reach my goals throughout. In addition, SPTS technologies and BioMEMs technologies for their continued collaborations and providing the equipment required to perform various fabrication techniques.

I would like to give my thanks to my best friend **Dr Olivia Howells**, for providing all the help and support throughout my PhD and teaching me everything I need to know about fabrication and drug delivery. She also was there to encourage me to carry on and went above and beyond to read through my thesis and taught me ways in which to improve my writing to allow it to flow better and the required amount of detail needed for each section.

To my husband, **Aled Cook** who was there throughout my PhD and provided me all the love and support I needed to get me through the stressful times. He would make sure to listen to my rants and stick by me through everything.

I would like to thank my Family, **my parents**, and **brother** for all their support throughout my life. Even though they live in London they were always there to answer all my calls to provide their guidance. My biggest thanks go to my parents **Shiromi Rajendran** and **Rohan Rajendran** for providing me with delicious home-cooked food and cups of tea whenever I was working on my thesis in London.

To my parents, husband, and brother

Abstract

Microneedle (MN) arrays were developed to provide a minimally invasive approach to detect biomarkers and deliver drugs into the ISF. Solid, hollow, and dissolvable MNs have been fabricated for various applications and have been evaluated to be very advantageous. These advantages include better patient compliance dur to painless and non-invasive administration, improved permeability and efficiency and provide targeted drug delivery by varying MN dimensions to specific regions in the skin.

Techniques to fabricate MNs vary based on the material and potential application requirements. The most common techniques are micro-moulding, wet and dry etching with lithography and laser cutting. Micro-moulding fabrication have been utilized to produce various polymer, hydrogel and dissolvable MNs by filling prepared moulds with a liquid formulation. Alternatively, lithography using wet and dry etching have been used to fabricate MNs. A mask is used as a template for generating the desired pattern on a wafer surface using either a positive or negative photoresist to generate the desired pattern. These wafers are then etched using a strong caustic agent or an etcher. Finally, laser cutting techniques have been used to produce metal MN using a computer aided design to create the desired shape and dimensions.

In recent studies, MNs have been created for a wide range of diagnostic and drug delivery applications. A wide range of MNs have been adapted for a variety of disease treatments such as cancer, arthritis and ophthalmic disorders. As diabetes mellitus affects approximately 30 million people and glucose monitoring has advanced from the initial self-monitoring of blood glucose levels to glucose biosensors, a high demand for MNs to be modified for diabetes management has been emphasized.

This thesis details the fabrication of MNs using silicon, polyvinylpyrollidone (PVP) and polycarbonate for sensing and drug delivery. Silicon wafers with the combination of photolithography and deep-reactive ion etching (DRIE) techniques are used to create solid and hollow MNs. The MN arrays have sharp tips that provide eased insertion and injectable capabilities.

Polycarbonate and PVP MNs were manufactured using micro-moulding techniques to create solid and dissolvable MNs respectively. These MNs were characterized to determine their penetration capabilities through the *stratum corneum* (SC) to provide

controlled transdermal drug delivery and diagnose biomarkers within the interstitial fluid (ISF).

For diagnostic applications, the polycarbonate MNs were modified for glucose sensing using first generation sending strategies wherein oxygen in used as the electron acceptor and the levels of glucose is proportional to the peroxide produced. To determine drug delivery capabilities of MNs, the solid polycarbonate and silicon MNs employed ‘poke and patch’ techniques with the use of a Franz cell to show calcein and FITC-insulin delivery over 24 hours. On the other hand, for drug delivery through the dissolvable PVP MNs, ‘poke and dissolve’ techniques were analysed with the use of Franz cells to show the release of encapsulated calcein and FITC-insulin within the polymeric matrix over 24 hours. The arrays were either left blank for basal drug delivery or metallised with silver for controlled drug delivery using the metals breakdown potential.

Contents

Abbreviations

SC – *Stratum Corneum*

A – Absorption

D – Distribution

M – Metabolism

E – Excretion

HILIC – Hydrophilic interaction liquid chromatography

TDDS - Transdermal drug delivery systems

POC – Point of care

CAGR – Compounded annual growth rate

UV – Ultraviolet

ISF – Interstitial fluid

GOx – Glucose oxidase

LOx – Lactate oxidase

GDH – Glucose dehydrogenase

FAD – Flavine adenine dinucleotide

CGM – Continuous glucose monitoring

TCNQ – Tetracyanoquinomethane

PMVE/MA – Poly(methyl vinyl ether – co – maleic acid)

PMVE/MAH – Poly(methyl vinyl ether – co – maleic anhydride)

PVA – Poly (vinyl alcohol)

pHEMA – Polyhydroxyethylmethacrylate

PDMS – Polydimethylsiloxane

NSAID – Nonsteroidal anti-inflammatory drug

CMC – Carboxymethyl cellulose

DPBS – Dulbecco's phosphate buffered saline

RhB – Rhodamine B

ELISA – Enzyme linked immunosorbent assays

IT – Immunoturbidimetry

LoC – Lab on chips

PEI – Poly (ethylenimine)

PEG-DE – Poly(ethylene glycol) diglycidyl ether

VF – Vinyl ferrocene

HB - β-hydroxybutyrate

GL - D-(+)-glucose anhydrous

ROS - Reactive oxygen species

DOx – Doxorubicin

PDI - Perylene diimide

PA - Photoacoustic imaging

TMOS - Tetramethyl orthosilicate

FEBP - Fatty acid-binding protein

GNR - Gold nanorods

ADE - Amyloid-degrading enzymes

MN – Microneedle

MNA – Microneedle array

PVP – Polyvinylpyrrolidone

TTF– Tetrathialfulvalene

DET– Direct electron transfer

OVA– Ovalbumin

PECVD – Plasma enhanced chemical vapour deposition

CVD – Chemical vapour deposition

ICP – Inductively coupled plasma

AIBN - Azobisisobutyronitrile

RF – Radiofrequency

SEM – Scanning electron microscope

AFM – Atomic force microscopy

CLSM – Confocal laser scanning microscopy

OCT – Optical coherence tomography

HPLC – High performance liquid chromatography

PAMPA – Parallel artificial membrane permeability assay

EDTA – Ethylenediaminetetraacetic acid

DRIE – Deep reactive ion etching

H&E – Hematoxylin and Eosin

TEER – Trans-epidermal electrical resistance

PBS – Potassium buffered saline

OECD – Organisation for economic cooperation and development

DTT – Dithiothreitol

CD – Critical dimensions

MB – Methylene blue

FITC – Fluorescein isothiocyanate

SMD – Small molecule drugs

FCA– Ferrocene carboxylic acid

PVD – Plasma vapour deposition

PC – Polycarbonate

Fe – Iron

Au – Gold

Ag – Silver

Cr – Chromium

Ti - Titanium

Pt – Platinum

K_m – Michelis Menten constant

S – glucose concentration

CV – Cyclic voltammetry

WE – Working Electrode

CE – Counter Electrode

RE – Reference Electrode

CA - Chronoamperometry

CNC – Computer numerical control

CAD – Computer aided design

Units

µl - Microliter

µm – Micrometre

mm – Millimetre

cm - Centimetre

nm - Nanometre

ml – Millilitre

mg – Milligram

µg - Microgram

J – Flux

V – Voltage

I – Current

h– Hours

min– Minutes

s – Seconds

a.u – Fluorescence

W – Watts

Hz – Hertz

N – Newton

°**C –**Celsius

% - Percentage

M – Molar

mJ – Millijoules

mPa.s – Viscosity

A - Angstrom

Figures

Tables

Publications

Concept Article: Olivia Howells, Natasha Rajendran, Sarah Mcintyre, Sara Amini-Asl, Pauline Henri, Yufei Liu, Owen Guy, Anthony E. G. Cass, May C. Morris, Sanjiv Sharma. Microneedle Array-Based Platforms for Future Theranostic Applications ChemBioChem 2019 20 (17) https://doi.org/10.1002/cbic.201900112

Conferences

Microneedles for theranostics. *Biosensors Conference* Oral Presentation 2021.

Part 1

Introduction and Literature Review

Chapter 1

Thesis outline

This thesis describes the fabrication of three MNs based on different substrates for diagnostics and transdermal drug delivery. The results obtained as part of this thesis is divided into five parts, which are further divided into chapters. The thesis layout is as follows:

Part 1- Introduction and Literature Review

Part 1 reviews the relevant literature for transdermal drug delivery systems and biosensors followed by the current classifications of MNAs, methods of fabrication and their applications for diagnostic, drug delivery and theranostics.

Part 2- Experimental Methodology

Part 2 discusses the equipment and methods used to fabricate and characterise MNs followed experiments to analyse their ability for transdermal delivery therapeutic compounds and diagnose biomarkers.

Part 3- Optimisation of Silicon MNs for Drug Delivery

This part describes how out-of-plane silicon MNs have been fabricated and characterised to determine their ability to penetrate through the SC followed by the ability of the MNs for transdermal delivery of therapeutic drugs.

Part 4- Optimisation of Polyvinylpyrrolidone MNs for Drug Delivery

Part 4 demonstrates the fabrication of PVP MNs and the characterisation of their ability for encapsulated therapeutic transdermal drug delivery. This part also demonstrates the ability of PVP MNs to carry out bolus and basal transdermal drug delivery.

Part 5- Optimisation of Polycarbonate MNs for Diagnostics and Drug Delivery

This section discusses how polycarbonate MNs have been characterised and used for diagnostic applications. This section also includes a study involving the use of hollow polycarbonate MNs for drug delivery.

Chapter 2

Introduction to transdermal drug delivery and diagnostics

2.1 Transdermal drug delivery

Therapeutic drug delivery systems are physicochemical technologies that control the delivery and release of pharmacologically active substances into tissues, organs, and cells to maximise therapeutic efficiency while minimising any side effects (1) (2). Existing delivery systems administer drugs through oral, nasal, ocular, and transdermal routes.

The most used route is the oral delivery route, which is adopted by approximately 90% of the global market. Additionally, more than 80% of the best-selling pharmaceutical products are administered orally (3). The oral delivery route is preferred because of its non-invasive nature, patient compliance, and convenience for drug administration. Despite these advantages, there are several drawbacks to drugs delivered through the oral route. Drugs administered orally have limited absorption, which could be attributed to poor chemical and biological stability and presence of physiological barriers including pH and metabolic enzymes (4).

More importantly, a 100% dosage will not be administered to the site of interest due to the large duration required for the drug to become active. To become active, a drug must undergo four different phases, which are:

- Absorption (A), which entails the movement of the drug from the site of administration to the site of action.
- Distribution (D), which involves the journey of the drug through the blood stream to tissues in the body
- Metabolism (M), which is the process to break down the drug.
- Excretion (E), which involves the removal of drug from the body.

Once the drug is orally administered, absorption into the bloodstream occurs in the stomach and intestine, which takes approximately one to six hours. The rate, at which the drug is absorbed depends on factors such as the presence of food in the intestine, particle size of the drug formulation, and the acidity of the intestinal contents (5).

Transdermal delivery presents a promising alternative due to its are minimally invasive nature, ability to be self-administered, and opportunities to prolong the duration of drug release. Furthermore, they are cost effective and improve patient compliances (6). Drugs administered transdermally do not pass through the gastrointestinal tract because of which there are no dosage losses due to first-pass metabolism. First pass metabolism is a process, by which a drug gets consumed at a specific location in the body that results in the reduction in concentration of the active drug upon reaching its site of action (7). In addition to reducing dosage loss, transdermal drug delivery can occur without interference from enzymes, pH, and intestinal bacteria.

Drug delivery system innovation is a key strategy that is employed to improve the bioavailability of active pharmaceutical ingredients. So far, oral drug delivery is still the most preferred method of administration through liquids, capsules and chewable tables. For drug administered orally, absorption may begin in the mouth and stomach, but most of the drug is usually absorbed from the small intestine. The drug passes through the intestinal wall and travels to the liver before being transported via the bloodstream to its target site. Intravenous drug delivery on the other hand utilises administration by injection in a vein. A solution of drug can be given in a single dose or by continuous infusion. For infusion, the solution is either moved by gravity or by an infusion pump through thin flexible tubing to a catheter inserted in a vein. Intravenous drug delivery is the best way to deliver a precise dose quickly and in a well-controlled manner throughout the body. Finally, transdermal drug delivery systems deliver drug body wide through a patch on the skin. The drugs administered through the patch can be mixed with a chemical that enhances penetration through the skin into the blood stream without an injection, these allow drug to be delivered slowly and continuously for many hours or days or even longer. Therefore, the level of drug in the blood can be kept relatively constant (8). These techniques have been summarized in Figure 2.1 (9).

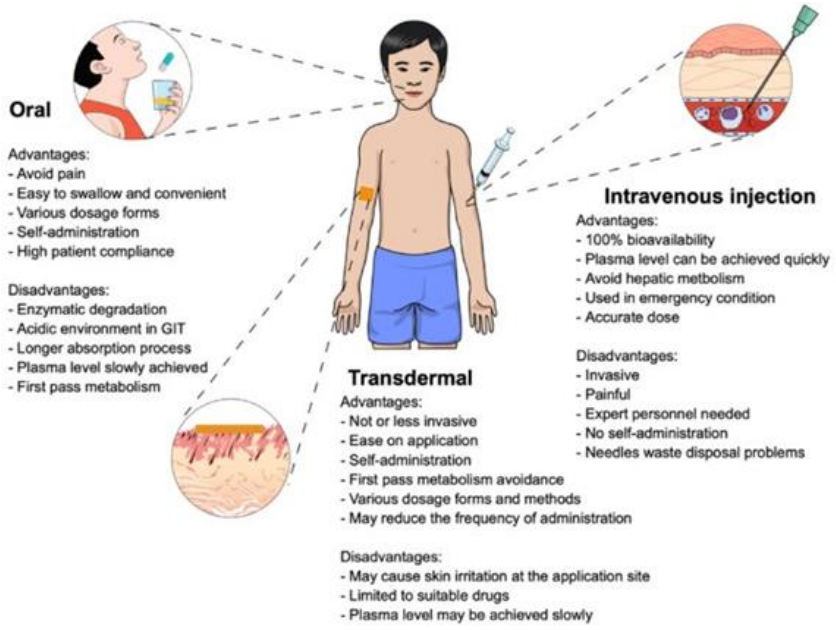

Figure 2.1 Comparison of three drug delivery routes; Oral, Transdermal and Intravenous Injections (9).

2.2 Point of care diagnostics

Point of care diagnostic (POC) testing is a laboratory test conducted close to the site of patient care. Currently the annual turnover for invitro diagnostic POC testing in Europe stands at approximately €3 billion (10). The home pregnancy test and personal glucose monitoring are the most developed POC devices available commercially. These devices have many advantages for rapid diagnosis over traditional laboratory-based testing. Laboratory based testing requires the collection of biological samples like blood, saliva, and urine, which may be considered invasive or intrusive. Blood sampling maybe painful and have an increased risk of infection due to the damage to the skin barrier. For these reasons, skin based biofluids where sampling is minimally invasive and self-managed is more favourable (11).

For better understanding of transdermal drug delivery, it is essential to understand the skin anatomy and for POC diagnosis and monitoring the components of interstitial fluid (ISF)

2.3 Skin anatomy

The skin is the largest organ in the body and is composed of an intricate network of cells, blood vessels and tissue which serves as an initial barrier against pathogens, UV light, chemicals, and mechanical injury. It also regulates body temperature and rate of

perspiration. The skin is made up of three layers; the epidermis, dermis, and hypodermis, all three of which vary in thickness dependent on their anatomy and function (Figure 2.1) (12).

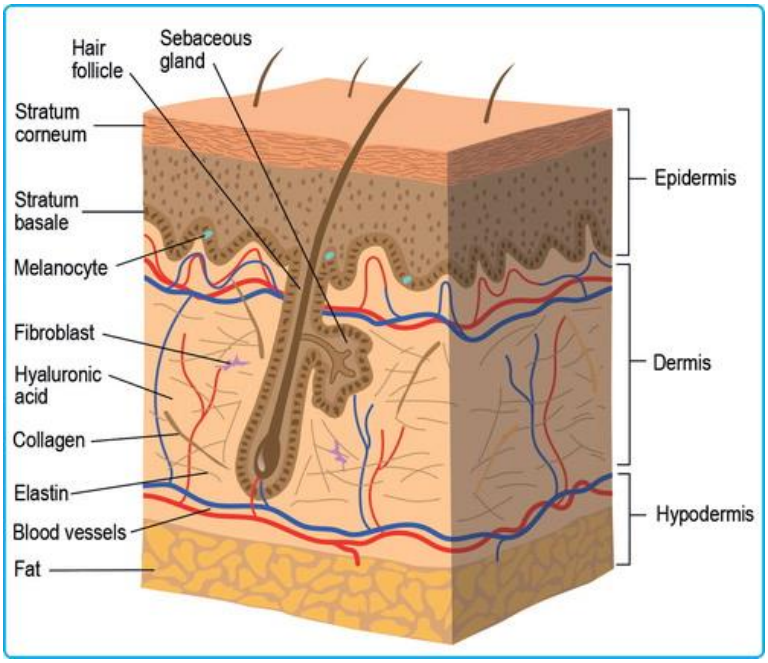

Figure 2.2 Schematic representation of skin anatomy (12).

2.3.1 The epidermis

The epidermis consists of 5 different layers, with the deepest portion being the *stratum basalis*, followed by the *stratum spinosum*, *stratum granulosum*, *stratum lucidum*, and the *stratum corneum* (the most superficial portion of the epidermis).

- *Stratum Basalis* also known as the basal cell layer is the closest to the dermis of the skin. This layer is mitotically active and contains a single layer of keratinocytes, melanocytes, and stem cells. The keratinocytes in this layer evolve as they travel upwards to create the remaining layers. Melanocytes produce melanin, which gives skin its colour.
- *Stratum Spinosum* consists of several layers of cells connected by desmosomes. The desmosomes allow keratinocytes to remain tightly bound to one another.

- *Stratum Granulosum* also known as the granular cell layer contains several layers of cells that contain lipid-rich granule. Within this layer, the cells begin to lose their nuclei as they move away from the nutrients located in the deeper tissue
- *Stratum Lucidum* exists within the thicker regions of the body like soles and palms and consist of cells without nuclei.
- *Stratum Corneum* is the outermost layer of the epidermis and this keratinized layer acts as a protective layer. Due to its lipid content and keratinization, this layer can regulate water loss by preventing internal fluid loss through evaporation (12).

2.3.2 The dermis

The dermis consists of two layers of connective tissue, the papillary, and reticular layers. The papillary layer is the upper layer, which is thinner than the reticular layer and is composed of loose connective tissue and is in contact with the epidermis. The reticular layer is the bottom layer of the dermis, which is less cellular and consists of dense connective bundles of collagen fibres. This layer houses hair, hair follicles, sweat glands, sensory neurons, and blood vessels (13).

2.3.3 The interstitial fluid

The ISF is the most prevalent fluid in the body and constitutes approximately 75 % of extracellular fluid and 15-25 % of body weight. The ISF surrounds all cells and tissues and acts as a bridge between blood and cells (14). Therefore, ISF contains systemic and local tissue biomarkers that can be used for continuous monitoring and provide information about cellular and tissue physiology. It is found in the lowermost skin layer of the dermis, and the dermis consists of approximately 70 % ISF by volume (15).

Studies have shown that 83 % of proteins found in serum are shown in ISF, but 50% of proteins in ISF cannot be found in serum (16).Additionally, further inspection showed that 94 % of features found in plasma using HILIC chromatography (which captures polar compounds) were also found in ISF. In comparison, 84 % of features were found in common between plasma and ISF using reverse phase C18 chromatography (which detects lipophilic compounds) (17).This indicated that hydrophilic compounds are more easily equilibrated between the ISF and plasma compared to hydrophobic compounds. Therefore, ISF maybe a source of unique biomarkers as well as biomarkers present in the blood (16).

The use of ISF for biomarker detection is advantageous as they provide avenues for real-time monitoring and early detection due to the presence of the biomarker in the ISF after its accumulation in the blood. However, extraction of ISF for diagnosis can be disadvantageous due to challenges associated with sample collection, limit volumes, and sample variabilities (18).

As dermal ISF does not clot like blood, extraction of the ISF can offer a new technique for continuous monitoring of glucose and other key health indicators. Although, ISF has been difficult to sample, it has been extracted through implanted sensors for monitoring glucose in addition to surgically implanted tubing and vacuum blisters for the monitoring of inflammation and wound healing. However, these techniques are not suitable for routine clinical diagnostics. Therefore, MNAs can be utilised to create shallow micropores that reach into the outer layer of the skin for ISF extraction (19).

2.4 Routes for transdermal drug delivery

Advances in drug delivery systems have improved patient compliance and drug effectiveness. To make use of human skin as a route of entry, systemic drug delivery also known as transdermal drug delivery can be employed. Transdermal drug delivery systems are patches that contain a predetermined volume of drug with a defined surface area. These patches are applied to the skin surface to deliver the drug at a programmed rate to reach the systemic circulatory system (20).

Transdermal drug delivery can deliver drugs through the skin across an intact SC layer; through either the intracellular lipid domains, through skin appendages or by a transcellular route (21). The intracellular lipid route consists of drug permeation through the continuous lipid matrix. Using the intracellular route is the most accepted pathway for small uncharged molecules (22). The appendageal route is permeation that occurs through the sweat gland or across hair follicles. Permeation through this route provides a continuous channel across the SC layer. Finally, the transcellular route allows drug to enter the skin through the corneocytes. This pathway requires partitioning into and diffusion through the keratin and the intracellular lipids (23).

2.4.1 History of transdermal drug delivery

Evidence of transdermal drug delivery systems have been predated to the Sumerians (4100-1750 BCE) (24) and these systems were used for defence against infection, skin

protection and cosmetic purposes. In AD 980-1037, the concept of drugs ability to cross the skin was applied by Ibn Sina, best known as Avicenna, where he suggested that drugs applied to the skin not only have local effects but also within the tissue beneath the skin and remote areas (25).Schwenkenbecker generalised in 1904 that the skin was permeable to lipid soluble substances but not to water and electrolytes (26) and this systemic absorption was discovered due to various cases of poisoning after topical application of nitrobenzene or aniline dyes in dyed clothing (27).

Transdermal drug delivery through a patch is advantageous as they are non-invasive and reliable in maintaining a constant delivery of drug over a 24 to 72 h period. Although they are advantageous there are only 20 approved transdermal drug delivery systems as these drugs are restricted in usage due to their physicochemical properties. With rapid advances in combinatorial chemistry occurring in the 1990s, scientists were equipped with tools to create large libraries of synthetic compounds for high throughput screening. There was a high volume of compound generation to increase the chances of finding a promising lead. For many years, potential molecular entities would move into development and remain stuck there because the physiochemical properties were not ideal. In 1997, the Lipinski rules were developed to determine whether drug molecules can provide effective and focused transdermal drug delivery. These rules include:

- The molecular weight should be < 500 Da to avoid drug being ineffective in drug permeability through the membrane
- A lipophilicity (log P) < 5 to improve affinity and selectivity of the drug candidate
- Consistent solubility in non-aqueous and aqueous medium as the drug needs to penetrate through the SC and be dissolved into the systemic circulatory system
- The number of hydrogen bond acceptors should be less than 10 to ensure drugs cross the non-polar membranes without strong interaction with water. If the drug molecule binds too strongly with water due to the number of hydrogen bond acceptors it can lead to the drug molecule not entering through the non-polar membrane (28).

The Lipinski rule is used to predict if a biologically active molecule is likely to have favourable chemical and physical properties to be transdermally delivered. For a drug to be transdermally active they can have no more than one violation of the five conditions.

Generally, a drug compound would be optimal if it has a lower molecular weight, be lipophilic and have fewer hydrogen bond acceptors.

If a drug compound breaks one or more of the rule of five they often come with greater lipophilicity and reduced water solubility compared to drugs meeting the Lipinski Rule of Five criteria. Therefore, these drugs are associated with reduced bioavailability; requiring alternative delivery strategies to ensure adequate accumulation at the target site. To improve the bioavailability, drug compounds can have further properties such as intramolecular hydrogen bonding, macrocyclization, dosage and formulations (29).

To overcome the barrier properties of the SC, there has been a move towards minimally invasive transdermal drug delivery systems which include MNs (Figure 2.3) (30). These MNs have been used with the main focus of single dose vaccine delivery as well long-term treatment methods and are the main focus of this thesis.

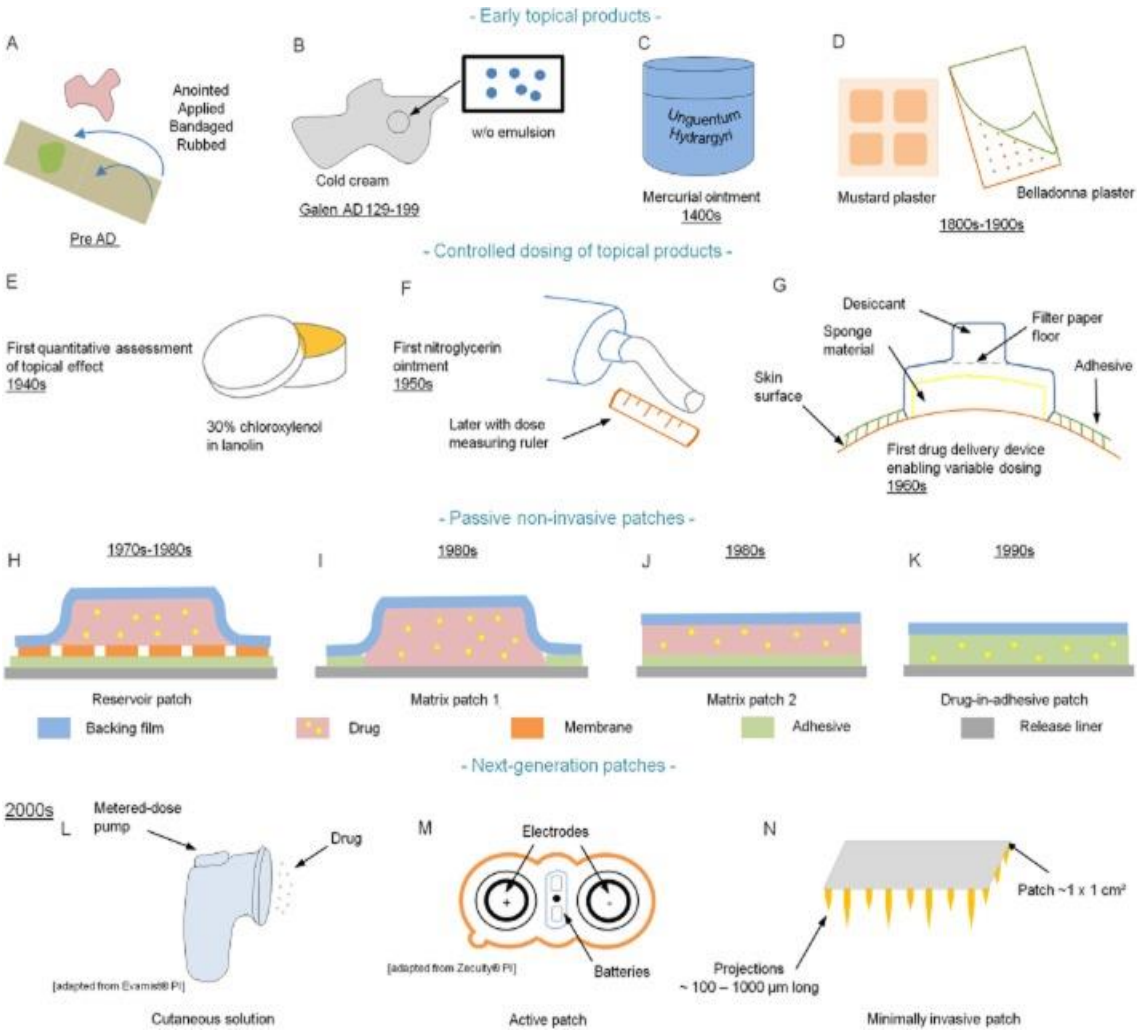

Figure 2.3 Historical development of transdermal drug delivery (30).

2.5 Introduction to Biosensors

Biosensors have attracted a high volume of attention in recent years due to the potential to provide insight into the physical condition of individuals. These technologies are advancing due to their good and high selectivity, fast analysis and low cost. A biosensor is an electrical device that measures biological signals and converts them into electrical signals based on the presence of an analyte in the medium of interest. Biosensors have allowed patients to detect disease at a very early stage to perform the treatment and these can be assess without the reliance of doctors. The first commercially available biosensor

and most well known is the glucose biosensor and these have been modified into three generations of sensing platforms (31).

2.6 Generations of Glucose Biosensing

Diabetes mellitus affects approximately 30 million people, where a vast majority are classified as suffering from type 2 diabetes (unable to produce enough insulin to meet metabolic requirements) (32). It is predicted that the number of individuals suffering from diabetes will increase by approximately 54% by 2030 (33).

The traditional method to monitor glucose for the insulin-dependent diabetic population has been through self-monitoring of blood glucose at a sampling frequency of four to ten times a day (34). This frequency variation is reflected upon lifestyle, activity levels, and insulin injection routine. Self-monitoring of blood glucose helps patients to achieve and maintain normal glucose levels to prevent the progression of micro and macrovascular conditions. Microvascular conditions consist of retinopathy, nephropathy, and neuropathy whereas macrovascular conditions consist of strokes and coronary artery disease (35).

Glucose biosensors were developed due to the need to maintain blood glucose levels. The glucose biosensor market is estimated to be $12.9 billion in 2022 and is forecasted to have a CAGR of 13% in the period 2023-2032 (36). A biosensor is defined as a ‘compact analytical device or unit incorporating a biological or biologically derived sensitive recognition element integrated or associated with a physio-chemical transducer’(37). These biosensors consist of a biological recognition element, a transducer, and a signal processing system. The biological recognition element detects the target molecules and these recognition elements include enzymes, antibodies, and receptors (38). A transducer can be either electrochemical, thermometric, optical, piezoelectric, and magnetic (39). Glucose biosensors are mainly electrochemical in nature due to cost effectiveness, superior sensitivity and reproducibility, and easy maintenance associated with the use of electrochemical sensors (40).

The most used glucose biosensor is enzyme based and these glucose measurements are centred on the interaction between glucose molecules and one of three enzymes; GOx hexokinase and GDH (40). Enzymatic glucose biosensors have evolved over the years and these are adapted for the screening, diagnosis, and long-term management of diabetes.

2.6.1 First generation of glucose biosensors

In 1962, the first-generation glucose biosensor was established by Clark and Lyons (38). The principle of the first-generation glucose sensor is based on three reactions. Initially, the immobilised GOx catalyses the β-D-glucose to produce gluconic acid and hydrogen peroxide. This reaction takes place due to the presence of FAD, which is the redox cofactor present inside GOx. The redox cofactor acts as the initial electron acceptor and is reduced to $FADH_2$ (Equation 1).

$$Glucose + GO_x - FAD^+ \rightarrow Glucolactone + GO_x - FADH_2 \qquad (1)$$

FAD is then regenerated by reacting with oxygen to form hydrogen peroxide (Equation 2).

$$GO_x - FADH_2 + O_2 \rightarrow GO_x - FAD + H_2O_2 \qquad (2)$$

The hydrogen peroxide produced is then oxidised at the platinum anode producing 2 electrons and therefore the number of electrons is proportional to the number of glucose molecules (Equation 3) (41).

$$H_2O_2 \rightarrow 2H^+ + O_2 + 2e \qquad (3)$$

First generation glucose sensors can be miniaturised in a facile manner. However, they possess common drawbacks like interference caused by redox active substances present in the blood such as ascorbic acid. Additionally, amperometric measurements of hydrogen peroxide requires a high potential (42). Therefore, further improvements require the use of electron mediators.

Just as the presence of exogenous and endogenous substances present in the blood can interfere with the accuracy of traditional glucose monitoring systems, the presence of such substances in the ISF will ultimately interfere with the accuracy of CGM systems resulting in high or low reported glucose values. These exogenous and endogenous substances include ascorbic acid, acetaminophen, maltose, xylose, dopamine, and mannitol. Ascorbic acid and acetaminophen are the most commonly used over the counter medication and are of particular concern and therefore, further improvements were performed using an electron mediator (43).

2.6.2 Second generation of glucose biosensors

To overcome the limitations found in first-generation glucose biosensors, the second-generation biosensor was established in the 1970s (44). This was achieved by replacing

oxygen with non-physiological electron acceptors also known as the redox mediators. The redox mediator carries electrons from the enzyme to the surface of the working electrode (45). Instead of producing hydrogen peroxide, a reduced mediator is formed, and this is then re-oxidised at the working electrode. The reduction of the mediator provides the amperometric signal, which is proportional to the glucose concentration (46).

There have been a variety of mediators used in second generation glucose biosensor like ferricyanide, ferrocene, quinines and TTF. Mediators are utilised as they do not react with oxygen, are stable in their oxidised and reduced states, and they react rapidly to the enzymes (47).

Although second generation glucose biosensors overcome the limitations of the first generation, the mediators have high toxicity and therefore can be harmful if leakage occurs during sensing (48). Although mediators are not biocompatible, the commercially available Freestyle Libre 2 and Freestyle Libre 3 use osmium mediators that have been FDA approved. Therefore MN systems utilising osmium mediators can be used in these patches similar to processes used in the FDA approved Freestyle Libre systems.

2.6.3 Third generation of glucose biosensors

This generation of glucose biosensors utilises DET between the enzyme and the electrode without the mediator, therefore overcoming the risk of toxic leakage. Electron transfer is performed using organic conductive materials based on transfer of charge complexes (49). These conductive materials include TTF-tetracyanoquinomethane (TCNQ), pyrrole-quinolinequinone enzymes (GDH-PQQ) and flavoproteins (GOx)

Third generation glucose biosensors are highly selective and are easy to fabricate (50).These biosensors are limited by the conductivity of electrode materials, on which DET enable enzymes are immobilized.

Utilising the various generations of glucose biosensors, MNAs have been fabricated to produce a glucose monitoring device. These MNAs use either extraction of extracellular fluids to detect glucose molecules or perform in-vivo monitoring of glucose. These MNAs have become an alternative sensing platform compared to the current blood glucose self-monitoring device (51).

Chapter 3

Introduction to MNs

3.1 Introduction

In 1976, MNs were initially conceptualised by Gerstel and Martin as a way to overcome the discomfort caused by drug administration (52). Although this laid the foundation for the initial development of MNs, it was only until 1998 when a novel approach for transdermal drug delivery using MNs were introduced (53). These MNs were fabricated using silicon to produce micron-sized needles that showed a dramatic increase in permeation of calcein through the skin. After a few years, the first commercially available micro projection array patch coated with a dosage of 1 and 5 µg of OVA was fabricated. The coated OVA was utilised to act as a model protein and provide a proof of concept for microprojectons as a drug delivery system (54). In recent years, MNAs have been utilized as a biosensor for point-of-care testing. These diagnostic platforms utilise two operating models:

1. Adapting MNs into in-situ electrochemical sensing.
2. Extracting ISF or blood that contain analytes through the MNs for further external testing.

Since initial conceptualisation of MNs, a literature search using key words “microneedle” and “microprojection” resulted in 3138 publications (Figure 3.1).

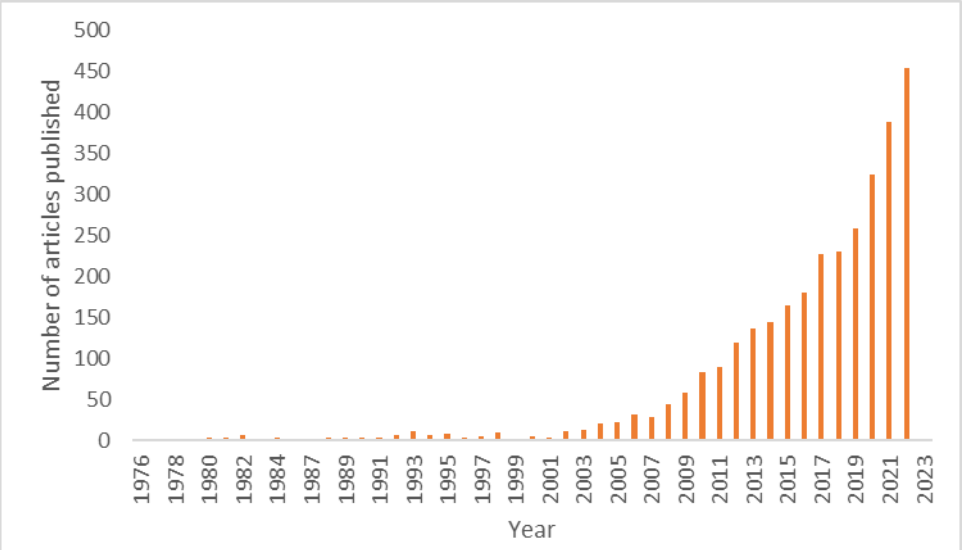

Figure 3.1 Graphical representation of the number of publications of MNs since initial conceptualisation

The use of MNs entails various merits and demerits as exhibited in Table 3.1 (55).

Table 3.1 Advantages and disadvantages of MNs (55).

Merits	Demerits
Allow drug molecules to surpass the SC, thus more drug molecules can enter the skin i.e. proteins and vaccines/antibodies.	Possibility of skin irritation or allergy to sensitive skin.
Better patient compliance due to painless and non-invasive administration.	As MNs are smaller and thinner, the tip can potentially break and remain inside the skin, causing prospective problems. Factors such as Young's modulus, tensile strength and MN geometry need to be consider to reduce the potential breakage upon insertion. Materials with high tensile strength and Young's modulus are preferable to reduce the hinderance of breakage. Furthermore, materials tensile strength greater than the yield strength will reduce fragility, as the yield strength is the point witnessed after the material deforms plastically and the tensile strength is the maximum stress the material can withstand (56).
Faster onset of action.	
Self-administration.	
Improved permeability and efficiency.	
Reproducibility in results with minimal inter-subject variability and bioavailability.	
Provide targeted drug delivery and diagnostics by varying MN dimensions to specific regions in the skin.	

Adapting MNs into sensors provide good applicability in continuous monitoring due to its coagulation-free characteristic	
MNs as biosensors provide high sensitivity towards the change of local tissues	

The demerits of MNs are fewer in number and can be overcome by using advanced material selection.

3.2 Types of MNs

The MNs can be classified into five types, dependant on their transportation method: solid, hollow, coated, dissolvable, and hydrogel MNs (Figure 3.2) (57). Each MN uses different strategies for drug delivery and biosensing that includes: “poke and patch”, “poke and flow”, “coat and poke” and finally “ poke and release”.

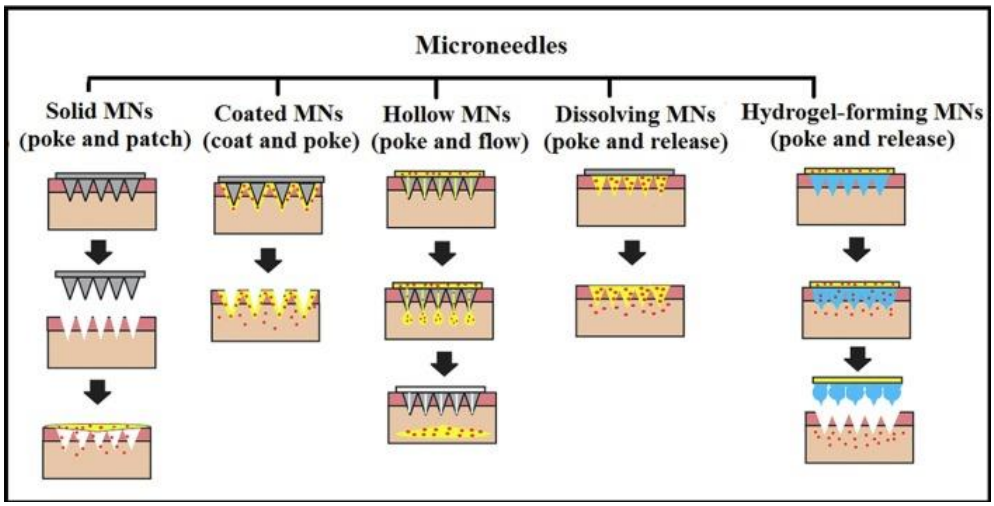

Figure 3.2 Schematic representation of the various sub-divisions of MNs (57).

The ‘poke and patch’ drug delivery is a technique utilising solid MNs to create reservoirs in the skin followed by a conventional drug application on the surface of the skin. Coating therapeutic agents on the surface of the MNs provides a ‘coat and poke’ drug delivery technique. Hollow MNs use a ‘poke and flow’ technique where the MNs are attached to a syringe and upon insertion can gradually inject drug dosages like a

hypodermic needle. Finally, for dissolvable MNs and hydrogel-forming MNs, these incorporate ‘poke and release’ through water soluble gels that will either dissolve or swell releasing drug upon insertion into the skin.

3.2.1 Solid MNs

Solid MNs are used as pre-treatment for the delivery of pharmaceutical compounds via the skin. This pre-treatment utilises a ‘poke and patch’ technique that is simply defined as; MNs poked into the skin to produce micron-sized channels followed by the application of a topical patch to the pores. Permeation of drug through these pores across the epidermis and dermis showed efficient and faster delivery of drug from a topical application (58). The simplicity of this fabrication makes it highly attractive, but this technique presents a few demerits (Table 3.2) (59).

Table 3.2 Advantages and disadvantages of solid MNAs (59).

Merits	Demerits
Easy to manufacture	The micropores remain open only for a limited period of time, therefore potentially stopping the delivery of active substances
Sharper tip comparative to hollow MNs	Risk of infection increases considerably
Greater mechanical properties due to geometry and materials	

Even solids MNs possess some demerits, these can be overcome by varying drug formulation or MN dimensions.

In 1998, the first solid MN for transdermal drug delivery was proposed using ion etching and photolithography of silicon wafers. Since the initial fabrication of solid MNs using silicon wafers, further materials such as glass, ceramic, metals, and polymers have been evaluated to produce a variety of different MNs with various dimensions for optimised application in drug delivery and diagnostics. (Figure 3.3) (60). Materials used to fabricate MNs have different mechanical and properties and this determines their application. The stiffness of MNs fabricated using metals, silicon, and ceramic is relatively high (over 10 GPa) and they do not degrade under normal conditions. Therefore, metal, silicon, and ceramic MNs are used to create pores within

the skin to promote drug permeation. Polymer based MNs have tuneable drug release characteristics by adjusting their concentration, crosslinking density, molecular weight, and charge properties. Diverse cross-linking methods and chemical modification enables polymers to mix with various drugs and forms hydrogels (61).

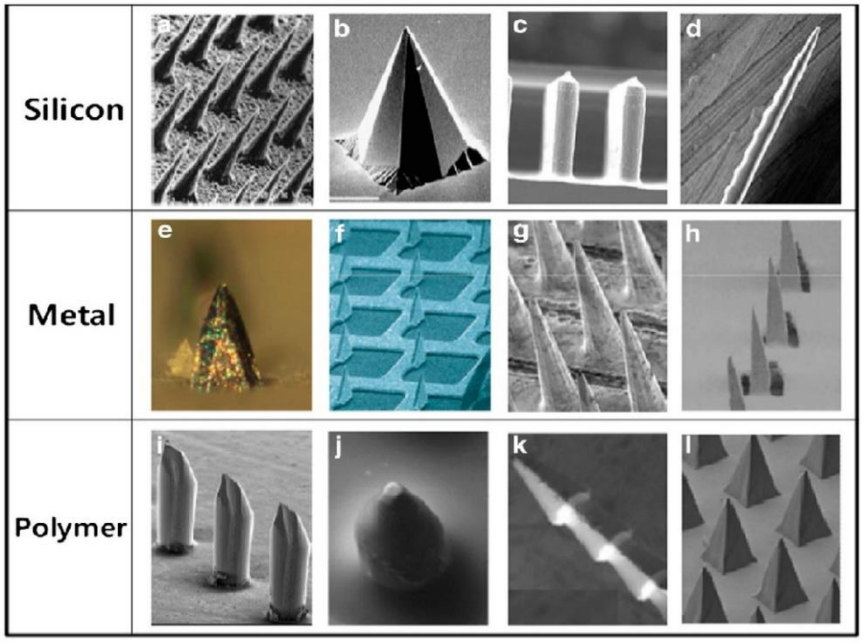

Figure 3.3 Various types of solid MNs made from metal, silicon and polymer (60)

3.2.2 Hollow MNs

Hollow MNs incorporate an empty core/chamber within a solid structure to enable drug to be injected or stored within the system. These MNs contain a bore and offer the possibility of injecting drug through the centre of well-defined needles by diffusion or by pressure driven flow for more rapid rates of delivery (62). Various hollow MNs have been fabricated and have shown a range of advantages compared to solid MNs, but have some drawbacks associated with them (Table 3.3) (63) (64).

Table3.3 Merits and demerits of hollow MNs (63) (64).

Merits	Demerits
Provides controlled drug release over time.	Relatively weaker structure compared to solid MNs.

Leveraging material formulation and fabrication parameters enable tuneable release kinetics.	Requires intensive care in terms of needle design and insertion methods.
Large doses of drug solution can be delivered.	Can suffer from leakage and clogging during the injection process. To determine dosage delivered is based on known concentrations of drug being dissolved to make up solutions of known concentrations. This dosage determination is similar to intravenous injections that employ known concentrations injected into patients.
Delivery of drug into the viable epidermis/ dermis allows high molecular weight compounds to be utilised.	
Due to the materials used for hollow MN fabrication, these can exhibit high stiffness.	

Even though hollow MNs can become blocked at the tip upon insertion into the skin, this can be overcome by either retracting the MNA or placing the bore on the side of the MN (65). These MNs can be fabricated using metal, silicon, ceramics, and glass where the width and height can be altered to allow rapid release, slow infusion or time-varying delivery rates (Figure 3.4) (66).

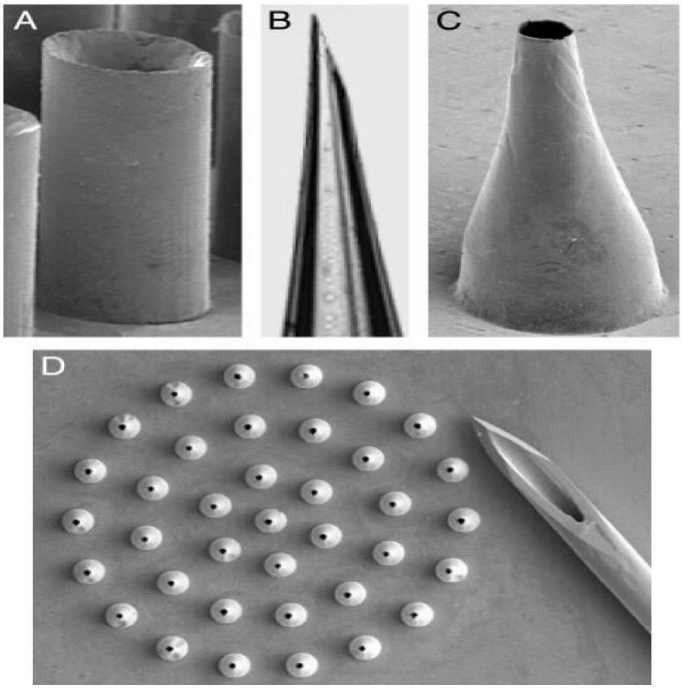

Figure 3.4 Image of various types of hollow MNs that have been fabricated (66).

3.2.3 Coated MNs

Coated MNs are solid MNs that are coated with a viscous drug solution that utilise the 'coat and poke' principle. The viscosity of the coated layer determines the volume of drug encapsulated within the coating (67). The most commonly used technique is the dip coating, but this can be complicated as there needs to be precise control on the dipping process (68).

Table 3.4 Merits and demerits of coated MNs (69) (70).

Merits	Demerits
Provides rapid delivery of drug to the skin	The remnant drug at the tip might lead to infections due to inaccuracy in coating methods. Can cause contamination on the substrate (71).
Delivers vaccines similar to intradermal and intramuscular routes	

Delivers proteins and DNA in a minimally invasive manner	

3.2.4 Dissolvable MNs

Dissolvable MNs were first produced in 2005 and facilitate rapid release of macromolecules. Drug delivery using these MNs involves a facile one-step drug application (64). Comparative to the most conventional route of topical creams, that provide convenience for therapeutic drug delivery, dissolvable MNs overcome the slow onset and short activation duration. This is obtained by penetrating the SC and dissolving into the ISF, thereby releasing the encapsulated drug at the epidermal layer. Encapsulating a higher concentration of drug within the array provides a platform for rapid and highly effective drug delivery without further application of MNs to reach the optimal therapeutic range (72).

Table 3.5 Merits and demerits of dissolvable MNs (73)

Merits	Demerits
Designed to encapsulate a variety of drugs.	Low mechanical strength.
Inexpensive.	Inconsistent penetration can lead to drug wastage.
Ease of use.	Inconsistency in fabrication.
The water-soluble material used to fabricate the dissolvable MNs are widely available.	
Cost-effective.	
Created without harsh processing conditions.	

The tip of the dissolvable MNs are loaded with drug using a two-step casting method (Figure 3.5) (74). Dissolvable MNs are made from water soluble materials such as maltose, polyvinyl pyrrolidone, and albumin (75). When they are inserted into the skin, the biocompatible and water-soluble MNs dissolve to release the drug encapsulated without leaving behind a biohazardous sharp tip (76).

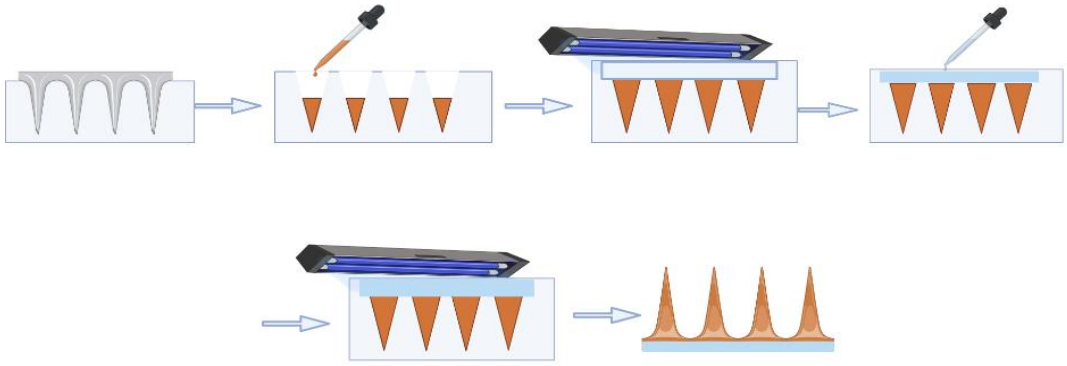

Figure 3.5 Schematic representation of the process to produce drug loaded dissolvable MNs

3.2.5 Hydrogel MNs

These MNs are fabricated using hydrogels were first reported by Donnelly et al in 2012 and are the newest form of MNAs (77). The polymers that form part of these MNSs swell upon insertion due to the hydrophilic nature of the crosslinked hydrogel. The swellable nature can be utilised for transdermal drug delivery and diagnostic applications as the MNs can either uptake biomarkers present in the ISF surrounding the cells in tissue spaces or deliver drug incorporated within the polymeric structure (78).

Hydrogel forming MNs are able to overcome some of the limitations associated with conventional MNs stated previously (Table 3.6)

Table 3.6 Merits and demerits of hydrogel forming MNs (79).

Merits	Demerits
Minimally invasive.	Cannot be reused.
Higher drug loading capacity.	Slow fluid uptake.
Tuneable drug release rate.	Delay in swelling.

Overcome biocompatibility issues associated with silicon or metallic MNs.	Maintenance of drug release within therapeutic levels following a burst release.
These MNs can be sterilised prior to insertion and can be removed with minimal damage to the MNs and skin.	

Since being reported in 2012, there has been a recent rise in the use of hydrogel based MNAs. Drug encapsulated within the hydrogel structure of the MNs is through the use of polymers that are crosslinked with tartaric acid or its derivatives with the incorporation of the therapeutic agent. In the dry state, hydrogels have a high mechanical strength, which means that they can penetrate through the skin without distorting the MN structure (80).

The hydrogel used to create the MNs must be biocompatible and therefore will exist within the tissue without causing any immunogenic response. Majority of hydrogels used in MN fabrication are biocompatible and any breakage occurring within the tissue upon insertion will have no effect on the patient and will degrade within the body using natural processes (Table 3.7). To support the biocompatibility of hydrogels, skin irritancy tests were performed on willing patients. Skin irritancy tests consisted of hydrogel forming MNs being inserted into patients for a set amount of time. This is followed by examination of the insertion region for any irritation that had occurred (81).

Table 3.7 Various hydrogels used in the fabrication of MNs and the merits and demerits of each type (82).

Hydrogel	Merits	Demerits
PMVE/MA	•Excellent mechanical strength. •Low toxicity. •Biocompatible. •Strong antimicrobial properties.	Slow swelling rate.

PMVE/ MAH	•Excellent mechanical strength. •Low toxicity. •Biocompatible. •Strong antimicrobial properties.	Slow swelling rate.
PVA	•Easily incorporate various other polymers to enhance certain properties. •Prolonged drug release.	Difficulty in synthesising MeHA.
pHEMA	Proven light responsive drug release.	Slow swelling rate.
PVP	•Excellent mechanical properties. •Efficient drug delivery •Biocompatible.	

Chapter 4

MN Fabrication Techniques

4.1 Introduction

The techniques used for the fabrication of MNs varies based on the material and the potential application requirements. The most commonly used techniques for MN fabrication are micro moulding, wet and dry etching with lithography and laser cutting.

4.2 Micro moulding Techniques

Various polymer, hydrogel, and dissolvable MNs have been produced by filling a prepared MN mould with a liquid formulation (Figure 4.1) (83). Majority of moulds have been created using either a lithographically modified silicon wafer or a PDMS mould (84). From there a polymeric solution is then poured into the moulds followed by air bubble removal using either a vacuum or centrifuge. Based on the polymeric complex, the moulds are either dried in an oven or UV cured and upon demoulding the MNs are produced (85). Micro moulding is advantageous compared to other fabrication techniques as they are relatively simple and cost-effective at an ambient temperature (86).

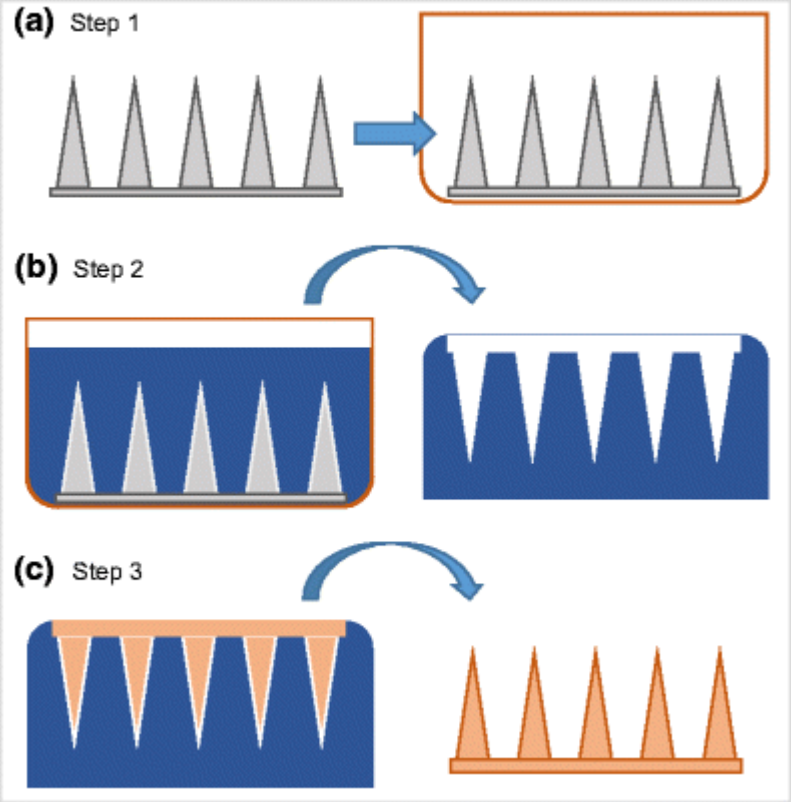

Figure 4.1 Schematic representation of micro moulding techniques: (a) step 1, a master mold is fabricated from a strong material, such as metal or silicon, and prepared for use as a master mold; (b) step 2, a negative mold is made from the master mold which is usually PDMS; (c) step 3, drug is loaded into the negative mold usually through a polymer solution that creates the final MN structure of the same shape and dimensions as the master mold (83).

MNs have been created from materials other than polymers such as silicon and these utilise alternative fabrication techniques. The most common process is lithography of silicon wafers followed by wet and dry etching to form the MNAs.

4.3 Lithographic Techniques

The most commonly used lithographic technique for MN fabrication is photolithography. In photolithographic techniques, a mask is used, which acts as a template for generating the desired pattern on a wafer surface. The mask consists of a quartz plate that allows UV light to pass through a predesigned pattern. To transfer the pattern from the mask, a photoresist is coated onto the surface of the wafer. A photoresist consists of:

- A polymer that changes solubility upon exposure to UV light.
- A solvent that thins the photoresist to a required thickness.
- A sensitiser.

- An additive used to control the reaction caused by exposure to UV light (87).

Two types of resists can be used, a positive and negative photoresist. Exposure of a positive resist to UV light results in degradation of exposed polymers, making them more soluble in a developer.

In the case of negative photoresist, the exposed polymer will strength and therefore regions not exposed to the UV light will be removed upon soaking in developer (88) (Figure 4.2) (89).

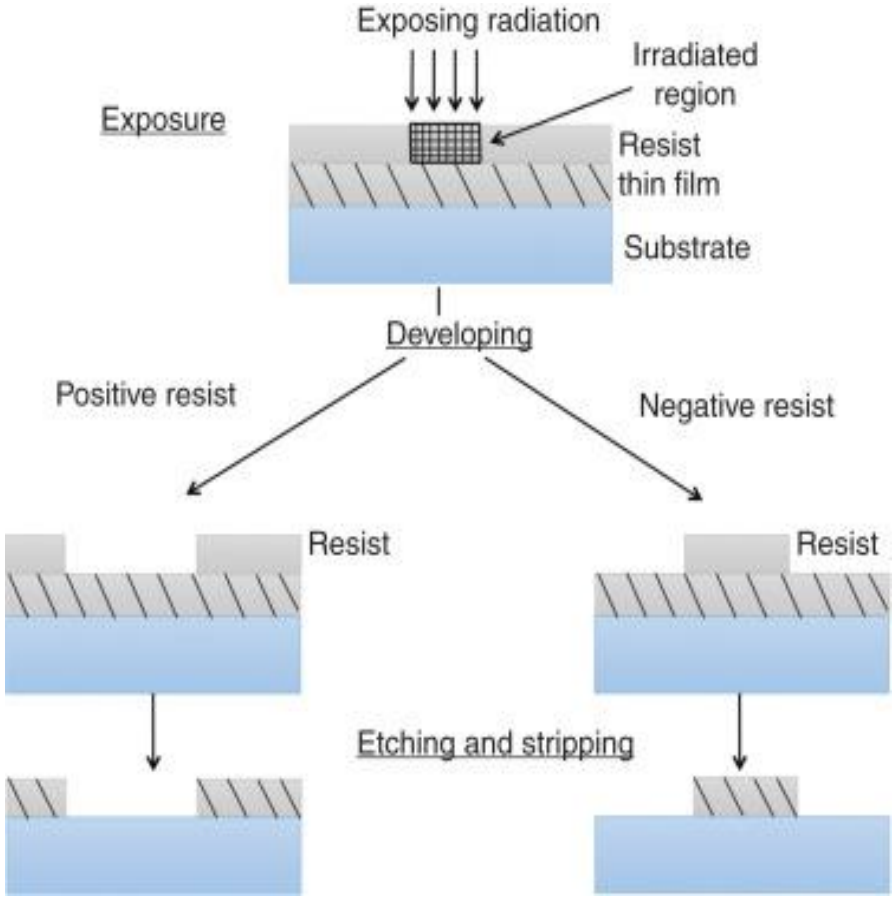

Figure 4.2 Schematic representation of positive and negative photoresist (89).

Post photolithography, the wafers can be etched by using a strong acid or caustic agent to etch the regions that are unprotected by the photoresist. There are two types of etching techniques used post photolithography masking: wet etching and dry etching. Wet etching removes unprotected regions by submerging the substrate in a strong acidic solution. For a silicon substrate, hydrofluoric acid is generally the acid used as it is capable of reacting

with the layer of silicon dioxide that forms on the surface of silicon (90). Wet etching possess merits and demerits as discussed in Table 4.1.

Table 4.1 Merits and demerits of wet etching techniques (91).

Merits	Demerits
Easy to implement.	Expensive.
Can be commercialised.	Highly isotropic, will attach the substrate in all directions leading to a semi-spherical etch process.
High etch rate that makes etching fast and avoids undercutting of the protective layer	Requires large amounts of chemicals.
Good material selectivity.	Etching solutions needs to be changed regularly to maintain the etch speed.
Simplicity of the equipment.	

Compared to the wet etching process, dry etching is achieved using a vapour phase or plasma etcher. The most commonly used type of dry etching is the reactive ion etching (RIE). This etching method is a plasma process where radiofrequency (RF) ions etch substrate in a low-pressure chamber. This technique allows anisotropic etching with reduced lateral etch rate and vertical sidewalls. This method is essential when narrow channels are required or when high aspect ratio structures need to be fabricated (92).

A further alternative for MN fabrication is the use of laser cutting techniques to produce metal MNs from nickel, titanium and stainless steel. Metal MNs provide good mechanical properties and biocompatibility compared to silicon MNs and have been widely used for drug delivery and sensing applications.

4.4 Laser Cutting Techniques

To produce metal MN, 3D laser cutter has been applied with the use of a CAD software to create a desired shape, geometry, and dimensions of a MN. As the MNs size and orientation are designed through a CAD software, scalability can be obtained by altering the design to obtain high volumes of MNs per flat metallic sheet. Therefore upon one manufacturing process, multiple arrays can be fabricated at a time.

For laser cutting, the laser beam follows a predetermined MN shape across a metal surface, then cleaned under hot water before being bent at 90° to the vertical plane of the

base. To make sure that the surface is smooth, the MN tip is sharpened and thickness is reduced. The cut MNs are then electropolished, washed, and dried with compressed air (68).

Chapter 5

MNs for Drug Delivery

5.1 Introduction

To overcome patients' discomfort and the disadvantages associated with oral and transdermal drug delivery, MNs have been utilised to incorporate needle delivery capabilities in addition to improving patient compliance and safety. These MNAs are a combination of parenteral and transdermal drug delivery systems. As MNs are similar to that of a transdermal patch, they provide minimal discomfort to paediatric patients as well as comparatively effortless application methods which makes them desirable for long term use. Moreover, the small dosage volume required by children eases the attainment of therapeutic concentrations (93). Varying between 50-900 μm in height, their short length allows MNs to be minimally invasive, overcome the SC barrier and therefore possess the ability to deliver drug into the systemic circulatory system. Upon application of the MN, they are secured into place using an elasticated bandage or tape to ensure they don't fall off prior to administration of dosage (76). The length and width of the MNs allow for effective delivery of drug through the dermis coupled with the reduction in pain experienced by patients. This pain is overcome by the avoidance of the nerves or puncturing of blood vessels found in the dermis.

By 2027, 50% of all novel therapies are predicted to be biological, these are mainly proteins and peptides due to their attributed target specificity, high potency, and favourable safety. Nonetheless, because of the inherent properties of proteins and peptides such as the high molecular weight, poor stability, and conformational flexibility they are mainly administered by injection. MNs are a promising strategy for protein and peptide delivery to treat various diseases but successful formulation and handling is required to ensure optimised stability and efficacy. Recently MNs have been employed to efficiently deliver macromolecules along with nanoparticle based therapies. These are advantageous as these can be leveraged to improve the transdermal delivery efficiency of proteins and peptides (94).

As MNs are becoming more desirable there is a wider range of applications to consider for drug delivery capabilities. This aspect of drug delivery considers the various types of

MN that can be fabricated whether it be solid, coated or hollow to provide optimised delivery of drug for optimised application for patients.

5.2 Acute vs Chronic for Transdermal Drug Delivery

Acute pain usually lasts less than 7 days but often lasts up to 30 days with a chance of reoccurrence periodically. Even though acute pain usually resolves quickly, in some cases it may be persistent that it becomes chronic. Chronic pain is defined as the pain lasting more than 3 months and substantially affects physical and mental functioning.

Transdermal patches are used for pain relief when the patient has intolerant side effects and is unable to take oral medication, the confidence of administration may improve pain control and can be used in combination with another potentiating strategy that produces a synergistic effect. On the other hand, transdermal patches are not used for the curing acute pain when a quick dosage is required and when the dosage is equal to 30 mg/ 24 hours or less.

For acute pain, the treatment should act on the cause and the sensation of pain should be treated as part of the treatment. In mild pain, the first option utilised is paracetamol and for moderate pain, NSAIDs alone or opioids are the best options. There are several options of transdermal patches that are available on the market whose active ingredients are ketoprofen, capsaicin and diclofenac. Having treatment in patches offer advantages such as self-administration without the need of a profession, the dosage is sustained, can continue with daily activities, comfortable to wear and avoids the hepatic metabolism step.

Chronic pain is usually associated with malignant and non-malignant conditions, therefore transdermal drug delivery is effective for the treatment of this type of pain as the amount administered through intravenous and oral treatment can be harmful in a short period of time. Approved transdermal drug delivery systems for clinical use are composed of opioids such as buprenorphine and fentanyl. These systems can be directed to elderly patients whose metabolisms have decreased and the ratio in the body of fat/muscle is altered, therefore the dosage of drug should be decreased. Alternatively, for young adults in the treatment of chronic pain they may suffer from respiratory depression when opioids and non-opioids are delivered by other routes. Therefore, transdermal drug delivery systems for chronic pain are contraindicated in the management of acute and post-operative pain (95).

5.3 Drug delivery mediated by dissolvable MNs

In recent studies, polymeric MNs have been used to assist in the delivery of Vitamin B12 for people a Vitamin B12 deficiency. This deficiency affects millions of people around the world and therefore could be considered as a public health problem. Subcutaneous or intramuscular injections of cyanocobalamin are the main point of treatment for patients suffering from vitamin B12 deficiency. The use of MNs will provide minimally invasive and easy to handle alternatives to this. Micro-moulding was used to incorporate the vitamin with the polymer matrix to produce dissolvable MNAs. For evaluation of the dissolution ability of the MNs, the array was inserted into porcine skin and it was found that 50% of the MNs had dissolved in 30 s. A complete dissolution of the MNs was achieved at 120 s. Franz cells, a technique used to determine ex-vivo and in-vitro drug permeation, were used to reiterate the ability of the MNs to deliver vitamin B12 and 70% of the incorporated drug was released within 5 h. This study clearly showed the ability to successfully incorporate vitamin B12 into dissolvable polymer MNs and deliver a therapeutically relevant dose within a duration (96).

Polymer MNs have also been used to produce implantable powder carrying MN systems for the administration of insulin powder. Micro-moulding techniques were used to fabricate the powder carrying MNs within the micro-shelled structure with an empty cavity in the central region. Insulin powder is then loaded into the empty cavity with a protective coating of Carboxymethyl Cellulose (CMC) on top. The MNs were inserted into the skin and in contact with ISF the MN began to dissolve releasing the insulin powder. To analyse the release of the powder, calcein was loaded into the empty cavity and the MNs were inserted into skin mimicking agarose gel and fluorescent images were obtained. Fluorescent imaging showed after insertion into the agarose gel, fluorescence increased as more calcein was dissolved. Franz cells were then used to test the release of both calcein and insulin over a period of 24 h. Calcein delivery into the Franz cell showed complete drug release after 24 h in comparison to insulin that delivered drug completely at 6 h (97).

Dissolvable polymer MNs have been used for the delivery of cetirizine hydrochloride, which is an anti-histamine drug used to treat allergies. Antihistamines are administered when a person has undergone an allergic reaction, in anaphylaxis rapidly develops airways, breathing, circulation problems and is usually associated with skin and mucosal

changes. In these scenarios oral drug delivery is not feasible and usually administered intravenously or intramuscularly by healthcare professionals (98). This was carried out by loading the drug into two different polymer matrixes, one containing chitosan dissolved in acetic acid and the other containing sodium alginate. For drug permeation through the skin, Franz cells using spectrophotometric methods were used with spectrophotometric absorption data following a linear regression over a concentration range of 10-60 μg/ml. The chitosan MNs showed a plateau after 7.5 h. In comparison the sodium alginate MNs steady state concentration was 973 $\mu g/cm^2$.hr. After 6 h of application, the chitosan and sodium alginate MNs had a 45 % and 25 % higher drug concentration, respectively (99).

5.4 Drug delivery mediated by coated MNs

Biodegradable gelatin methacryloyl MNs have been fabricated using micro moulding for the delivery of anticancer drug doxorubicin. The gelatine methacryloyl delivered the drug through both swelling and enzymatic degradation of the scaffold, which allowed gradual release especially at high crosslinking degrees. To assess the MNs swelling ability, DPBS was used to simulate the body fluid and tested the swelling ratio. Different crosslinking times resulted in a higher swelling ratio, which was due to the relatively high solubility of the MNs with low crosslinking degrees. The enzymatic degradation of the MNs was explored by the incubation in collagenase solution. This showed that a high crosslinking degree results in slow degradation after 24 h. This was reiterated by testing the fluorescence of the drug in the presence of protease. The fluorescence showed that after being crosslinked for 60 s the MNs released approximately 50% of the encapsulated drug within the first 2 h and then the remaining volume was released slowly over a period of 22 h (100).

3D printing has been used to prepare scaffold MNs for the fabrication of RNA membrane-based MNs. An RNA membrane was created with extremely long RNA strands that were generated by complementary rolling circle transcription followed by evaporation induced self-assembly and hybridisation of the RNA transcripts. The RNA membrane-based MNs showed sequential release of the RNA membrane over a period of 5 min, which showed the RNA membrane can be easily detached from the MN surface. The study also showed that over 80% of the RNA on the MN surface had been efficiently transferred to the

porcine skin, showing rapid transfer of the RNA contents and therefore potential utilisation in subcutaneous drug delivery (101).

Coated MNs have been used for the treatment of hyperhidrosis, which is the excessive sweat secretion beyond the amount needed for thermoregulation, using botulinum neurotoxin A (BoNT/A). L-Polylactic acid MNs were fabricated with micro-milling process and dip-coated in a solution of BoNT/A, a thickening agent of CMC, surfactant (Tween 80) and a stabiliser (HSA). The rate of diffusion was tested using a FITC-conjugated mouse IgM that has a similar weight to BoNT/A and can be seen using a fluorescent microscope. On insertion into porcine skin, 58.9% of IgM-FITC dissolved within 2 min, with the dissolution rate gradually increasing for a further 30 min (102).

5.5 Drug delivery mediated by hollow MNs

Hollow MNs have been used for the delivery of insulin for patients suffering from type 1 diabetes in a two phase study. The hollow MNs were fabricated by pulling fire-polished borosilicate glass pipettes using a micropipette puller and beveller. In phase one the minimum MN insertion depth was determined based on the pharmacodynamic response to insulin at different MN insertions. To determine this, 10 units of 100-U insulin was administered using a conventional catheter. Initially plasma free insulin levels rose to a peak after 1 h and glucose levels in the plasma decreased accordingly. This was followed by the insertion of 10 and 15 units of 50-U Humalog at depths of 5 mm and 3.5 mm and showed insulin levels increasing to a peak at 30 min after delivery. Areas under the insulin curves were analysed and showed after an hour the 1 mm MN led to higher insulin absorption and compared with the change in plasma glucose levels revealed that the shallow 1 mm MN delivery was most effective in reducing the glucose levels. Phase 1 established that the 1 mm MN depth was not only the minimum, but also the optimal transdermal depth for effective insulin delivery. In phase 2, the minimum depth was used in determining the efficacy of hollow MNs for insulin delivery to reduce postprandial glucose levels. This was assessed using bolus infusion immediately before a 75 g carbohydrate meal, followed by assessing the insulin delivery through a subcutaneous catheter using a bolus of 7.5 U of 100-U Humalog insulin. In the first hour the plasma free insulin levels gradually rose before a steady decrease and the plasma glucose levels increased for an hour and a half followed by a decline. Evaluating these results showed the area under the insulin curve over a 1 and 2 h periods demonstrated that the

pharmacokinetics of the insulin delivery was faster from the MNs compared to the catheter and that they were effective in the reduction of plasma glucose levels (103).

Hollow MNs have been investigated in providing a minimally invasive method to inject nanoparticles and microparticles into the suprachoroidal space for drug delivery at the back of the eye. The MNs were fabricated from borosilicate micropipette tubes and these were inserted to the base of the sclera to target the suprachoroidal space. Initially red fluorescent sulforhodamine B was used to test whether the MNs were able to inject a liquid into the suprachoroidal space and spread this formulation around the eye from a single injection. A cross section of a pig's eye that had been frozen after the injection of 35 µl of sulforhodamine clearly shows selective delivery just below the sclera and above the choroid. Different sized particles were then administered into the suprachoroidal space. The findings indicated that smaller particles can flow through the scleral tissue more easily than larger particles that were blocked once injected, increasing MN length will therefore be able to overcome this hurdle (104).

5.6 Drug delivery mediated by solid MNs

Solid MNs have been used for on demand delivery of liquid phase macromolecular drugs by integrating the MNs with transdermal patches. Using micro moulding techniques, polymethyl methacrylate MNs were fabricated and attached onto medical tape at the centre of an anti-seepage gasket. A sponge that acted as a liquid drug reservoir was placed in the inner circle of the gasket and bonded on the medical tape to form a touch actuated MNA patch. Rhodamine B (RhB) was used to act as the model drug and was soaked into the sponge followed by the touch actuated MNA patch being taped onto fresh rabbit skin. A press and release method was used to push the MNs through the sponge and into the skin and this method showed a maintained delivery of RhB for a period of 10 min. The solid MNs were also poked into the skin under a maximum compression of 5 N and a patch containing RhB was placed onto the punctured skin for a period of 30 min. Poke and patch showed that the solid MNs were able to assist rhodamine B across the subcutaneous layer due to the microchannels created. In comparison, the touch actuated MNA patch showed a faster diffusion rate, which therefore resulted in a deeper diffusion depth and this could be due to the insertion of the needles repeatedly opening up the microchannels for permeation and carrying the drug into these microchannels (105).

Galanthamine was transdermally delivered using 70-80 μm long solid silicon MNs test feasibility. The MNs were made using wet etching of silicon using potassium hydroxide, which is a combination of photolithography and reactive ion etching techniques. For diffusion studies the skin was pre-treated four different ways, firstly sharp tipped super short MNs were pierced into the skin at different forces, then sharp tipped and flat tipped MNs were pierced into the skin at a pressure of 7 N. This was followed by flat tipped MNs being inserted into the skin at 7 N for different times and finally three flat tipped MNs were pressed into the skin at 7 N. When increasing the insertion force from 1 to 5 N, a significant increase in the amount of galanthamine permeating was found, and also histological section verified a formation of micro-conduits with different diameters and depths. After increasing the insertion force over 5 N the permeation of galanthamine did not increase and therefore no significant differences from 5 to 8 N were present, showing that the insertion force does not significantly affect the transport enhancing properties. When looking into flat tipped and sharp tipped silicon MNs, flat tipped MNs were better at facilitating galanthamine across the skin. Finally, galanthamine permeation was increased when the retention time was increased, however the volume of galanthamine permeated after 1 min did not show much statistically different (106).

Chapter 6

MNs for Diagnostics

6.1 Introduction

Biosensors are devices that measures biological or chemical reactions by producing a signal that is proportional to the analyte present in the matrix. These biosensors can be used in applications such as disease monitoring, drug discovery, or markers that are indicators of a disease in bodily fluids (107). Biosensors consist of five components: the analyte, bioreceptor, transducer, electronics, and display. The analyte is a substance of interest whose concentration is to be measured and the bioreceptor is a molecule that specifically identifies the analyte. To obtain a measurable signal from the biorecognition a transducer is used, which the electronics process ready for it to be displayed for interpretation. The transducer used can alter the type of biosensor and can be either electrochemical, optical, electronic, piezoelectric, gravimetric or pyroelectric (108).

Table 6.1 History of biosensors (107)

Year	Biosensor	Discoverer
1906	Electric Sensor	M.Cremer
1909	pH Sensor (concept)	Soren Peder Lauritz Sorensen
1922	pH Sensor	W.S.Hughes
1909-1922	Enzyme-based Sensor	Griffin and Nelson
1956	Oxygen Sensor	Leland C.Clark Jr
1962	Glucose Sensor	Leland Clark
1969	Urea Sensor	Guilbault and Montalvo Jr
1970	Ion sensitive field effect transistor	Bergveld
1975	Fibre optic biosensor for CO_2 and O_2 detection	Lubbers and Opitz
1975	Commercial glucose sensor	YSI
1975	Microbe-based immunosensor	Suzuki

1982	Fibre optic biosensor for glucose detection	Schultz
1983	Surface plasmon resonance immunosensor	Liedberg
1984	Mediated amperometric glucose biosensor	
1990	Surface plasmon resonance-based biosensor	Pharmacia Biacore
1992	Handheld blood biosensor	i-STAT

For the rapid detection of analytes, PoC testing was developed which facilitated better disease diagnosis, monitoring, and management. This will therefore lead to improved outcomes to patients as the disease can be diagnosed at early stages and enables early treatment (109). These PoC devices have key requirements, which includes simplicity of use, robustness of reagents and consumables in storage, concordance of results with established laboratory methods and safety of use. Devices meeting these criteria can then be classified into small handheld devices and large bench top devices with more complex built in fluidics. Small handheld PoC devices often use fingerstick, capillary samples, which are inserted into the instrument without a sample container. By using this method, it becomes highly convenient and therefore reduces associated risks. As a result, the testing process must be designed to minimise risk with appropriate training and documentation (110).

Lateral flow biosensors are self-operating chromatographic devices that perform rapid assays on a membrane with the addition of a single sample. Pregnancy tests are the most well-known lateral flow biosensor, but they have been applied to the detection of parasites, bacteria, viruses and biological markers. These biosensors consist of a membrane and several functional pads that are connected to each other and are assembled onto an adhesive backing card. The membrane is deposited with detection molecules such as antibodies and are adhered next to the conjugate pad. Furthermore, the conjugate pad is bonded next to the sample pad, and this is where the analyte detection molecules are deposited. Finally, the absorbent pad enhances the capillary driving force and absorbs all unreacted substances. When loading an analyte, the lateral flow biosensor will either show both a coloured test line and a coloured control line if a positive result is obtained

or a single-coloured control line for a negative result (111). Lateral flow biosensors are advantageous as they provide cost effective, rapid and easy testing. They also have a long shelf life and do not need special storage such as refrigeration. The major demerits associated with lateral flow strips is that they have limited sensitivity and cannot be used to measure multiple analytes. They also cannot have enzymes immobilized on the sensor surface (112).

Multi-analyte dipsticks for urine analysis are performed in any hospital, clinical laboratory or health clinic. Dipsticks are a cost effective method and have been shown to be sensitive for diagnosing urinary tract infections. These dipsticks can be used to assess scope for further sample analysis. There are also limitations associated with this test, which include the inaccuracy in quantifying specific indicators of a disease, which can be detrimental in determining the presence of common conditions. Therapeutic drugs and chemical preservatives can interfere with the tests and therefore make them invalid. Test strips, which have been stored poorly or are near their expiration date have the additional possibility of creating false negative results (113).Most commonly used immunoassays are enzyme-linked immunosorbent assays (ELISA) and immunoturbidimetry (IT). ELISA are advantageous as it is an easy to perform simple procedure, which is highly specific and sensitive making it both efficient and cost effective. Despite the positives, immunosensors do have their drawbacks, namely that it is labour intensive and expensive to prepare the antibody, and there is a high possibility of false positives and negatives which can be caused by insufficient blocking of the immobilised antigen (114).

Most biosensors reported till date are electrochemical in nature. Electrochemical sensors are analytic devices that transduce biochemical events to electrical signals such as enzyme-substrate reactions (115). An electrochemical sensor consists of an electrode for the immobilisation of a bioreceptor, which is specific to the biomarker of interest. The electrode also facilitates the transfer of electrons, which are produced as a result of the reaction between a redox active molecule and bioreceptor-biomolecule complex. The reaction being monitored generates either a measurable current (amperometry), charge accumulation or potential (potentiometry) or alters the conductive properties of the medium between electrodes (conductometry) (116).

The most widely used electrochemical sensors are lab on chips (LoC), which are miniaturised biomedical or chemical laboratories that are built onto a glass or plastic chip.

These devices have a network of microchannels, electrodes, sensors, and electrical circuits, which can duplicate various specialised functions such as clinical diagnostics, DNA scanning, and electrophoretic separation. LoC are advantageous as they are dramatically reduced in sample size, much shorter reaction and analysis time, high throughput, automated and portable (117). At microscale levels, chemical interactions between materials can be more significant, but this can result in complications during experiments that are not found in other laboratory equipment. To overcome this complication, lab on a chip devices can operate on nanoscale levels and these provide stronger chemical interactions between materials.

Recently, sensing platforms have been adapted to MN platforms to detect biomarkers present in the ISF. As stated in previous sections there are different types of MNs and each of these MNs have been reported in literature to have been used for diagnostic applications.

6.2 Solid MNs for diagnostics

Solid poly(L-lactide) was used for the detection of specific miRNAs with the use of a hydrogel containing alginate-peptide nucleic acid. The hydrogel was developed using three steps. Briefly, 0.01 wt % of positively charged poly(L-lysine) was applied to the surface of the MNs, which forms an absorbed layer that facilitates electrostatic adhesion of the alginate hydrogel. Once the solution had dried on the surface of the MNs, a solution comprising of alginate-PNA, sucrose and double-distilled water (ddH_2O) was pipetted onto the surface and finally a cross-linking solution comprising of $CaCl_2$ was applied. The ability of the MNs to sample and isolate nucleic acid in a sequence specific manner was tested by dipping the needles into various solutions containing different amounts of DNA-210 labelled with Alexa 647 dye. After a period of 15 min the MNs were washed and left to dry overnight before the fluorescent scanner was used. A plot of mean fluorescent intensity against DNA concentration illustrates the MN ability to detect target concentrations as low as 6 nM over a 0-500 nM range. A plot of mean fluorescent intensity against DNA concentration illustrates the MNs ability to detect target concentrations as low as 6 nM, with a linear regime across almost 2 orders of magnitude (6-500nM). Sequence specificity was the confirmed by demonstrating statistical significant ability of the MN patch to discriminate between a complementary and non-complementary DNA target, both labelled with the same fluorophore (118).

Solid polycarbonate MNs have been developed for continuous detection of β-lactam, which is an antibiotic used for the management and treatment of bacterial infections. Two of the working electrodes were coated with an enzyme hydrogel containing β-lactamase, poly(ethylenimine)(PEI), glycerol and poly(ethylene glycol) diglycidyl ether (PEG-DE). For a control, the reference electrode and one of the working electrodes were coated with a hydrogel containing PEI, glycerol and PEG-DE. Once the hydrogel mixtures were applied to the surface of the MNs, they were inverted and cured at 45 °C for 2 h. In a 10 mM PBS solution the LOD was found to be 6.8 ± 1.04 μM. The MNs were also inserted into healthy patients for 6 h, which showed the stability of the coating on the MNs (119).

Polymer MNs have been used for multi-analyte sensing using a three-electrode system for the measurement of glucose and lactic acid. The MNs fabricated employing photocurable hydrogels incorporating 20 mg/ml of GOx and 15 mg/ml LOx. A 1 ml pre-polymeric solution consisting of 2% v/v of Darocur and 1% w/v of redox mediator vinyl ferrocene (VF) to liquid PEGDA was deposited onto a quart slide and exposed to UV light. The MNs that were created by mixing the pre-polymeric solution with an enzymatic solution which created a negative photoresist were adhered to the PEGDA layer. A three-electrode system was used to test the performance of the biosensor, this consisted of a platinum wire, a saturated silver chloride reference electrode and the MNs as the working electrode. A solution containing a mixture of PBS and $MgCl_2$ was used to mimic the interstitial fluid. To demonstrate the activity of the redox mediator, the influence of the polymeric matrix on the redox kinetics and the reversibility, cyclic voltametric measurements were carried out. To test the effect of analyte concentration on the electron production, chronoamperometry was performed for a period of 5 min after the aliquots were added. The CV showed clear anodic and cathodic peaks at 300 and 200 mV, respectively, which correlate with typical peak values of free VF. This result confirmed that the polymeric matrix had no effect on the activity of the redox mediator. The biosensors exhibited a linear response to glucose with a sensitivity of 18 ± 3 nA mM^{-1} in the range of 0 to 4 nM. For lactic acid the response was also linear with a sensitivity of 3.5 ± 0.2 nA mM^{-1} in the range of 0 to 1 mM. The sensors exhibited sensitivities of 2.7 ± 0.7 mM and 0.45 ± 0.03 mM for glucose and lactate, respectively (120).

6.3 Hollow MNs for diagnostics

Hollow MNs have been used in the detection of L-Dopa, which is used as an anti-Parkinson's drug. The MNs have been used as electrochemical sensors for continuous monitoring and measurement of the targeting ability of L-Dopa. Two of the bores in the MNAs were filled with carbon paste electrode transducers and therefore were acting as two working electrodes. One of the working electrodes had carbon paste that had been unmodified, while the other working electrode had the enzyme tyrosinase incorporated. The third MN was used as a reference electrode which contained a silver wire through the bore. Chronoamperometry was used to analyse the response of the enzymatic MNs to L-Dopa in artificial ISF over the range of 20 to 300 μM. The dose response curve showed high linearity with a sensitivity of 0.048 nA/μM. Additionally, SWV was used over a dynamic range between 20 and 360 μM. Clear oxidation peaks are present at a potential of 0.2 V and the peak current increases linearly up to 160 μM before slight curvature occurs (121).

Hollow MNs have also been used to continuously monitoring of ketones, which can be useful in the early diagnosis of insulin deprivation. Two of the MNs were filled with carbon paste to be used as a working electrode to detect both β-hydroxybutyrate (HB) and D-(+)-glucose anhydrous (GL) therefore making it a multimodal sensor. A second hollow MN was filled with carbon paste to work as the counter electrode and the fourth array embedded a silver wire to act as the reference electrode. One of the working electrodes was functionalised by first producing a mixture of β-hydroxybutyrate dehydrogenase and NAD^+ in 0.1 M Tris-HCl buffer. The mixed solution was then drop-casted onto the surface of the working electrode followed by 2% GA solution and 0.5% Chit solution. The second working electrode was coated with a solution of GOx followed by 2% GA solution and 0.5% chit solution, the sensor was then left overnight in the refrigerator. Chronoamperometry was carried out to show the analytical performance of the MN sensor, using a dynamic range of 1-10 mM HB followed by the detection of μM of HB ranging from 0-1 mM. The dose response curve showed high linearity and also indicated high sensitivity for the detection of HB in the desired concentration range (122).

Chapter 7

MNs for Theranostics

7.1 Introduction

The concept of theranostics was coined by John Funkhouser in 1998 to describe a concept that combines diagnosis, treatment and follow up of a disease (123). This method allows for the selection of the sub-population of patients that are likely to benefit from a targeted therapy as well as providing personalised medicine (124). Although the term theranostics was popularised by John Funkhouser, the principle had been applied to imaging and treating thyroid diseases for over 50 years (125). Theranostic platforms provide a window for both monitoring pharmacokinetics and pharmacodynamics of drugs injected into the body. Initially focused on cancer treatment (126), theranostics has now expanded its reach to cover inflammatory diseases (127), autoimmune disorders (128), cardiovascular diseases (129), and neurological disorders (130). These devices contain three main components; an imaging agent, a therapeutic agent, and a carrier, which will cover the imaging and therapeutic agents (131). The initial goals for theranostic platforms was to have the ability to image and monitor diseased tissue, delivery kinetics and drug efficacy, have the ability to tune therapy and dose with unattainable control (132).

Theranostics can use remote triggering, which means that the treatments can be administered different factors. This ability in comparison to treatments that are always administering drug allows for reduced toxicity and this will also have control over location on a patient, quantity and timing, therefore tailoring drug release profiles and localised treatments (133).

Many patients require different dosages to achieve ideal therapeutic effects which reflects their individuality in drug absorption and body responses and incorrect administration due to this can lead to adverse consequences. Therefore, personalised dose response characteristics, rapid physiological analysis and precision medicine are required for customised dosage and improved therapeutic efficiency. Utilising feedback controlled theranostic systems can assist in clinical decisions and improve therapeutic efficiency. Controlled theranostic systems can be split into 2, open and closed loop systems. Open loop theranostic systems consist of two independent units for diagnosis and therapy without a direct feedback from each other. The relationship between drug delivery and

diagnosis is bridged by the intervention of the patient or medical staff. The administration dose should be self decided based on data detected from physiological signals. Theranostic systems using open loop methods can precisely detect analytes and achieve on demand drug delivery in the presence of human intervention.

Closed loop theranostic systems integrate an accurate biosensing unit and on demand drug delivery unit in one system. The strategy of a closed loop system is to accurately monitor analytes and from there adjust the drug release dosage in real time based on the direct feedback data detected. The feedback data is provided through a built in control algorithm which results in a drug level fluctuation within the expected safe therapeutic range. Therefore, closed loop theranostic systems provide exact detection of physiological signal, optimal calculation of drug dosage and on demand drug delivery without human intervention (134).

7.2 Recent advances in Theranostics

Recently, there have been major developments in the field of theranostics. Between 1998 and 2020, numerous platforms have been developed combining biomarkers bound to either nanoparticles, hydrogels or liposomes with a therapeutic agent such as doxorubicin, artemisone or aspirin for the treatment of inflammatory disease or autoimmune diseases.

Polymer MNs have been modified for simultaneous delivery of cancer immunomodulatory drugs and detection of skin biomarkers. MNs were crosslinked hyaluronic acid and loaded with model immunomodulatory nanoparticle-containing drug, CpG oligonucleotides (TLR9 agonist), for cancer therapy in melanoma and colon cancer models. The transdermal delivery of nanoparticles containing the CpG oligonucleotides induced anti-tumor immune responses in multiple syngeneic mouse cancer models. The MNs stimulated innate immune cells and reduced the tumor growth and microscopy showed deposition and spatiotemporal co-localization of the CpG nanoparticles withing the tumor microenvironment. An analysis of the ISF revealed similar immune signatures to those in the bulk tumor homogenate, such as increased populations of macrophages and effector T cells (135).

A dihydrolipoic acid coated gold nanocluster RDT were irradiated by low dose of X-ray were utilised to investigate the production of cytotoxic reactive oxygen species (ROS), killing efficiency of cell level and living body level, antitumor immune mechanism and biosafety. Highly efficient in vivo treatment of solid tumors had been achieved by a single

drug administration and low dose X-ray radiation. Enhanced antitumor immune response was involved, which could be effective against tumor recurrence or metastasis (136).

There have been major developments in the field of theranostics and a variety of these have been summarised in Table 7.1.

Table 7.1 Recent advances in the field of theranostics

Platform	Preparation	Therapeutics	Diagnostic	Benefits	Application	Reference
Fe^{3+}/TA modified Dox nanoparticles (DFTNPs)	Doxorubicin (Dox) nanoparticles were prepared using reprecipitation method.	Responsive drug release of Dox from low pH levels or high ATP concentration	Fe^{3+}/TA provided the ability for MRI imaging due to the strong binding affinity of Fe^{3+} to ATP as well as its capability to serve as a photoacoustic imaging and photothermal contrasting agent	Successfully constructed for tumour growth inhibition with high selectivity, specificity and efficiency	Cancer management for bladder, breast and ovarian cancer	(137)
Humanised murine antibody to transformed mucin 1 (hTAB004) as theranostic agent for triple-	Humanised murine antibody to transformed mucin 1 (hTAB004) was prepared by combining hybrid sequences that fuse with selected parts of the parental antibody sequence with human framework	Antibody-radioisotope complexes were fabricated by conjugating hTAB004 with a chelator	Overexpression of Transformed Mucin 1 was being detected using labelled molecules with Actinium-225 and Iradium-111 due to their high affinity and	Allowed the delivery of safe doses of Actinium-225 to orthotopic HCC70 tumours resulting in	Treatment for breast cancer	(138)

negative breast cancers	sequences of the light and heavy chains.	(DOTA) to allow for radiolabelling with Actinium-225, which is used for alpha radiotherapy	the use of flow cytometry and ELISA	shrinkage in tumours and greater survival		
Acid responsive amine-substituted perylene diimide derivative for cancer management	The perylene diimide based theranostic nano agent (THPDINS) consisting of doxorubicin, hydroxyl-perylene diimide (PDI) and IR825 dye, which is a pH inert photoacoustic imaging (PA) matrix is prepared using a nanoprecipitation method	Mild acidic tumour microenviron ment accelerates the release of doxorubicin, which is used in chemotherape utics for effective	Molecular photoacoustic imaging was used for imaging of tumours acidic environment as well as monitoring drug release	The pH sensitive agent can prove specific imaging of the tumour region and a map of the pH, as well as allowing on demand drug release to inhibit tumour growth	Cancer management for bladder, breast, and ovarian cancer	(139)

		antitumor efficacy				
Silica sealed mesoporous polymer for cancer therapy	The biodegradable magnetic silica sealed mesoporous polymer was prepared using a templated self-assembly with mesoporous polymer resin, which produced monodisperse nanospheres followed by a coating of biodegradable magnetic silica using ethanol-assisted hydrolysis condensation reaction of tetramethyl orthosilicate (TMOS) and Iron (III) ethoxide for the core shell structure	The acidic tumour environment generates sustained drug release of doxorubicin which is used in chemotherapeutics for effective antitumor efficacy	The magnetic targeting property and MRI ability of the silica sealed mesoporous polymer	The silica sealed mesoporous polymer possessed high water dispersity and good biocompatibility which provides an excellent platform for MRI guided tumour targeting chemotherapy	Cancer management bladder, breast and, ovarian cancer	(140)

Fluorescent silica nanoprobes for imaging and theranostics of cancer cells	The fluorescence silica nanoparticles were synthesised by a facile reverse microemulsion method	The nanoparticles were conjugated with 2'-O-methyl-miR-21-MB, which hybridises with intracellular microRNA-21 of MCF-7 cells and will inhibit cell growth	The tris(2',2'-bipyridyl)dichlororuthenium (II) hexahydrate (Ru-(bpy)$^{2+}$3) doped silica nanoparticles hybridise with over expressed micro-RNA-21 in breast cancer patients and provide a red fluorescent emission at 518 nm	By conjugating nanoparticles with polyethylene glycol and functionalised amine groups provide biocompatibility and allow subsequent bioconjugation	For the treatment of breast cancer	(141)
^{89}Zr-PET imaging for the early monitoring of response following α- and β-particle	^{89}Zr was synthesised through proton beam bombardment of yttrium foil and isolated in high purity as ^{89}Zr-oxalate.	[^{225}Ac]Ac-DOTA-PEG$_7$-Tz (α- PRIT) and [^{177}Lu]Lu-DOTA-PEG$_7$-Tz (β-PRIT)	PET imaging of DNA damage was utilised as a non-invasive tool for the monitoring of early therapeutic responses	Early radiotherapy response is a critical tool for clinical translation of	For monitoring of responses following radioimmunotherapy in pancreatic	(142)

radioimmunotherapy in pancreatic ductal adenocarcinoma	DOTA-PEG_7-Tz were synthesised in a three-step process and these were followed by radio labelling with ^{225}Ac and ^{177}Lu	were injected into mice subjects to act as a radiotherapeutic payload	following α- and β-particle radiotherapy	new radiotherapy approaches as well as being applicable to numerous radiotherapeutic delivery platforms, including small molecules, peptides, antibodies and nanoparticles and will help streamline development and translation	ductal adenocarcinoma	
Fatty acid binding proteins	The micro-RNA mimics and siRNA of FABP5 were	FABP5 was involved in	High expression of fatty acid-binding	Identifies a crucial	Promotion of lymph node	(143)

(FABP) for the promotion of lymph node metastasis in cervical cancer	designed and synthesised by GenePharma and were transfected into cancer cells using Lipofectamine RNAiMAX	reprogramming fatty acid metabolism in cervical cancer cells	protein 5 (FABP5) was detected by immunohistochemistry analysis, which positively correlates with the presence of lymph node metastasis in cervical cancer	mechanism of crosstalk between FABP5 and fatty acid metabolism that promotes lymph node metastasis and this also supplies a potential early diagnostic biomarker and therapeutic target for cervical cancer patients with lymph node metastasis	metastasis in cervical cancer	

Anti-CUB-domain containing protein I (CDCPI) antibodies have been used for imaging and treatment of epithelial ovarian cancer	10D7 and a second anti-CDCP1 mAb, 41-2, have been characterised as they are able to bind to CDCPI	10D7 was labelled with a highly potent cytotoxin monomethyl auristatin E through a link incorporating a lysosomal protease cleavage site. Specific delivery of potent cytotoxic drug to epithelial ovarian cancer cells inhibited proliferation	Positron emission tomography (PET)-CT imaging was used to investigate the potential for 10D7 to target CDCPI expressing cells in epithelial ovarian cancer cells in vivo	CDCPI internalising antibodies showed the potential to kill and detect CDCPI expression in ovarian cancer cells	For imaging and treatment of epithelial ovarian cancer	(144)
Albumin-binding carriers	Using Pet25b(+) expression vector containing immune	Increasing the lymph node	Promoting the antigen presentation of the	The complex created	Vaccine providing	(145)

for the targeting of cytotoxic T lymphocyte vaccines to lymph nodes and improving the efficacy of the vaccine	tolerant elastin like polypeptide (iTEP) and iTEP fusion genes, E.coli cells were transformed.	and dendritic cell accumulation of the vaccines from the binding of mice serum albumin and a fusion protein termed albumin binding domain and an immune tolerant elastin like polypeptide (ABD-iTEP) can lead to the initiation of cytotoxic T	vaccines and T cell activation due to the complex formed from between mice serum albumin and ABD-iTEP-pOVA	between mice serum albumin and the albumin binding carriers showed an increased cytosolic accumulation and an increased stability in acidic intracellular compartments that could facilitate antigen presentation	immunotherapy for cancer	

		lymphocytes and therefore halt metastasis				
Thermoresponsive nanogels for the encapsulation of anti- tumour necrosis factor alpha (anti-TNFα) fusion protein etanercept for treatment of several inflammatory skin diseases such as psoriasis	The thermoresponsive nanogels were synthesised using precipitation polymerisation of N-isopropylacrylamide (NIPAm) and hyperbranched polyglycerol (PG)	The nanogels encapsulated with ETR and FITC-BSA as a model protein, will swell releasing the drug	Rise of temperature in inflammatory regions lead to release of encapsulated drug	Biocompatible and easily manufactured material for stable protein encapsulation and also topical delivery into barrier deficient skin	Treatment of skin disease such as psoriasis	(146)
Self-healing antibacterial exosomes	The hydrogel was composed of Pluronic F127, oxidative hyaluronic acid and Poly-ε-	Exosome release under weak acidic	The immunohistochemical staining of cytokeratin	Multifunctional properties were seen	Promotion of wound healing	(147)

hydrogel for the promotion of wound healing and skin regeneration in diabetic patients	L-lysine and synthesised using a reversible Schiff base reaction between oxidative hyaluronic acid and Poly-ε-L-lysine and the thermal-responsive property of F127	environments as a result of the breaking of Schiff base bonds	which is the biomarker for the differentiation and re-epithelialization of the epidermis and therefore shows wound healing	including injectability, self-healing, antibacterial activity and stimuli-responsive exosome release	and skin regeneration	
Gold nanorods (GNR) have been utilised for the detection and targeting for the photothermal treatment for Alzheimer's disease	GNRs were fabricated by seed mediated surfactant directed method	The GAS has smart synergistic effects and therefore degrades Aβ monomers, inhibits Aβ accumulation and disaggregates Aβ fibrils.	Aβ aggregation was detected using GAS complexes as a bio probe and the utilisation of localised surface plasmon resonance as well as the absorbance characteristics of GAS in the absence of Aβ fibrils to therefore monitor the dynamics	First report of the preparation and testing of a smart complex using concomitant single chain variable fragment (*scFv)*, thermophilic amyloid-	Treatment of Alzheimer's disease	(148)

		Additionally, it also reducesng Aβ-mediated peroxidase activity	of Aβ fibrillogenesis ex situ	degrading enzymes (ADE) and GNR for the treatment of Alzheimer's disease		
Indocyanine green liposomes have been used for the treatment of Cerebral Malaria	Liposomes were synthesised by extrusion method	Artemisone is administered for treatment of cerebral malaria and diminishes the fluorescence produced by the indocyanine green liposomes bound to	Indocyanine green liposomes are up taken by vascular and perivascular activated phagocytes that are prominent in cerebral malaria and are monitored using near infrared imaging	Indocyanine green liposomes improve cerebral malaria diagnosis and therapeutic monitoring and also the results support the idea that migrating phagocytes	Treatment of Cerebral Malaria	(149)

		activated phagocytes		have a role in induction of cerebral malaria		
Hemozoin generated vapor nanobubbles for the treatment of malaria	Vaporisation of the molecules are produced by the photothermal effect in the hemozoin nanocrystals and evaporation is generated by the optical energy being absorbed into the nanocrystal which transfer the heat to adjacent liquids. Resulting in the expansion and collapsing of the nanobubbles	Hemozoin nanocrystals destroy the malaria parasites mechanically due to the intra-parasital explosive impact of vapor nanobubbles	Detection of optical scattering by the vapor nanobubbles showing the presence of malaria parasites	The mechanism provides a rapid, highly specific detection and destruction of malaria parasites in one procedure	Treatment of Malaria	(150)
Magneto liposomes loaded with poly-unsaturated fatty acids as	Superparamagnetic nanoparticles containing magnetite (Fe_3O_4) core with poly(acrylic) acid coating, acting as an MRI detectable	ω-3 PUFA-EE is the therapeutic agent useful in the treatment	Liposomes containing both nanoparticle superparamagnetic or rhodamine-100 dye allowed for both	Magnetoliposomes loaded with the drug allowed for magnetic	Treatment of atherosclerosis, neurodegeneration, diabetes and obesity	(151)

anti-inflammatory agents for the treatment of atherosclerosis, neurodegeneration, diabetes or obesity	probe was encapsulated in liposomes prepared using the film hydration method	of the inflammatory component of colonic inflammation or glioma was encapsulated in the liposomal formulation	magnetic resonance imaging or fluorescence for in-vivo and in-vitro studies of large volume liposomal distribution in colonic inflammation	resonance imaging and therefore improved the outcome for inflammatory diseases, decreasing significant colonic inflammation and delaying or even reversing glioma development		
Aptamer based biosensors for the release of aspirin upon detection of a	A glassy carbon electrode was modified by electrochemical reduction of 4-carboxyphenyl followed by the immersion	Aspirin is released into rat models after being triggered by	The presence of IFN-γ generates the release of redox probes and therefore results in a electrochemical signal	First study to provide a technology for in vivo real-time	Monitor and measure the hosts inflammatory response	(152)

target level of a proinflammatory cytokine interferon-γ-(IFN-γ) in real time	in 1-ethyl-3-(3-dimethylaminopropyl)carbodiimide (EDC) and N-hydroxysuccinimide (NHS) in 2-(N-morpholino)ethanesulfonic acid (MES) buffer solution. Finally, the electrode was incubated in streptavidin followed by immersion into aptamer (aspirin)	the inflammatory cytokine IFN-γ and is able to inhibit inflammation	that measures the concentration of IFN-γ	monitoring of proinflammatory cytokines and then deliver anti-inflammatory molecules. By varying the aptamer probe and availability of small therapeutic drugs, this method has potential for personalised medicine.		
Au NPs loaded into pegylated-poly(D,L-lactic-	Au NPs were synthesised by the Burst method and the outer nanospheres were	Methotrexate was loaded on the pegylated-	Au NPs were used as a contrast agent for	The multifunctional nanosphere	Treatment of rheumatoid arthritis	(153)

co-glycolic acid) for the treatment of rheumatoid arthritis	prepared using solvent emulsification.	poly(D,L-lactic-co-glycolic acid) gold nanospheres and provided release of drug in a temperature and pH responsive mode	photo-acoustic imaging	represents a theranostic platform for rheumatoid arthritis diagnosis and intracellular treatment for highly effective targeted chemo-photothermal therapy		
Light activated nano agents have been used for targeted macrophage ablation in	The nanoscaffolds were modified with AlexaFluor 750 and also meso-tetraphenylchlorin derivative. The nanoagent was synthesised by modifying	Atheroma was irradiated using 650 nm of light, which activates the therapeutic component	The nanoagents were synthesised by the modification of animated crosslinked dextran coated iron oxide (CLIO) nanoparticles that	The nanoagents showed limited skin photosensitivity, were highly effective and	Targeting macrophage ablation in inflammatory atherosclerosis	(154)

inflammatory atherosclerosis	aminated CLIO nanoparticles	and results in eradication of inflammatory macrophages	were reacted with AlexaFluor 750 in order to provide the agent the ability to fluorescently image localisation at macrophage-rich regions within inflamed atherosclerotic lesions	also provided an integrated imaging and therapeutic nanoplatform		
Formyl peptide receptor 2 (FPR2/ALX) in combination with two rhodamine derived fluorescent tags for targeting acute vascular inflammation	FPR2/ALX targeting unit Quin C1 was prepared using 4-hydroxymethyl benzoate combined with rhodamine B as a fluorescent dye. The Quin C1 was appended onto the aromatic amine functional site to produce Rho-pip-C1	BMS-470539 treated mice via intraperitoneal injections	Rho-pip-C1 were isolated and incubated with neutrophils. These displayed bright fluorescent labelling once bound to activated neutrophils that are involved in the activation of the inflammatory cascade	These probes enable the visualisation of inflammation for biomedical research and can be used as screening tools for drug discovery	For the targeting of acute vascular inflammation.	(155)

Dextran sulphate-graft-methotrexate conjugate (DS-g-MTX) has been used for the treatment of collagen induced arthritis a common autoimmune model for rheumatoid arthritis	Condensation reactions were used to synthesise both dextran sulfate-graft-methotrexate conjugate (DS-g-MTX) and dextran-graft-methotrexate (Dex-g-MTX) with 1-ethyl-(3-(dimethylamino)propyl) carbodiimide hydrochloride (EDC HCl) as the condensing agent and 4-N,N-dimethylaminopyridine (DMAP) as a catalyst	Dextran sulfate-graft-methotrexate conjugate (DS-g-MTX) was used as a first line conventional drug for rheumatoid arthritis therapy as it can selectively target activated macrophages	Scavenger receptors, which are overexpressed on activated macrophages is a specific biomarker for targeted therapy for rheumatoid arthritis. DS-g-MTX selectively targets activated macrophages due to the recognition of dextran sulphate to scavenger receptors	The cell targeted polymer conjugate holds broad prospects in the targeted treatment of rheumatoid arthritis and this may prevent patients from synovitis, articular cartilage and even joint replacement	Treatment of collagen induced arthritis	(156)
Graphite electrodes for the sensing of	The sensing system was created by the modification of a graphite electrode with	The bioelectrocatalytic electrode,	A graphite electrode was modified with polyclonal anti-E. coli	The Sense and Treat system is the first step to	Treatment of meningitis, pneumonia,	(157)

bacterial cells and activated release of antibacterial drug	a mixture composed of pyrroloquinoline quinone (PQQ) and polyclonal anti-E.coli IgG antibodies. These were attached to the surface coated with adsorbed polyethyleneimine (PEI) by the formation of amide bonds between the carboxylic group from the PQQ and protein and the amino groups of PEI.	which sensed the presence of bacterial cells, is electrically connected to the actuating electrode that is coated with Fe^{3+}-cross-linked alginate gel containing an antibacterial drug Polymyxin B. When the negative potential and the corresponding reducing	IgG antibody which has a high affinity to bacterial cells	future theranostic applications where bacteria presence leads to an automatic antibacterial treatment	sepsis and urinary tract infections	

		current were generated on the sensing electrode, the alginate gel on the connected electrode was electrochemically dissolved due to reduction in the cross-linking Fe^{3+} cation and thus the release of the entrapped Polymyxin B				
FR+ targeted theranostic liposomes loaded with rifampicin	Unilamellar pegylated liposomes were prepared using the rotary method	Liposomes were loaded with rifampicin and	Liposomes were radiolabelled with technetium-99m by direct labelling	The features of the drug loaded liposomes can	Treatment of M. tuberculosis	(158)

and ofloxacin for the treatment of M. tuberculosis		ofloxacin that are first- and second-line drugs for multi-drug resistant tuberculosis	methods, and these were used as a Single Photon Emission Computed Tomography (SPECT) imaging agent	be prepared on scale, have excellent radiolabelling efficiency with radiotracer that remain stable		
Injectable microgels as closed-loop insulin delivery systems	The nanogel capsules were synthesised using a two-step procedure. Vinyl groups were covalently bound to the enzyme and compact nano capsules were prepared following free radical polymerisation in aqueous solutions containing acrylamide and N-(3-aminopropyl)methacrylamide) monomers and N,N'-	FITC-conjugated insulin were encapsulated within the nanogel. Under hyperglycaemic glucose levels led to the increase in microgel size and therefore the gradual	Enzyme GOx was encapsulated in the nanogel, which reacts with glucose to generate a pH change. Catalase is used to regenerate oxygen and allow glucose catalysis and the consummation of hydrogen peroxide	The nanogels provide uniform accessibility, enhanced enzymatic stability and stimuli controllable capabilities, which allows for the generation of a glucose	Treatment of diabetes mellitus	(159)

	methyl-enebisacrylamide as a crosslinker	release of the encapsulated insulin		responsive insulin delivery system		
Nanoparticles and MRI incorporation has been used to promote proliferation of insulin-secreting cells in type 1 diabetes	The nanodrugs were synthesised by the combination of dextran coated magnetic nanoparticles and the conjugation of Cy5.5 fluorescent dye and finally the addition of antisense locked nucleic acid (LNA) or miRNA mimics through heterobifunctional linker N-succinimidyl 3-[2-pyridyldithio]-propionate to produce MN-ASO or MN-miRNA	Magnetic nanoparticles encapsulated, miR-216a that mimic nanodrugs to pancreatic islets and result in increased secretion of insulin and proliferation of beta cells	MRI imaging was used to monitor miRNA-216a delivery	There is potential for delivery of multiple RNA molecules that can therefore alter various aspects of diabetogenesis and MRI used for monitoring of drug delivery provides added value for future clinical	Therapeutic targeting for the treatment of diabetes	(160)

				implementation		

Recently MNs have been explored for use in transdermal monitoring of biomarkers and therefore provide routine PoC health monitoring. Combining drug delivery and diagnostics on a MN platform will allow a push towards precise and personalised medicine. These devices can therefore be used for patients with cancer, autoimmune diseases, and infectious diseases.

7.3 MNs for Theranostics

A MN patch was fabricated by crosslinking of 3-aminophenylboronic acid-modified sodium alginate and chondroitin sulfate. The tip of the MNA contained mineralised insulin particles and GOx for insulin release. The base of the structure contained 3,3',5,5'-tetramethylbenzidine and HRP for real time glycemia sensing. As the sensor comes into contact with glucose, the GOx produces hydrogen atoms and hydrogen peroxide and this leads to the dissolution of the calcium layer releasing the insulin particles within. The production of peroxide led to a visible colour change at the base of the MN surface to be read out. This theranostic MN patch has potential for clinical applications (161).

Hyaluronic acid-based MN platforms have been fabricated for cancer therapy. The MNs were synthesised using hyaluronic acid and loaded with immunomodulatory nanoparticle-containing drug for cancer therapy. The therapeutic response is then monitored by longitudinal analysis of entrapped immune cells with the MNA. The MNs were then able to carry out simultaneous delivery of nano-encapsulated drugs in the vicinity of tumours and sample ISF from the tumour microenvironment to monitor the response to the drug delivered and this hydrogel based theranostic device showed effective transdermal drug delivery into the tumor microenvironment and the retrieval enabled analysis of the immune response over time (135).

Part 2

Experimental Methodology

Chapter 8

Experimental methods and materials for MN fabrication

In this chapter, we will discuss the methods and materials employed for the fabrication of silicon and polyvinylpyrrolidone (PVP) microneedle arrays (MNAs). The functionalisation of these MNAs will be presented in subsequent chapters.

8.1 Photolithography

8.1.1 Spin coater

A Laurell WS-650 spin coater was used to coat uniform layers of resist onto a 1.2 mm and 1.4 mm thick silicon wafer (4 inch diameter) for fabrications MNs possessing heights of 700 µm and 900 µm, respectively. For the bevel and bore photolithography, unless otherwise stated nLOF2070 negative photoresist has been utilised. The spin parameters have been discussed in the silicon MN fabrication Chapter 12, Section 12.3 & 12.5.

8.1.2 Spray coater

To create the shaft pattern, a SUSS MicroTec AS8 spray coater has been used to deposit both nLOF2070 and AZ4999 (Figure 8.1) (162). These resists were used for the photolithographic patterning of the shaft due to their ability to be more stable during the etching process. nLOF2070 and AZ4999 are resists used in lift off processes. Lift off in photolithography means that the photoresist remains on the surface post etch and this sturdiness is useful for the shaft as it prevents the shaft pattern from losing its shape during the etch process and therefore won't impact the MN structure.

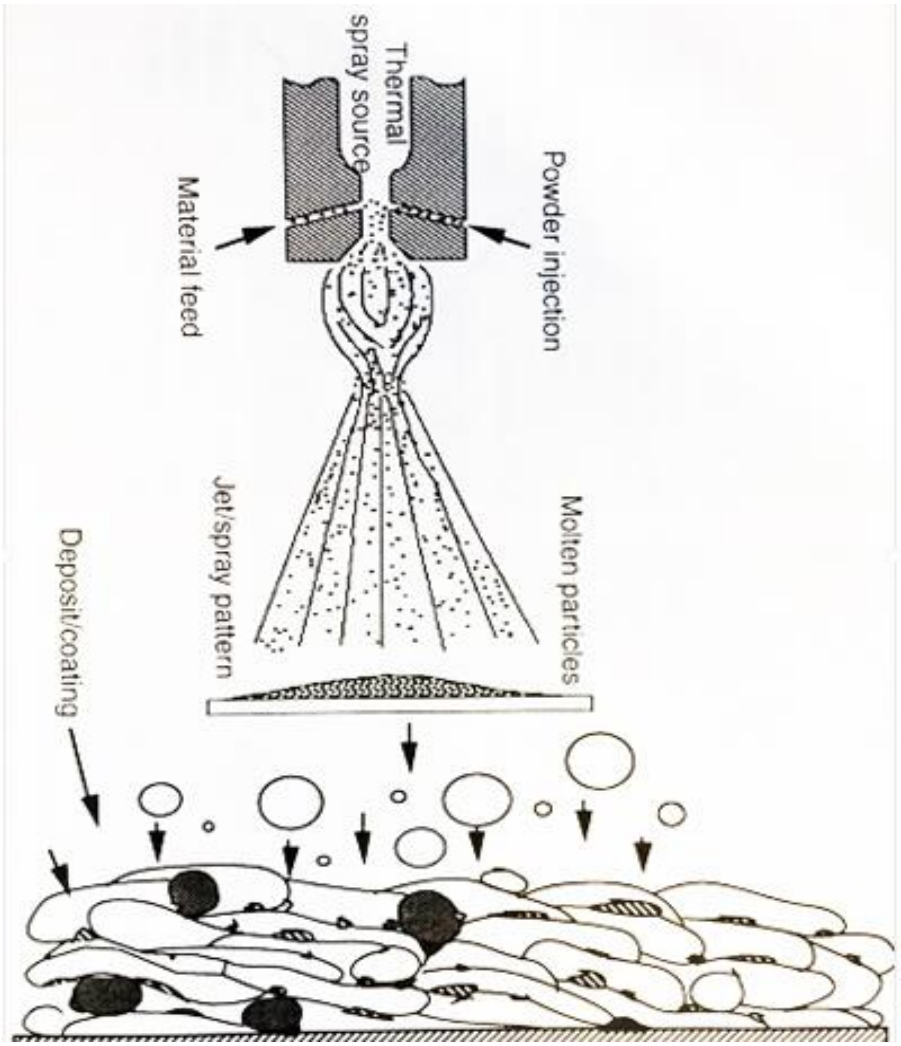

Figure 8.1 Schematic representation of the spray coating technique (161)

For the nLOF2070 photoresist, dilution in acetone in a ratio of 1:8 is required due to the high viscosity of the photoresists. The dilution allows the resist to amalgamate and form a uniform coating after spray coating. AZ4999 is a resist dedicated to the spray coater where it provides defect-free and conformal coatings onto surfaces and therefore dilution with acetone is not necessary. The parameters used for uniform spray coating are discussed in the subsequent chapter 12, section 12.9 on silicon MN.

8.1.3 Mask aligner

A SUSS MicroTec MA8 UV mask aligner was employed to transfer each MN mask onto the photoresist on the wafer. Due to polymerisation upon UV-exposure, UV exposed negative resists will become insoluble. Developer solutions are used to dissolve unexposed regions in the case negative resists. This will then leave an inverse pattern of the original, which is applied on the wafer.

Initially, a glass mask, which contains each stage of the MN (designed on AutoCAD), is placed into the mask holder. Once inserted, the mask is then held using a vacuum before being inserted into the mask aligner. The inserted mask is then secured in the mask aligner once again with a vacuum. Each wafer that has been coated with a photoresist is placed onto the sample stage and is held with a vacuum. Using alignment marks to line up the wafer and the mask, the sample stage is manoeuvred left and right or up and down to an accuracy of < 0.5 μm. Once the wafer and mask have been aligned correctly, the sample stage rises slowly bringing the wafer and mask into soft contact with one another. The wafer is then exposed to UV light through a 1000 W mercury arc lamp perpendicular to the mask. The tool calculates the exposure time based on the UV dosage set and the optimisation is discussed in the silicon MN fabrication chapter 12, section 12.3, 12.5 & 12.9.

8.2 Plasma Enhanced Chemical Vapour Deposition (PECVD)

For the protection of the bevel etched silicon wafer and to create a hard mask for the marker fabrication, a layer of silicon nitride is deposited onto the wafer surface using an SPTS Technologies plasma enhanced chemical vapour deposition (PECVD). The PECVD is a widely used technique to achieve thin films at low substrate temperatures. The thin films are obtained by the decomposition of source gases in plasma as the energetic electrons and gas molecules collide.

8.3 Inductively Coupled Plasma (ICP)

To etch through the deposited silicon nitride layer, an SPTS Technologies inductively coupled plasma etcher (ICP) is used. The plasma etches away the silicon nitride to reveal the silicon below in the patterned mask design. The ICP source will generate a high-density plasma due to an inductive coupling between the plasma and the RF antenna. In the plasma generation region, the antenna creates an alternating RF magnetic field and this induces an RF electric field. This electric field energises electrons that participate in the ionization of gas molecules and atoms at low pressure. A 2 MHz RF generator applies power to an ICP coil, which controls ion fluxes. At the same time, a bias power is applied to the lower electrode using a 13.56 MHz RF generator to extract and accelerate ions and radicals from the plasma towards the substrate surface. This configuration results in an independent control of ion density and energy to obtain higher etch rates, greater flexibility and profile control, and reduced damage of the sample (163).

8.4 Deep-Reactive Ion Etching (DSi-V)

Deep reactive ion etching (DRIE) of silicon is a highly anisotropic etch process to create deep, steep sided holes and trenches in wafers/substrates with a high aspect ratio. Deposition of a passivation layer is carried out by employing SF_6 and C_4F_8 gases to rapidly etch silicon and generate fluorocarbon polymer, respectively. The passivation layer is used to protect the substrate from chemical etching. These 2 steps are repeated multiple times, resulting in etching cavities with a 50 to 1 aspect ratio and an etching rate 3 to 4 times higher than the ones used in wet etching (164). The parameters used for silicon etching of the bevel, bore, and shaft is illustrated in the silicon fabrication chapter.

8.5 PVP MNA Fabrication

The process to fabricate PVP MNA utilises a mixture of the liquid monomer, vinyl pyrrolidone (Sigma Aldrich), and a free-radical initiator Azobisisobutyronitrile (AIBN) (1.5 wt%, Sigma Aldrich). For the tips of the array, drugs would be incorporated into the mixture of vinyl pyrrolidone and AIBN and for the base of the array only vinyl pyrrolidone and AIBN is combined. Dragon Skin (Smooth-On) is used to create master moulds from polycarbonate MNs and the PVP polymer mixture is then applied filling the tip. After the solution is applied to the mould, they are placed into a vacuum chamber to ensure the tips are fully filled and any air bubbles are removed within the mixture, which may have been caused by pipetting. To induce photopolymerisation, the system is placed

under a UV torch (100 W, 300 nm) for 30 min at room temperature. After the tips of the MNs have been cured, the base solution is pipetted and the process is repeated. The PVP MNA fabrication was initially established utilising techniques illustrated by Prausnitz et al (165) and these are optimised further in the PVP fabrication chapter 15, section 15.2.

8.6 Polycarbonate MNA Fabrication

Polycarbonate MNs were produced using an electrical discharge machining technique demonstrated by Sharma et al in 2017 (166). A FANUC ROBOCUT α-OiC for wire erosion is set to make 3 milling passes over a copper-tungsten block, which creates a master electrode. The master electrode is then used for spark erosion of an aluminium block in JOEMARS EDM AZ50DR to produce a metalised inlay. Polycarbonate is dried at 110 °C for 24 h prior to the injection molding process. For injection molding of the polycarbonate MNs the following conditions are utilised:

Table 8.1 Injection moulding parameters for PC MNs

Parameter	
PC melt temperature (Tm)	270 °C
Tool temperature (T_w)	80 °C
Injection speed (v_i)	20 cm^3s^{-1}
Shot volume	4.4 cm^3
Cooling time (t_c)	5 s

Chapter 9

Experimental methods and materials for MN characterisation

In this section, methods and materials employed for the characterisation of silicon and PVP MNs are described.

9.1 Imaging Techniques

9.1.1 Scanning Electron Microscopy

The SEM produces detailed, magnified images of an object by scanning its surface using an electron beam to create a high resolution image. The resulting image shows information about the composition and topology of the object. For the imaging of the MNAs, a Hitachi S-4800 ultra-high-resolution SEM was used. The main components of an SEM are as follows:

- Electron source
- Electron detector
- Sample chamber
- Column in which electrons travel down with electromagnetic lenses
- Computer used to display the images

Samples are mounted onto a stage and placed into the chamber area where a combination of pumps are utilized to place the system under a vacuum. Electrons are then generated at the top of the column and are then accelerated through the column passing through a combination of magnetic coils to produce a focused beam of electrons. The beam then strikes the surface of the sample and as the electrons interact with the sample, they create

secondary electrons. A detector collects the secondary electrons to form an image, which is then displayed on the computer screen (Figure 9.1) (167).

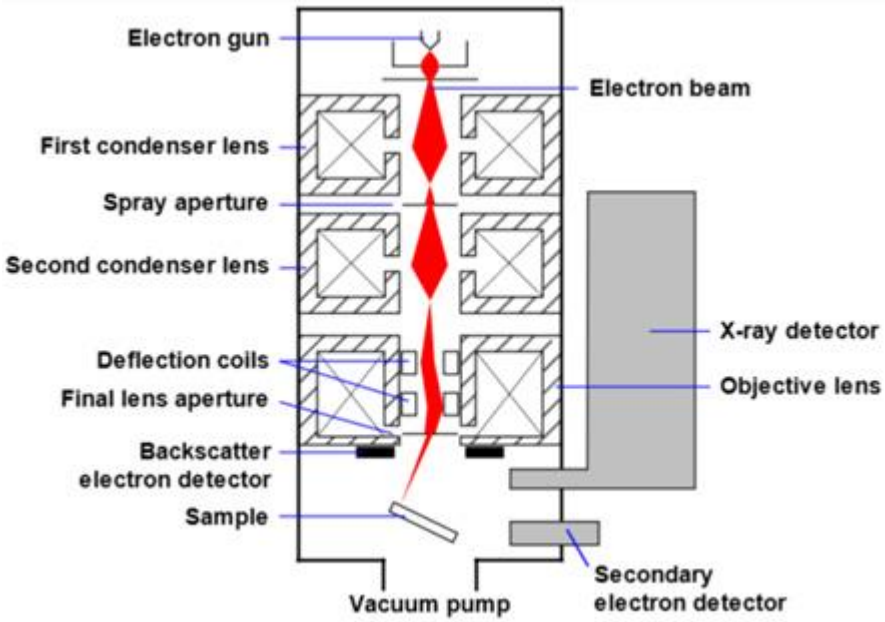

Figure 9.1 Schematic Diagram of a scanning electron microscope (166)

Alternative to SEM, MN topology can be determined using atomic force microscopy (AFM). AFM is based on the interaction between a sharp probe tip and a sample surface that involves the following main steps: Probe and Cantilever, Approach, Deflection, Feedback, Scanning and Analysis. To quantify surface roughness and the roughness corresponding to specific nanotopography or the dimensions of the nanostructures an AFM has been widely used. The AFM imaging provides a 3D spatial overview of nano-engineered implant surfaces to visualize both the micro-roughness and the nanotopography (168).

Another option to determine MN topology is the use of confocal microscopy by collimated laser beam across the MN surface. The laser beam is reflected by a dichroic mirror and passes through the objective lends of the microscope in a focused manner on the specimen, which excites the fluorescent probe in the sample. The light is emitted at a longer wavelength which can come through the dichroic mirror and is focused on the upper pinhole aperture, which then hits the electronic detector. By using CLSM, it is possible to obtain high-resolution images from the MN samples (169).

9.1.2 Optical Microscopy

Throughout the MN fabrication optimisation and characterisation, a Keyence VHX-950F series optical microscope was used to examine the wafer and the porcine skin samples. An optical microscope uses a combination of an objective and an ocular lens to image various samples. The objective lens consists of several lenses that magnify an image and project a larger image. According to the difference in focal distance, lenses of varying magnification are available. As well as the magnification, indexes are built in to show the performance of an objective lens include the numerical aperture and the working distance. To magnify the image further, an ocular lens is used for observations and the ocular lens consists of one to three lenses and a mechanism known as the field stop that removes any unnecessary reflected light and aberrations. Additionally, to the magnification, the lens performance is represented by the field range which represents the range for the field-of-view. Opposite to the objective lens, the higher the magnification of the ocular lens, the shorter the length. From there, the observation magnification is the product of the magnification of each of the lenses and this generally ranges from 10 times to 1,000 times (170).

Optical microscopy is used rather than an SEM due to the time consuming nature of preparing the skin samples to allow the moisture to be fully removed and therefore allowing the electrons to propagate through the sample. The optical microscope will provide a less time consuming, high resolution image of the porcine skin layers to provide analysis of MN insertion regions and photoresist development effectiveness. The Keyence microscope has the capabilities to take angled measurements of samples at a magnification of up to x 5,000. Users are able to analyse the images using a computer application that enables 3D imaging as well as false colourisation (Figure 9.2).

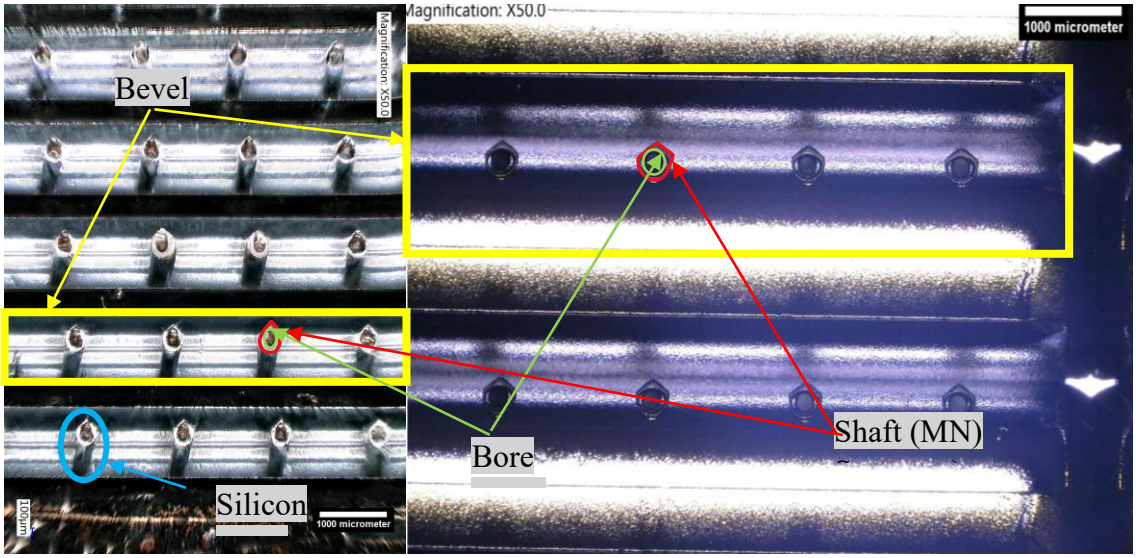

Figure 9.2 Keyence microscope images showing 3D imaging and false colourisation of hollow silicon MNs.

9.2 Mechanical Testing

To evaluate the safety margin of the devices, the MNA devices were subjected to axial and transverse forces. The safety margin was calculated as a ratio between the force required to pierce the SC and the force, at which the MNA tips break. MNA fracture force should possess a value greater than the insertion force required to break the SC. Dependent on the material composition of the MN, the fracture and the insertion force will vary.

A Hounsfield compression analyser (model H1-KS) was used to perform axial compression tests to test the mechanical strength of the PVP MNs. Each MNA was secured to a sample stage and a 100 N load cell was programmed to 5, 10, 20, and 50 N forces. The displacement and force are continuously measured to determine the amount of force applied and the point along the MN where failure is initiated. As the MN begins to break the energy within the system will decrease. Each mechanical test was run thrice on the same batch of MN and the average results for each force was plotted.

9.3 Porcine Skin Preparation

9.3.1 Introduction

To prepare skin samples for testing, full thickness porcine skin was purchased from Wetlab Ltd. Warwick. On the morning of delivery, the pig is euthanised and these are

delivered to the laboratory on ice. The sections of the pig are then defrosted, and the fat and muscle are removed. For dye staining and histological characterisation, a full thickness skin is sectioned, and these are wrapped in foil and frozen. Franz cells require thinner skin with thicknesses varying between 100 and 1000 µm. Skin possessing these thicknesses is obtained using a Pagett electric dermatome. Once sliced, the skin samples are then cut into diameter of the Franz cell mounting platform, before being wrapped in foil and frozen. All prepared porcine skin samples are to be places in -20 °C unless otherwise specified.

9.3.2 Histological Sectioning

Histological sectioning refers to a thin slice of tissue that is viewed under a microscope to visualise the skin anatomy. Histological skin cross sections are obtained to visualise the MN microchannels post penetration. Initially, MNs are penetrated into full thickness porcine skin and immediately frozen at –20°C for 24 h. The samples are then secured onto a Leica cryostat stage using Optical Coherence Tomography (OCT) embedding medium purchased from Sigma. Each sample is inserted into the cryostat and the blade used to section the skin is brought forward until it comes into contact with the skin to produce 30 µm skin slices. The sliced skin is then mounted onto a glass slide to analyse the penetration regions. Post slicing, the samples were then subject to the Hematoxylin and Eosin (H&E) staining process adapted from a standard process in an established protocol. H&E staining is used to identify the various layers of the skin due to Hematoxylins and Eosin ability to illustrate nuclear details and cytoplasm in cells respectively. The protocol used for the H&E staining is summarised as follows:

1. Wash samples in PBS for 2 min.
2. Stain the samples in Harris' Haematoxylin for 1 min.
3. Wash the samples in DI Water.
4. Wash the samples in 1% acid alcohol for 1 s.
5. Dip the samples in DI Water
6. To obtain blue pigmentation in the sample, wash the sample in Scoots tap water for 1 min.
7. For counterstaining, place the samples in 0.5% Shandon Eosin Y for 1 s.

8. Wash the samples in DI Water

Once the samples have dried, the samples were then placed under a microscope to determine whether the MNs had disturbed the SC and the depth, in which they punctured.

9.3.3 Trans-epidermal electrical resistance

To evaluate whether there are any defects in the porcine skin, trans-epidermal electrical resistance (TEER) is used. The TEER values are a strong indicator of the cellular barrier prior to the evaluation of the drug delivery capabilities of MNs. The TEER measurements are able to be performed in real-time without damaging the cellular barrier and are generally based on measuring the ohmic resistance across the membrane (171).

Trans-epidermal electrical resistance consists of the membrane being placed on top of a receptor chamber from a Franz Cell containing 0.01 M PBS with a dosing chamber containing 0.1 M PBS sealed onto the membrane. Over a half an hour time period, resistance readings are measured to determine any significant changes that may entail a deformation in the membrane (Figure 9.3). The concept is that the resistance across the skin should not change if the SC is still intact. If the SC is broken, the resistance will change significantly as the solution from the dosing chamber mixes with the solution in the receptor chamber

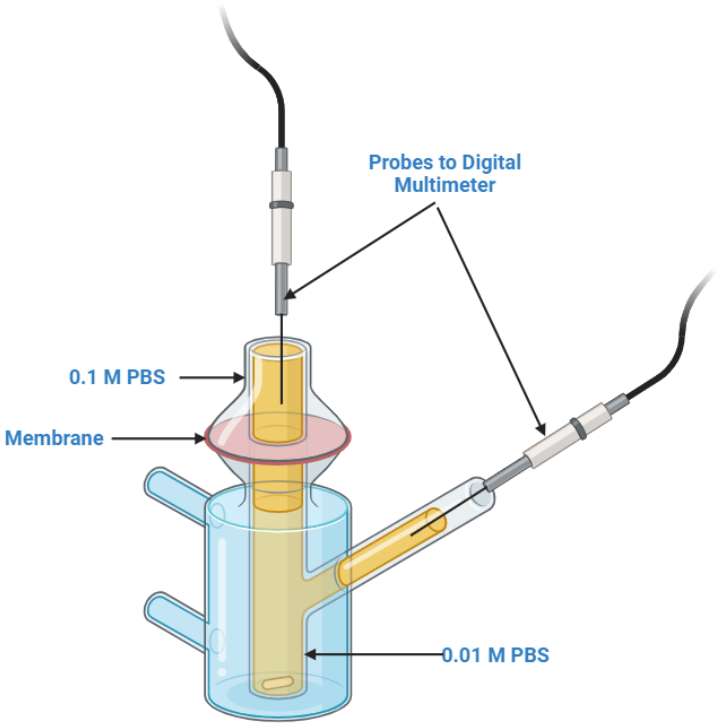

Figure 9.3 Schematic representation of TEER set-up for membrane damage caused prior to Franz Cell Experimentation

Chapter 10

Experimental methods for characterisation of transdermal drug delivery

The equipment and methodology used in this chapter were used to demonstrate the transdermal drug delivery capabilities for each MNA.

10.1 Franz cell assay

The standard method used to assess the drug delivery capabilities is in vitro drug delivery techniques. The most frequently used technique was developed by Thomas J.Franz in 1970 called the diffusion Franz cell. The Franz cell functions with limited tissue handling, no continuous sample collecting, and finally requires low amounts of drug for analysis. There are a few drawbacks in the use of these cells like a lack of skin appendages that can affect the transdermal kinetics, limited dynamic conditions, lack of metabolic/ enzymatic activity and finally is a simplified skin model.

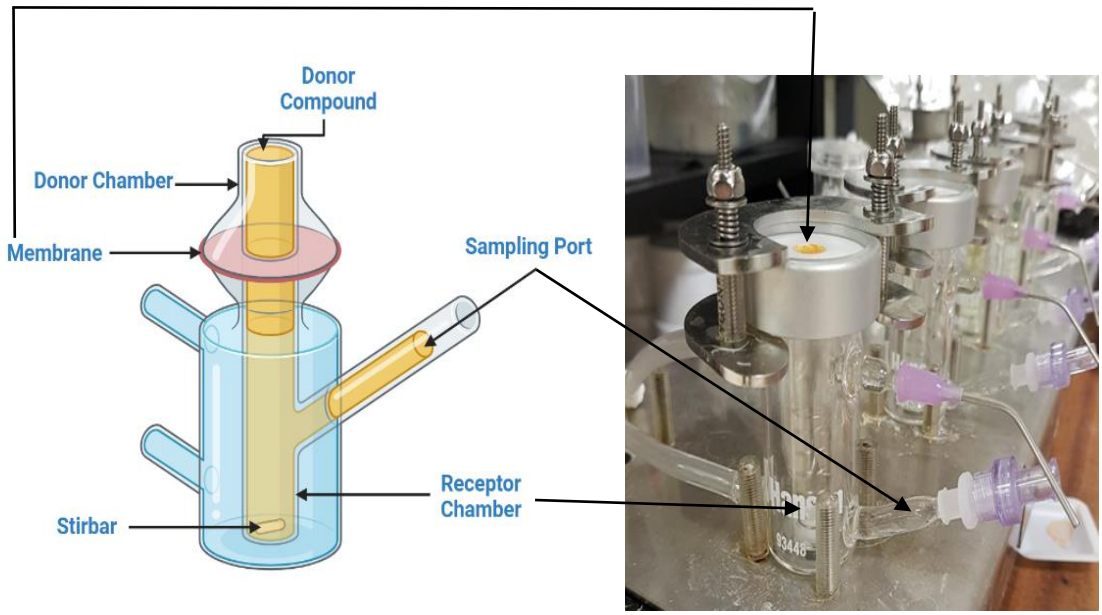

Figure 10.1 Schematic representation of a Franz cell and Franz cell set up with porcine skin as the membrane and PBS in the receptor chamber for drug sampling.

The 'Organisation for Economic Co-operation and Development (OECD) guideline for the testing of chemicals' are testing regulations that have been designed to provide

information on absorption of a test substance applied to excised skin. The principle of this test is as follows:

1. For a Franz cell the components include the donor chamber, the skin surface rinsing, the skin preparation, and the receptor chamber. The skin can be fractioned into the areas of the skin that include the SC, epidermis, and dermis regions. The substance being tested through dissolvable MNs or topically applied after MN 'poke and patch' techniques, is applied to the surface of the skin that is separating the two chambers of a diffusion cell. The drug then remains on the skin for a specified amount of time (24 h) under specified conditions (37 °C), before being removed by appropriate cleaning procedures. The fluid in the receptor chamber is sampled at various time points throughout the experiment and analysed for the drug based upon a standard curve produced with known concentrations of drug. Either high-performance liquid chromatography (HPLC), enzyme-linked immunosorbent assay (ELISA) or fluorescence are used for analysis of the dosage output.

2. The drug that remains in the SC, epidermis and dermis layers should be considered as absorbed, unless it is demonstrated that absorption is determined from the receptor fluid only. Analysis of material that has been washed off and remaining in the skin layers allows for further evaluation that includes the total test substance disposition and percentage recovery.

The key features of the methodology used in a Franz cell experiment are:

1. The diffusion cell consists of a donor and receptor chamber with the skin membrane positioned between the donor and receptor chambers. There should be a good seal around the skin and should enable easy sampling, good mixing within the receptor solution and good temperature control of the cell and contents within.

2. Physiologically conducive receptor fluid is preferable, and the precise composition should be provided. Adequate solubility of the drug in the receptor fluid should be demonstrated so that it shows it is not act as a barrier to absorption.

3. Skin from animal or human sources can be used and viable skin is preferred but if non-viable skin is used, the integrity of the skin must be demonstrated. Split thickness skin, with a typical thickness range of 200-400 μm, prepared with a dermatome is acceptable. A minimum of four replicates per test is seen as acceptable data.

4. It is essential that the skin is prepared properly. Inappropriate handling can result in damage to the SC. Therefore, skin integrity must be checked by measuring the trans-epidermal electrical resistance techniques. Freshly excised skin should be used as soon as possible, but acceptable storage periods could vary depending on the enzyme system and storage temperature.

5. A sampling period of 24 h is required to allow for adequate characterisation of the absorption profile. Skin integrity could start to deteriorate past 24 h due to the skin cells beginning to breakdown through hydrolytic enzymes. Due to the loss in skin integrity after 24 h, drug permeation through the skin membrane will be much higher and therefore could cause over prediction of the drugs diffused into the receptor chamber.

6. Every region of the experiment the drug permeates through needs to be analysed and the recovery needs to be determined.

Before carrying out the Franz cell experiment, a calibration curve was created to determine the concentration of the drug in the receptor chamber. This is done by comparing the unknown concentration in the receptor chamber to a standardised sample. of known fluorescence (Figure 10.2). In this thesis, the maximum concentration utilised was the maximum dosage applied to the surface of the membrane followed by a set of serial dilutions to produce the required concentration points for a robust calibration curve. For a robust calibration curve, a series of replicates of approximately 6-8 expected concentration values are recommended. A linear regression model between calculated standard points and the nominal ones used to evaluate the quality of the fit should have a unit slope and a zero intercept. Linearity of the calibration curve is expressed through the coefficient correlation (R), or the coefficient of determination (R^2). A coefficient close to unity (R^2=1) is considered sufficient evidence to conclude that the calibration curve is linear.

(A)

Calibration curve	
Concentration (µg/ml)	Fluorescence (a.u)
2.50000	46822
1.25000	22301
0.62500	11022
0.31250	5250
0.15625	2392
0.07813	1005
0.03906	367
0.01953	143
0.00977	136
0.00488	153
0.00000	153

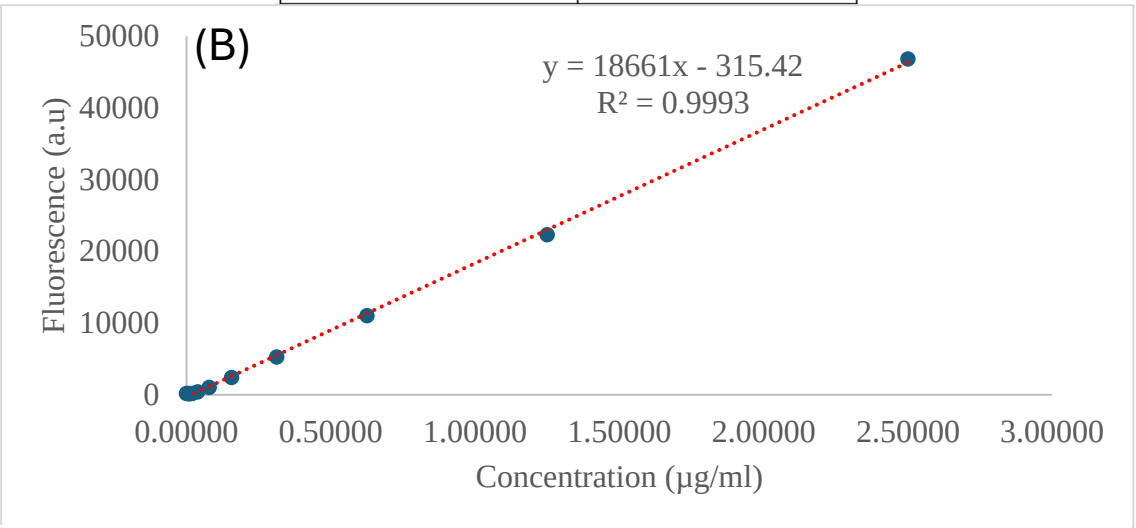

Figure 10.2 (A) Example of data used to produce a calibration curve; (B) Example of a calibration curve showing fluorescence obtained for set concentrations of test compound calcein.

For the Franz cell, initially the receptor chamber is filled with 4 mL of 0.1 M PBS and is placed onto a heated magnetic stirring pad set to 32 °C. Setting the temperature to 32 °C mimics the skin surface temperature. At the bottom of the receptor chamber a magnetic stirrer is placed to maintain a homogenous mixture. The porcine skin is placed onto the receptor chamber and is secured into place using a cell clamp. Samples are collected from the receptor chamber using two spouts which protrude from the side of the chamber. 400 µl of 0.1 M PBS was injected into the top spout, also known as the inlet spout and this pushes sample solution out of the bottom spout, which is collected into an Eppendorf tube. For all Franz cell experiments, 11 samples are collected at 5 min, 15 min, 30 min, 1 h, 2 h, 4 h, 6 h, 8 h, 10 h, 12 h, and 24 h. The results obtained are used to create a cumulative concentration curve.

In this thesis, the hypodermic needles and solid silicon MNs were applied to the skin to create the vias in the membrane before the membrane is applied to the receptor chamber

and the test compound is drop casted onto the holes created. Therefore, the test compound will permeate through the vias into the SC, the epidermis, dermis layer and finally into the receptor chamber. The PVP MNs are dissolvable and therefore penetrate the skin membrane and remain in the skin for the entire duration of the Franz cell experiment for diffusion to occur through the skin layers into the receptor chamber. Finally, for the control, the test compound is applied to the untreated skin membrane to compare how diffusion occurs naturally through the skin layers over the Franz cell experiment.

After each sample is taken and replenished with 400 µl of 0.1 M PBS, the concentration of solution in the receptor chamber is diluted. Solution replenishment and therefore dilution is required rather than reintroducing sampled solution back into the receptor chamber to simulate the bodies conditions. This simulates drugs being introduced into the body and diffuse through to the circulatory system where it is absorbed by cells and are therefore not freely available in the ISF for long periods of time. In the diffusion of drug out of the ISF into the circulatory system, diffusion flux will be influenced across the membrane causing high volumes of drug being pushed through the body. By removing sampled solution and diluting the receptor will mimic this diffusion flux change and therefore is a key consideration to consider. Therefore, to factor in this dilution and calculate the exact concentration in the Franz cell, the following calculations were used:

Table 10.1 Table for Dilution Factor calculations for each time point.

Time (h)	Dilution Factor	Factor (f)
0.25	1000/4000	0.25
0.5	2000/4000	0.5
1	3000/4000	0.75
2	4000/4000	1
4	5000/4000	1.25
6	6000/4000	1.5
8	7000/4000	1.75
10	8000/4000	2
12	9000/4000	2.25
24	10000/4000	2.5

To account for the dilution, each aliquoted sample was multiplied by the respective dilution factor for the timepoint. Therefore, the overall concentration of drug in each aliquot will be proportional to the concentration of drug in the receptor chamber at each time point (Table 10.2).

Table 10.2 Table calculating the sample concentration taking the dilution factor into account using test compound calcein.

Concentration found * dilution factor			
Time (h)	Microneedle	Control	Hypodermic
0.08	0.22	0.01	1.05
0.25	0.1 ± 7.10E-06	0 ± 4.31E-10	0.3 ± 7.70E-11
0.5	0.36 ± 1.31E-05	0 ± 8.29E-11	0.66 ± 2.89E-09
1	0.49 ± 1.03E-04	0 ± 1.97E-09	0.8 ± 7.80E-09
2	0.57 ± 5.61E-05	0 ± 5.63E-10	0.94 ± 2.71E-08
4	0.55 ± 1.45E-04	0 ± 3.00E-09	0.95 ± 2.69E-08
6	0.61 ± 1.99E-04	0.01 ± 3.24E-09	1.09 ± 4.32E-08
8	0.55 ± 7.88E-05	0.01 ± 6.39E-10	1.04 ± 1.88E-08
10	0.57 ± 2.51E-04	0.01 ± 1.90E-09	1.11 ± 1.45E-08
12	0.51 ± 2.65E-04	0.01 ± 2.28E-10	1.01 ± 3.51E-08
24	0.59 ± 3.75E-04	0.01 ± 1.51E-09	0.75 ± 4.83E-08

Once the dilution factor is incorporated into the sample calculation, the next stage is to generate a cumulative concentration curve. Cumulative concentration is calculated by determining the concentration difference between each time point and then adding these values together (Table 10.3 and Table 10.4).

Table 10.3 Table showing the concentration difference between each set of samples using test compound calcein.

Difference between concentrations, cumulative (µg)			
Time (h)	Microneedle	Control	Hypodermic
0.08	0.22	0.01	1.05
0.25	0.12 ± 7.10E-06	0 ± 4.31E-10	0.76 ± 7.70E-11
0.5	0.26 ± 6.03E-06	0 ± 3.48E-10	0.37 ± 2.81E-09
1	0.13 ± 9.00E-05	0 ± 1.89E-09	0.13 ± 4.91E-09

2	0.08 ± 4.71E-05	0 ± 1.41E-09	0.14 ± 1.93E-08
4	0.02 ± 8.91E-05	0 ± 2.44E-09	0.01 ± 2.92E-10
6	0.06 ± 5.42E-05	0 ± 2.38E-10	0.14 ± 1.64E-08
8	0.06 ± 1.21E-04	0 ± 2.60E-09	0.05 ± 2.44E-08
10	0.02 ± 1.73E-04	0 ± 1.26E-09	0.07 ± 4.33E-09
12	0.06 ± 1.39E-05	0 ± 1.67E-09	0.1 ± 2.06E-08
24	0.08 ± 1.09E-04	0 ± 1.28E-09	0.27 ± 1.32E-08

Table 10.4 Table showing the addition of the concentration difference to produce the cumulative concentration using test compound calcein.

Cumulative concentration			
Time	Microneedle	Control	Hypodermic
0.08	0.00	0.00	0.00
0.25	0.12	0.00	0.76
0.5	0.38	0.01	1.12
1	0.51	0.01	1.26
2	0.60	0.01	1.40
4	0.62	0.01	1.41
6	0.68	0.01	1.55
8	0.74	0.01	1.60
10	0.76	0.01	1.67
12	0.82	0.01	1.77
24	0.90	0.02	2.03

During the Franz cell experiment, the drug will permeate from the donor chamber through the SC into the epidermis and finally the receptor chamber. Therefore, the cumulative drug concentration within the system as a function of time can be represented as follows in an infinite and finite drug dosage system:

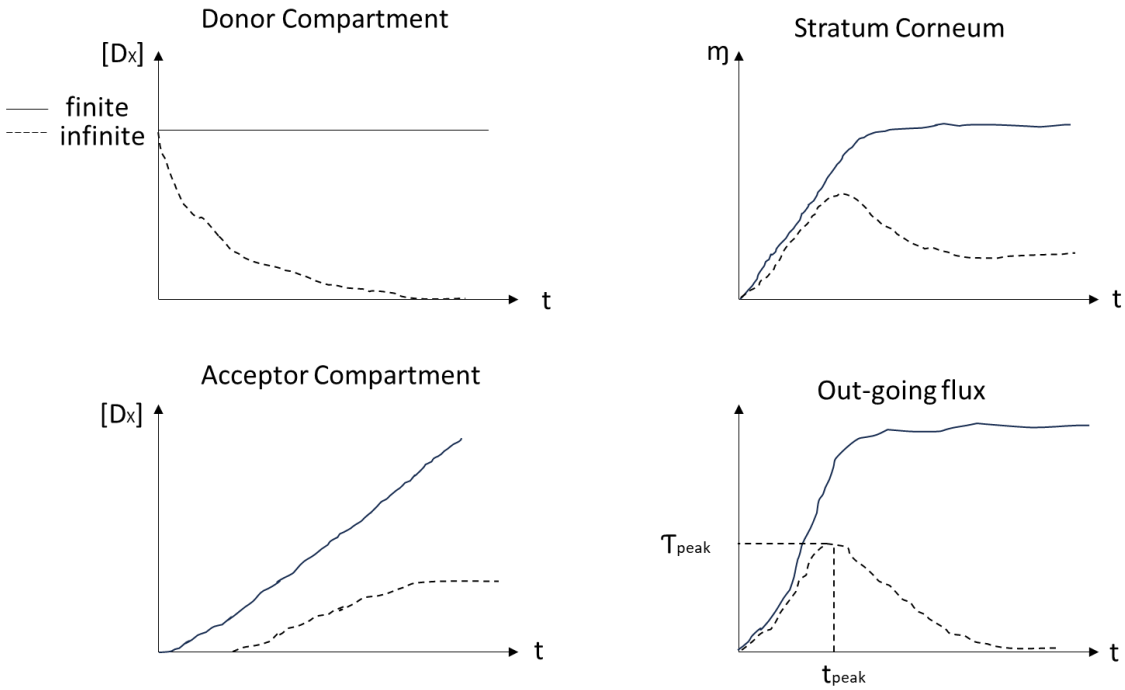

Figure 10.3 Graphical representation of cumulative drug concentration within a Franz cell system as a function of time for an infinite and finite drug dosage systems.

A cumulative concentration curve can then be created by plotting the concentration against time (Figure 10.4).

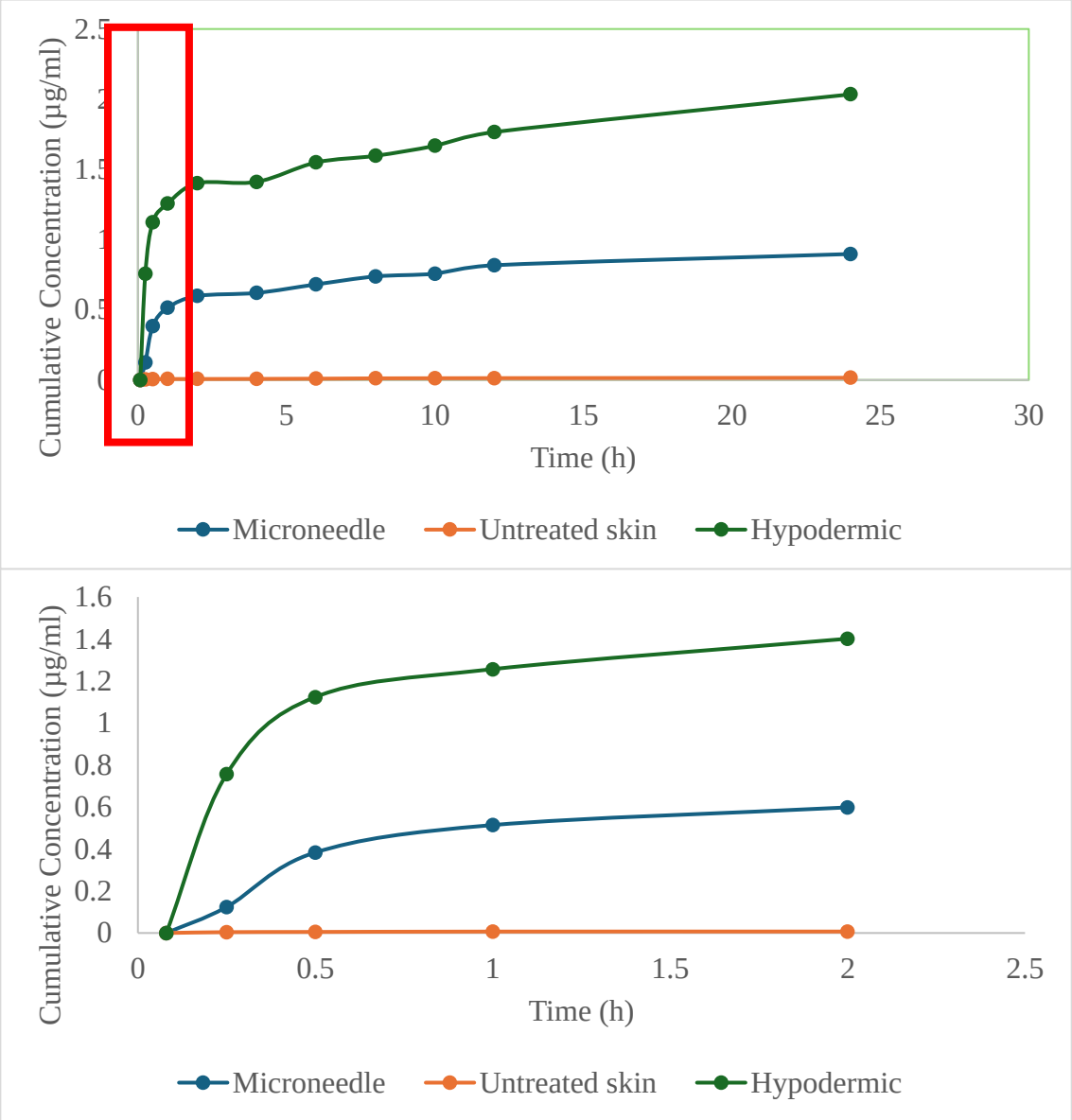

Figure 10.4 Graphical representation of an exemplar cumulative concentration curve using test compound calcein

For each Franz cell, the flux rate is determined to show the rate, at which the drug diffuses into the receptor chamber. To calculate the flux rate, the concentration was divided by the surface area of the Franz cell opening and the time point for the sample. Each Franz cell opening had a radius of 0.45 cm, therefore the surface area is calculated as follows (Equation 4):

$$A = \pi r^2 \quad (4)$$

$$A = \pi(0.45)^2$$

$$A = 0.636cm^2$$

Using the following equation, the flux rate can be determined (Table 10.5) (Equation 5):

$$flux\ rate = {aliquot\ concentration}\Big/{0.636\ cm^2}\Big/{time\ point} \quad (5)$$

The apparent permeability coefficient within the Franz cell can therefore be represented as follows (Equation 6):

$$K_p = \frac{D_x}{Z} \quad (6)$$

where K_p is the partition coefficient, D_x is the diffusivity which is the diffusion through the membrane and Z is the combination of membrane area and initial concentration applied to the membrane.

Table 10.5 Table representing the flux rate calculation from the cumulative concentration.

Flux Js (µg/cm²/h)			
Time (h)	Microneedle	Control	Hypodermic
0.08	0.00	0.00	0.00
0.25	0.78	0.03	4.76
0.5	1.21	0.02	3.53
1	0.81	0.01	1.98
2	0.47	0.01	1.10
4	0.24	0.00	0.55
6	0.18	0.00	0.41
8	0.14	0.00	0.31
10	0.12	0.00	0.26
12	0.11	0.00	0.23
24	0.06	0.00	0.13

A flux rate curve is then created by plotting the flux rate against time (Figure 10.5)

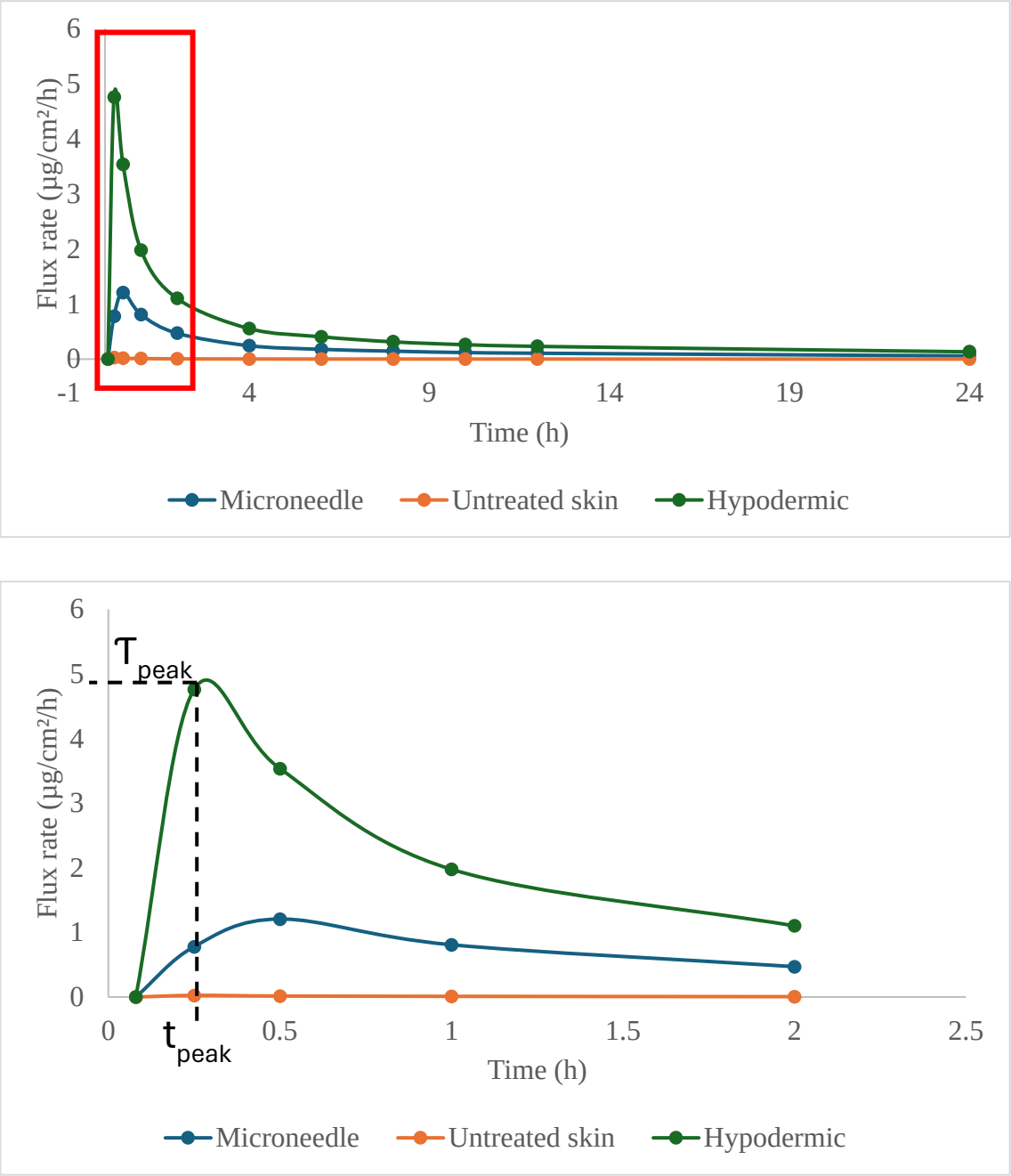

Figure 10.5 Graphical representation of an exemplar flux rate curve

To improve on the Franz cell set-up, the apparatus could be placed into an environmental chamber to mimic the body. Alternatively, various other techniques have been created to provide permeability capabilities of drugs through the skin membrane. The Skin Parallel Artificial Membrane Permeability Assay (PAMPA) test system was design that utilises an in-vitro skin permeation assay. The test is performed using a 96 well plate and the membranes are placed between a donor compartment, to which the test/solution is applied and a receptor compartment filled with buffer solution. The permeation through the

membrane is then measured by determining the portion of substance appearing in the receptor compartment after incubation (172).

Another alternative to a Franz Cell is a MIVO system, this is a disposable cell culture chamber able to host living tissues or artificial membranes under physiological conditions, providing multiple fluidic circulation that mimics the human circulatory system with vascularisation of the tissue of interest (173).

10.2 Tape Stripping

Post Franz cell experiments, tape strips are used to determine the concentration of drug that remain on the surface of the porcine skin and in the SC. Tape stripping is a widely used method in transdermal drug delivery to quantify the drug that is retained in the SC in a minimally invasive way (174). A singular tape strip is placed onto the top side of the skin where the drug was applied and then removed. This tape strip was placed into a centrifuge tube filled with 4 mL of 0.1 M PBS. Following the initial tape strip, 10 consecutive tape strips were placed onto the surface at a consistent rate (175) and these were placed into another centrifuge tube filled with 4 ml of 0.1 M PBS. By using 10 tape strips ensures the entire thickness of the SC is removed and therefore drug concentration measured in the PBS will be accurately represented and not underestimated and measured within the epidermis/dermis layer. Each of the centrifuge tubes were then rotated on a roller mixer for 24 hours to remove the drug from the tape strip into the solution. These samples were then analysed to evaluate the amount of drug that had not been absorbed and in the SC.

The tape stripping technique shows that the physicochemical properties of the compounds are interconnected with the drug amounts retained in the SC and therefore an accurate representation of drug diffusion. By utilizing tape strips to obtain drug concentration within the SC layer, it enables both hydrophilic and hydrophobic molecules to be pulled from the skin compartments. If the skin samples were placed directly into the solution, it can cause the drug molecules to remain within the skin matrix and lead to inaccurate representation of concentration present in the skin (176).

10.3 Skin Homogenisation

Post tape strips, the next step was to determine the amount of drug that was present in the epidermis/dermis layer. Skin homogenisation in either papain or collagenase was used to

break down the epidermis/dermis layer and therefore release the drug encapsulated. Papain is a proteolytic enzyme that helps to break down proteins into peptides and amino acids (177). For drugs that are protein-based, collagenase is an alternative as it is an enzyme that breaks down the native collagen that holds animal tissues together (178).

Depending on whether the active ingredient is protein-based, the following recipes are used:

Table 10.6 Enzymatic recipe used for skin digestion to determine the volume of drug present in the epidermis/dermis layer.

Enzyme	Recipe
Papain	2 mg/mL of Papain 20 mM Sodium Acetate 1 mM EDTA 2 mM Dithiothreitol (DTT) Enzyme solution heated to 60 °C for 2 hours
Collagenase	20 mg/mL of Collagenase 0.01 M PBS Enzyme solution kept at room temperature for 2 h.

Once the porcine skin has been digested, the samples are centrifuged at 3300 rpm for 10 min to cause the skin debris to separate from the enzyme solution. This solution is then analysed to determine the concentration of drug in the epidermis/dermis layer.

By using tape strips and skin homogenisation in drug concentration analysis enables drug distribution analysis through the skin over a 24 hour Franz cell. This can determine how MNs have improved the drug diffusion through the skin into the Franz cell comparative to untreated skin samples.

Alternatively, to tape stripping and skin homogenisation to estimate the concentration of drug present in the various compartments of the skin, mass balance measurements of the donor chamber, skin and receptor chamber can be used. This technique consists of measuring the weight of the donor chamber, skin, and receptor chamber before and after the Franz cell and the mass difference will show where the drug is present. Mass balance

measurements will provide information on the non-absorbed drug, skin, and dosage within the Franz cell in a less time consuming manner. Although it is a quicker technique, the measurements obtained from the mass difference of the skin before and after the Franz cell will only provide information on the drug present within the skin and not the concentration in each compartment which tape strips and skin homogenisation simulates.

10.4 Drug Analysis

The concentration of test compound in the Franz cell is determined using fluorescent spectrometry (179). A FLUOstar Omega spectrophotometer was used as it is a versatile multi-mode microplate reader with three detection modes, which utilises an ultra-fast UV-vis spectrometer for absorbance (FLUOstar Omega).

UV-vis spectrometry is a technique based upon the absorption of ultraviolet light or visible light by chemical compounds, which results in the production of distinct spectra.

To analyse each sample aliquot for each time point, 100 µL is pipetted into a 96 well plate for triplicate analysis and remove the risk of overestimation that can be caused through pipetting and readings pulled from spectrophotometry. Once all the samples have been pipetted into the 96 well plate, the plate is placed into the spectrophotometer, which is programmed to emit the excitation wavelength of the drugs. The values that are generated are then compared to the measurements from the calibration curve generated for known concentrations.

Chapter 11

Experimental methods and materials for diagnostic applications

11.1 Plasma Vapour Deposition

The PVD is a widely used technique to fabricate thin films and surface coatings. Sputtering, ion-plating, magnetron sputtering and electron beam sputtering are common times of PVD. Initially atoms are removed from the target material by using a high energy ion source in the presence of a vacuum and an inert gas, usually argon. The high energy source is provided to the target materials so that the atoms are vaporized from the target surface. From then, the vaporised atoms move towards the substrate surface and are placed in the chamber. The vaporised atoms will then reach the substrate surface and are deposited in the form of a thin layer (180). In this thesis a PRO Line PVD 75 Platform is utilised. A sputter deposition technique is utilised to create a thin film of metal onto the surface of the MNs. A metal target is bombarded with an Argon plasma and the substrate is placed in front of the target. A bias voltage is applied to the substrate holder and the positive ions of the plasma gas begins to hit the target. The target surface is erupted and the eventually is deposited onto the MN substrate (180). Parameters utilised for the PVD are discussed in Chapter 18 section 18.2 and Chapter 21 section 12.2. The PVD was performed to coat the PVP MNs with Pt, Ag and Au for controlled drug release as well as used to coat the polycarbonate MNs with Ti and Pt for diagnostic applications.

11.2 Cyclic Voltammetry

The CV is a frequently used technique to understand the redox potential at an electrode surface and the associated electrochemical reaction rate. This technique varies the potential at the working electrode in a cyclic manner between the initial potential (V_1) and the end potential (V_2) measuring the current flow during the cycle. The scan rate is set and is the time taken to scan between V_1 and V_2, this is defined as follows (Equation 7):

$$Scan\ rate = \frac{V_2 - V_1}{t_2 - t_1} \quad (7)$$

By setting the scan rate at a sufficient value meaningful electrochemical change can be detected. To ensure that the diffusion of the redox mediator, in this circumstance ferrocene carboxylic acid, occurs. The scan rate is set to 100 mVs unless otherwise stated if potential is applied too fast or too slow you won't be able to obtain the current output for the oxidation and reduction of ferrocene carboxylic acid and therefore the connectivity of the MNs post wire bonding.

In CV, a three-electrode set up is used consisting of working, reference, and counter electrodes. The voltage of the WE is measured with respect to the RE and current is measured with respect to the CE. These measurements result in a voltammogram, where an oxidative peak and a reductive peak is present dependant on the sample.

In this thesis 5 mM of FCA is applied as a redox probe as it undergoes both oxidation and reduction in a reversible redox reaction (Equation 8):

$$Fe^{3+} \leftrightarrow Fe^{2+} + e^{-} \quad (8)$$

As the potential is varied from V_1 to V_2, the current also varies due to the redox of the Fe species. As the Fe^{2+} is oxidised the current increases forming the oxidative peak. When the voltage sweep is reversed the Fe^{3+} is reduced to Fe^{2+} and the current will begin to flow in the opposite direction. As the reduction reaction is fulfilled, the current will begin to return back to zero and a reduction peak is observed (181).

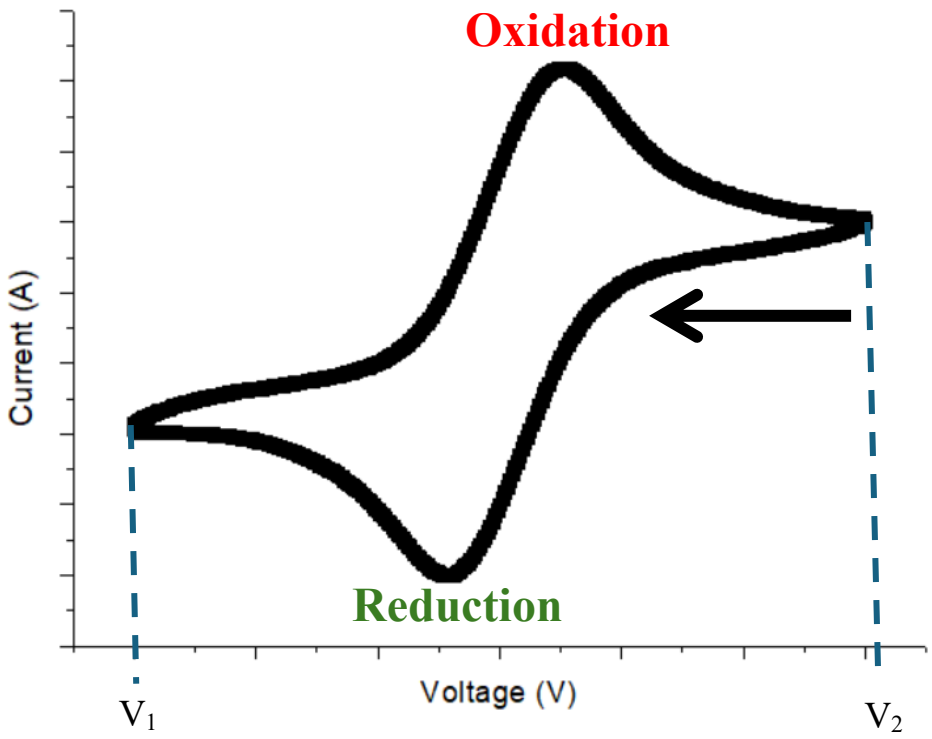

Figure 11.1 Schematic representation of an ideal CV plot for a working electrode

In this thesis, all CV experiments are performed using a multichannel potentiostat, CHI 1030b potentiostat.

11.3 Electropolymerisation

Electropolymerisation is based on the deposition of a polymer on the surface of a solid electrode material. This is based on the multiple potential cycling, and this leads to the polymer being deposited on the surface. The coverage is caused formation of polymer layers. Commonly used monomers that undergo oxidative polymerisation is aniline, pyrrole, and thiazine. These form conductive polymeric films and can be used for the electroanalysis of a wide range of substances. Phenols are also utilised to provide an insulating coverage and these thin coatings allow diffusion of species to and from an electrode surface.

During electropolymerisation, the phenol forms a phenoxyl radical and these can undergo oxidation to quinone or an addition reaction in o- and p- position to form a poly(phenylene oxide) film. The rate of polymerisation is dependent on the monomer concentration, electrode material, electrolysis parameters and pH (182). For this thesis, 50 mM phenol

solution is polymerised with 10 mg/ml of glucose oxidase to form a polyphenol film with the encapsulation of glucose oxidase within. By encapsulating the enzyme using electropolymerisation allows immobilisation onto the sensor surface and upon insertion into the skin the enzyme doesn't delaminate and leak into the skin in case it is not biocompatible.

In this thesis, all electropolymerisation is performed using a multichannel potentiostat, CHI 1030b potentiostat. Each polymerisation cycle comprises of holding the working electrode at 0 V for 20 seconds followed by polarising it to 0.9 V against the integrated RE and an external CE for 15 min. This cycle is repeated 6 times to obtain the desired film thickness and GOx loading.

11.4 Chronoamperometry

The study of the current response over time under potentiostat control is termed as CA. An initial voltage is applied between the WE and the CE where no electrochemical reactions occur at the WE and no net current flows in the cell. At an initial time of t_0, a step voltage is applied to the system causing the solution at the surface of the electrode to be reduced. After a given time period, (60 s), the applied potential is stepped back to a voltage that allows the surface to be oxidised back (183).

In this thesis, all CA is performed using a multichannel potentiostat CHI 1030b potentiostat. The surface of the MNs is drop casted with 200 µl aliquots of varying glucose concentrations prepared in 100 mM PBS. The device is then polarized at 0.7 V against the silver/silver chloride reference electrode and platinum counter electrode for 60 seconds.

11.5 Dose Response

From CA of various glucose concentrations, the steady state current is recorded and these are plotted as a function of the glucose concentrations. The plot is then fitted to a Michaelis Menten plot. Michaelis Menten kinetics is a model of enzyme kinetics that explains how the rate of an enzyme-catalysed reaction depends on the concentration of the enzyme and its substrate. The Michaelis Menten equation is clarified as (Equation 9):

$$v = \frac{V_{max}[S]}{K_m + [S]} \quad (9)$$

where v is the initial rate of the react which is affected by the substrate concentration (S). The V_{max} is the maximum rate of the reaction, where all the enzymes active sites are saturated by the substrate and K_m is the Michaelis Menten constant where the substrate concentration at which the reaction rate is half the V_{max}. The K_m value represents the affinity an enzyme has for the substrate, the lower the value the more efficient the enzyme is at carrying out its function at lower substrate concentrations (184).

In this thesis, all the dose response curves with a Michealis Menten fit have been fitted using software GraphPad Prism 6 XML Project.

Part 3

Optimisation of Silicon MNs for Drug Delivery

Chapter 12

Silicon MN Fabrication

12.1 Introduction

Through a collaboration between Swansea University and SPTS Technologies, a silicon-based MN was developed. SPTS Technologies (Newport, UK) is an experienced industrial leading semiconductor and microdevice company, which has developed and manufactures advanced wafer processing equipment such as PECVD, ICP and DSi-V tools. Swansea University houses a fully equipped nanofabrication and characterisation class 1000/100 cleanroom for silicon-based device development. The cleanroom contains a class 100 photolithography lab that includes a SUSS Microtech mask aligner and spray coater. This offers commercial opportunities that would be impossible for a small or medium-sized enterprise to develop alone. Thus, a collaboration to optimise and find applications for these MNAs was initiated and resulted in patent EP3415465A1.

Fabrication of silicon MNAs, involves three key etching steps:

1. etching of the bevel to create the needle tip,
2. etching of the bore to create the hollow channel through the needle, and
3. etching of the shaft to create the overall MN shape and height (Figure 12.1).

At Swansea University, photolithography patterning of these steps are conducted, while tools such as the DSi-V are used to DRIE etch the MN shapes. Before starting my Ph.D.in 2018, optimisation of the fabrication of MN bevel and bore steps had already begun in collaboration with Dr Olivia Howells. Subsequently, further work on the shaft photolithography patterning and etch process was required to resolve the remaining issues, which are discussed in detail throughout this chapter.

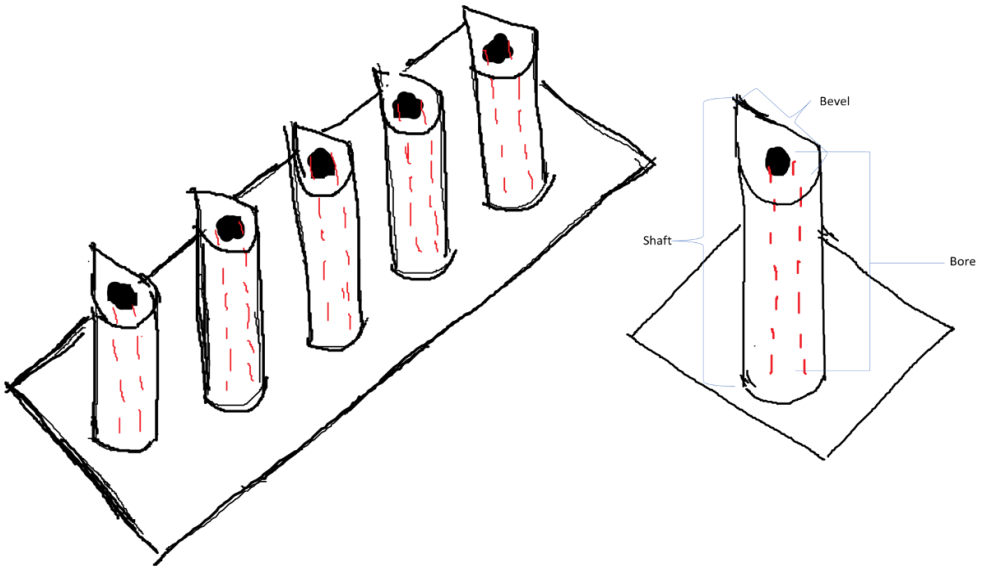

Figure 12.1 Schematic diagram of a MNA (1 x 5) and a single MN

The first step of MN fabrication is photolithography, as described in the Chapter 8, Section 8.1. The mask patterns demonstrated in Figure 12.4 were designed in AutoCAD and manufactured onto glass photomasks Figure 12.2. A photomask is used to mirror the mask design onto a silicon wafer to guide how the etching takes place to form the MN shape and these were created at Photronics Inc. The photomasks were created by applying a photoresist onto a quartz substrate with chrome plating on one side. To harden/develop the mask the substrate is exposed through a process called maskless lithography, also known as electron beam photolithography, where a mask is not required to produce the final pattern. Instead, a digital image on a computer is used to create the final pattern by controlling an electron beam while it scans across a resist-coated substrate, where the chrome is unprotected from the mask and is etched away using a corrosive/acidic solution also known as an etchant solution and the remaining photoresist is stripped using a Technistrip resulting in a mirror image of the mask onto the silicon wafer.

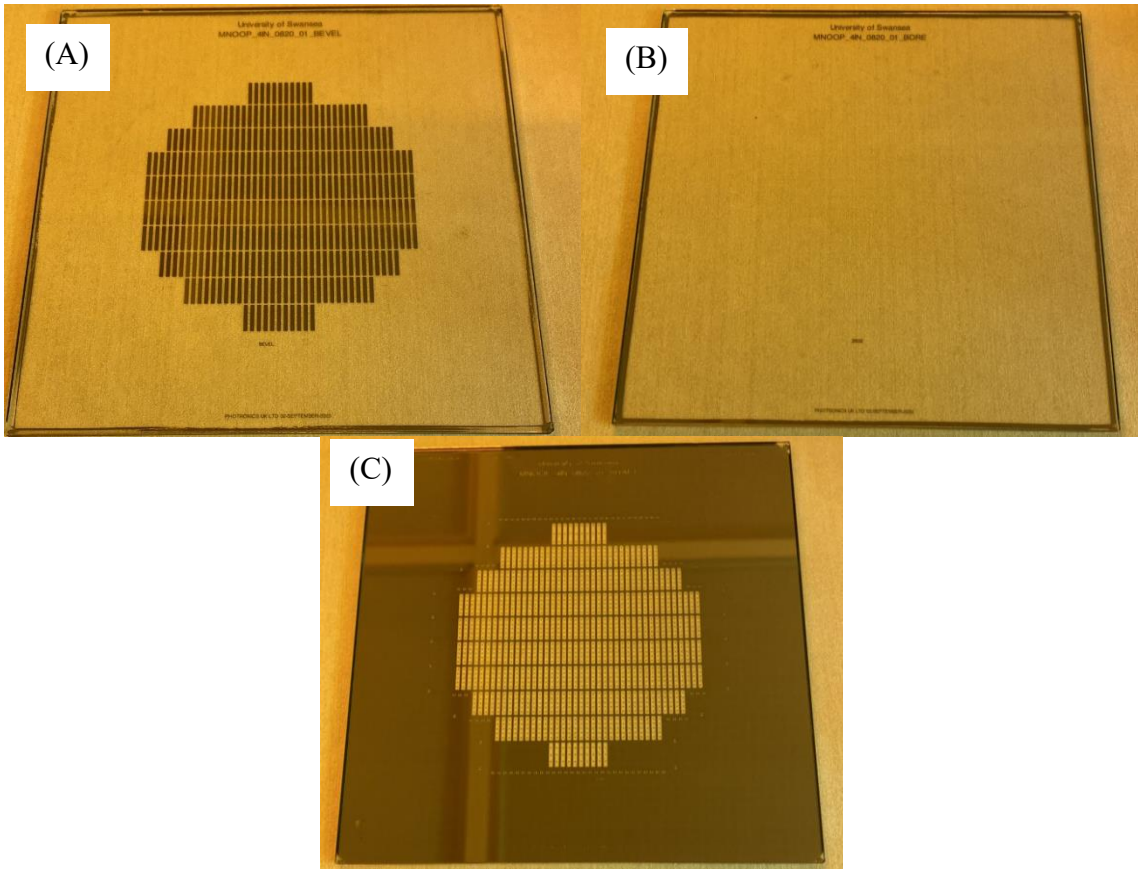

Figure 12.2 Glass Mask used for each stage of the MN photolithography process: (A) Bevel; (B) Bore; (C) Shaft. A negative mask used for the bevel and bore to account for the negative photoresist utilised and a positive mask used for the shaft for the positive photoresist used.

To fabricate a 1× 5 MNA, three masks are used (Figure 12.3). Once the first stencil is designed as a solid rectangle, it is transferred on the wafer and is isotopically etched to undercut the resist and form bevels, which is utilised for the tip of the MN. To create the bore (the hollow centre of the MN), a stencil consisting of five solid circles 1300 µm distance apart, is patterned onto the backside of the wafer in line with the previous mask. Bore patterning occurs on the back of the wafer to protect the bevel etched regions during the DRIE etch of the bore. The stencil is designed to create the overall MN shape, which consists of five tear drop shapes. Once in position, the bores are surrounded to encapsulate them into the shaft of the MN.

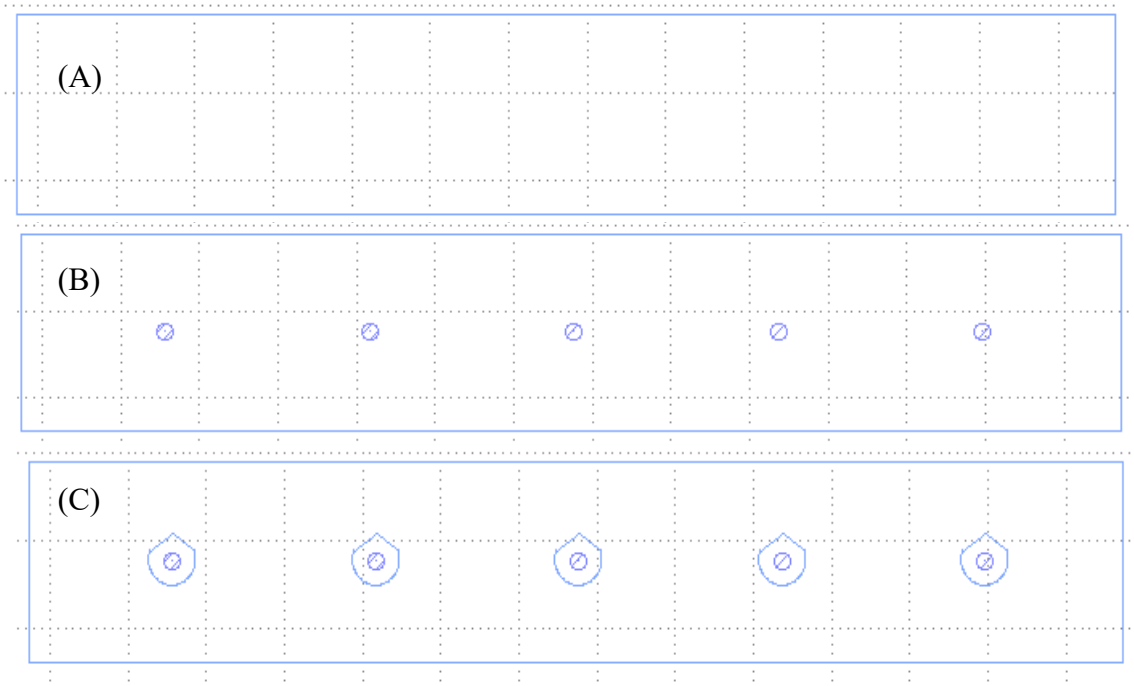

Figure 12.3 AutoCAD Design for a Singular MNA: (A) Bevel; (B) Bore; (C) Shaft

Each photomask stencil is designed to maximise the amount of MN produced from a single silicon wafer and for a 4-inch wafer approximately produces 350 1 x 5 MNAs.

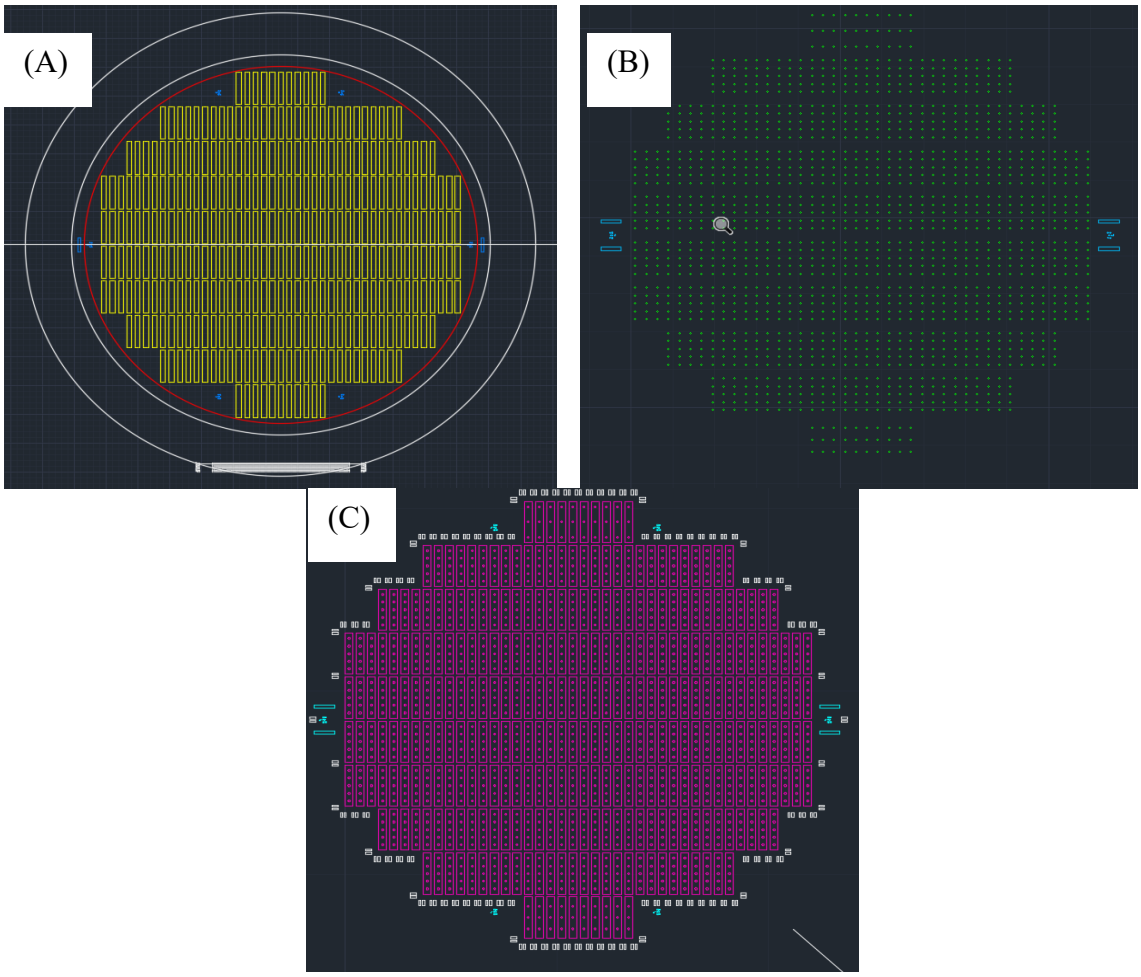

Figure 12.4 AutoCAD Design for a 4-inch silicon wafer: (A) Bevel; (B) Bore; (C) Shaft

12.2 Original MN Fabrication Process

The stages of MN fabrication, involved the following (Figure 12.8):

a. Dependant on the height of the MN required, either a 1.2 mm or a 1.4 mm thick silicon wafer is used for a MN with height 700 µm or a 900 µm. The base of the MNA needed to remain consistent for both heights to make sure the array is robust enough for insertion into skin. These wafers are then deposited with 50 nm of nitride onto the surface of the wafer via CVD.
b. To pattern the bevel mask, negative resist (AZ125nXT) is spin coated over the wafer to a thickness of 25 µm, and UV cured through the photolithography process.
c. Any exposed nitride is removed by ICP etching to expose the silicon wafer surface below.

d. Using an isotropic etch on the DSi-V, the rectangles from the bevel mask are undercut to create the bevel shape at an angle of 89°.

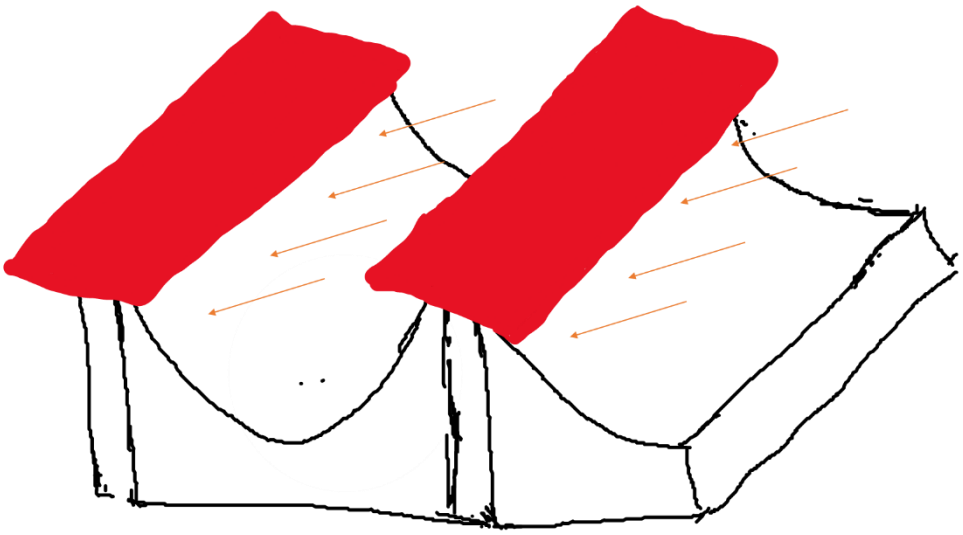

Figure 12.5 Schematic Diagram of the Isotropic Etch for the Bevel Step

e. Post etches, the wafer is cleaned using Technistrip to remove any silicon or resist residue that may affect any further photolithography and etch steps.

If solid MNs are being fabricated stages f-i are skipped from the recipe as these steps create the bore on the back of the wafer.

f. If hollow MNs are required, either resist or nitride is deposited onto the bevel surface to act as an etch stop. An etch stop is a protective layer that is not affected by deep reactive ion etching (DRIE) and is placed over the bevel surface to protect the bevel shape.
g. On the reverse of the wafer, five circular points aligned to the bevel, are patterned using a photolithography process.

h. To etch the cylindrical bore through the centre of the MN, the BOSCH process was utilised.

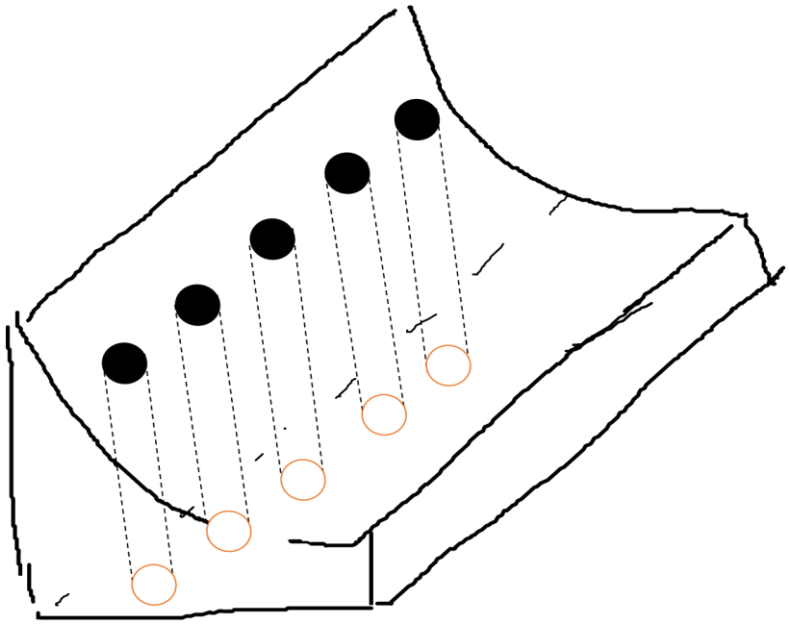

Figure 12.6 Schematic Diagram of the BOSCH etch for the Bore Step

i. Wafer is cleaned using Technistrip to make sure no resist residue remains on the wafer surface.

j. The wafer is flipped, on the newly etched bevel surface, positive/ negative resist is sprayed coated.

k. The shaft pattern is transformed into the resist via photolithography and excess resist is removed.

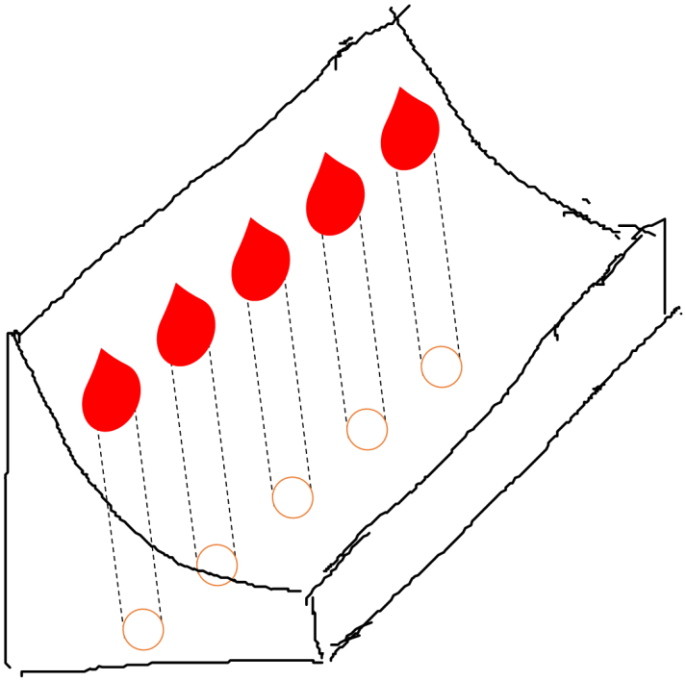

Figure 12.7 Schematic Diagram of the shaft patterning

l. Any exposed nitride left on the wafer is etched away to expose the silicon wafer.

m. Removal of the resist layer over the remaining nitride is cleaned using Technistrip.

n. The wafer is etched using the DSi-V to reveal the shaft that produces the final MNA.

o. The nitride etch stop is removed by applying a high-pressure gust of air through an air gun, to expose the hollow bore.

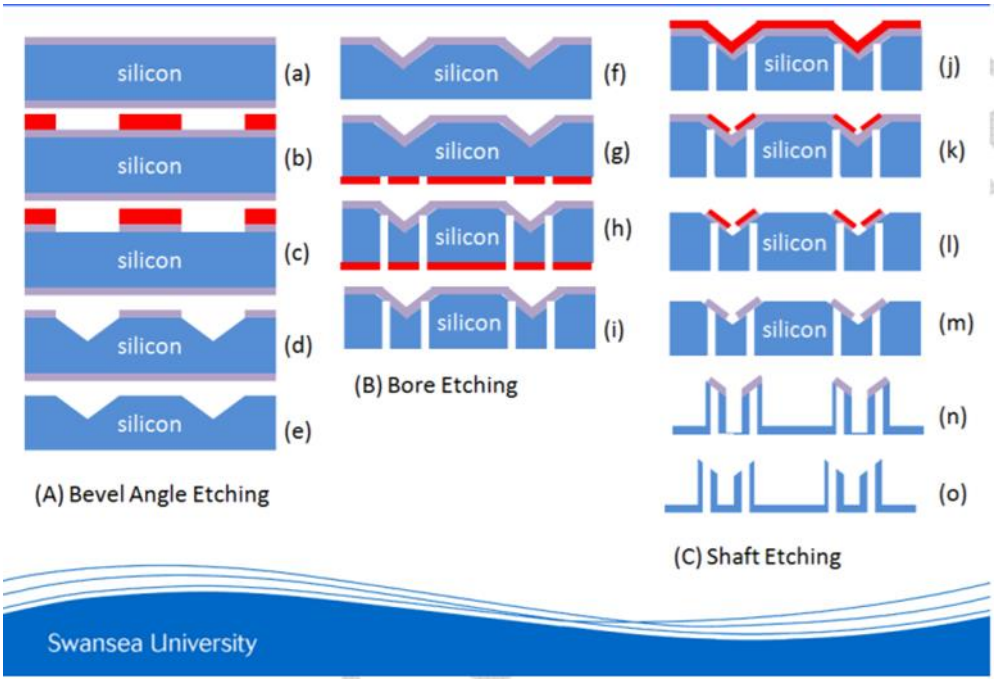

Figure 12.8 Schematic representation of hollow MN production, Silicon wafer (blue), Silicon Nitride Layer (grey) & Photoresist (red)

12.3 Bevel Photolithography

Creating the bevel of the MN is the most important step of MN fabrication as the bevel acts as the tip of the MN and determines how it penetrates the skin without causing significant damage or inflammation to the skin. If the bevel is too shallow the angle of the MN tip will be too large and blunt, which could potentially cause pain or prevent the MN from penetrating. Thus, tuning the bevel etch to an angle of 17.6° was found to produce sharp and robust tips as reported by Howells et al (185).

To create the bevel, a negative photoresist AZ125nXT_10A was spin-coated onto the surface of a silicon wafer, see parameters in Table 12.1, to obtain a thickness of 25 µm. A thickness of 25 µm was applied to make sure that the resist on the surface of the wafer would be able to withstand the DRIE etch process. Using etching experiments, it was identified that there was a resist etch selectivity of 1:50 (resist: silicon) and therefore for achieving an isotropic bevel etch of approximately 500 µm the resist layer was suitable.

Table 12.1 Bevel Photolithography Recipe

	Recipe
Wafer Cleaning Parameters	Sonicate for 10 min in Acetone
	Sonicate for 5 min in IPA
	Air dry with nitrogen gas
	Bake for 10 min at 150 °C
AZ125nXT Spin Coating Parameters	Spin at 300 rpm at an acceleration of 150 for 10 seconds
	Spin at 3800 rpm at an acceleration of 300 for 30 s
Soft Bake	Bake for 5 min at 130 °C
Mask Aligner UV Exposure Parameters	Expose at a dosage of 1500 mJ/cm^2
Post Exposure Bake	Bake for 1 min at 100 °C
AZ726 Development Time	2-min development

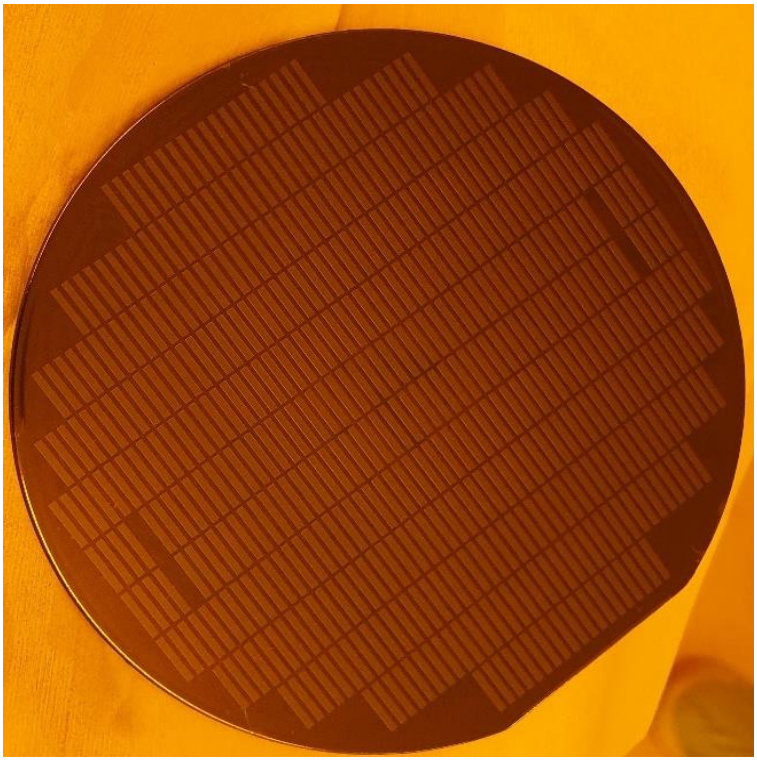

Figure 12.9 4-inch Silicon wafer with bevel photolithography patterning

The CD checks in the 6 regions around the wafer and the bevels were imaged and measured under a microscope to ensure that the bevels were developed to the exact sizes from the glass mask as seen in Figure 12.10. Optimisation of this will be described in subchapter 12.13.

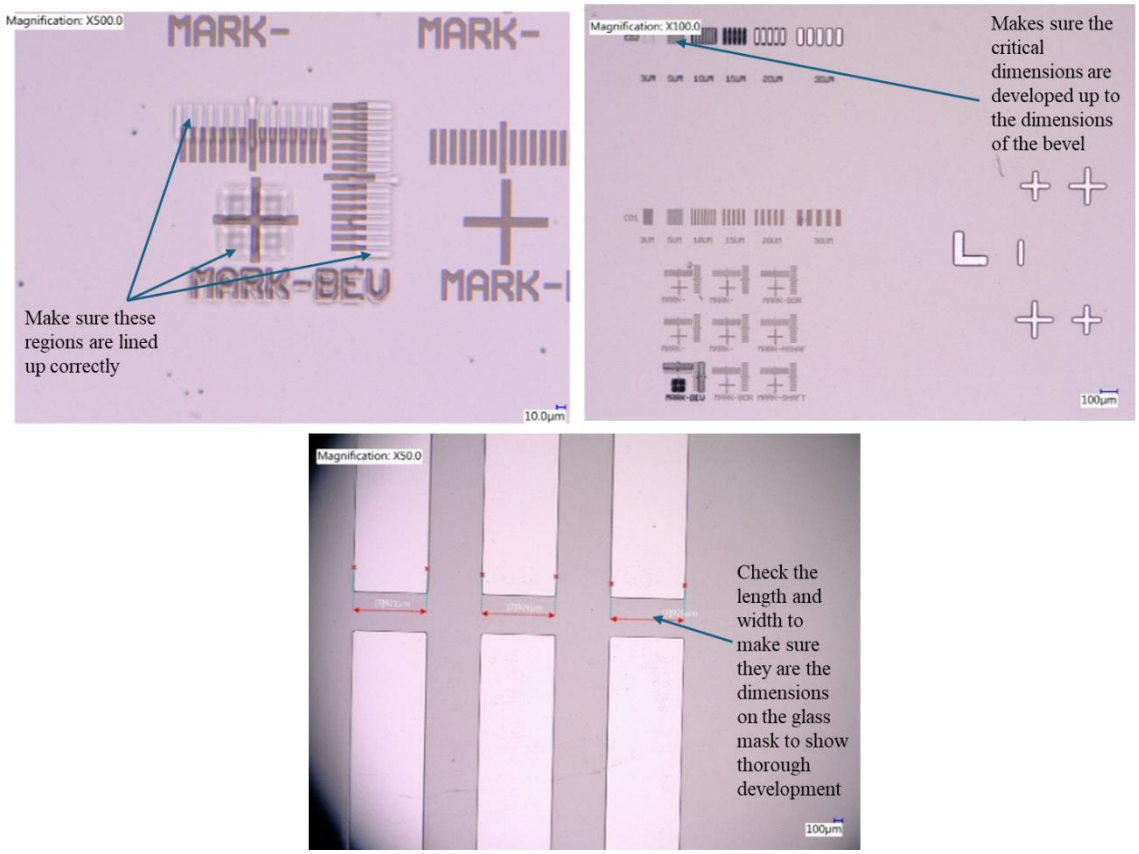

Figure 12.10 Critical dimension checks for each stage of the MN photolithography stage

12.4 Bevel DSi-V Etching

The MN bevel is created using an SPTS deep silicon etch tool known as the DSi-V. To achieve the bevelled surface post bevel patterning uses an isotropic etch optimised in collaboration with SPTS researcher Chris Bolton (Table 12.2).

During the etching step, a platen RF bias is applied, which draws the gaseous ions towards the base of the vacuum chamber where the silicon wafer is located. Here the wafer surface is bombarded by ions. The directions, in which the ions interact with the wafer to form the bevel is controlled through a passivation step in conjunction with vertical and horizontal etching. Enabling the direction of the etch to be tuned implies that the angle from the isotropic etch can be altered to the desired MN tip angle.

Table 12.2 Optimised etch recipe inputted into the DSi-V using an isotropic etch to achieve a bevel etched surface.

		1	2
Step Name		Strike	Etch
Process Time	s	2.0	4250
Process Pressure	mTorr	40 ±0 %	70 ±50 %
APC Mode		Automatic	Automatic
Source 1 Power	W	2000 ±0 %	2500 ±50 %
Source MU tune capacitor		2	2
Source MU load capacitor		1	1
Source 1 RF Control Mode		Load	Load
Platen Frequency		Hi Freq	Hi Freq
Platen HF Power	W	0.0 ±0 %	40.0 ±0 %
Plater HF Capacity Adjust		Preset	Automatic
Platen HF Tune Capacitor	%	70 ±5%	
Platen HF Load Capacitor	%	80.0 ±5%	
Platen HF Padding Capacitor		1	4
Platen HF Control Mode		Load	Load
Platen HF Modulation Enabled		Enable	Enable
Platen HF Modulation Frequency	Hz	150	150

Platen HF Modulation Duty Cycle	%	25	25
Helium Pressure	Torr	10.0 ±10 %	10.0 ±10 %
Helium Flow Warning Level	sccm	5.0	5.0
Helium Flow Fault Level	sccm	8.0	8.0
Coil Current	A	0.0 ±0%	10.0 ±40 %
Loop destination		0	0
Number of loops		0	0
Loop Variation Parameter		0.0	0.0
ESC Voltage	V	5000 ±10%	5000 ±10%
Gas Line Config		Flow	Flow
P1 Nitrogen	sccm	0.0 ±0%	0.0 ±0%
P2 Oxygen	sccm	1.0 ±0%	80.0 ±0%
P3 CF4	sccm	0.0 ±0%	0.0 ±0%
P4 Argon	sccm	500.0 ±0%	0.0 ±0%
P5 SF6	sccm	100.0 ±0%	575.0 ±20%
P6 C4F8	sccm	100.0 ±0%	100.0 ±20%

12.5 Bore Photolithography

The bore of the MN is created by etching vias through the full length of the silicon wafer. These vias act as the hollow portion of the MN, which enables injectable drugs to be delivered into the skin or other tissue. Fabrication of hollow MN enables pressure-driven flow of liquid formulation and therefore can be modified for rapid bolus injections. For solid silicon MN, stages f to I are skipped for skin pre-treatment applications.

Initially, the bore is patterned on the back of the wafer using resist AZ125nXT-10A and spin-coated to a thickness of 35 µm (Table 12.3). However, issues occurred in forming a vacuum on the chuck due to the minimal surface area. Therefore, a unique designed chuck from Laurell Technologies Corporation was used to make sure that the wafer can form a vacuum using the outer flat regions around the edge (Figure 12.11).

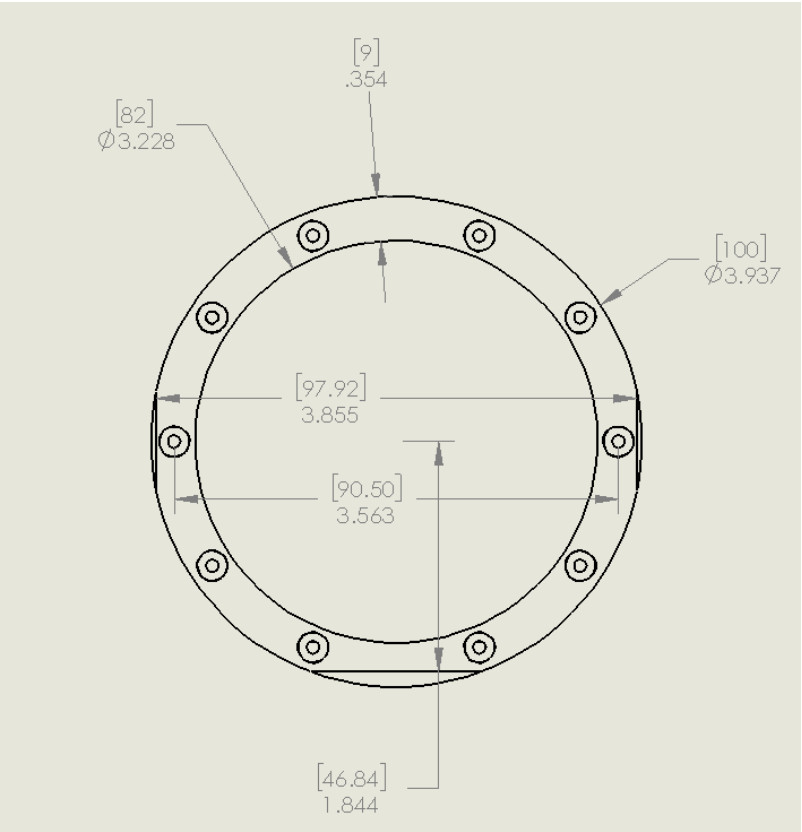

Figure 12.11 Check for spin coating photoresist onto the back of the silicon wafer post bevel etch using an AutoCAD software.

Next, the bore mask (Figure 12.2) is utilised to pattern the bore details onto the reverse of the wafer via photolithography (Table 12.3).

Table 12.3 Bore Photolithography Recipe

	Recipe
Wafer Cleaning Parameters	Sonicate for 10 min in Acetone
	Sonicate for 5 min in IPA
	Air dry with nitrogen gas
	Bake for 10 min at 150 °C
AZ125nXT Spin Coating Parameters	Spin at 300 rpm at an acceleration of 150 for 10 s
	Spin at 2500 rpm at an acceleration of 300 for 30 s
Soft Bake	Bake for 14 min at 130 °C
Mask Aligner UV Exposure Parameters	Expose at a dosage of 2500 mJ/cm^2
Post Exposure Bake	Bake for 1 min at 110 °C
AZ726 Development Time	7-min development

12.6 Bore DSi-V Etching

Following the bore patterning, the wafer is placed in the DSi-V to be etched anisotropically known as the BOSCH process. The BOSCH process consists of a traditional switch etch process, which consists of a polymer deposition coating followed by an anisotropic etch. This process is used specifically to etch bores through a silicon wafer without etching the surrounding material. With the application of a polymer coating step a protective layer forms over the side walls of the etch feature, this means that during the anisotropic etch step will preferentially etch the base of the feature. Each etch step can therefore be recognized as a ‘scallop’ on the sidewalls of the vias, consequently the increase in etch depth leads to an increase in the scallop number (Figure 12.12). The process used for the bore etch was once again optimised in collaboration with Chris Bolton.

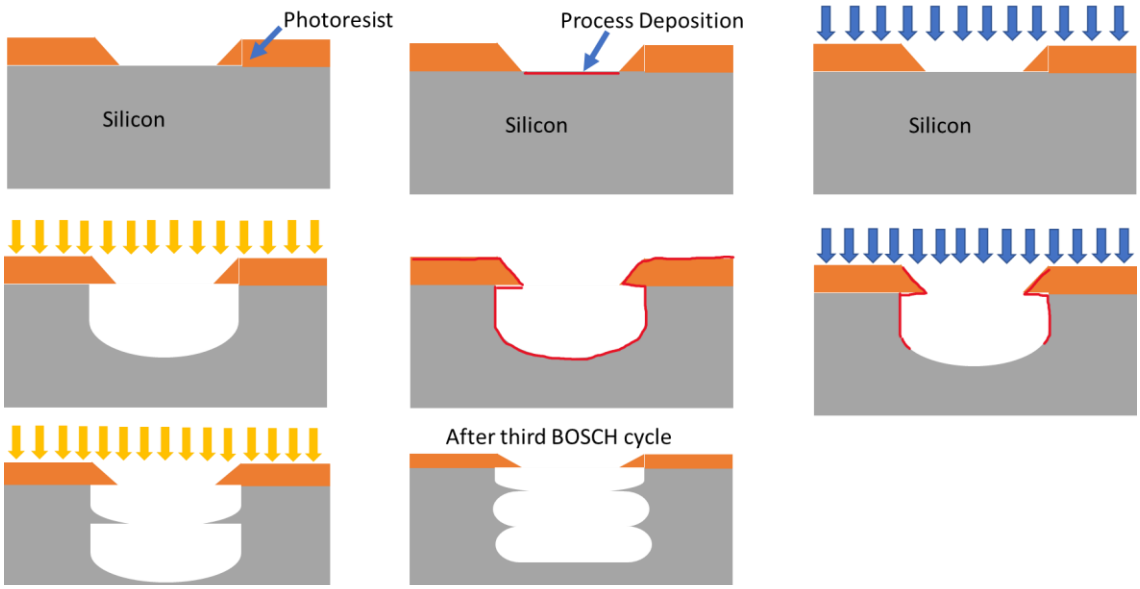

Figure 12.12 Schematic Diagram describing the BOSCH Etch process.

Prior to the bore, DRIE etch process, the etched bevel surface needs to be protected using a spray-coated recipe outlined in section 12.7. The hardened spray-coated resist acts as a defensive layer that stops the bevelled features from being etched as well. The bevel features can be etched, when the vias for the bore are etched through the wafer. The hollow bore can result in an opening where etchant gases can flow through and subsequently damage the front of the wafer.

To achieve the vertical, etch, a two-step anisotropic etch process is required. The Bosch process begins with a fluorocarbon-based protective film deposition by a procedure of quick gas switching, followed by cyclic isotropic etching. SF_6 plasma cycle etches are used to etch away at the silicon and the C_4F_6 plasma cycle creates a protective layer. By using the BOSCH process, it enables the holes through the silicon wafer as seen in Figure 12.13. The spray-coated resist on the surface of the bevel is also used to act as an etch stop to make sure the BOSCH process only etches through the wafer and nothing further.

Table 12.4 Bore etch recipe.

		1	2	3	4
Step Name		Strike	Dep	E1	E2
Process Time	s	2.0	2.2 2.7	1.1 1.2	4.0 7.3
Process Pressure	mTorr	40 ±0 %	80 47.0 ±50 %	27.0 27.0 ±50 %	140.0 107.0 ±50 %
APC Mode		Automatic	Automatic	Automatic	Automatic
Source 1 Power	Watts	3000 3000 ±50 %	3000 3000 ±50 %	3000 3000 ±50 %	3500 3500 ±50 %
Source MU tune capacitor		4	4	4	4
Source MU load capacitor		1	1	1	1
Source 1 RF Control Mode		Load	Load	Load	Load
Platen Frequency		Hi Freq	Hi Freq	Hi Freq	Hi Freq
Platen HF Power	W	5.0 5.0 ±0 %	5.0 5.0 ±0 %	160.0 226.0 ±50 %	18.0 33.0 ±50 %
Plater HF Capacity Adjust		Manual	Manual	Automatic	Automatic
Platen HF Tune Capacitor	%	70.0	70.0 ±0 %		
Platen HF Load Capacitor	%	80.0 ±0%	80.0 ±0%		
Platen HF Padding Capacitor		4	4	4	4
Platen HF Control Mode		Load	Load	Load	Load
Platen HF Modulation Enabled		Enable	Enable	Enable	Enable

Platen HF Modulation Frequency	Hz	150	150	150	150
Platen HF Modulation Duty Cycle	%	50	50	50	50
Helium Pressure	Torr	10.0 ±10%	10.0 10.0 ±10%	10.0 10.0 ±10%	10.0 10.0 ±10%
Helium Flow Warning Level	sccm	5.0	5.0	5.0	5.0
Helium Flow Fault Level	sccm	8.0	8.0	8.0	8.0
Coil current	A	0.0 ±0%	10.0 ±40%	10.0 ±40%	10.0 ±40%
Loop destination		0	0	0	2
Number of loops		0	0	0	20
Loop Variation Parameter		0.0	1.0	1.0	1.0
ESC Voltage	V	5000 ±10%	5000 ±10%	5000 10%	5000 ±10%
Gas Line Config		Flow	Flow	Flow	Flow
P1 Nitrogen	sccm	0.0 ±0%	0.0 0.0 ±0%	0.0 0.0 ±0%	0.0 0.0 ±0%
P2 Oxygen	sccm	1.0 ±0%	1.0 1.0 ±0%	200.0 200.0 ±20%	1.0 1.0 ±0%
P3 CF4	sccm	0.0 ±0%	0.0 0.0 ±0%	0.0 0.0 ±0%	0.0 0.0 ±0%
P4 Argon	sccm	500 ±0%	0.0 0.0 ±0%	0.0 0.0 ±0%	0.0 0.0 ±0%
P5 SF6	sccm	1.0 ±0%	1.0 1.0 ±0%	100.0 100.0 ±20%	720.0 720.0 ±20%
P6 C4F8	sccm	100 ±0%	450.0 450.0 ±20%	1.0 1.0 ±0%	1.0 1.0 ±0%

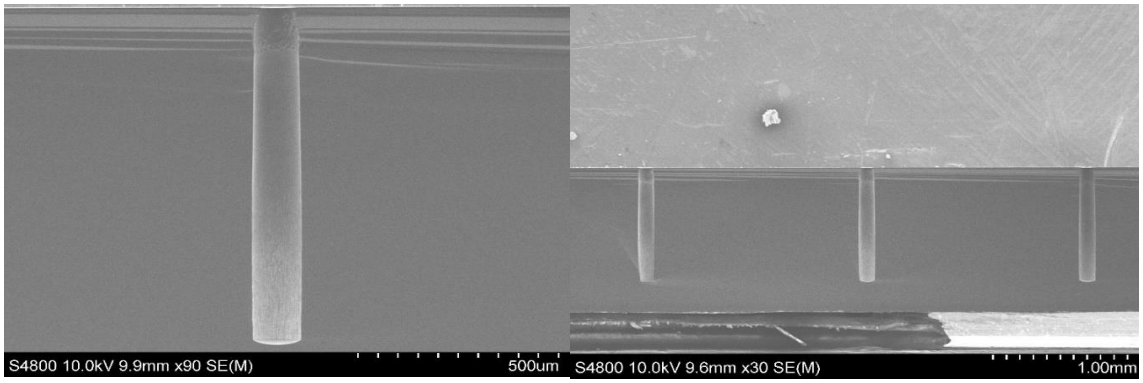

Figure 12.13 Post bore etch through a silicon wafer

12.7 Shaft Photolithography Optimisation

The shaft of the MN is the main shape that combines the bevelled tip to a 300 µm cylindrical shaft. For delivering drugs into the epidermis layer, MNs with a length less than 600 µm showed a 2 to 8-fold increase. The MNs larger than 600 µm showed a 50 to 100-fold increase. Dependent on drug delivery applications, the length can be tailored to penetrates into various regions of the skin.

To produce the shaft of the MN, the last step in the fabrication process is to pattern shafts onto the bevel. Due to the wafer having bevels etched on the surface, the silicon wafer is no longer level and therefore spin coating a resist layer on to the surface would no longer be suitable. Therefore, to obtain a uniform coating of resist onto the wafer surface a spray coater is used. A spray coater deposits atomised photoresist with droplets in the µm and as they land on the surface will combine to form a closed resist film.

Table 12.5 Initial shaft spray coater photolithography recipe

	Recipe
Wafer Cleaning Parameters	Sonicate for 10 min in Acetone Sonicate for 5 min in IPA Air dry with nitrogen gas Bake for 10 min at 150 °C
AZ4999 Spray Coater Parameters	Pump flow: 2.5 mL/min Chuck Temperature: 70 °C Nitrogen Flow: 1.3 bar Sled Speed: 120 mm/s Pitch: 4 Nozzle Height: 20 mm
Soft Bake	Bake for 1.5 min at 90 °C
Mask Aligner UV Exposure Parameters	Expose at a dosage of 3600 mJ/cm^2
AZ400K Development Time	10-min development

The spray coated shaft patterning was optimised using a diluted recipe of a negative resist (nLOF2070) and acetone in a ratio of 1:8. When repeating the patterning of the shaft using the parameters in Table 12.5 it was found that there were many issues in the procedure. Post spray coating of resist, the uniformity required was inadequate which meant development after exposure led to residue around the shaft pattern as seen in Figure 12.14.

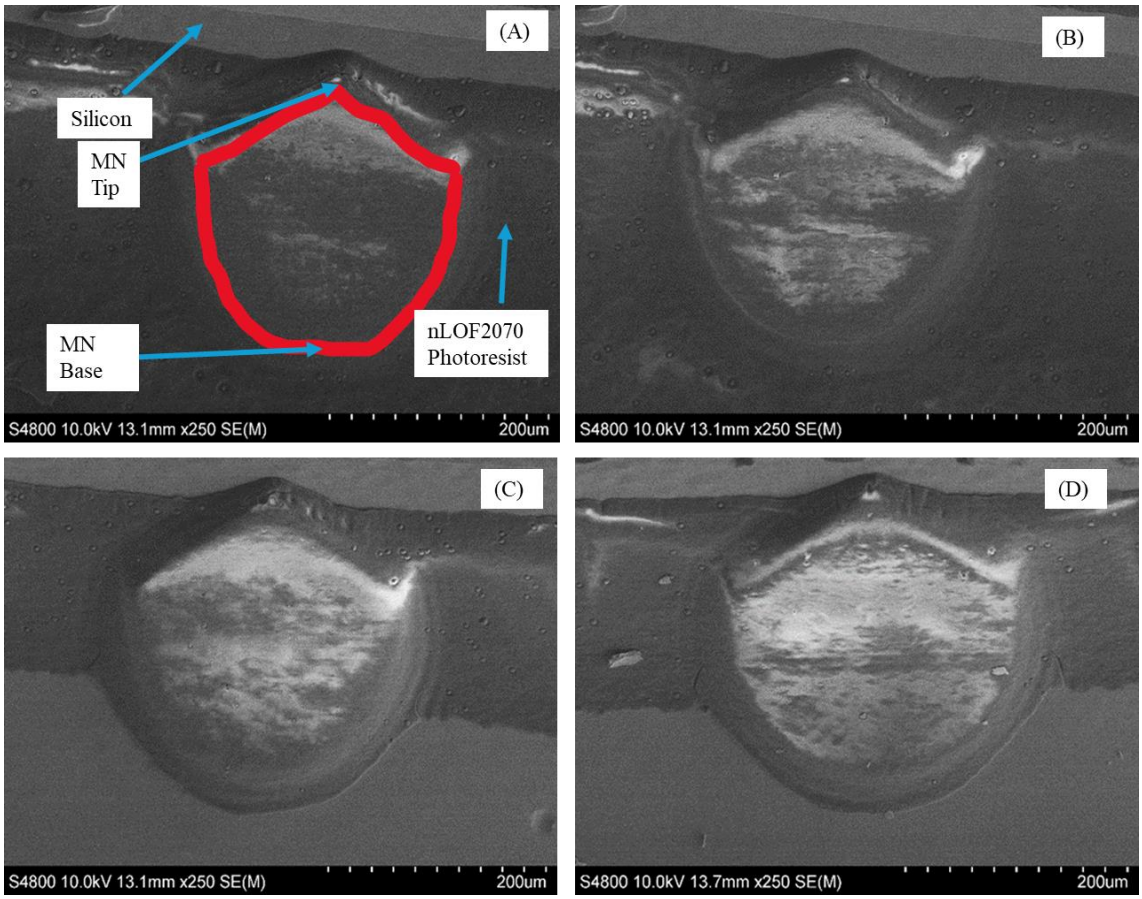

Figure 12.14 Increase in development time: (A) 2 minutes development; (B) 6 minutes development; (C) 10 minutes development; (D) 20 minutes development. With no removal of excess photoresist surrounding the shaft post 8 scan spray coating with nLOF2070 after 20 minutes development

12.8 MN challenges

During the development stages of the shaft photolithography, challenges arose while using the original resist of diluted nLOF2070. nLOF2070 is a negative resist that is usually applied for lift off processes where the resist is removed post processing. Therefore, during development, the resist forms undercut edges and during the etch process the edge of the shaft patterning etches quicker than the centre. The perimeter etching faster than the centre leads to exposure of the edges of the silicon and therefore a

rough surface. In addition, it was observed that the shape and design of the MNA was not satisfactory. Due to nLOF2070 causing an undercut edge post lithography, the shaft of the MN would be smaller than required or the edges of the shaft would be fragile and prone to breaking post etching. Additionally, silicon between individual MN if not completely etched away would consequently inhibit their penetration abilities.

Therefore, the following concerns will be individually addressed in the subsequent section to improve the shape and fabrication of the MNs.

- Optimisation of spray coating resist over the bevel.
- Removal of the silicon wall between the MNs.
- Improvements to alignment marks used to align each mask.

12.9 Shaft Photolithography Optimisation

Initially, to address the issues with nLOF2070 explained in the subchapter 12.8, a new positive resist (AZ4999) that is purposely designed for spray coating, to provide a defect-free and conformal coating on silicon wafers, was sought. As AZ4999 is a photo-initiator based on DNQ-sulphonates, it means that it requires a precise concentration of water during exposure for the photoreaction to occur.

As per Table 12.5, the original parameters of spray coating using nLOF2070 has the arm of the spray coater scanning 8 times over the whole wafer. A single scan consists of the nozzle moving back and forth over a stationary wafer, dispensing the photoresist across the entire surface. Once the entire wafer is coated, the chuck is rotated 90° for the process to be repeated. Each full wafer coating and rotation of the chuck correlates to a scan. Thus, to evaluate how the new resist performs, this recipe was used as a starting point for optimisation. The AZ4999 possesses a lower viscosity in comparison to nLOf2070. Thus, using the same nozzle parameters as nLOF2070 meant that the uniformity from the spray had been compromised. Spray coating optimisation began on blank wafers and it was observed that there were thicker lines where the central region of the nozzle opening was exposed to the wafer (Figure 12.15).

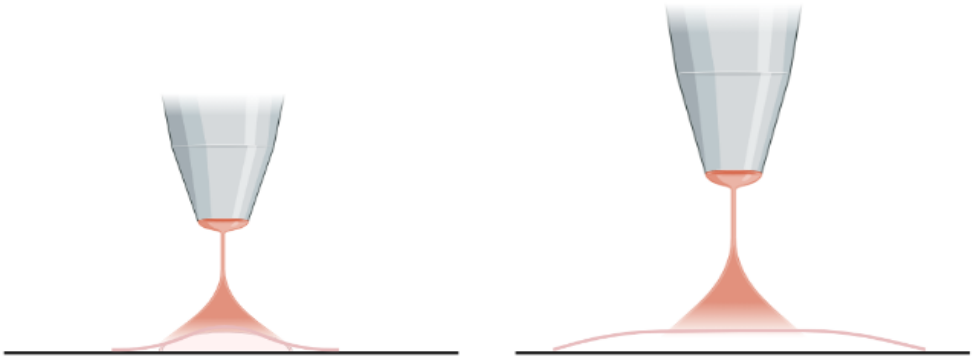

Figure 12.15 Schematic diagram of the nozzle height affecting the uniformity of the spray coating

Surrounding these prominent lines, were splattering caused by the high pressurised spray through the nozzle.

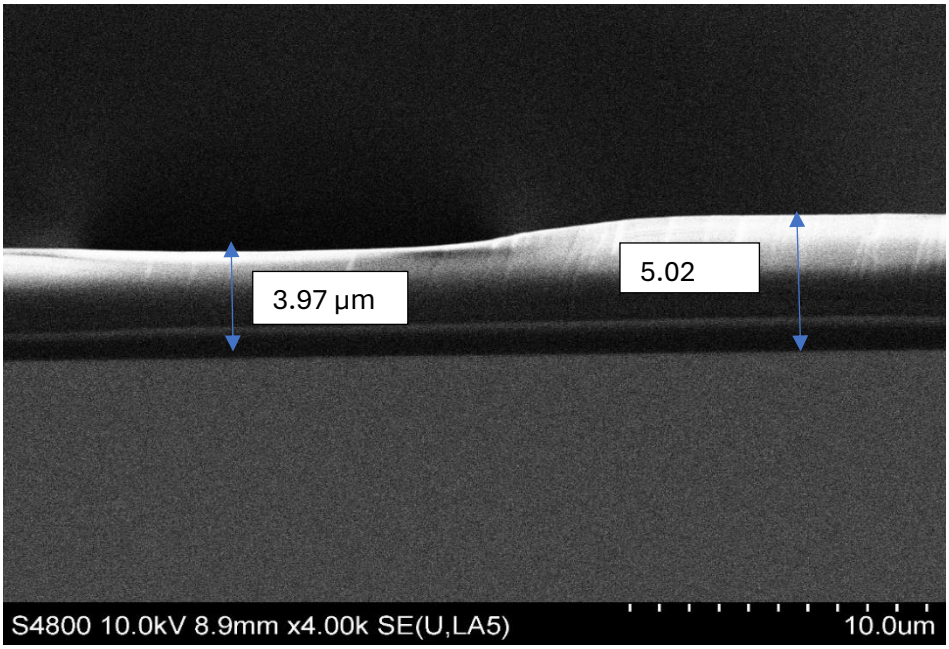

Figure 12.16 SEM image of the non-uniformity of the resist due to the nozzle height

This streaking caused by the nozzle height can be seen in Figure 12.16. As the uniformity was compromised, the height between the nozzle and the chuck was increased to 25 mm to obtain regularity across the wafer as seen in Figure 12.17.

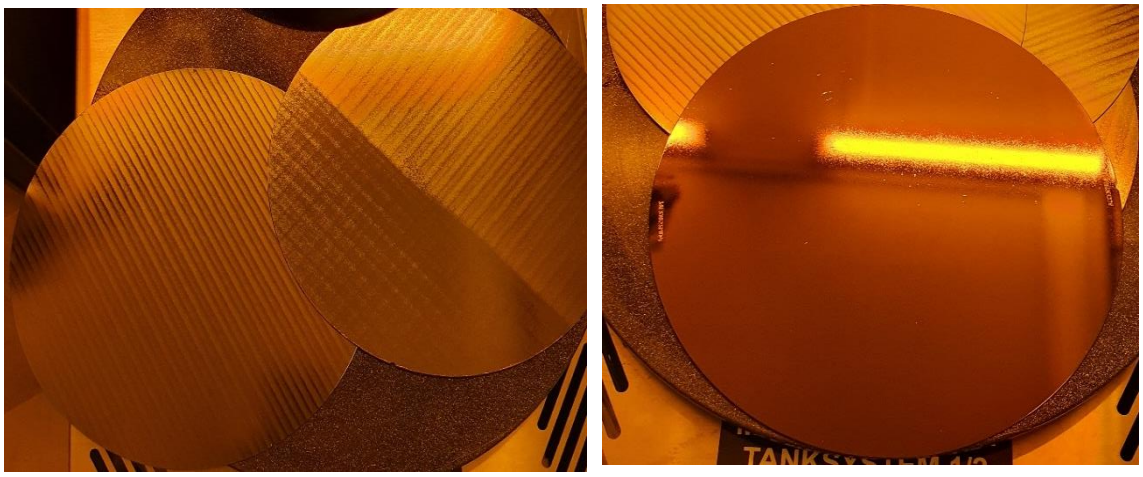

Figure 12.17 Images showing the increase in height allowing better coating of the silicon wafer.

Once spray coating over a flat wafer was optimised to form a 20 µm uniform coating, the next focus was on the development time post UV exposure (Figure 12.18). It has previously been found that curing the resist at too high a UV density or for too long a period of time, could lead to overbaking. This makes it difficult for the developer to remove all the resist and subsequently causes residue to remain over areas of the wafer that need to be clear for etching.

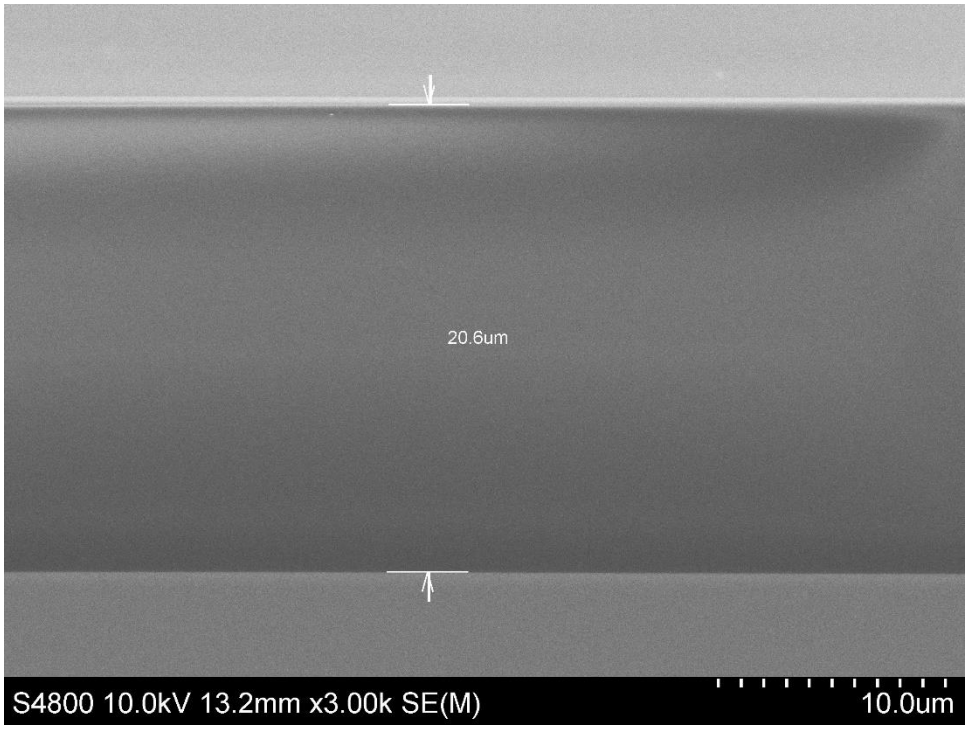

Figure 12.18 SEM image of the optimised resist thickness obtained from the spray coater.

To test development parameters, a single wafer was photolithographically patterned with the shaft mask and then diced into smaller pieces so each piece can be developed at a different time ranging from 2 to 20 min. Once developed, the pieces were examined under SEM to observe whether the resist had been completely removed.

During this initial optimisation, all parameters in the original recipe were kept as independent variables to visualise the effect of development time. Compared to nLOF2070, AZ4999 is a photo-initiator based on DNQ-sulphonates, which requires a precise concentration of water during exposure for the photoreaction to occur. Post spray coating, the original recipe soft baked the wafer at 90 °C for 90 seconds after exposure, which means the resist coated is heated and water is being removed. The purpose of the soft bake is to remove residual solvent present in the resist for:

- Stopping the mask sticking to the resist and avoiding the contamination of the photomask with the resist.
- Improving the resist adhesion to the silicon substrate.
- Preventing bubbling by evaporating solved during dry etching and increasing the softening regions of the resist for the subsequent dry etching.
- Minimising the dark erosion of positive resists during development.

Thus, insufficient amount of water is left in the resist film for the photoreaction to occur. Therefore, a rehydration step was added to the process to make sure the water is fed back in. Without a rehydration step or insufficient rehydration time, this would lead to an increase in development time of over 2 h, which is impractical. As the resist thickness was measured to be 20 μm, using the AZ4999 data sheet provided by MicroChemicals, the full rehydration was determined to be 1.5 h due to the location humidity being quantified as 50 % (Figure 12.19).

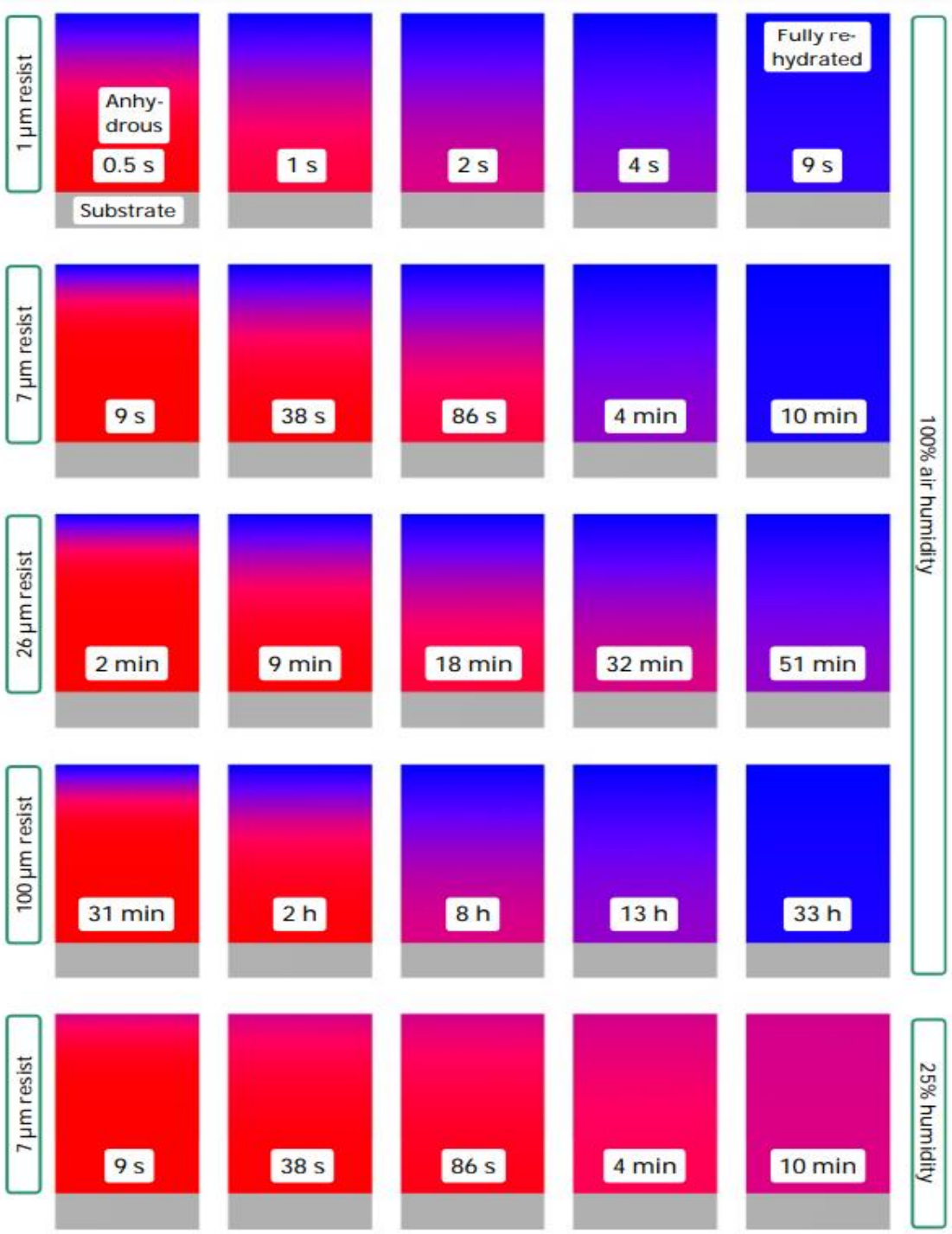

Figure 12.19 Numerical simulation of rehydration time to obtain an equilibrium water concentration in the photoresist whereby the water free resist is shown in red and complete rehydration is shown in blue.

As AZ4999 is a positive resist, using the technical datasheet provided by Merck, diluting AZ400K in a ratio of 1:4 with DI water, was utilised. AZ400K in this ratio provides control of process development and reduces risk of contamination caused by resist removal.

From the SEM images, at development times ranging from 2 - 8 min, there is substantial amounts of AZ4999 residue surrounding the shaft pattern. As the time increased by 2 min, the regions with excess resist began developing away and the shaft teardrop shape was the only resist feature on the silicon surface.

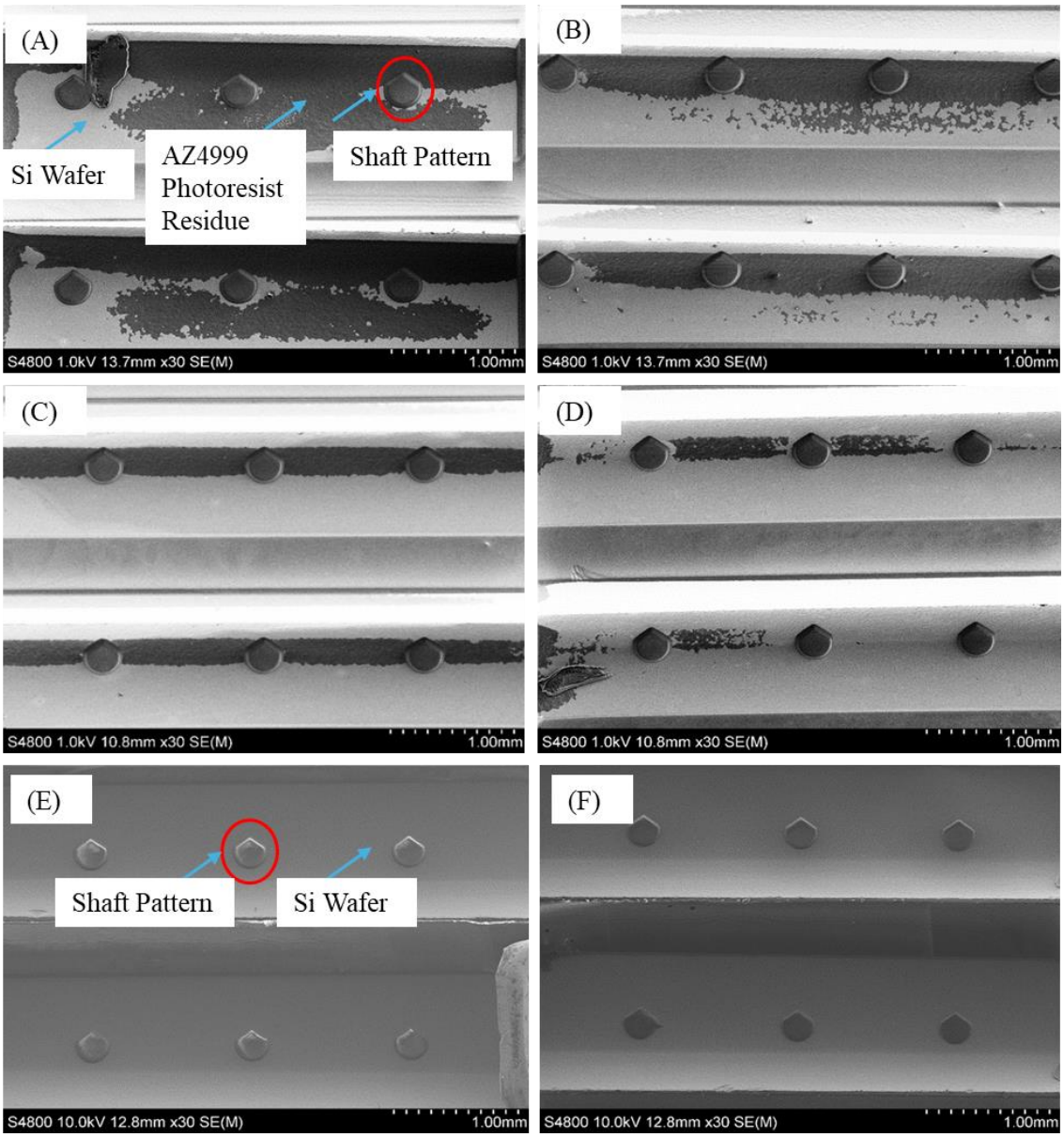

Figure 12.20 Optimisation of development time to remove excess resist of AZ4999 between the shaft pattern after 8 scans of spray coating: (A) 2 minutes development; (B) 4 minutes development; (C) 6 minutes development; (D) 8 minutes development; (E) 10 minutes development.

After 10 min, the residue on the bevel surface had been removed and only the shaft pattern (tear drop shape) remained on the wafer (Figure 12.20). Therefore, the development time utilised for 20 µm photoresist would be 10 min.

Once the development time was optimised, the next step was to determine the UV exposure dose provided by the mask aligner. Exposure dose correlates to the amount of time the photoresist is exposed to the UV light, which will either break down or harden the photoresist coated on the substrate. For positive photoresists, the chemical bonds are

weakened and will become more soluble upon exposure to UV light. The original nLOF2070 exposure dose was set at 500 mJ/cm^2 , thus it was decided that higher UV dosages needed to be tested.

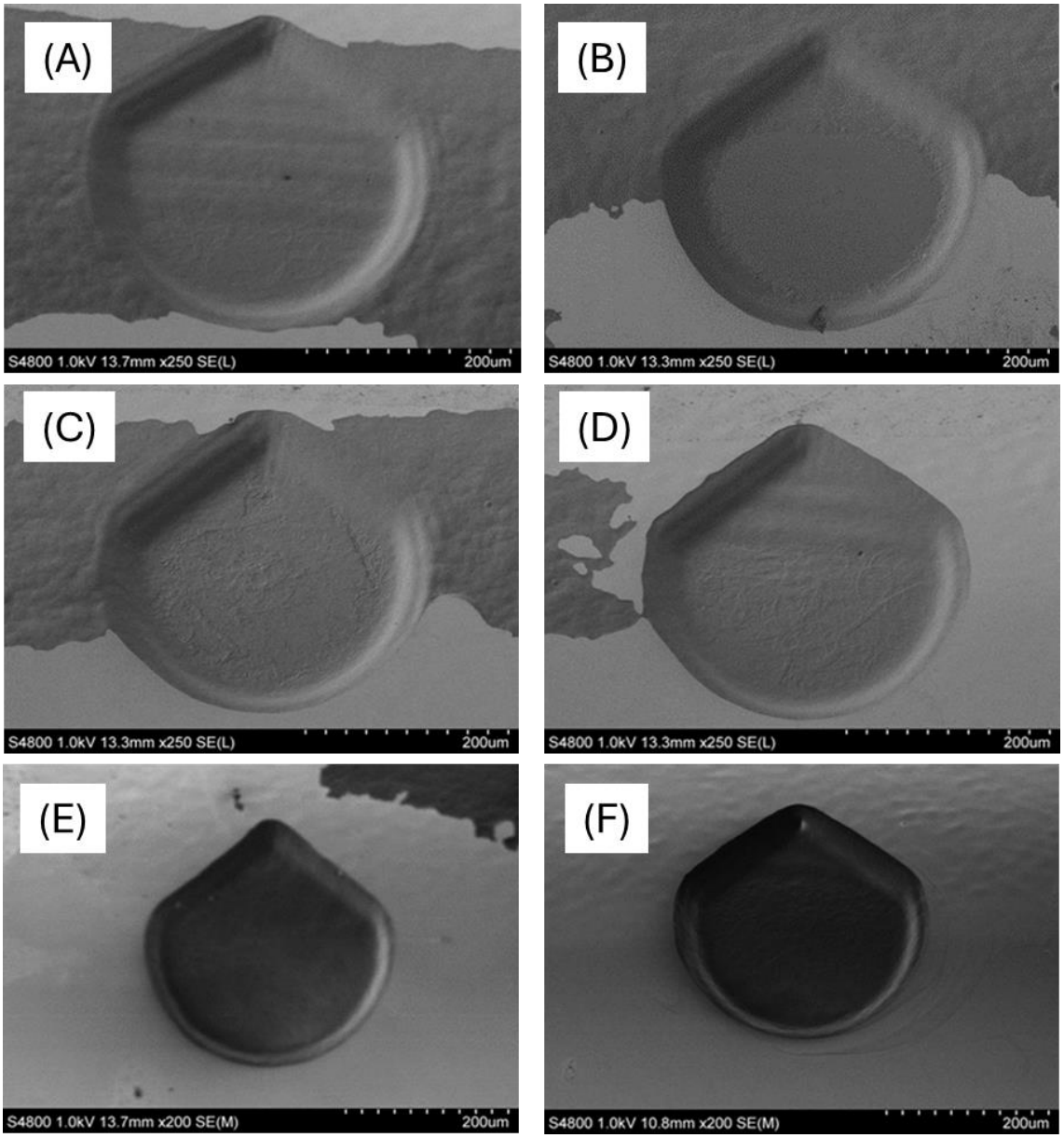

Figure 12.21 Exposure dose optimisation of the 8-scan spray coater photolithography: (A) 500 mJ/cm^2 Exposure Dose; (B) 1000 mJ/cm^2 Exposure Dose; (C) 2000 mJ/cm^2 Exposure Dose; (D) 2500 mJ/cm^2 Exposure Dose; (E) 3000 mJ/cm^2 Exposure Dose; (F) 3500 mJ/cm^2 Exposure Dose

Post exposure, the samples were developed in diluted AZ400K for 10 min and imaged using SEM to determine the optimal exposure dosage. The SEM images show exposure dose below 3600 mJ/cm^2 showed a slow reduction in the residue on the bevel surface exposing the shaft pattern from the resist coating (Figure 12.21). At an exposure dose of 3600 mJ/cm^2 there was no significant residue along the bevel surface and therefore this exposure dose was selected as the optimal value.

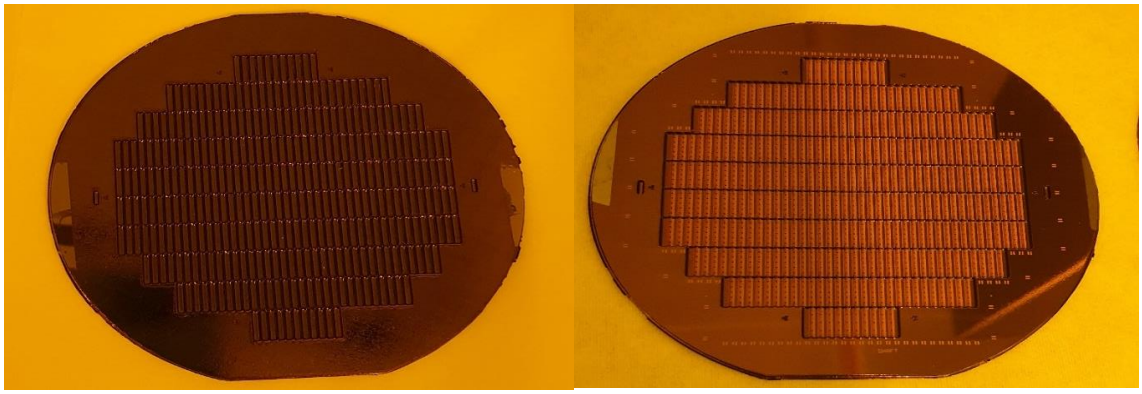

Figure 12.22 Images of a 4-inch silicon wafer post shaft photolithography

Table 12.6 Optimised shaft photolithography recipe for 8 scans.

	Recipe
Wafer Cleaning Parameters	Sonicate for 10 min in Acetone Sonicate for 5 min in IPA Air dry with nitrogen gas Bake for 10 min at 150 °C
AZ4999 Spray Coater Parameters	Pump flow: 2.5 mL/min Chuck Temperature: 70 °C Nitrogen Flow: 1.3 bar Sled Speed: 120 mm/s Pitch: 4 Nozzle Height: 20 mm
Soft Bake	Bake for 1.5 min at 100 °C
Rehydration Time	1 hour
Mask Aligner UV Exposure Parameters	Expose at a dosage of 3600 mJ/cm^2
AZ400K Development Time	10 minute development

12.10 Shaft Etching Optimisation

The initial etch process (Recipe R07) showed a few challenges that have to be overcome to produce the 700 µm silicon MNs as defined in subchapter 12.8. A major issue found was the wall produced between the individual columns (Figure 12.23). Having a wall between the individual MNs could cause an implication in penetration due to either the height reduction caused by the wall or the wall leading to a suction effect rather than breaking through the SC. For a 650 µm MN etch, the height of the wall was approximately 282 µm, which implied that 56.6% of the MNA is able to be penetrated into the skin. A reduction in height could lead to complications in delivery of drugs due to the region, in

which the MNs are positioned. The wall between the MNs can also penetration to be compromised.

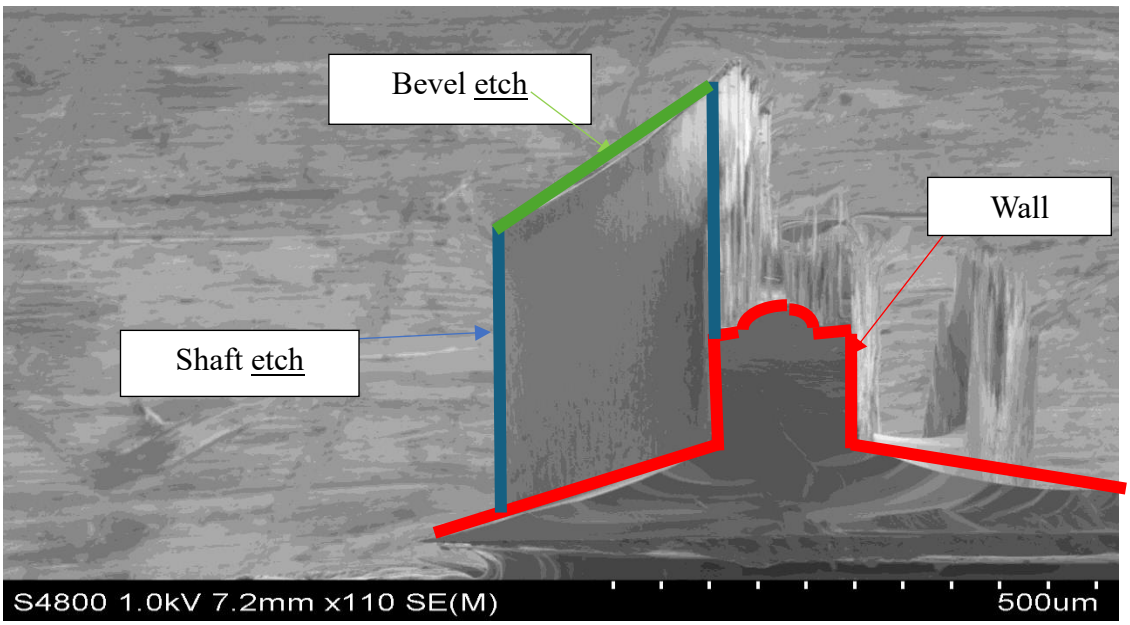

Figure 12.23 SEM image of the wall produced post shaft etch.

Secondly, the thickness of the resist of 20 µm was not substantial enough to act as a protective layer during the etch process and therefore le to roughness towards the tip of the MN (Figure 12.24). Therefore, an increase in the number of scans and hence the thickness of resist is required to overcome this issue.

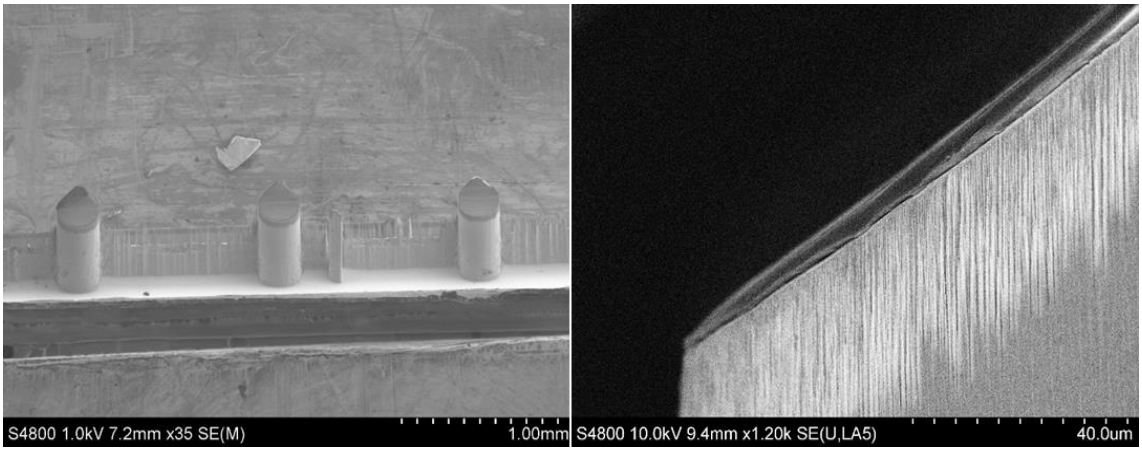

Figure 12.24 SEM Image of the roughness towards the tip of the MN due to the removal of the protective photoresist coating

To produce the shaft, a DRIE etch process is used to etch the regions of silicon that are not protected by the photoresist. The initial etch process was optimised earlier and the parameters of this are shown in Table 12.7.

Table 12.7 Initial etch recipe (Recipe R07) inputted into the DSi-V to achieve a DRIE etch of the regions not protected by the photoresist.

		1	2	3	4	5
Step Name		Strike	Descum	Dep	E1	E2
Process Time	s	2.0	225.0	1.0	1.5	4.0 2.8
Process Pressure	mTorr	40.0 ±0 %	20.0 ±50 %	40.0 ±50 %	20.0 ±50%	20.0 20.0 ±50%
APC Mode		Automatic	Automatic	Automatic	Automatic	Automatic
Source 1 Power	W	2000 ±0 %	2500 50 %	2500 ±50 %	2500 ±50 %	2700 2700 ±50 %
Source MU tune capacitor		4	4	4	4	4
Source MU load capacitor		1	1	1	1	1
Source 1 RF Control Mode		Load	Load	Load	Load	Load
Platen Frequency		High Frequency	High Frequency	High Frequency	High Frequency	High Frequency
Platen HF Power	W	0.0 ±0 %	80.0 ±50 %	0.0 ±0 %	112.0 ±50%	36.0 36.0 ±50%
Plater HF Capacity Adjust		Preset	Automatic	Automatic	Automatic	Automatic
Platen HF Tune Capacitor	%	70.0 ±5%				
Platen HF Load Capacitor	%	80.0 ±5%				

Platen HF Padding Capacitor		1	4	4	4	4
Platen HF Control Mode		Load	Load	Load	Load	Load
Platen HF Modulation Enabled		Enable	Enable	Enable	Enable	Enable
Platen HF Modulation Frequency	Hz	150	150	150	150	150
Platen HF Modulation Duty Cycle	%	10	10	10	10	10
Helium Pressure	Torr	10.0 ±10 %	10.0 ±10 %	10.0 ±10 %	10.0 ±10%	10.0 10.0 ±10%
Helium Flow Warning Level	sccm	5.0	5.0	5.0	5.0	5.0
Helium Flow Fault Level	sccm	8.0	8.0	8.0	8.0	8.0
Coil Current	A	0.0 ±0%	10.0 ±40 %	10.0 ±40 %	10.0 ±40 %	10.0 ±40 %
Loop destination		0	0	0	0	3
Number of loops		0	0	0	0	750
Loop Variation Parameter		0.0	0.0	0.0	0.0	1.0
ESC Voltage	V	5000 ±10%	5000 ±10%	5000 ±10%	5000 ±10%	5000 ±10%
Gas Line Config		Flow	Flow	Flow	Flow	Flow

P1 Nitrogen	sccm	0.0	±0%	0.0	±5%	0.0	±0%	0.0	±5%	0.0	0.0 ±5%
P2 Oxygen	sccm	0.0	±0%	300.0	±20%	0.0	±0%	0.0	±5%	0.0	0.0 ±5%
P3 CF4	sccm	0.0	±0%	0.0	±5%	0.0	±0%	0.0	±5%	0.0	0.0 ±5%
P4 Argon	sccm	400.0	±0%	0.0	±5%	0.0	±0%	0.0	±5%	0.0	0.0 ±5%
P5 SF6	sccm	1.0	±0%	1.0	±0%	1.0	±0%	320.0	±20%	315.0	315.0 ±20%
P6 C4F8	sccm	270.0	±0%	1.0	±0%	360.0	±20%	1.0	±0%	1.0	1.0 ±0%

12.11 Photoresist Etching Optimisation

Transferring the shaft patterning of the new spray coater resist introduced new challenges to create the final MNA. From Figure 12.25, it can be seen that after the shaft etch process, the surface showed roughness towards the tip. The roughness indicates that the resist had begun to fail to protect the silicon during the etch process. Therefore, the thickness of the resist for the shaft needed to be increased and entails further optimisation.

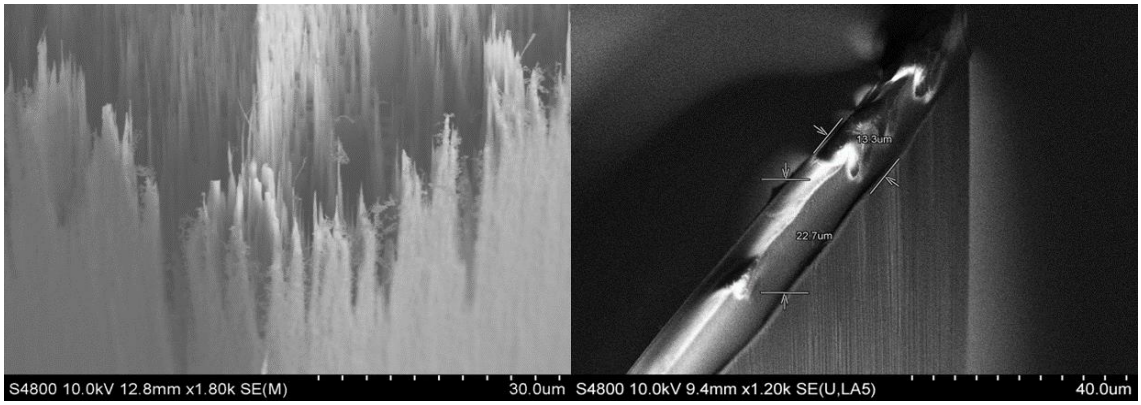

Figure 12.25 SEM image of the roughness at the tip of the MN due to the removal of the photoresist coating during the shaft etch process.

To overcome this, the number of scans in the spray coater recipe is increased. Increasing the number of scans leads to a thicker resist coating on the wafer surface. Increasing the resist thickness led to further challenges:

- Development time was not substantial.
- Exposure dose was not high enough.
- Resist over the maximum thickness range led to a lack of adhesion.

The number of scans were increased from 8 to 12 scans, to produce a thickness of 30 µm (Figure 12.26).

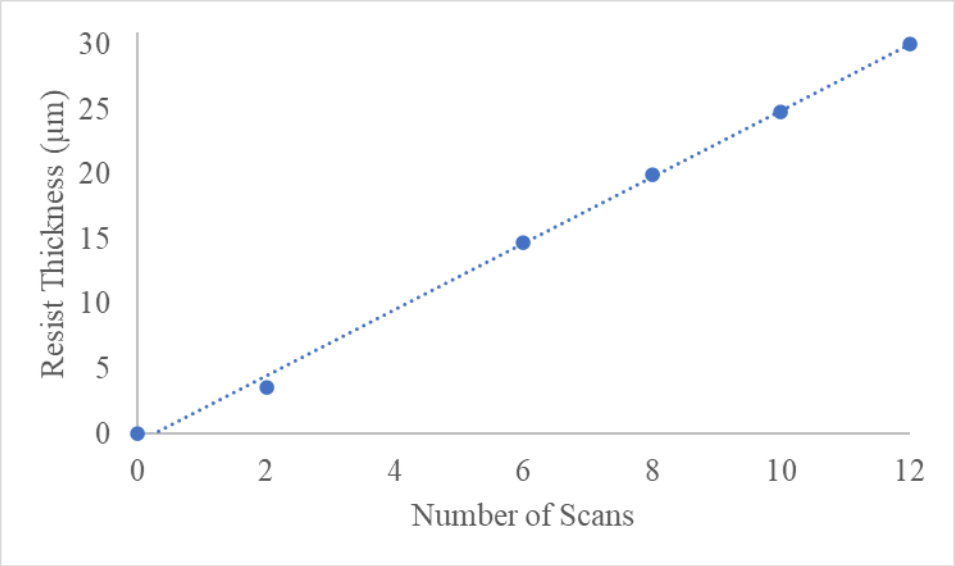

Figure 12.26 Graphical representation of the relationship between resist thickness and the number of scans

Therefore, the exposure dose and development time were required to be adjusted according to the resist thickness. Once again, the development time is initially determined using a whole wafer spray coated with a 12-scan recipe and due to the increased thickness, the rehydration of the wafer is increased to 2 h. To determine the development time, the dose exposure from the mask aligner remained the same from the 8-scan resist recipe. The wafer is then diced into samples to develop over a period of 2 - 10 min with 2 min intervals.

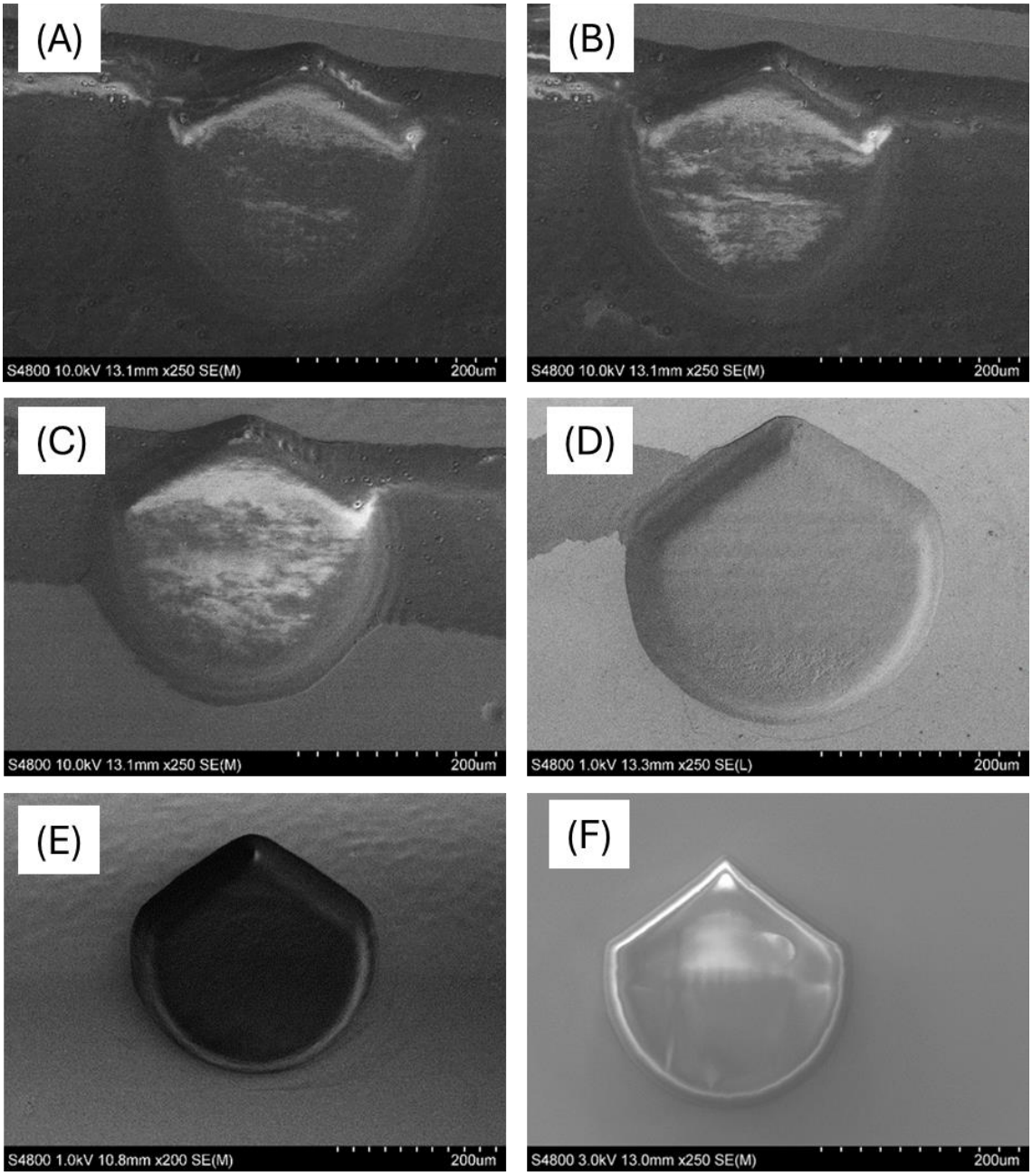

Figure 12.27 Optimisation of the development time for 10 scans of the spray coater: (A) 2 minutes development; (B) 4 minutes development; (C) 6 minutes development; (D) 8 minutes development; (E) 10 minutes development; (F) 12 minutes development

As the development time had been determined, the exposure dose is ranged from 2250 to 3800 mJ/cm^2 to ensure that the curing provides the solubility to the developer and therefore removes the residue surrounding the shaft mask. Exposure dosages lower than 2800 mJ/cm^2 showed residue surrounding the shaft mask. Above 2800 mJ/cm^2, the shaft mask showed overexposure and therefore features on the wafer were narrower and an

inexact transfer of the mask. Hence, the dose exposure used was 2800 mJ/cm^2 for a resist thickness of 30 µm.

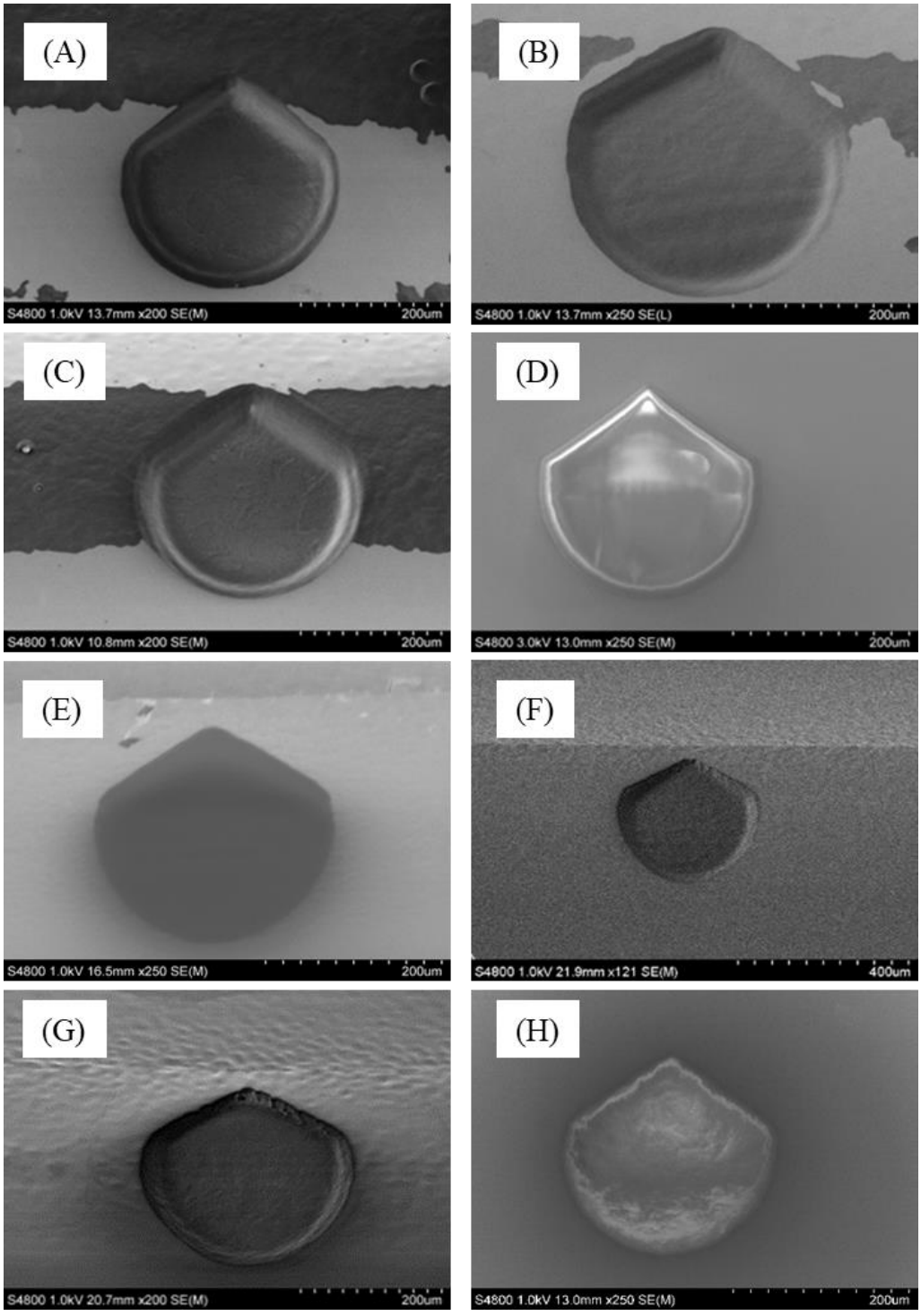

Figure 12.28 Optimisation of the exposure dose for 10 scans of the spray coater: (A) 2250 mJ/cm2 Exposure Dose; (B) 2500 mJ/cm2 Exposure Dose; (C) 2750 mJ/cm2 Exposure Dose; (D) 3000 mJ/cm2 Exposure Dose; (E) 3200 mJ/cm2 Exposure Dose; (F) 3400 mJ/cm2 Exposure Dose; (G) 3600 mJ/cm2 Exposure Dose; (H) 3800 mJ/cm2 Exposure Dose

Although 12 scans provided a thicker resist coating of 30 µm, it was still inadequate to protect the top of the shaft and consequently led to roughness once again. As there was an increase in the resist coating, the protective barrier from the resist remained on the surface for longer before begun failing further along the etch process (Figure 12.29).

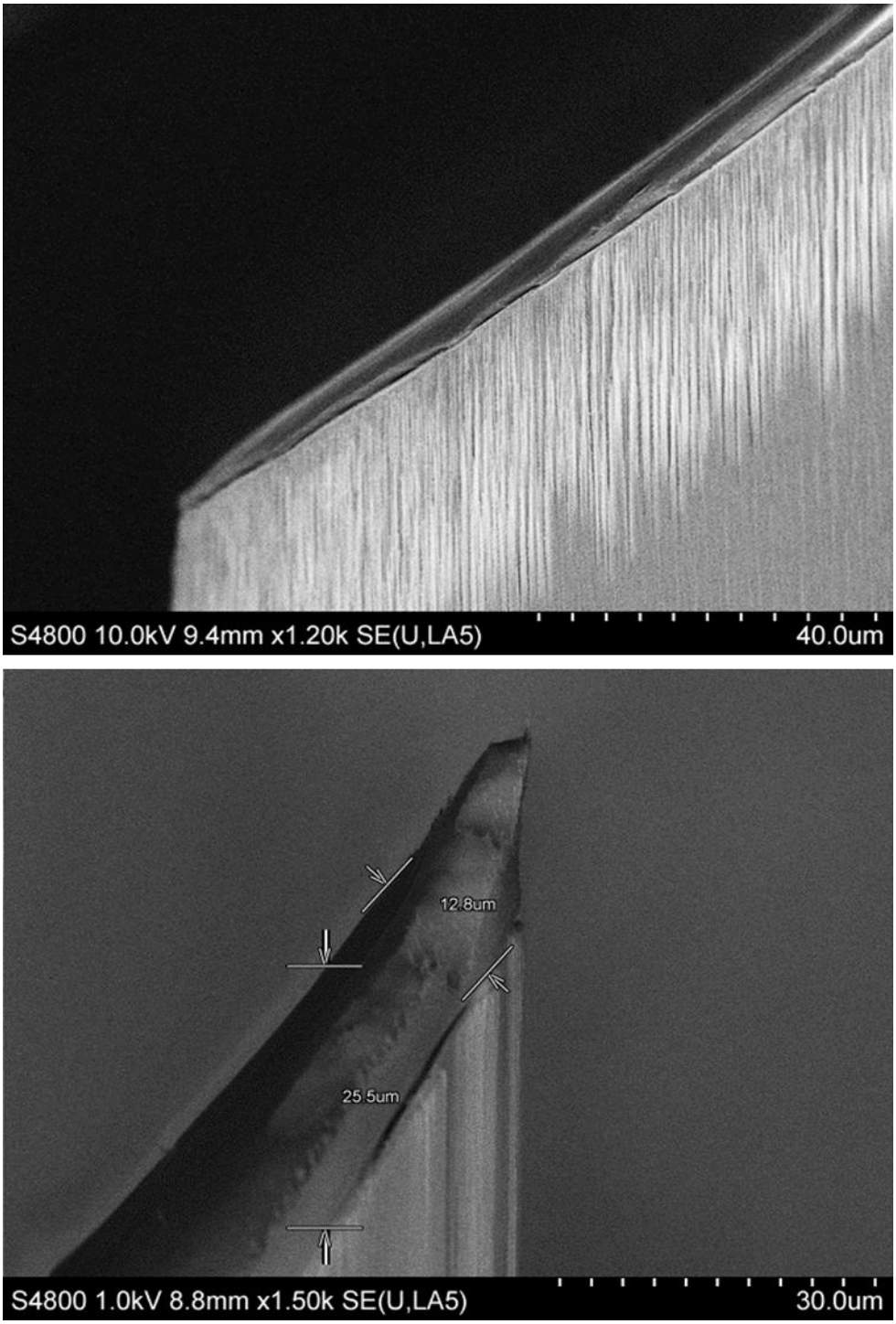

Figure 12.29 SEM Images showing the roughness of the MN tip post shaft.

As a result, the patterning of the shaft needed to be thicker than 30 µm but this is already higher than the 25 µm resist thickness specified for effective coating and adhesion. Due to the inadequacy of resist thickness, further development was needed to protect the wafer throughout the shaft etch, which would not include increasing the number of scans.

Table 12.8 Optimised shaft photolithography for a 12-scan spray coater.

	Recipe
Wafer Cleaning Parameters	Sonicate for 10 min in Acetone Sonicate for 5 min in IPA Air dry with nitrogen gas Bake for 10 min at 150 °C
AZ4999 Spray Coater Parameters	Pump flow: 2.5 mL/min Chuck Temperature: 70 °C Nitrogen Flow: 1.3 bar Sled Speed: 120 mm/s Pitch: 4 Nozzle Height: 20 mm
Soft Bake	Bake for 2 min at 100 °C
Rehydration Time	1.5 h
Mask Aligner UV Exposure Parameters	Expose at a dosage of 3000 mJ/cm^2
AZ400K Development Time	10-min development

12.12 Isotropic Etching Optimisation

This sub-chapter focuses on the silicon residue known as a “wall” present between each MN in the MNA (Figure 12.30). The wall is a consequence on incomplete etching of the bevel during the final shaft etch.

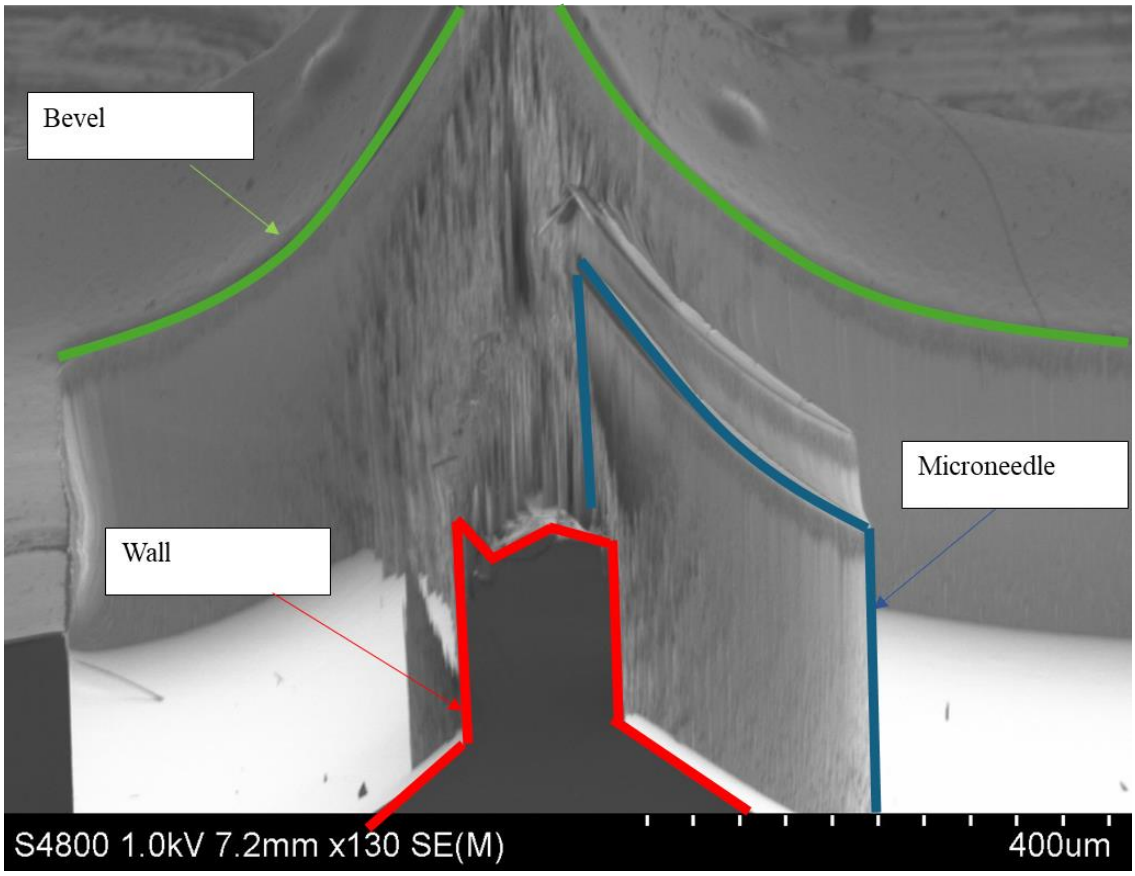

Figure 12.30 SEM Image showing the wall between the MN post shaft etch

As the bevel is used to create a sharp MN bevel the angle of 89° is almost vertical. The shaft etch is a directional etch to produce vertical straight walls, the gasses cannot come into contact with the vertical area, preventing it from being etch away.

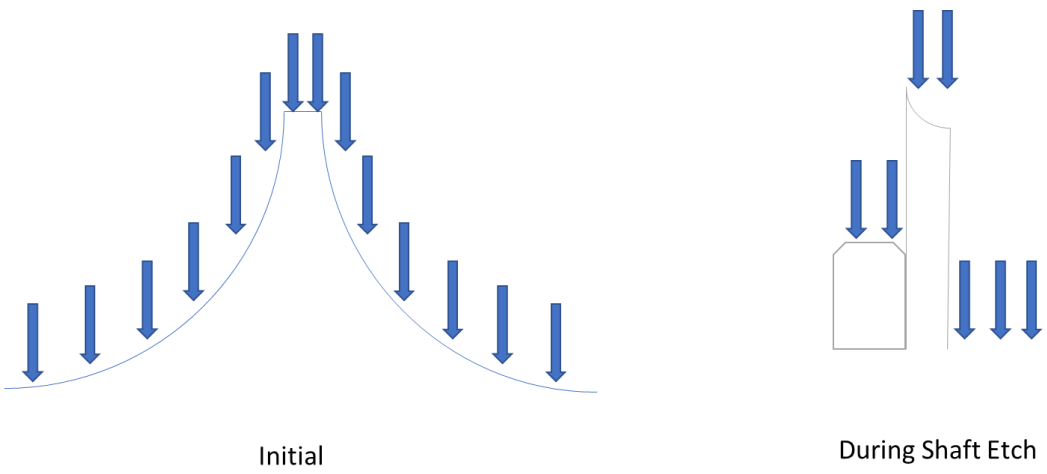

Figure 12.31 Schematic representation of an isotropic etch profile.

The recipe (Recipe R08) used for the shaft etch is seen in Table 12.12 where the successive E2 process steps were changed from 4.0 s and 2.8 s to 6.0 s and 4.0 s. The increase in the etch process led to an increase in the etch rate. Although this led to the removal of the wall, tapering towards the base of the MN were visible (Figure 12.33). Tapering means that the MNs become weak at the base and can break during penetration for both solid and hollow MNs. For the hollow MNs, as there would be a reduction in the silicon surrounding the bore, when fluid is pushed through the array at high pressure the base could fail during injection (Figure 12.32).

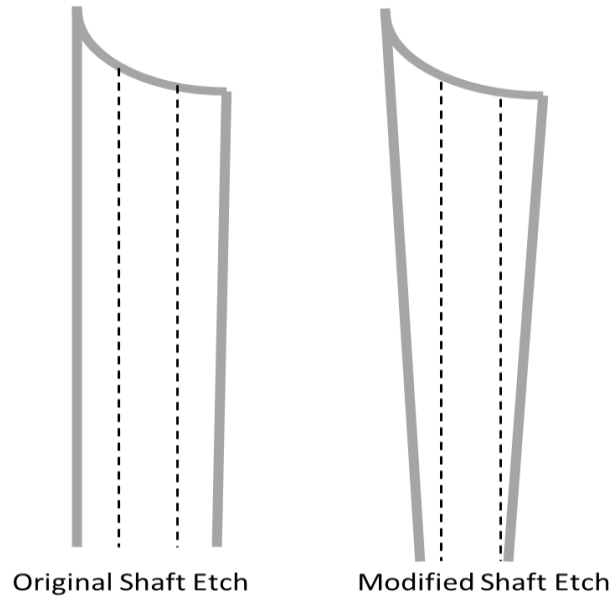

Figure 12.32 Schematic diagram showing the difference between the original shaft etch recipe and the modified etch recipe and the tapering towards the base of the MN.

Therefore, although the wall was removed during the etch process, the tapering will affect the penetration capability of the MN and would not be viable for drug delivery and diagnostic applications.

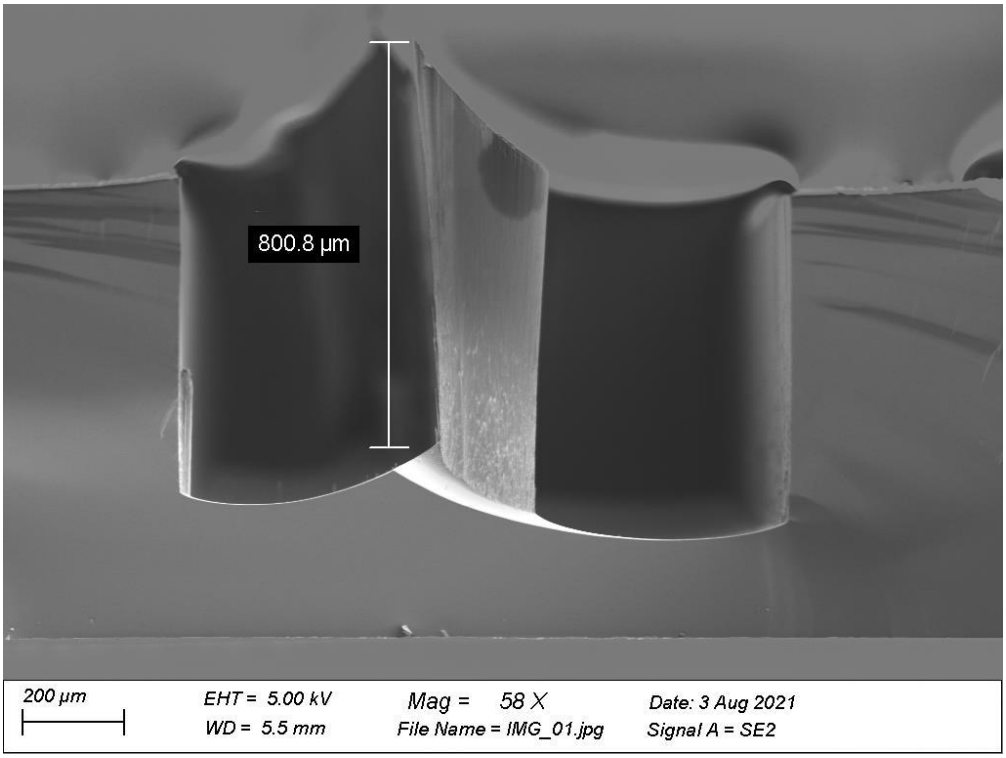

Figure 12.33 SEM image of the modified shaft etch process.

Table 12.9 Modified etch recipe (Recipe R08) to remove the wall between the MNAs.

		1	2	3	4	5
Step Name		Strike	Descum	Dep	E1	E2
Process Time	s	2.0	225.0	1.0	1.5	6.0 4.0
Process Pressure	mTorr	40 ±0 %	20 ±50 %	40 ±50 %	20.0 ±50 %	20.0 20.0 ±50%
APC Mode		Automatic	Automatic	Automatic	Automatic	Automatic
Source 1 Power	W	2000 ±0 %	2500 ±50 %	2500 ±50 %	2500 ±50 %	2700 2700 ±50%
Source MU tune capacitor		4	4	4	4	4
Source MU load capacitor		1	1	1	1	1
Source 1 RF Control Mode		Load	Load	Load	Load	Load
Platen Frequency		High Frequency	High Frequency	High Frequency	High Frequency	High Frequency
Platen HF Power	W	0.0 ±0 %	80.0 ±50 %	0.0 ±50 %	112.0 ±50 %	36.0 36.0 ±50%
Plater HF Capacity Adjust		Preset	Automatic	Automatic	Automatic	Automatic
Platen HF Tune Capacitor	%	70.0 ±5%				

Platen HF Load Capacitor	%	80.0 ±5%				
Platen HF Padding Capacitor		1	4	4	4	4
Platen HF Control Mode		Load	Load	Load	Load	Load
Platen HF Modulation Enabled		Enable	Enable	Enable	Enable	Enable
Platen HF Modulation Frequency	Hz	150	150	150	150	150
Platen HF Modulation Duty Cycle	%	10	10	10	10	10
Helium Pressure	Torr	10.0 ±10 %	10.0 ±10 %	10.0 ±10 %	10.0 ±10 %	10.0 10.0 ±10%
Helium Flow Warning Level	sccm	5.0	5.0	5.0	5.0	5.0
Helium Flow Fault Level	sccm	8.0	8.0	8.0	8.0	8.0
Coil Current	A	0.0 ±0%	10.0 ±40 %	10.0 ±40 %	10.0 ±40 %	10.0 ±40%
Loop destination		0	0	0	0	3

Number of loops		0	0	0	0	750
Loop Variation Parameter		0.0	0.0	0.0	0.0	1.0
ESC Voltage	V	5000 ±10%	5000 ±10%	5000 ±10%	5000 ±10%	5000 ±10%
Gas Line Config		Flow	Flow	Flow	Flow	Flow
P1 Nitrogen	sccm	0.0 ±0%	0.0 ±5%	0.0 ±0%	0.0 ±5%	0.0 0.0 ±5%
P2 Oxygen	sccm	0.0 ±0%	300.0 ±20%	0.0 ±0%	0.0 ±5%	0.0 0.0 ±5%
P3 CF4	sccm	0.0 ±0%	0.0 ±5%	0.0 ±0%	0.0 ±5%	0.0 0.0 ±5%
P4 Argon	sccm	400.0 ±0%	0.0 ±5%	0.0 ±0%	0.0 ±5%	0.0 0.0 ±5%
P5 SF6	sccm	1.0 ±0%	1.0 ±0%	1.0 ±0%	320.0 20%	315.0 315.0 ±20%
P6 C4F8	sccm	270.0 ±0%	1.0 ±0%	360.0 ±20%	1.0 ±0%	1.0 1.0 ±0%

An alternative method to remove the ‘wall’ between the MNs is to carry out an isotropic etch prior to the shaft patterning. Carrying out the isotropic etch would lead to the removal of the vertical region between each bevel (Figure 12.34). By carrying out the initial isotropic etch prior to patterning implied that in the DSi-V for the shaft DRIE etch, the etchant gasses have a wider area of shallower regions to be accelerated towards. Prior to carrying out a full process run; optimisation was essential to determine the etch rate as well as the capability for the isotropic etch at the steepest region.

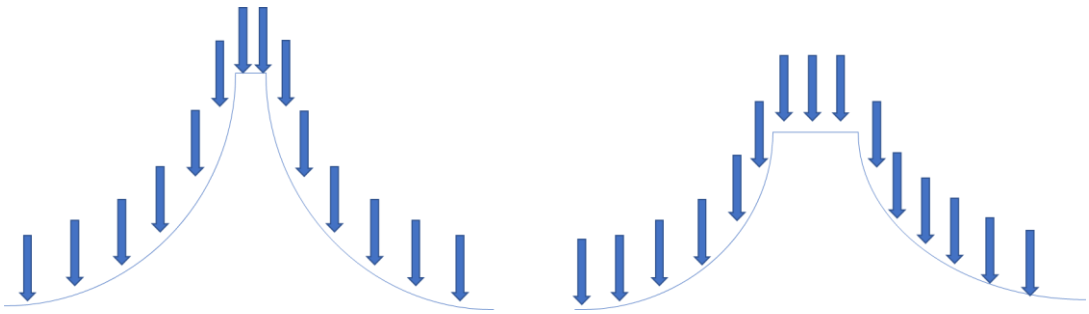

Figure 12.34 Schematic diagram representing the use of an initial isotropic etch prior to the shaft patterning to increase the area for isotropic etch.

To determine the etch rate for the isotropic recipe, a 365 nm wafer is placed in the DSi-V for a 5-minute process. Post etch, the etched region is masked with masking tape and the wafer is once again etched for a further 5 min. The 5-min etch process is repeated and each are masked for a further four times before being placed in a profilometer to measure the step height.

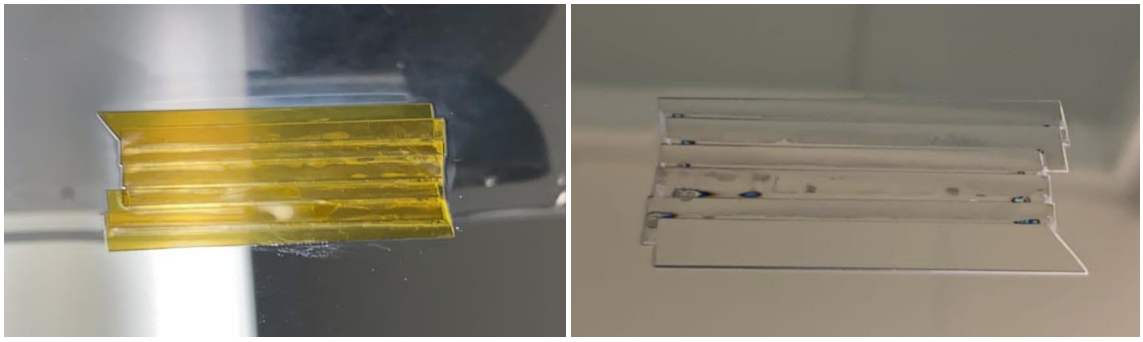

Figure 12.35 Image of the isotropic etch optimisation on a blank silicon wafer.

Step heights were plotted against time to determine the etch rate by fitting a line of best fit (Figure 12.36).

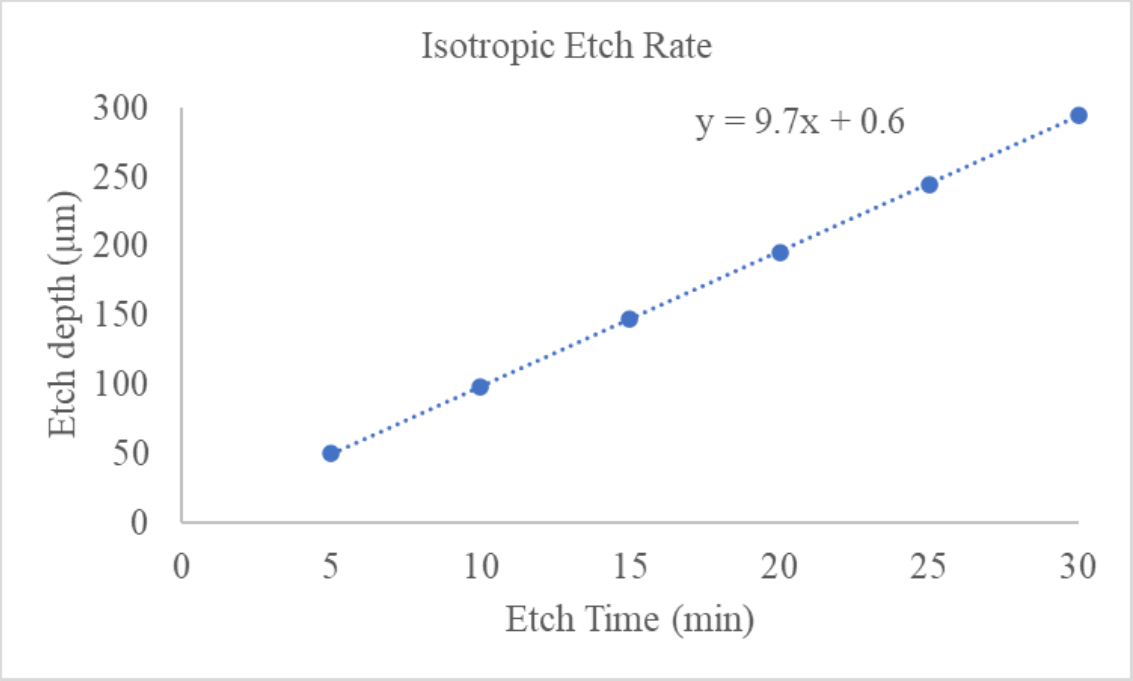

Figure 12.36 Graphical representation to determine the isotropic etch rate.

The etch rate was determined as 9.7 µm/min and further work may be carried out to conclude whether carrying out an isotropic etch prior to shaft etch will overcome the challenges of the wall.

12.13 Marker Photolithography Optimisation

It was observed after initial fabrication that there were issues with over-etching of the alignment marks post DSi-V etch of the bevel as described in subsection 12.8. Alignment marks ensures that the X, Y, and Z direction of the silicon wafer to the photomask is not distorted and therefore is not detrimental to further fabrication processing.

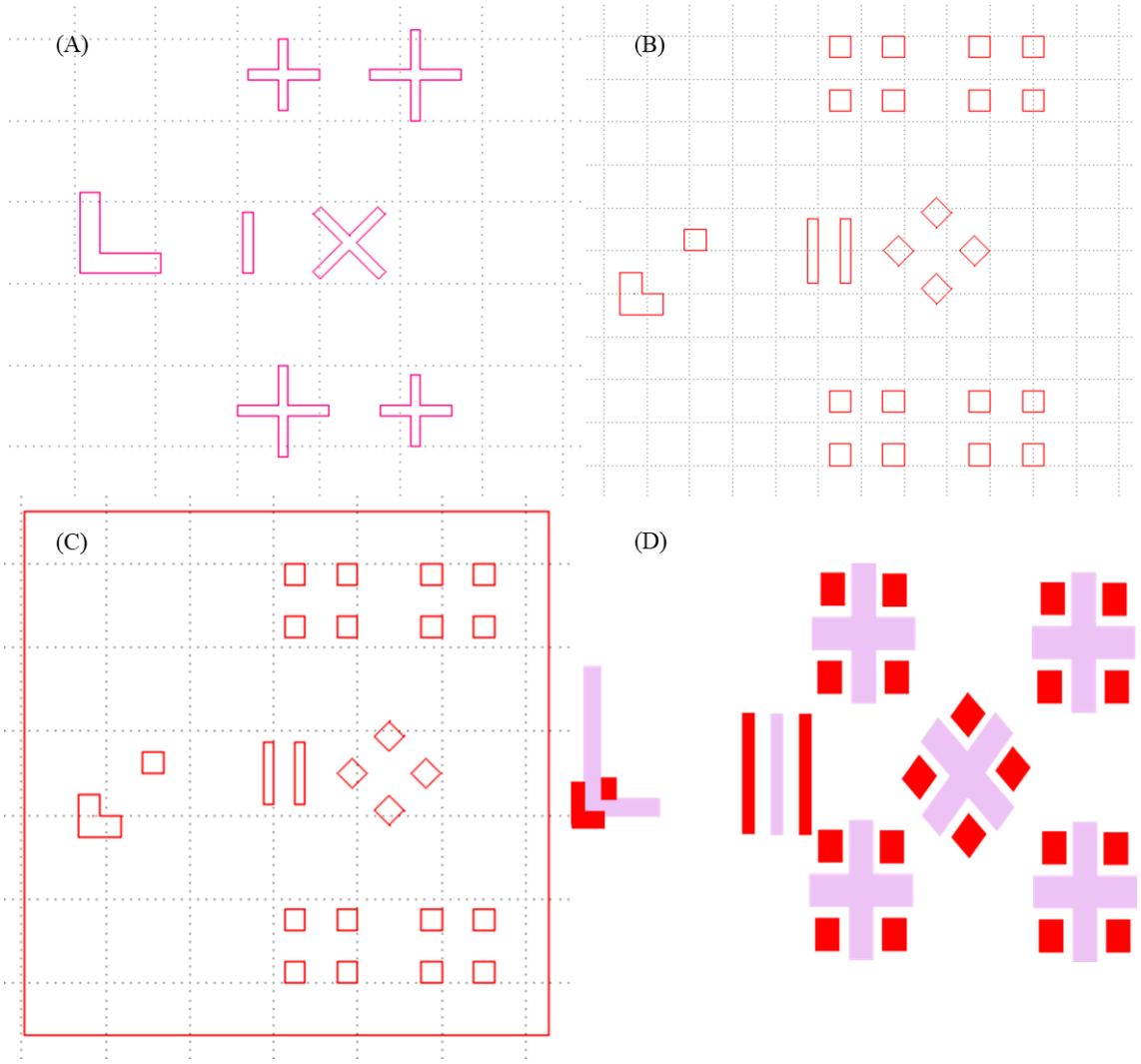

Figure 12.37 AutoCAD drawings of the alignment markers for each MN step: (A) Alignment marks for bevel; (B) Alignment marks for bore; (C) Alignment marks for shaft; (D) Overall alignment marks.

In the original process both sets of alignment marks were found to over etch during the initial isotropic etch for the bevel. For the right bevel structure to be produced an etch time of 30 min is needed and this meant the intricate alignment markers would begin to deform into undefined regions. As there is a significant size difference between the bevel and the alignment marks, it would imply that the bevel is able to withstand the etch and hold the shape compared to the smaller alignment marks. If the etch time was reduced, the markers would remain intact, but the bevel structure would not have reached the depth required for the desired MN structure. The over etching of the alignment marks leads to the inability for them to be used to line up with the further stages (Figure 12.38).

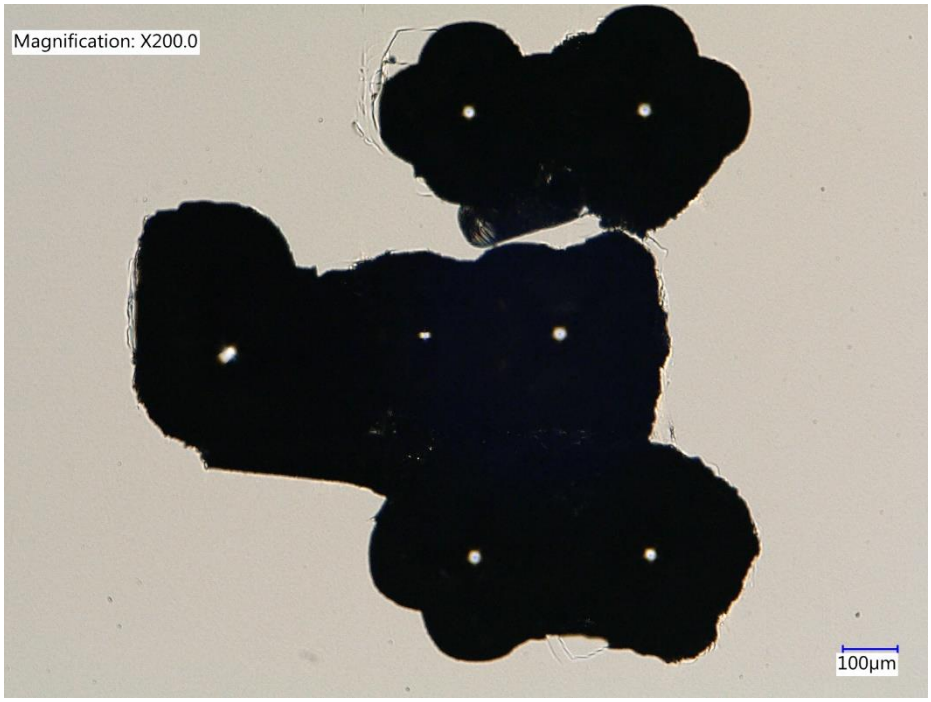

Figure 12.38 Microscope image of the over etching of the alignment marks post bevel etch

As alignment markers are a fundamental step to ensuring each mask of the MN patterning process is correctly overlayed, this was key component in need of optimisation. If misaligned it can lead to the MN structure differing in height and the bore placement being off centre (Figure 12.39). These changes can affect both penetration and injectability of solution from the MNAs.

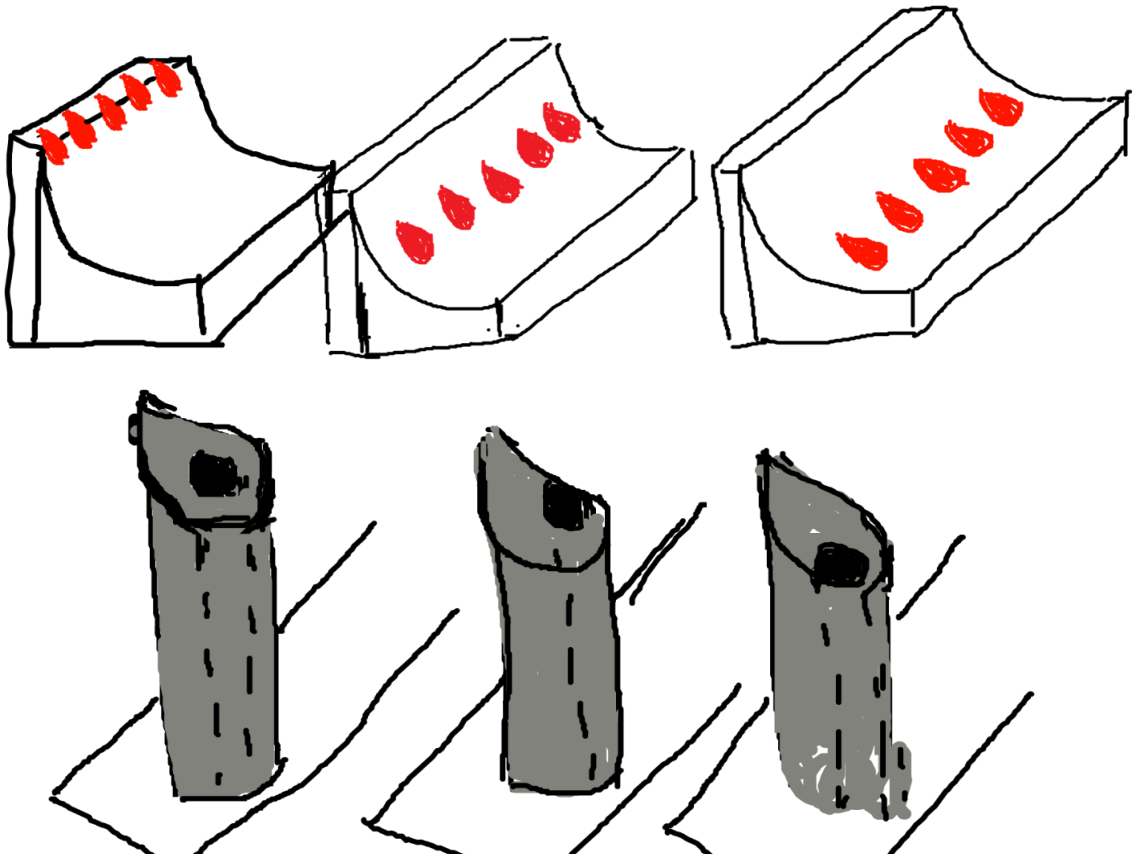

Figure 12.39 Schematic diagram showing how alignment marks are important for the bore and shaft to produce the optimal silicon MN shape.

As alignment markers are a fundamental step to ensuring each mask of the MN patterning process is correctly overlayed, this was key component in need of optimisation. To improve this, incorporation of reproducible Critical dimension (CD) checks would aid in comprehensive mask patterning if the alignment markers failed. The CD checks were drawn in 6 regions around the circumference of the wafer (Figure 12.40). This ensures that each wafer being manufactured has the specified tolerances for the exposure and processing of the stages of photolithography for each region of the wafer.

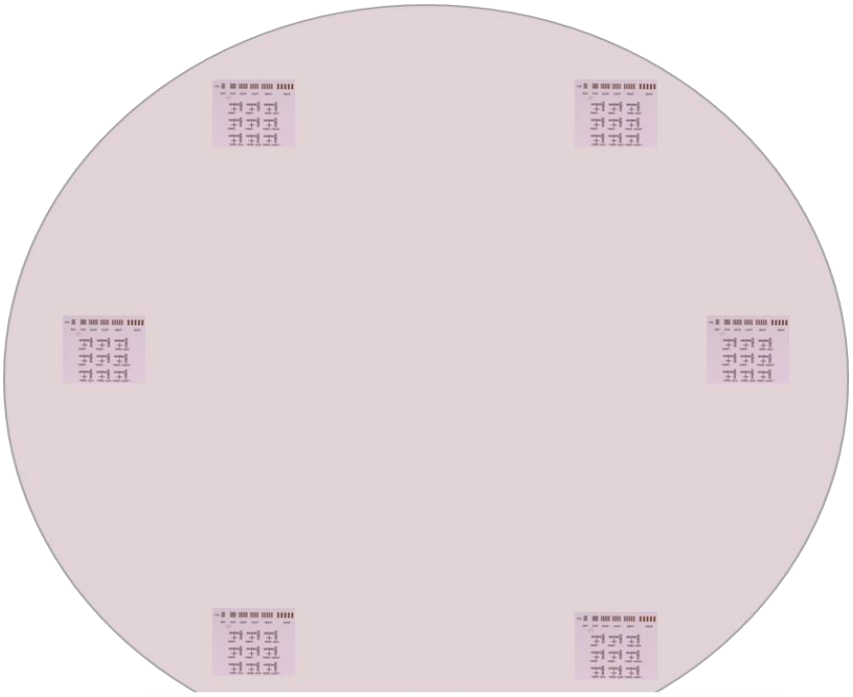

Figure 12.40 Image of the 6 critical dimension marks around the wafer to ensure reproducibility during the photolithography process.

To visualise how the CD check markers react after each stage of photolithography development. (bevel, bore, and shaft), the 6 regions were observed under the microscope to ensure that each CD mark was uniformly developed across the wafer. If development had occurred satisfactorily, it would mean that the resist up to 3 µm would have been removed ensuring features of these dimensions will be precisely developed (Figure 12.41). If the resists had been removed, the rectangles would change in color from black (resist) to white (silicon). This guaranteed that the end photolithography of each stage would be fully cleared of any residual resist through patterning. If residue is present in regions that should be clear, this could therefore impact the following etch step and consequently the functionality and design of the MNA are compromised.

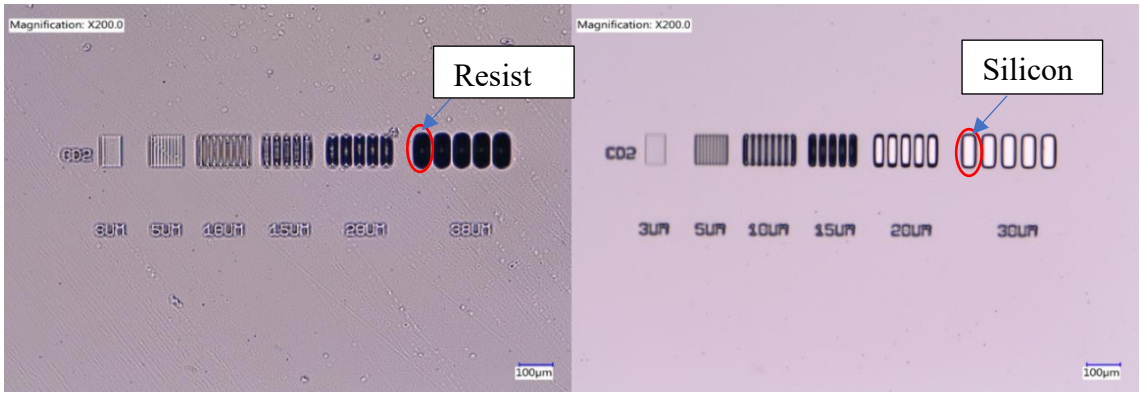

Figure 12.41 Microscope image showing before and after development of the CD checks to determine how long the wafer is required to be in the developer.

The design of the alignment markers was individually produced so that upon mask alignment of the wafers at each stage could be interpreted easily without confusing the markers of another stage. This is useful in the MN fabrication process as it means that if post etching of the first alignment mark fails from either not completely etching there are further 2 that can be used to align against. Further to adding extra alignment marks for each stage, X and Y alignment marks were also added. This set of alignment is useful in making sure that the more intricate patterning steps of the MN process are exactly in line with one another. When in line with one another, this would mean that the bore would be centralised to the shaft. If misalignment occurs whether it be in the X or Y direction, the silicon surrounding the bore would increase in fragility. The increase in brittleness could result in the MNs breaking when inserted into skin or upon injection forces through the bore.

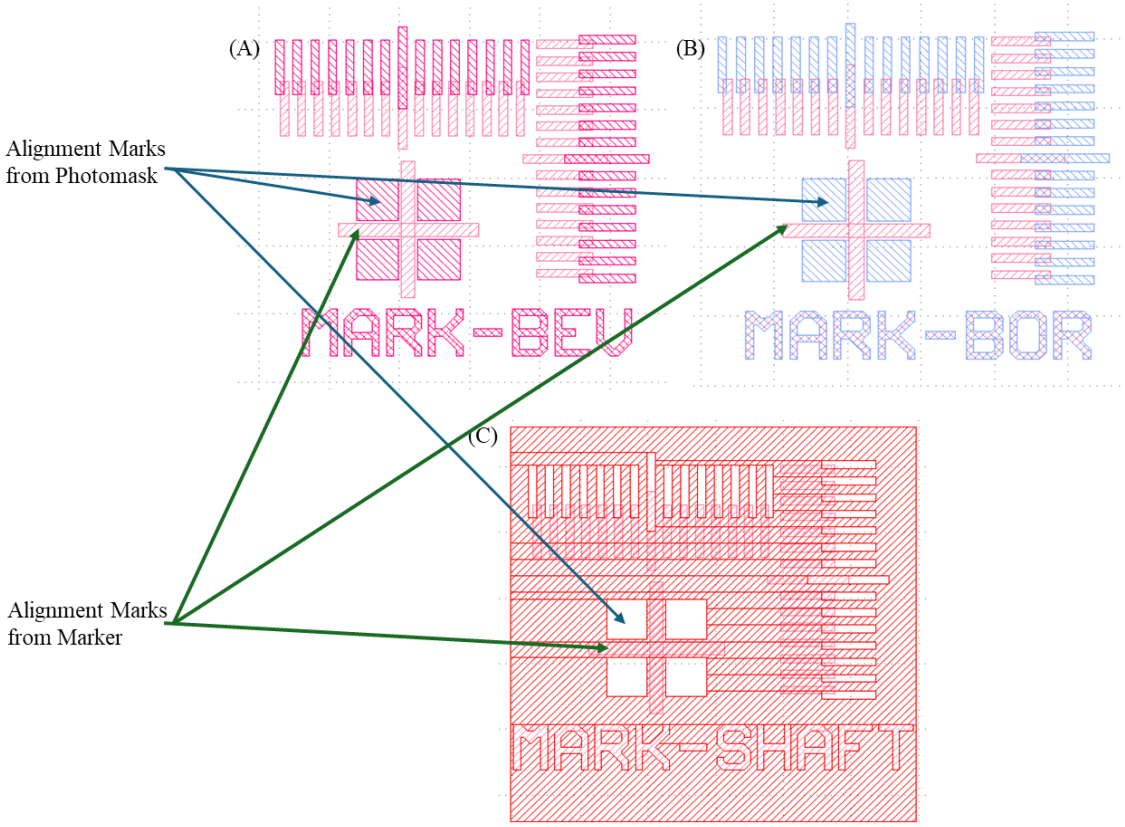

Figure 12.42 AutoCAD design showing how each alignment mark lines up with the markers present on the silicon wafer: (A) Alignment marks for bevel; (B) Alignment marks for bore; (C) Alignment marks for shaft.

To create the alignment and CD markers onto the wafer, 50 nm of silicon nitride is deposited on the wafer using a PECVD. The thickness of nitride was used to create a uniform coating onto the surface of the wafer that will not be affected by further processing stages for the marker. Post deposition, the wafers are spin coated using an in house spin coater recipe for a reversal resist AZ 5214E at a speed of 3000 rpm, acceleration of 1000 for 45 s. As the nitride causes the surface to become hydrophobic, the hydrophilic resist would not be able to adhere to the surface, thus a Ti prime layer is used between these to act as an adhesion promotor prior to resist deposition. Ti prime is spun on the surface of the wafer.

After both resist layers have been coated, they were exposed to UV (50 mJ/cm^2) and then initially developed in AZ726 for 1 min. After 1 min, it was clear that the marker regions were visible but had not fully developed to reveal the nitride layer before. Therefore, the development time is increased to 3 min and this showed a greater improvement in the removal of resist in each of the marker points. Post exposure, the wafer was then developed in AZ726 for 3 min (Figure 12.43).

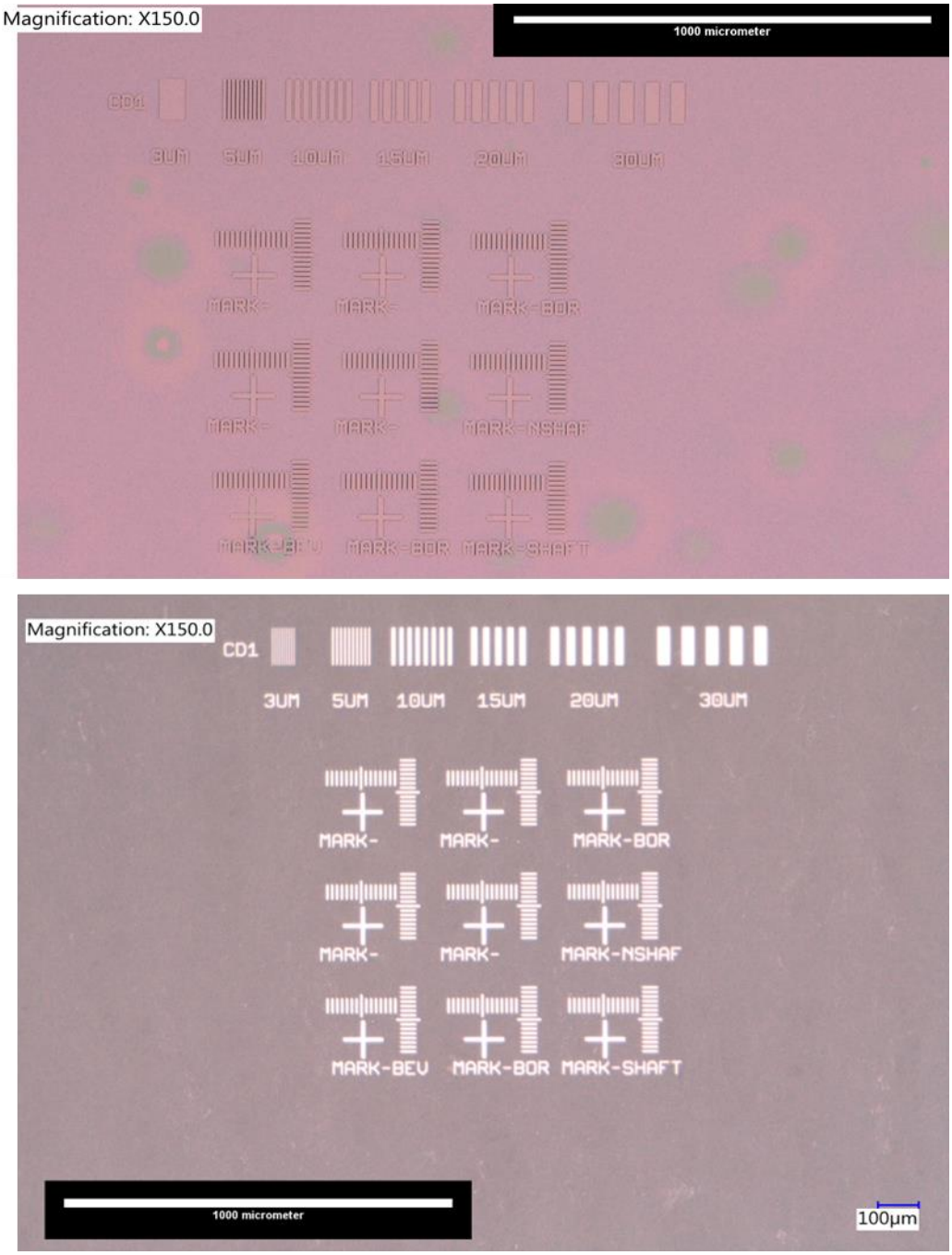

Figure 12.43 Microscope image showing the photolithographic development of the marker patterning.

12.14 Marker Etching

To remove the excess nitride surrounding the marker patterning, an ICP etching tool is utilised, which creates chemically reactive plasma under low pressure conditions leading to the material etching (see Chapter 8.3). An in-house recipe was utilised to etch away the 50 nm nitride (Table 12.10).

Table 12.10 Optimised ICP etching recipe.

	Input Values
C_4F_8	100 sccm
SF_6	575 sccm
O_2	80 sccm
Coil Power	2500 W
Platen Power	40 W
Pressure	70 mT
Temperature	0 °C
Helium Pressure	10 T

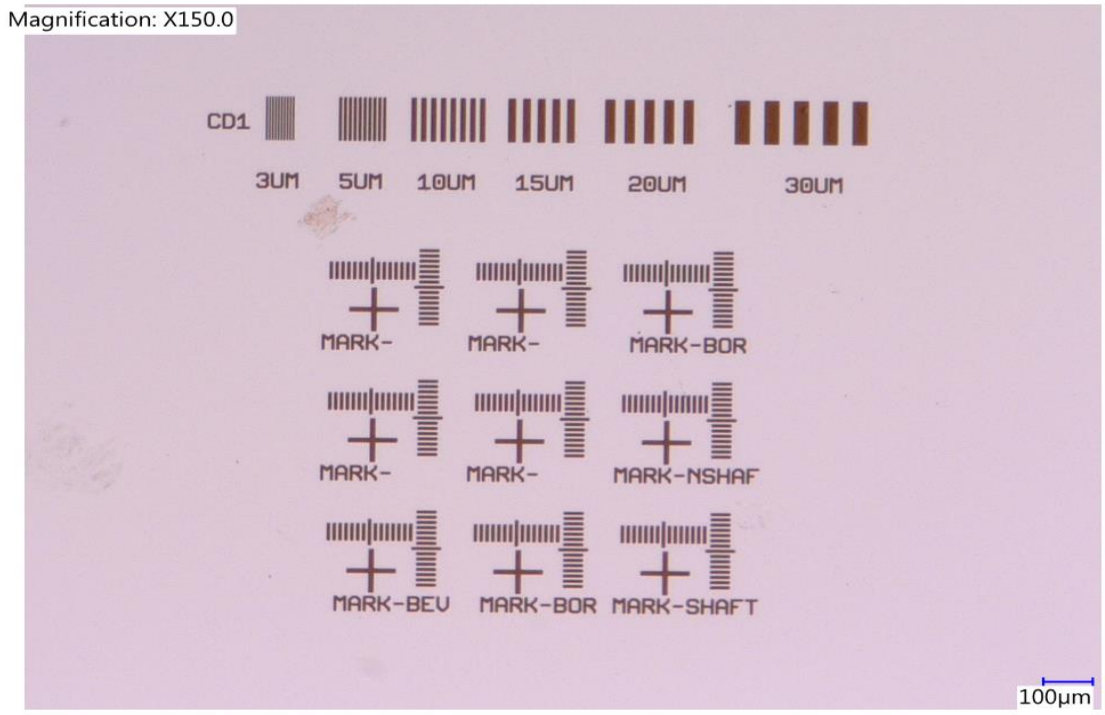

Figure 12.44 Optimised marker design and CD checks on the surface of the silicon wafer

Chapter 13

Silicon MN Characterisation

13.1 Introduction

The previous section describes the fabrication of solid and hollow MNs using photolithography and etch processes. As these silicon MNs were produced using different etching protocols, characterisation is required to determine whether the resulting MNs are suitable for drug delivery. As observed in Figure 12.23 the shaft of the MN fabricated using recipe 07 also creates a silicon wall between the MNs, which results in the overall height of the MNA to decrease from 700 µm to 500 µm. Thus, the MN penetration capabilities could be affected by the wall of silicon. The ideal penetration depth is 200 µm to 500 µm for cosmetic applications and a height greater than 600 µm for therapeutic drug delivery (62).Thus the wall between the MNs would be useful in cosmetic applications and therefore characterisation is required to determine whether the wall between the MNs may impact the penetration, also known as the 'bed of nails' affect. The 'bed of nails' effect is where the pressure exerted by each MN tip can be reduced to a potentially insufficient level to penetrate as deeply into the skin compared to an array of lower density where the same force is spread over a large number of needles (186). This means that the force applied to the needles are spread across the array and therefore penetration of the MNs would be challenging. The MNs fabricated using recipe 08 created a MNA with a height of 700 µm and no wall between the shaft, but this also led to tapering towards the base Figure 12.33. This tapering means that it could cause an increase in fragility upon insertion under thumb pressure and lead to a breakage during penetration.

13.2 Dye Staining

To detect whether microchannels have been created post penetration, dye staining was used. The dye used to determine the insertion capabilities was methylene blue (MB). As the MNs penetrate the skin, they breakthrough the SC to expose the viable cells below. The MB will then bind to the DNA within the viable cells. If the SC is not broken by the MNAs, the staining will not take place as this layer contains dead cells with no DNA present. Compared to MB staining techniques, fluorescent dye staining can be used to generate penetration marks using calcein. These skin samples are then sectioned before being placed under a fluorescent microscope for analysis. Although this technique is

widely used, compared to MB, fluorescent dyes are not as visible to the naked eye, which makes penetration analysis time consuming.

A single 1×5 silicon MNA and multiple arrays consisting of 2×5, 3×5 and 4×5 were tested by penetrating into porcine skin under moderate thumb pressure (~ 10 N) for 1 min. To ensure reproducibility, the MNs were inserted into porcine skin of the same thickness and a weighing scale was used to determine the weight of each thumb insertion and therefore the generated force (Equation 10).

$$F = mg \tag{10}$$

$$F = 1.05 \times 9.81$$

$$F = 10.4\ N$$

where F is the force produced upon insertion, m is the weight measured from the weighing scale and g is gravitational constant represented by 9.81 m/s^2.

Due to the brittleness of silicon MNs and structural dimensions, the applicator incorporated in PVP and PC MN insertion (Figure 16.1) would cause a higher insertion pressure that could lead to breakage upon application. Post penetration, MN was carefully applied to the surface of the skin and was washed off using methanol after 5 min. Penetration efficiency was calculated as follows (Equation 11):

$$Penetration\ Efficiency = \frac{Number\ of\ blue\ spots}{Number\ of\ MNs\ in\ an\ array} \times 100 \tag{11}$$

To determine methylene blue penetration capabilities compared to indentation and pooling, also known as the number of blue spots, the following criteria was utilized:

- The depth of colour post removal of excess methylene blue
- The location of the penetration point comparative to the shape of the MNs.
- The uniformity of each of the penetration points to one another
- The size of the point comparative to the MN diameter from tip to base

For efficient drug delivery capability, 75% penetration efficiency is required. As 75 % correlates to ¾ this ensures that the desired threshold dosage required is administered upon insertion.

13.2.1 Wall Presenting Shaft Etched MNs

In the case of the silicon MNs etched with a wall, each array observed a penetration efficiency of over 85%, however arrays, which were fabricated with MNs in the 3×5 formation, saw the penetration efficiency decreases to 93.3 % while a 4×5 decreased to 85%. The drop in efficiency of MN insertion is due to the fragmentation of the silicon MNs as they are brittle and therefore tip damage and fracturing is very likely. As the tip could possibly be left in the skin upon application, methylene blue won't be able to permeate as the vias would be blocked by the needles. Arrays where the needles are closer together lead to a weight distribution across the array under thumb pressure also known as the 'bed of nails' effect (Figure 13.1).

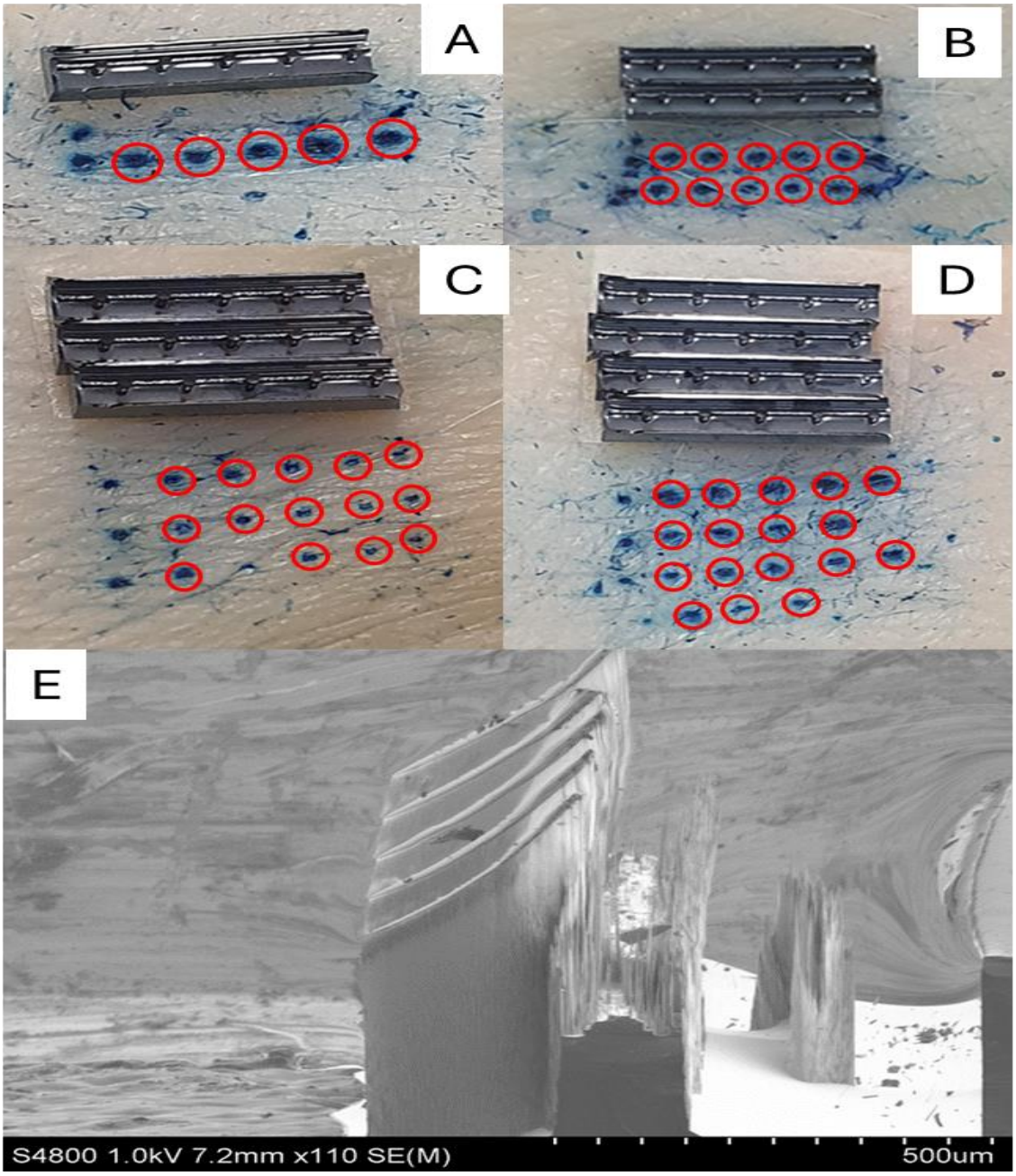

Figure 13.1 Penetration efficiency of singular and multiple silicon MNAs using moderate thumb pressure: (A) 1 x 5 MNA with 100 % penetration efficiency; (B) 2 x 5 MNA with 100 % penetration efficiency; (C) 3 x 5 MNA with 93.3 ± 0.3 % penetration efficiency; (D) 4 x 5 MNA with 85 ± 0.2 % penetration efficiency; (E) SEM image of the silicon MN post R07 etch.

13.2.2 Tapered Shaft Etched Hollow MNs

Silicon MNs with the wall removed showed a penetration efficiency of over 85 % after 4 (1x5) arrays were joined together (Figure 13.2). When the wall is removed between the MNs, the penetration observed is much higher when joining arrays together. This means that the wall between the MNs causes a slight implication to the penetration capabilities.

Due to similarities between the dye staining results obtained from R07 and R08, it is evident that the wall and the tapering does not alter the penetration abilities of the MNs through the SC.

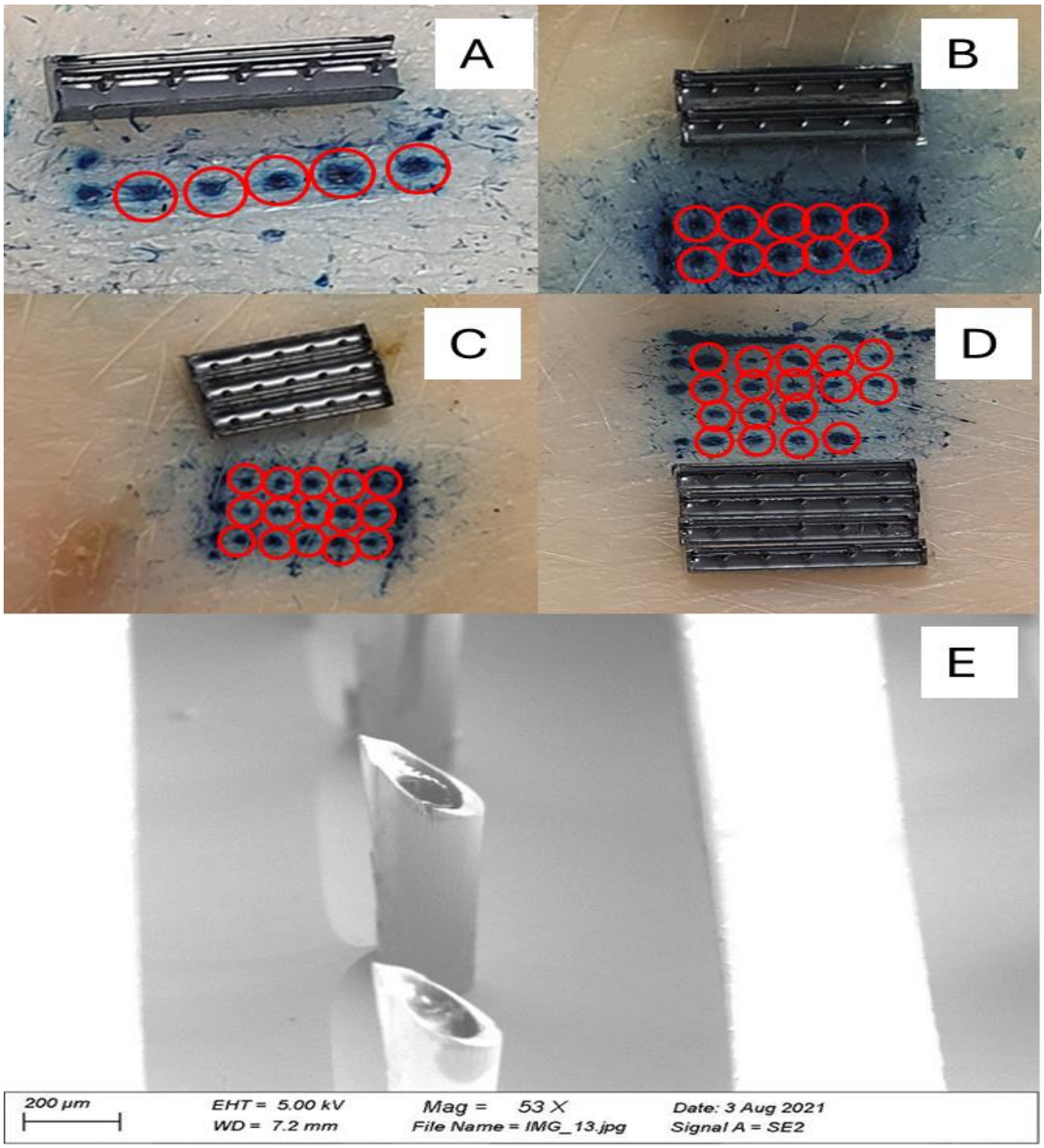

Figure 13.2 Penetration efficiency of singular and multiple silicon MNAs: (A) 1 x 5 MNA with 100 % penetration efficiency; (B) 2 x 5 MNA with 100 % penetration efficiency; (C) 3 x 5 MNA with 93.3 ± 0.3 % penetration efficiency; (D) 4 x 5 MNA with 85 ± 0.2 % penetration efficiency; (E) SEM image of the silicon MN post R08 etch.

13.2.3 Conclusion

Dye staining in porcine skin has shown no immediate variation between the silicon MN etched using recipe R07 and R08. Due to the wall between the MNs in the array created using recipe R07, it was expected that the MN tips would have indented the skin and the wall forms a barrier that blocks penetration through the SC to reveal the viable cells for the MB to bind to. Although MB is a useful way in visually confirming whether there have been successful penetration points, there are various limitations to using this method. The main drawback is that lateral diffusion can take place with the MB dye used and this can lead to overestimation of pore diameter. Furthermore, this technique could result in false positive results, as the SC may not have formed vias but instead indentations which the methylene blue can pool in. To improve penetration efficiency, an applicator can be utilised to ensure effective application and reproducibility between each injection into the skin compartment. In addition, the MB does not determine the depth that the MNs penetrate through. Therefore, further characterisation is required to determine these capabilities, this includes techniques such as histology and optical coherence tomography (OCT).

13.3 Histology

To determine the depth, at which the MNs lay in the epidermis layer and whether they have disrupted the SC, histological sectioning was used as described in Chapter 9.3.2 Histology is the study of tissues and cells under a microscope (187).

It is important to understand the natural morphology of the porcine skin to understand the changes that occur once the MNs are inserted. Sections of the skin were taken prior to treatment with MNs to determine the structure and these are analysed in Figure 13.3. Untreated skin samples represent various layers of the skin: the SC, the epidermis and dermis. Figure 13.3 shows a dark line at the top of the skin showing the intact SC layer (red line) and directly below that is the epidermis layer (blue section); There is a further distinct dark line underneath the epidermis (yellow line) and this is separating the epidermis and dermis layer (green section). From these characteristics, porcine skin penetrated with the silicon MNs had been analysed in conjunction with the untreated porcine skin samples. The MNs penetrate into full thickness porcine skin, followed by being frozen for 24 h before being histologically sectioned and stained using H&E method illustrated in section 9.3.2.

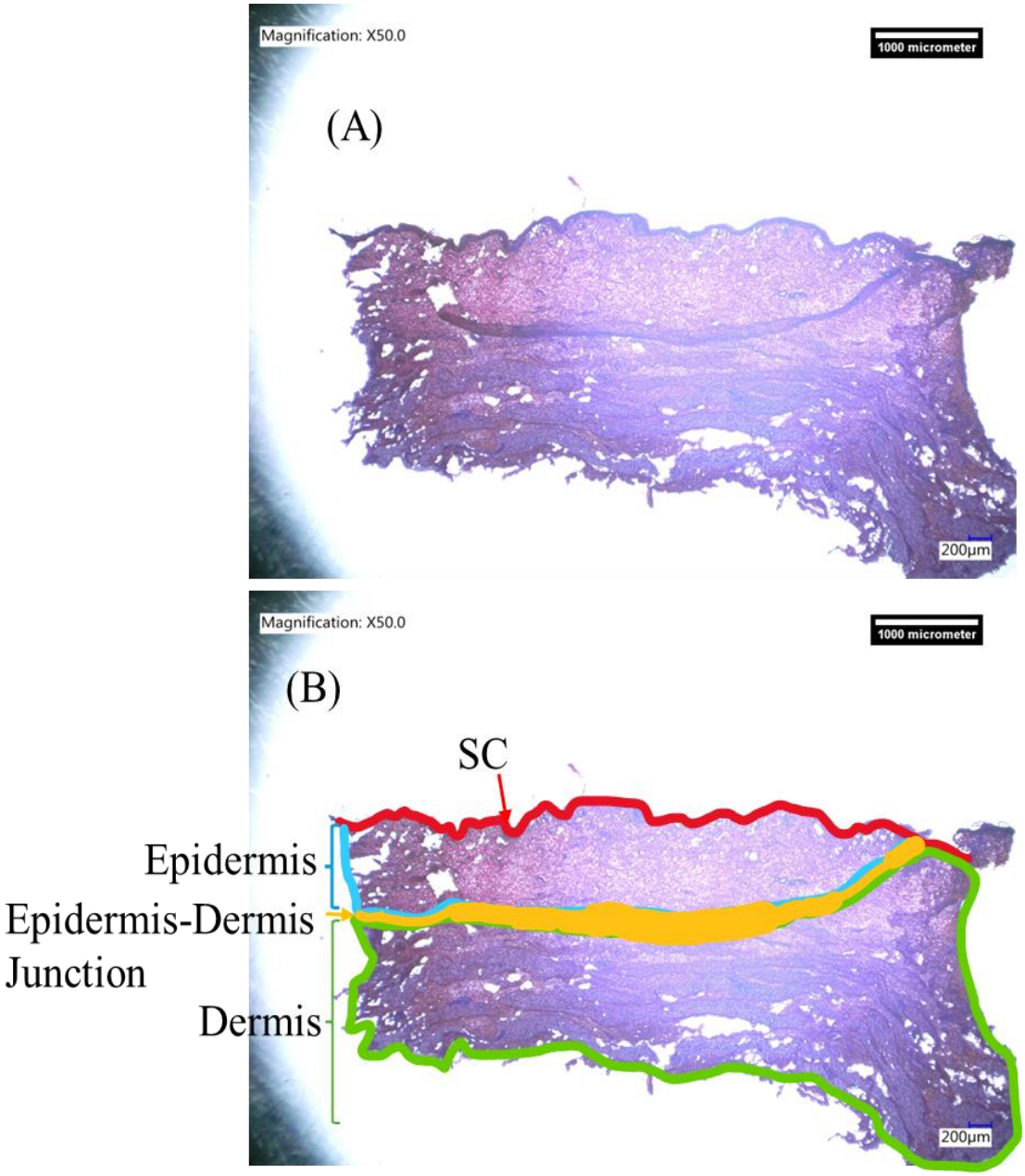

Figure 13.3 (A) Microscope image of the histology of untreated porcine skin; (B) Microscope image of the histology of untreated porcine skin with SC represented by the red line, epidermis represented by blue section, epidermis-dermis junction represented by yellow line and dermis represented by green section.

To denote the disruption of the SC, epidermis and dermis layer, coloured arrows on the stained image are shown in Figure 13.4.

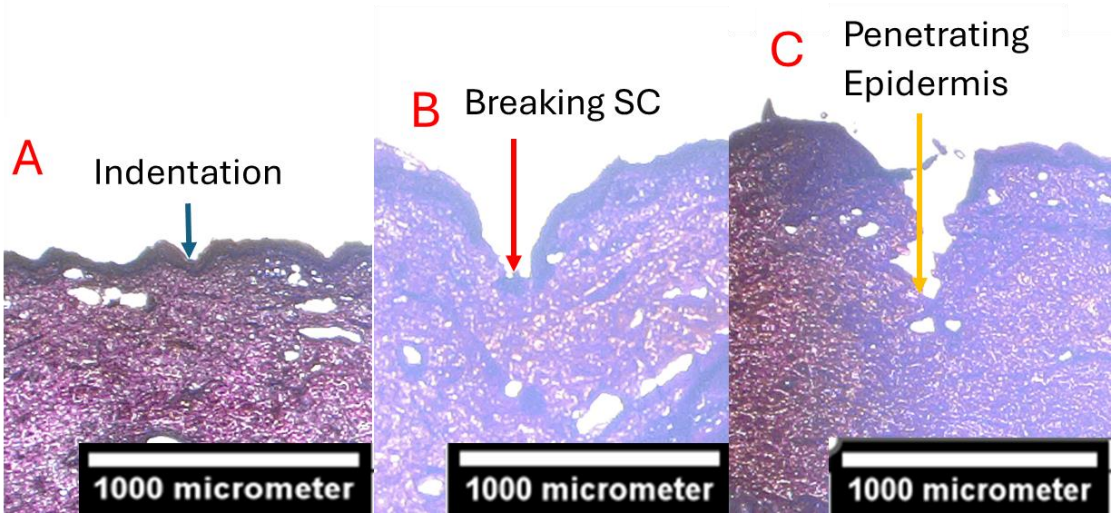

Figure 13.4 Microscope images of the skin with MN indentation, MNs breaking the SC and MNs penetrating into the epidermis/dermis.

13.3.1 Wall Presenting Shaft Etched MNs

Histological samples subject to tests using silicon MNs (etched using recipe 07), had evidently disrupted the SC layer and clear regions were dislodged to a profile similar to the shape of the array containing. The reference point to determine an accurate depth measurement of each penetration point is the highest flat region of the SC surrounding the indentation marks and these are shown in Figure 13.5. In doing this it avoids any over estimation that can be caused by skin height reduction upon thumb pressure insertion of MN into the skin. Analysis of the microscope images using ImageJ showed a penetration depth of 253 ± 15 µm. The reduction in height is 49.4 % lower than the 500 µm etched MN.

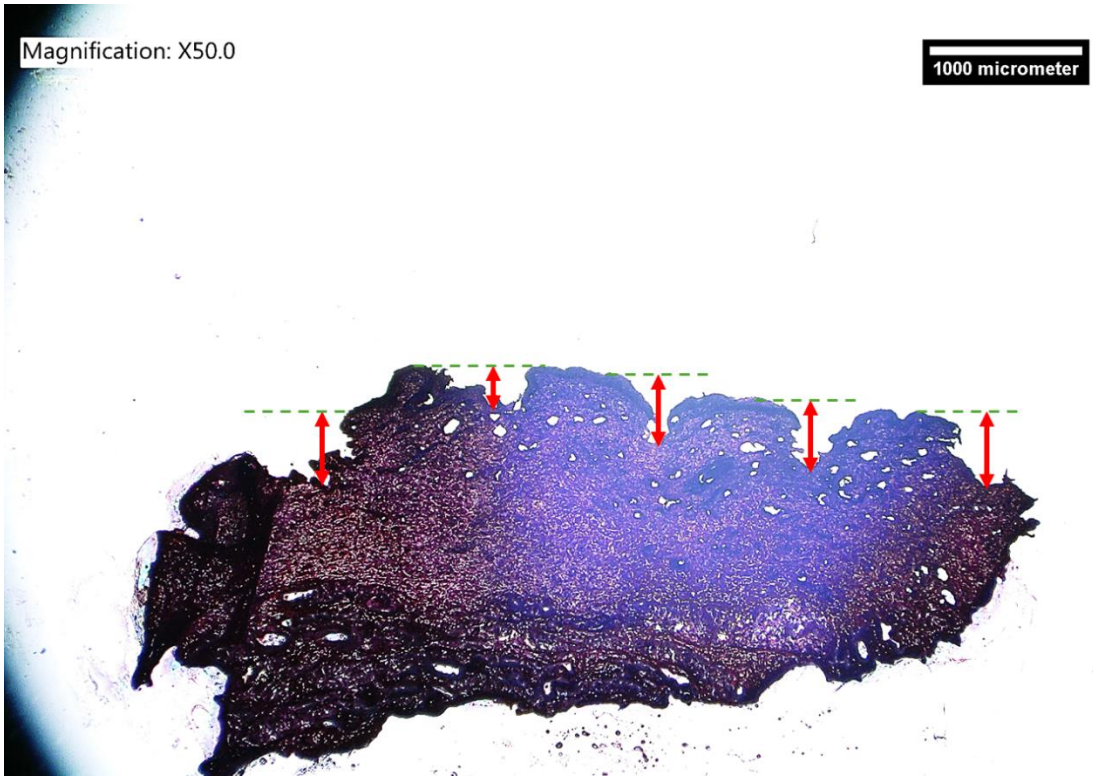

Figure 13.5 Microscope Image showing 5 penetration sites (red arrows) of the R07 silicon MNAs into porcine skin with the green line representing the points of measurement.

Performing histological cryosectioning can be a factor to the reduction in measured penetration depths and this can include the elasticity of the skin can causing retraction post removal of the MNA. To minimise this factor, the samples could be frozen in nitrogen upon insertion to ensure instant fixation of the penetration points Alternatively, the MNs could remain in the skin and frozen in place and removed just prior to cryosectioning. The retraction of the skin tissue means that the pores produced from the MNs could deform and would alter the microchannel dimensions. Furthermore, carrying out cryosectioning with a thickness slice of 30 µm may lead to difficulty in locating the perforation regions caused by the MNs.

13.3.2 Tapered Shaft Etched Hollow MNs

The MNs etched using recipe 08 demonstrated that although the MNs are tapered, they have the capability to disrupt the SC. Similar to the MNs etched using recipe 07, the samples were analysed using ImageJ to establish the depth of 440 ± 46 µm. There is once

again a reduction in the penetration depth of 37.04 % for an array height of 700 µm, which can be seen in Figure 13.6.

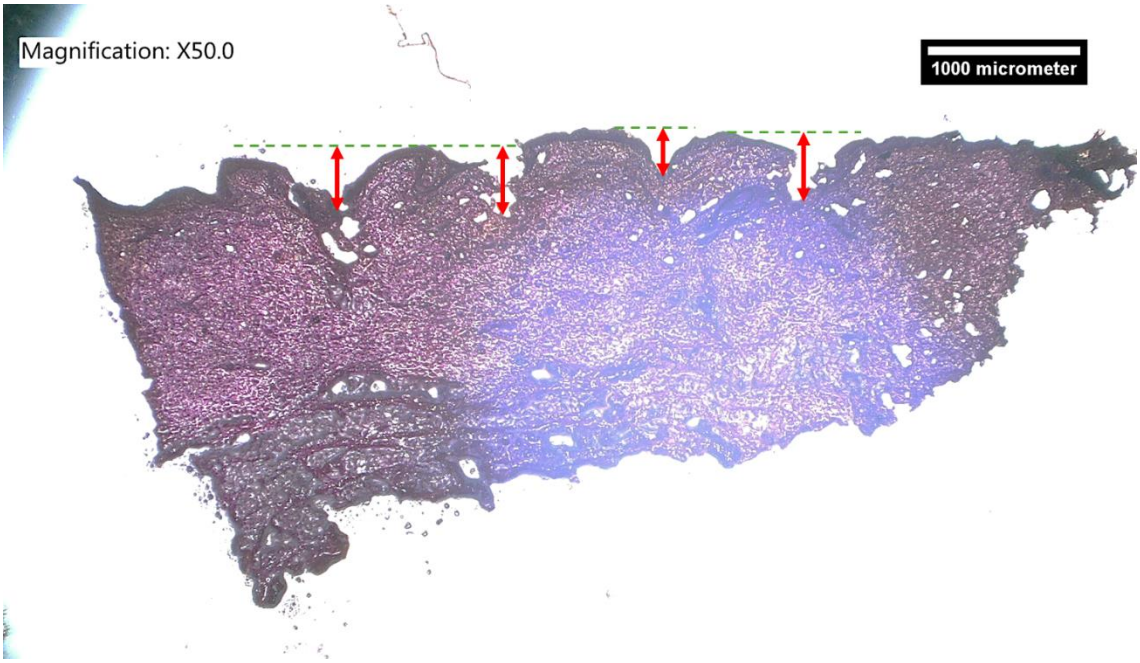

Figure 13.6 Microscope Image showing 5 penetration sites (red arrows) of the R08 silicon MNAs into porcine skin with the green line representing the points of measurement.

Once again, the histological cryosectioning can be a resulting factor to the dimension variation.

13.3.3 Conclusion

From this study, it has been highlighted that the wall created using the etch recipe R07 that reduces the height from 700 µm to 500 µm has no significant variation in the insertion profile. The 500 µm silicon MNs broke through the SC and penetrated at a MN depth of 253 µm. Tapering caused by recipe R08 towards the base of the MNA, the outline post penetration provided no significant impact in the depth, in which the MN remained.

As the MNs were penetrated into the skin under controlled conditions:

- Same skin thickness
- Same batch of porcine skin
- Similar skin morphology

Comparing penetration depths of a MNA with and without a wall after triplicates showed a penetration height increase of 187 ± 30 μm. This was anticipated as the wall acts as a barrier between the MNs and can lead to indentation rather than penetration through the layers of skin post insertion.

Chapter 14

Silicon MN for Drug Delivery

14.1 Drug Delivery Capabilities

14.1.1 Introduction

In the previous section, the characterisation for the silicon MNs were evaluated to determine whether they could break the SC and the region in which it would sit. The next study would be to assess the drug delivery capabilities of the hollow silicon MN as well as the maximum viscosity of drug that can be injected through the bore. For subcutaneous administration, the acceptable viscosity of formulations limit must be approximately 20–25 mPa.s. A higher could lead to pain at the site of injection as well as potentially higher injection force (188).

14.1.2 Viscosity Analysis

To determine the maximum viscosity, which an injectable drug should possess to be pushed through the hollow silicon MNs, initially vegetable oil was measured using a Rheometer at various temperatures. 1000 µL volume of oil was placed onto the peltier plate and shear rate tests were run on the sample.

Every 2 minutes the oil on the plate was warmed up from 25 to 60 at 5 increments, these were measured using a built in thermometer that accurately measures the temperature within the system. The viscosity was then measured when the oil reached the required temperate which is illustrated in Figure 14.1. Once the final temperature was set and the viscosity was obtained the peltier plate was cleaned and the experiment was repeated a further two times to ensure reproducible viscosity output. To determine the viscosity using a Rheometer, the shear rate is changed within the system once thermal equilibrium is reached. A series of viscosity measurements can measure the relationship between the shear rate and the shear stress of the liquid. To analyse further viscosities injection capabilities, silicone oil with pre-determined viscosities of 9.5 mPa.s and 990 mPa.s and water with a known viscosity of 1 mPa.s were used . This technique was utilised as it provided representation of how viscosity of fluids can be injected through the bore of the MNs as well as whether temperature impacts the fragility of the MNs. Temperature

changes through the vias could lead to the MNs becoming more fragile upon liquid injection and therefore could break under pressure.

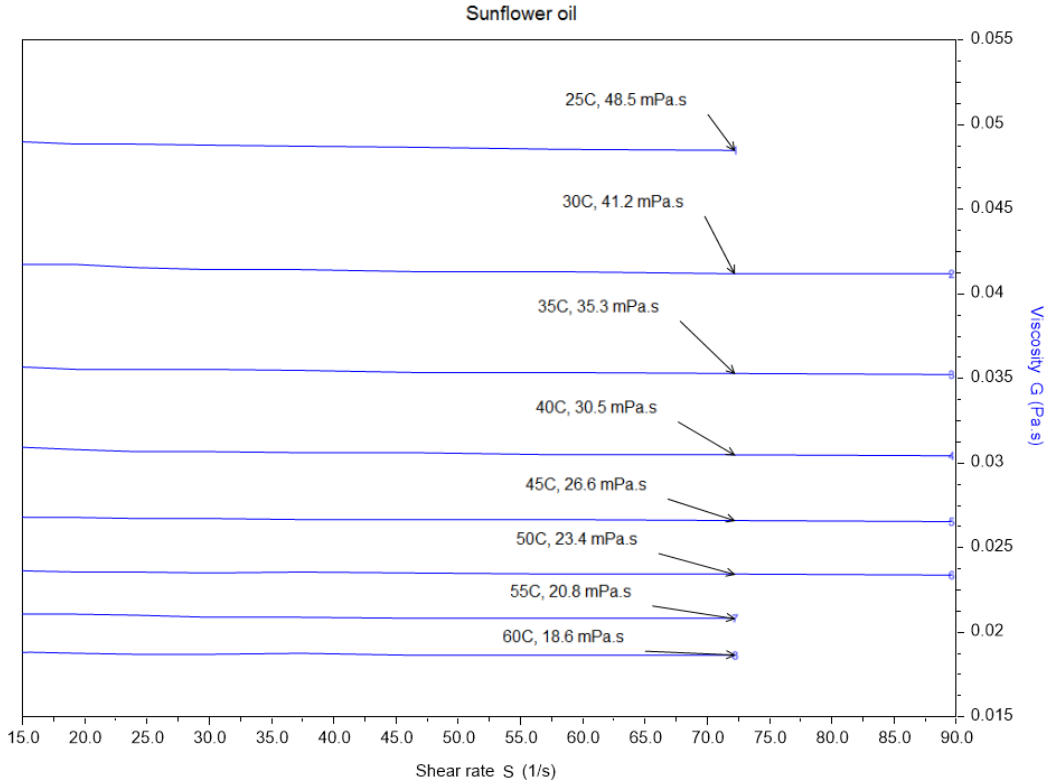

Figure 14.1 Graphical representation of the viscosity of sunflower oil at various temperatures

Post measurement, the solutions were pushed through a syringe at a force of 79.8 N and the injectability was determined (189). To enable the injection of solutions through the MNs, they are inserted into an adaptor that contains a Leur-lock set up at the base to allow attachment to a syringe. The adapters contain a ledge where the MNs can sit, and this gap aligns with the bores (Figure 14.2). This enables solution to be pushed through the MNs.

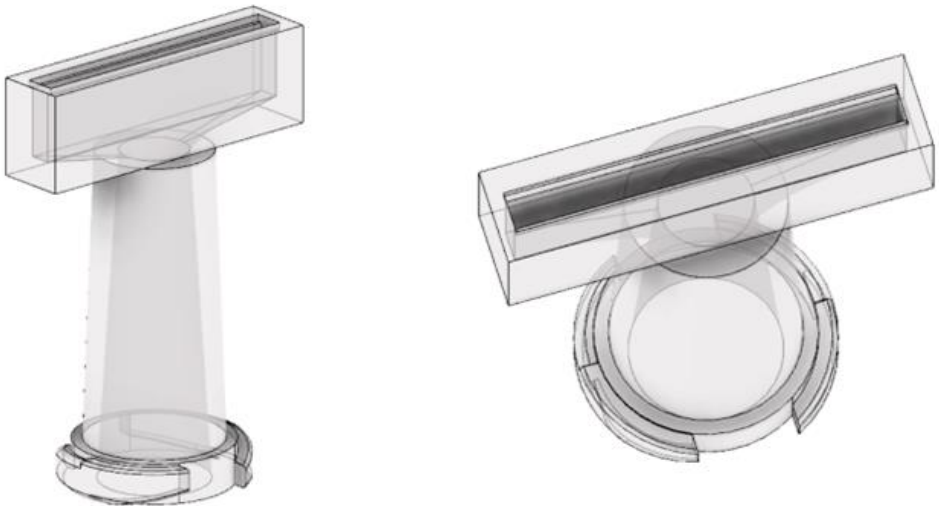

Figure 14.2 Autodesk designed applicator utilised for silicon MN application with Leur Lock addition for syringe attachment and step opening for MN insertion.

Once the MNs are placed onto the ledge, they are glued into place using a BONDIC® liquid glue that hardens with the use of an LED UV light. Using the BONDIC® glue allows precise administration around the MNA without blocking the bores at the base of the MNs (Figure 14.3).

Figure 14.3 Images of the silicon MNs glued to leur lock adapters.

To ensure that the force applied was constant over time, the syringe was attached to a syringe pump to control the force in which the solution is injected through the syringe (Figure 14.4). The syringe driver will allow a steady flow of the injectable solution out of the syringe through the MN.

Figure 14.4 Syringe pump to enable controlled injectability force through hollow silicon MN.

As seen in Figure 14.5, viscosity of solution over 50 mPa.s and 990 mPa.s pushed through the MN bores resulted in a compromised injection capability. Although it shows solutions injecting through the MNs, it can be seen that some of the MNs are blocked. The precision of the glue can lead to the MNs becoming blocked as the glue could run towards the base of the array before hardening and therefore injection can only be observed through the active MNs. Reducing the number of active needles can affect delivery as there are fewer points for the solution can exit through. Having fewer needles can build pressure within the MNs and higher force is required for the solution to be pushed through. This can lead to solution leaking out of the penetration points rather than into the skin layers decreasing delivery. Therefore, more open needles lead to more entry points and lower force for solution injection.

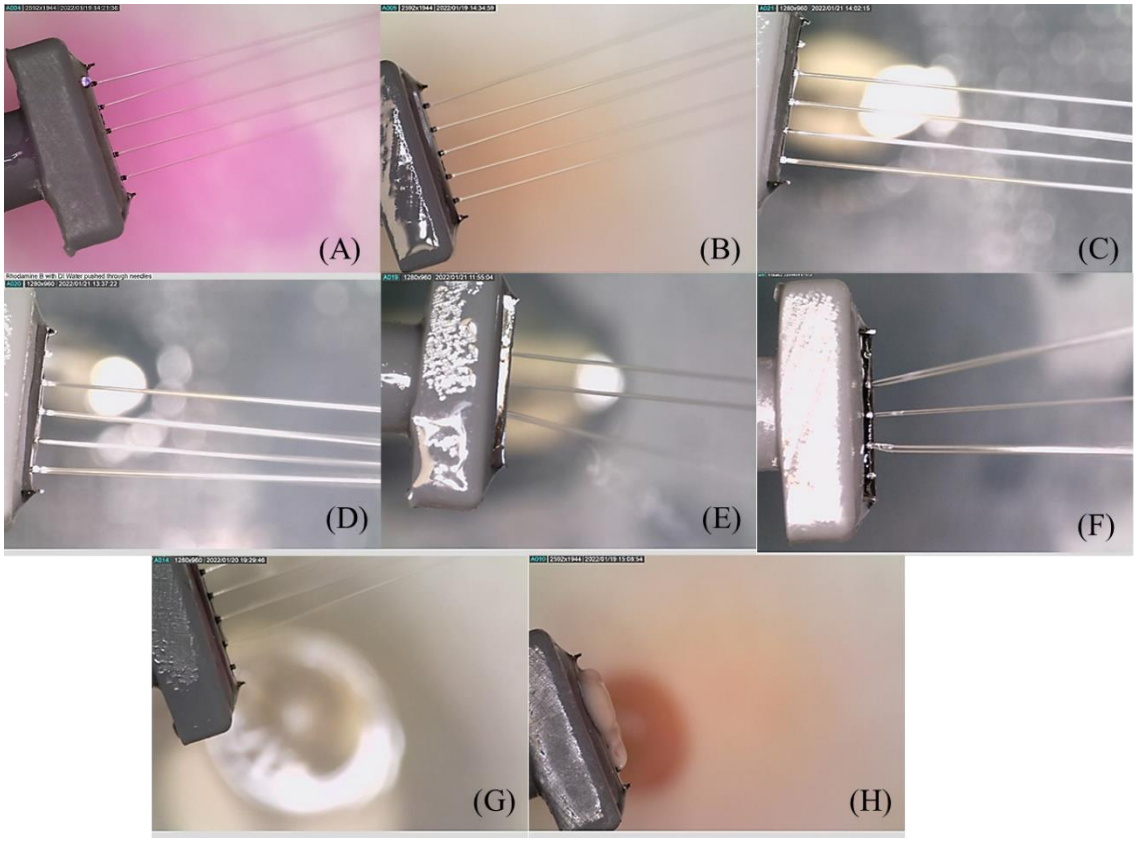

Figure 14.5 Hollow silicon MN injection capabilities with various viscosity liquids: (A) 1 mPa.s (DI Water with Rhodamine B pigment); (B) 9.5 mPa.s (Silicone oil with pigment); (C) 18 mPa.s (Vegetable oil at 60 °C); (D) 20 mPa.s (Vegetable oil at 55 °C); (E) 23.4 mPa.s (Vegetable oil at 50 °C); (F) 25 mPa.s (Vegetable oil at 45 °C); (G) 50 mPa.s (Vegetable oil at 25 °C); (H) 990 mPa.s (Silicone oil with pigment)

Although this technique provided partial information on injectability based on viscosity, the temperature increase of the oils pushed through the MN could lead to over estimation of injectability. This is due to the temperature of the inner lumen increasing in diameter and therefore injectability will ease. An alternative to give a more accurate and reproducible injectability studies is to either diluting known glycerol percentages in PBS solution or various known hydrogel percentages. This is a useful technique as the viscosity would be the only variable component to determine their injectability through the silicon MN bore.

14.2 Silicon MNs for potential drug delivery applications

14.2.1 Introduction

Using the OECD guidelines in Chapter 10, section 10.1 and in collaboration with Dr Olivia Howells, the Franz cell experimental method was employed to quantitatively define the drug delivery capabilities of the MNs.

14.2.2 Franz Cell Methodology

Silicon MN fabrication has been outlined in a previous chapter to provide a singular array with a height of either 500 or 700 μm dependent on the etch recipe. For Franz cell experimentation, non-scolded porcine skin is harvested and a dermatome is used on the skin to obtain samples at a thickness of 500 μm. The integrity of these samples need to be measured, due to the low thickness of the skin samples used in the Franz cell, by employing a transepidermal electrical resistance technique (Chapter 9.3.3).

After measurement of the integrity of the skin membrane, they are penetrated with either a hypodermic needle, a 500 μm MNA or a 700 μm MNA. After the MNs are removed from the skin membrane, the skin is placed onto the surface of the Franz cell receptor chamber containing 4 ml of 0.01 M PBS. Following membrane mounting onto the receptor chamber, 50 μL of either 0.2 mg/mL of calcein or 0.1 mg/mL of FITC - insulin are pipetted onto the surface of the porcine skin. This technique is also known as ‘poke and patch’ and is defined as MNs poked into the skin membrane to produce micron-sized channels followed by the application of the compound being analysed. At various intervals over a 24-h period, 400 μL aliquots are removed from the receptor chamber.

To quantify the concentration of drug permeating into the receptor chamber a standard curve is created for each molecule delivered. The various drug molecules are measured using a FLUOstar Omega spectrophotometer for fluorescent intensity, absorbance, or luminescence. For calcein and FITC - Insulin the spectrophotometer was set at an excitation of 490 nm as this is the peak wavelength that allows light to be absorbed most efficiently and there can be used to determine the fluorescent intensity (Figure 14.6).

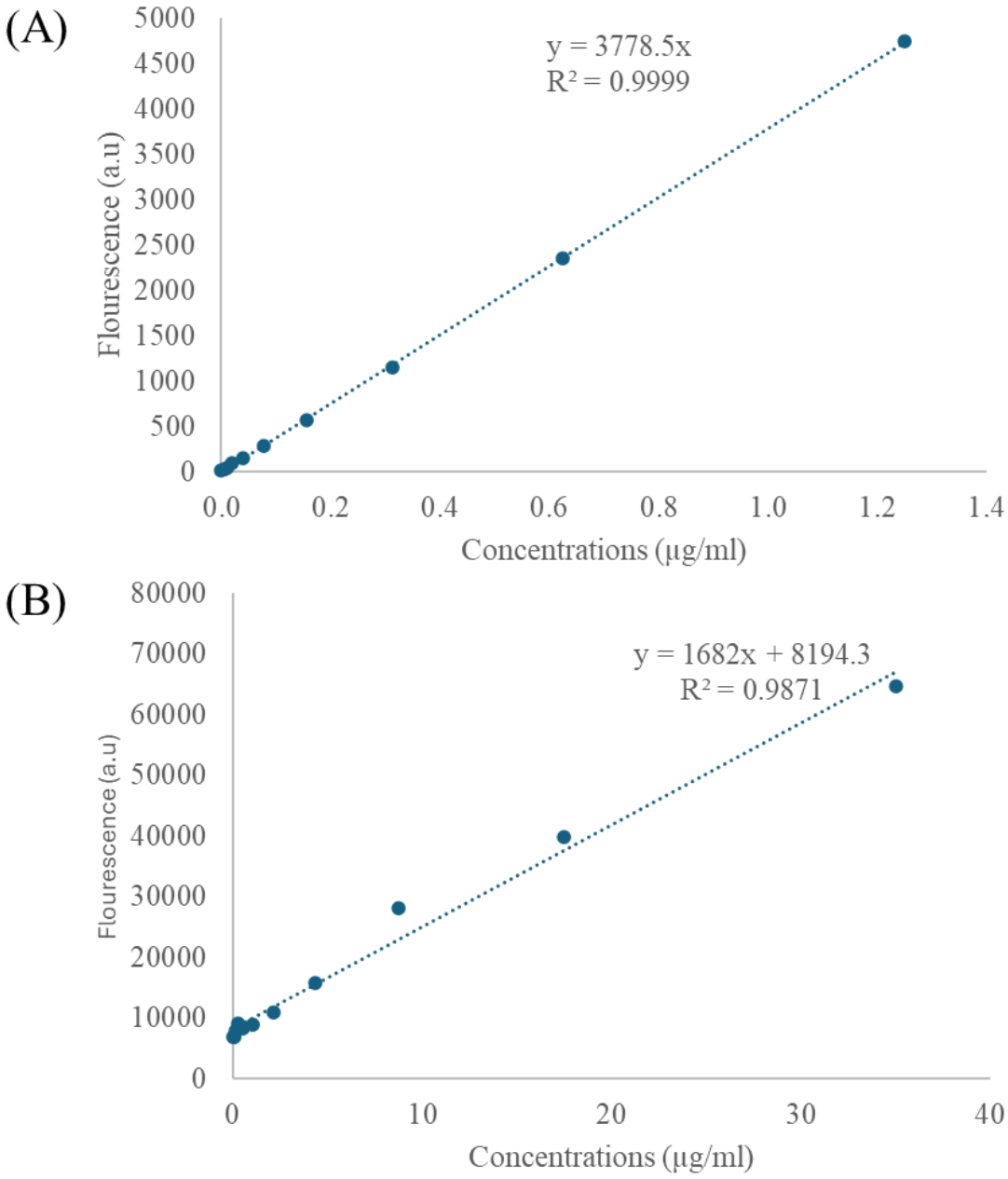

Figure 14.6 Standard curve created for (A) Calcein; (B) FITC-Insulin

Post Franz cell experiments, the skin membrane undergoes further analysis to determine regions where any unaccounted amount of drug would be present. Initially a singular tape strip is placed under pressure onto the surface of the porcine skin to measure drug that has not been absorbed onto the skin. This is followed by a further 10 tape strips, which are placed consecutively onto the surface. The concentrations calculated represent the amount of drug present in the SC. For drug diffused into the epidermis/dermis layer, the skin is homogenised with either collagenase or papain enzymes dependent on whether the

drug itself contains proteins that can reduce the volume obtained post digestion. To carry out skin homogenisation using papain or collagenase the sample is initially diced into smaller segments and these are placed into 4 mL of either enzyme solution illustrated in Table 10.6. Post digestion, the samples are centrifuged at 3300 rpm for 10 min to allow the debris to form a pellet and the drug/ enzyme solution to form the supernatant.

14.2.3 Franz Cell Results

14.2.3.1 Calcein

For initial evaluation of drug delivery capabilities of both the 500 and 700 µm silicon MNs, calcein, which is a model molecule was utilised. Calcein has been used as a model drug to simulate small molecule drugs (SMD). These drugs are defined as compounds with low molecular weight that are capable of modulating biochemical processes to diagnose, treat or prevent diseases (190). The molecular weight for SMDs is <900 Da and these make up 90% of pharmaceutical drugs including aspirin, diphenhydramine, and penicillin (191).

14.2.3.1.1 Wall Presenting Shaft Etch MNs

The results show that MNs with an etch depth of 500 µm produced an initially high permeation rate of 0.51 µg/cm^2/h in the first 4 h time period before plateauing off at a steady rate of 0.12 µg/cm^2/h as seen in Figure 14.7.

In comparison the hypodermic needle observed a penetration rate of 4.76 µg/cm^2/h, almost 10 times larger than the MNA. The same pattern as the 500 µm MNA is observed where the flow then begins to reduce and plateau to 0.32 µg/cm^2/h. The final MN delivered dosage into the receptor chamber was 0.98 µg/mL compared to the hypodermic needle being 1.97 µg/mL, which is approximately double the overall concentration.

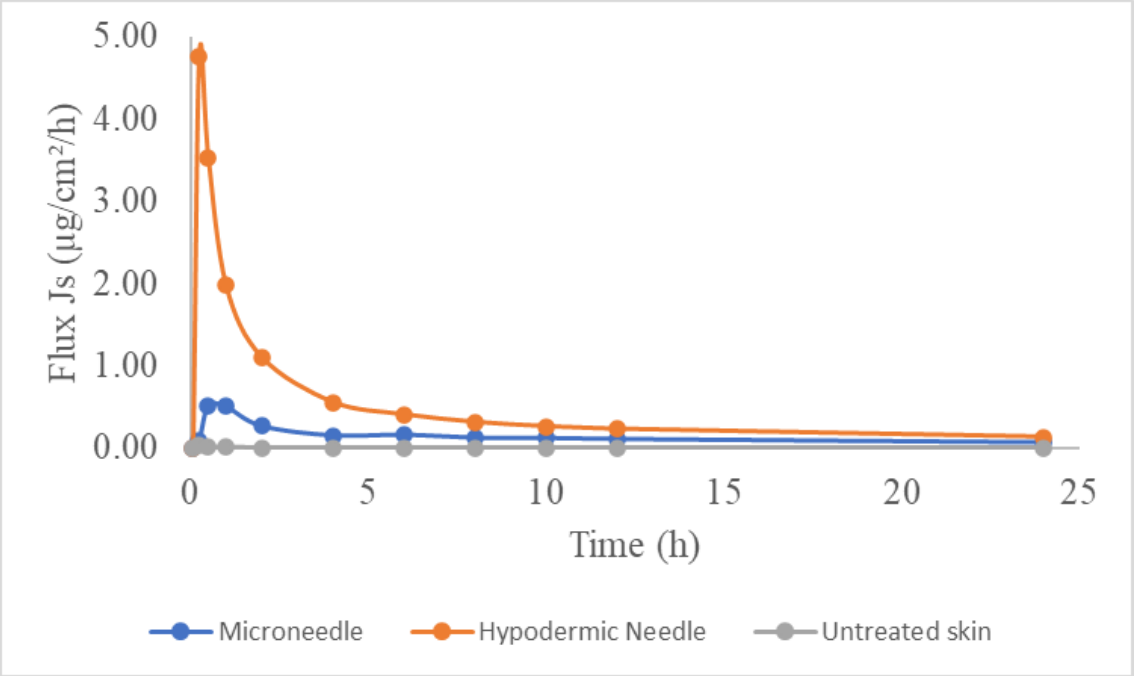

Figure 14.7 Flux Rate of Calcein after a 24 hour Franz Cell

Although calcein had diffused through the skin into the receptor cell of the Franz cell, only 39 % was measured after a 24 h period compared to the hypodermic needle that measured 81 % of calcein in the receptor chamber (Figure 14.8).

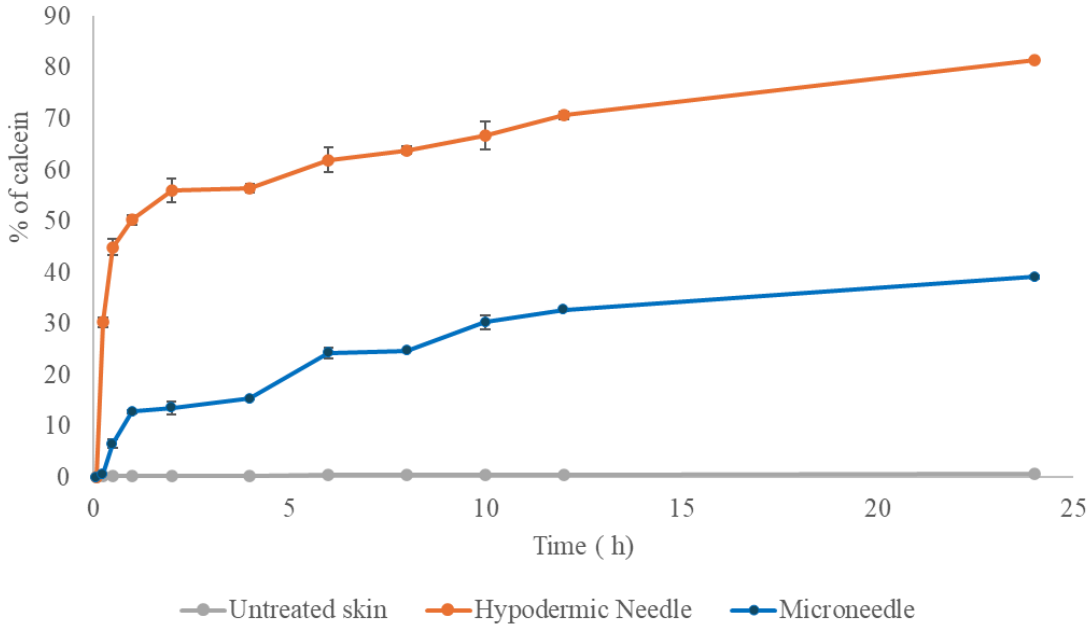

Figure 14.8 Percentage of calcein delivered into the Franz cell after 24 h.

To determine the movement of the remnant drug through the skin, tape strips and homogenisation of the skin was carried out as discussed in Chapter 10, Sections 10.2, and Section 10.3. The remaining calcein showed a high percentage in the epidermis/dermis layer with a value of 24.63 %. the lowest percentage of calcein was present in the initial tape strip with a value of 14.87 %, which in turn corresponds to the non-absorbed area as seen in Figure 14.9.

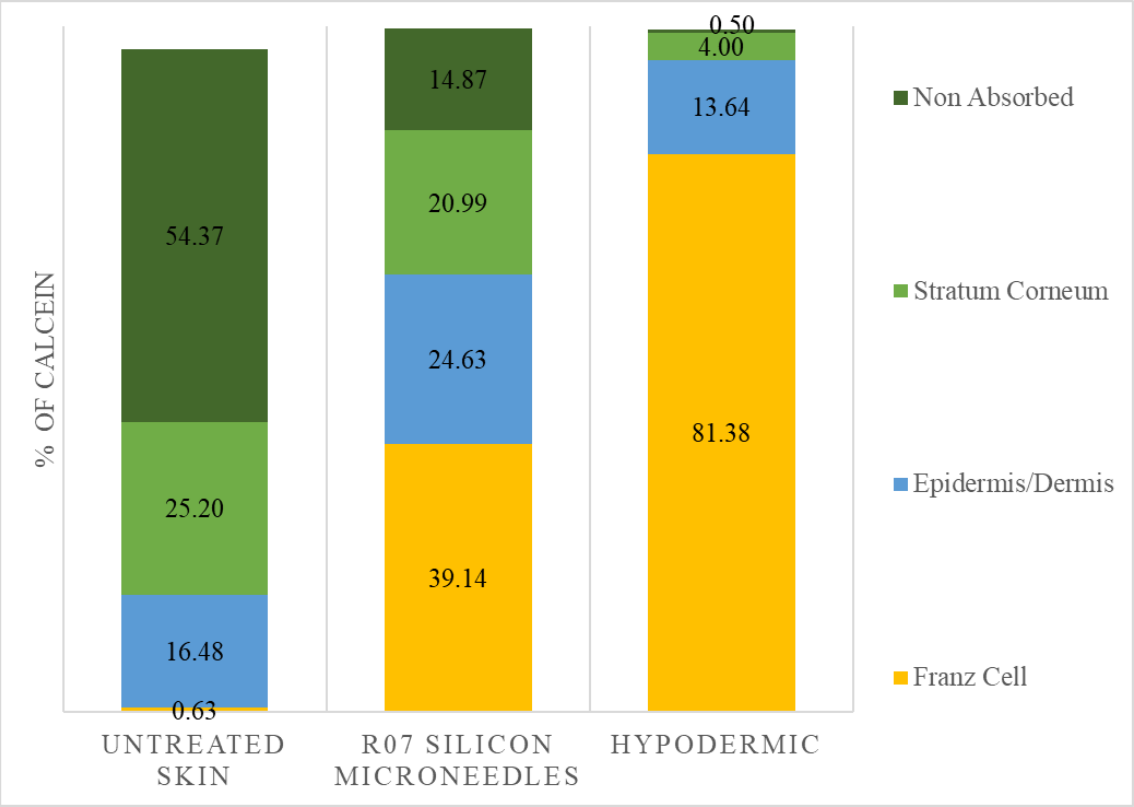

Figure 14.9 Graphical representation of the amount of calcein present in each region of the skin and delivered into the Franz cell after 24 h.

For porcine skin penetrated with a hypodermic needle, 81.38 % of calcein had diffused directly into the receptor cell which is over twice the percentage of calcein obtained from the MNA. It was also seen that 13.64 % remained in the epidermis/dermis layer that is almost half the percentage of calcein obtained from the MNA. Finally, 4.00 % was extracted from the SC which is four times lower than the percentage of calcein obtained from the MNA as seen in Figure 14.9.

Compared to skin samples subject to a MNA, skin which had no treatment with any type of needle showed that only 0.63 % of calcein was extracted from the receptor cell which

is approximately forty times lower than the percentage of calcein from the MNA. As well as that, 16.48 % was obtained from the epidermis/dermis layer which is ⅔ lower than the percentage of calcein obtained from the MNA. Finally, 25.20 % was extracted from the SC which is ⅘ greater than the percentage of calcein obtain from the MNA as seen in Figure 14.9.

14.2.3.2 FITC – Insulin

Patients suffering from advanced type 2 and type 1 diabetes mellitus, require insulin to maintain a constant level of glucose in the body. It is found that approximately 422 million people worldwide have diabetes, and a majority of patients suffering from diabetes are majorly found in low- and middle-income countries. About 1.5 million deaths are directly attributed to diabetes each year and this is due to the absence of affordable treatments. Insulin is usually delivered through injections subcutaneously using vials and syringe, insulin pen and continuous subcutaneous insulin infusions. Due to trypanophobia and pain through injections, alternative methods like the pulmonary route have been utilised. The pulmonary route is a vast and well perfused surface and the absence of peptidases that break down the insulin is advantageous. The first inhaled product was first produced in 2006, which utilised a dry powder formulation to be taken using an inhaler device. This device was found to have pharmacokinetic and pharmacodynamic properties that are similar to insulin aspart but with a faster action onset. However, although useful, administering insulin through an inhaler can lead to throat irritation and concerns of lung toxicity. As well as that, the technique requires multiple inhalation to provide the required amount of insulin and is expensive to produce (192). The oral route has also been investigated for the delivery of insulin as this is the most patient friendly and closest in mimicking the physiological insulin delivery and have the peptidases in the lumen of the intestines that enable the breakdown of the insulin delivered. Intranasal delivery as an alternative mode of insulin delivery is advantageous over both the oral, subcutaneous, and inhalation route as it bypasses the gastrointestinal tract, is non-invasive, painless and does not induce lung function. An alternative technique to administer insulin is through MNs as they have a faster onset of action, painless, sufficient bioavailability and have much better patient compliance.

Using the silicon MNs, the aim is to analyse the delivery of insulin into the receptor chamber. Further to analysing the ability of the silicon MN to deliver insulin, this test

would also lead to an understanding of whether the MNs are able to enhance the administration of larger drug molecules as the molecular weight of insulin is approximately 5,808 Da.

14.2.3.2.1 Wall Presenting Shaft Etched MNs

The cumulative flux rate for the 500 µm silicon MN begun at a pace of 13.03 µg/cm^2/h which was a similar rate of the skin which had not been treated with any MN which was initially 10.74 µg/cm^2/h, but was ⅓ of the rate of the skin treated with a hypodermic needle that had a rate of 38.07 µg/cm^2/h. After 4 hours both the control and the MN flux rate drastically reduced to 1.72 µg/cm^2/h and 1.38 µg/cm^2/h respectively. Compared to the MNA, the hypodermic flux rate drastically reduced to 3.50 µg/cm^2/h after 4 hours. These rates steadily plateaued off to 1 µg/cm^2/h on average after 8 hours (Figure 14.10).

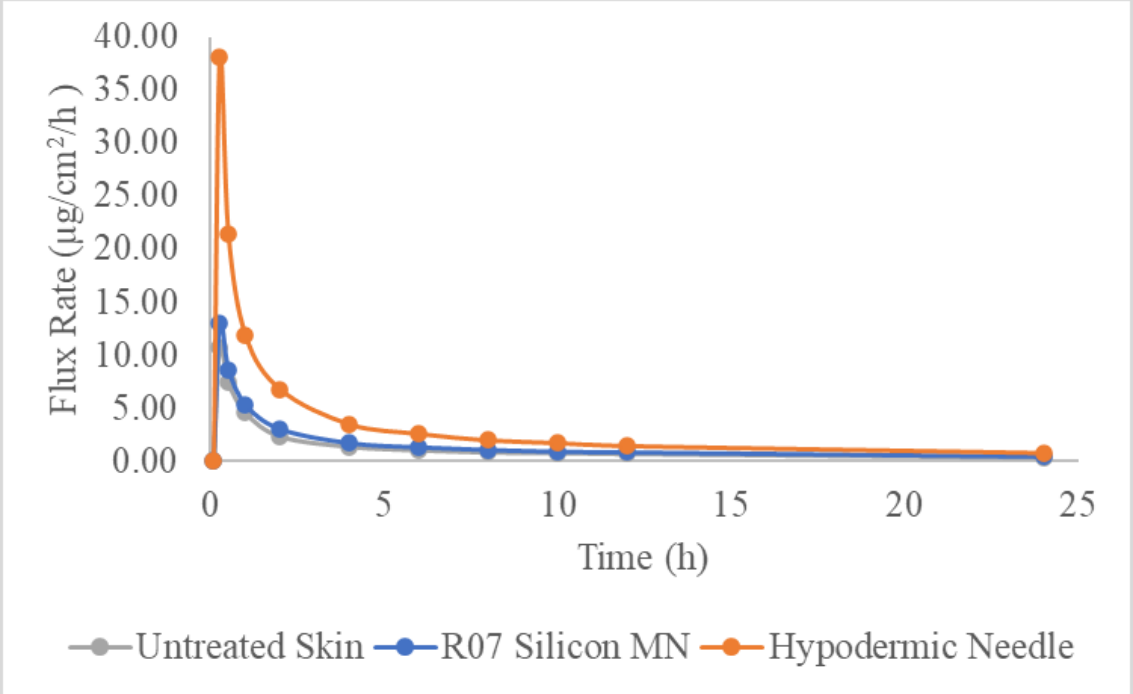

Figure 14.10 Flux Rate of FITC-Insulin after a 24 hour Franz Cell

The rate of permeation into the receptor chamber demonstrated an overall percentage delivery of insulin of 35 % (12 µg/ml), 20 % (7 µg/ml) and 16 % (6 µg/ml) for the hypodermic needle, silicon MN and untreated porcine skin respectively (Figure 14.11).

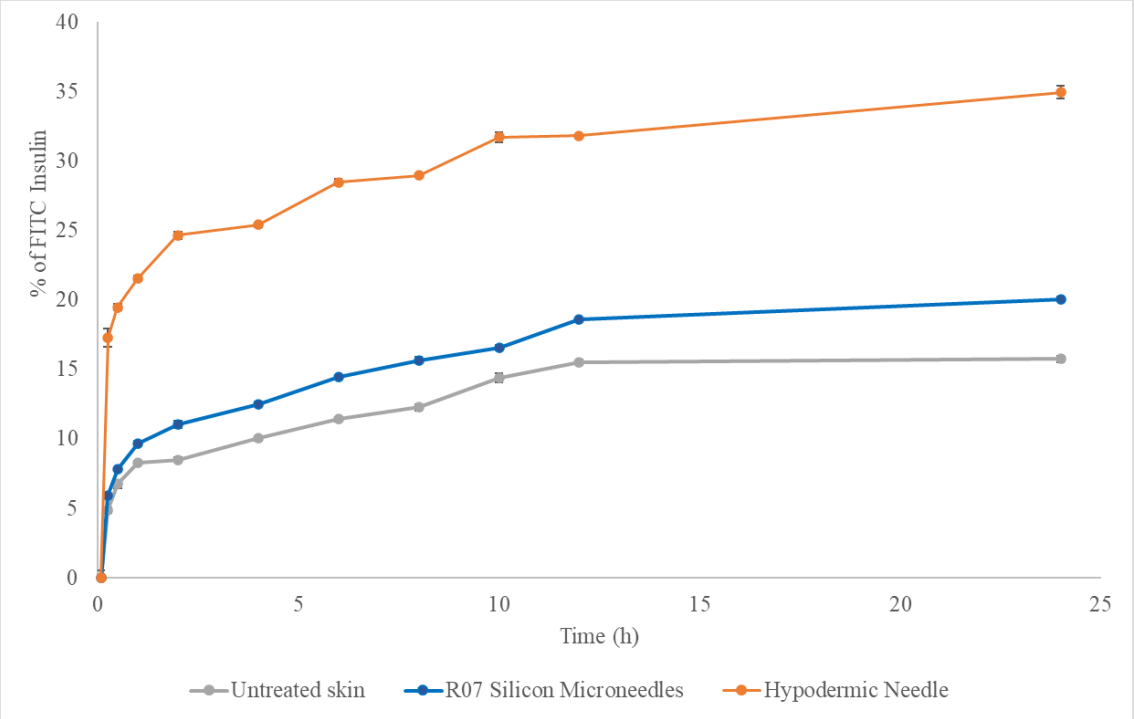

Figure 14.11 Percentage of FITC-Insulin delivered into the Franz Cell after 24 h.

Although insulin delivered into the Franz cell using the MNAs shows negligible difference compared to the control and moderate variation to the hypodermic needle, tape stripping and homogenisation using collagenase was carried out to decipher the concentration of insulin within the skin layers. In comparison to the control, a large percentage of the insulin had diffused from the top of the skin membrane into the SC and epidermis/dermis layers for both the MNAs and the hypodermic needle (Figure 14.12). Insulin is renowned to prefer acidic regions, because of which it is injected in the abdomen or the thigh that have a pH ranging from 1.5 to 3.5. The abdomen and thighs contain high levels of fatty acids comparative to other regions of the body and therefore as the insulin is injected, they will diffuse towards the acidic environment and in that pushed towards the systemic circulatory system to be distributed around the body. Consequently, the insulin delivered has remained in the SC and epidermis/dermis layer as these have a pH of 4.9 and 4.7 respectively.

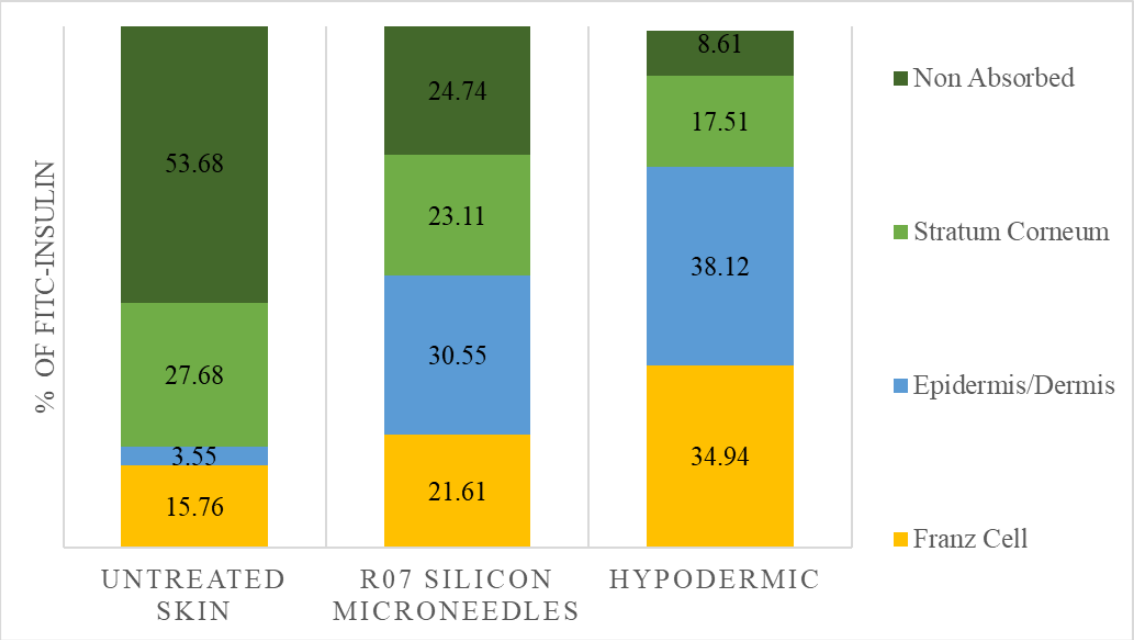

Figure 14.12 Graphical representation of the amount of FITC-Insulin present in each region of the skin and delivered into the Franz cell after 24 h.

Due to the neutral pH of the PBS solution in the Franz cell, the FITC-insulin being delivered over 24 h will not diffuse further than the SC and epidermis/dermis layer. If the receptor chamber contained a more acidic solution that is more favourable for FITC-insulin, the compound will have diffused deeper into the system over a 24 h period.

To overcome this issue, insulin is usually encapsulated into nanoparticles, hydrogels, microgels or membranes that are chemically responsive to glucose. These systems may shrink, swell, or degrade in a pH responsive or peroxide sensitive environment to release the therapeutic protein on demand. Therefore, the next stage for delivering insulin through the MN and overcoming these challenges is to encapsulate the drug. This implies that the encapsulation platform surrounding the insulin would be delivered into the body and would only release insulin in response to pH, glucose, or peroxide.

14.3 Conclusion

Comparing calcein and FITC-insulin delivered (Figure 14.6 & 14.8), a higher volume of compound had diffused through the layers into the Franz cell for calcein compared to FITC-insulin. Using the poke and patch technique for the silicon MNs showed that FITC-insulin had remained on the surface of the porcine skin and slowly begun diffusing through the layers over 24 hours before reaching the Franz Cell. Over 24 hours, calcein

had diffused further through the skin layers to the Franz Cell before and this is due to the molecular size of the compounds as well as the hydrophobicity of FITC-insulin and the hydrophilicity of calcein.

Drug delivery using silicon MNs have shown the ability to deliver calcein a model molecule through porcine skin. Further development can be looked into to determine molecular parameters for small molecule drug administration. These parameters consist of solubility, lipophilicity, stability, and whether enhancers are required. This is useful for a wide range of pharmaceutical drugs. The silicon MNs also showed potential for insulin delivery. However, further studies were required for achieving the successful delivery of insulin due its affinity to acidic environments. Further formulations including drug encapsulation that are mobilised by either chemical or physical enhancers will allow the MNs to deliver insulin effectively.

Part 4

Optimisation of Polyvinylpyrrolidone MNs for Drug Delivery

Chapter 15

Self-Dissolvable PVP MN Fabrication

15.1 Introduction

In this chapter, we describe polyvinylpyrrolidone (PVP) MNAs fabricated employing moulding techniques reported by Prausnitz et al in 2008 (165). The fabrication steps involve casting, encapsulation, and curing to form MNAs that deliver a range of drugs through the dissolution of the array. PVP is utilised for dissolvable MNs as they are biocompatible and has been used as a binder in many pharmaceutical tablets (193).

15.2 Fabrication Process

Initially, polycarbonate MNAs were used as a master structure to create moulds that can replicate the MNs. The moulds were made using Dragon skin^{TM} (purchased from Smooth-on Inc), which is a high-performance platinum cured silicone rubber. This was poured over the polycarbonate MNs in a mixture of 1: 1 v/v. After curing at room temperature after 1 h, the master moulds are ready to be used for PVP MN fabrication as seen in Figure 15.1.

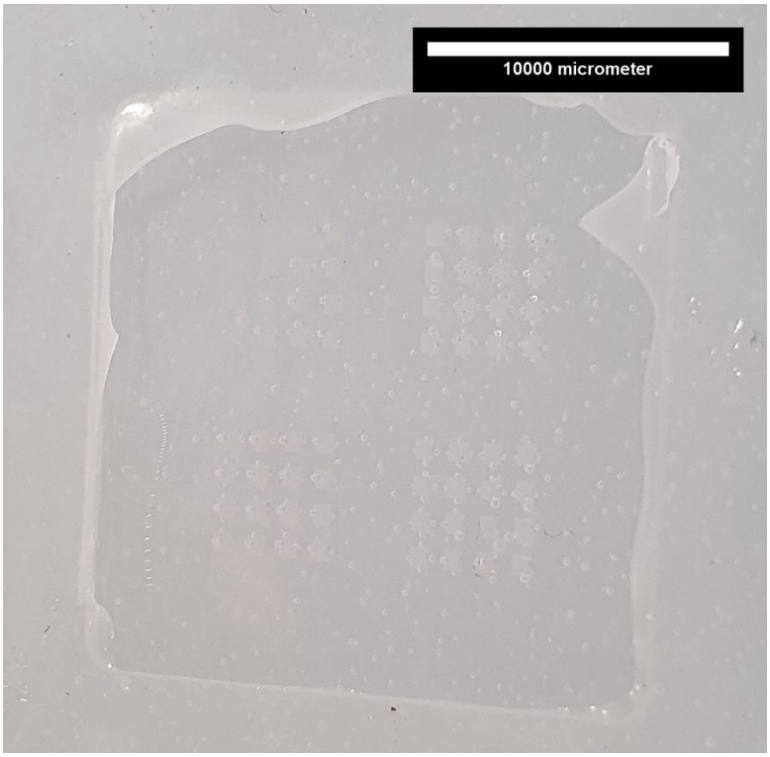

Figure 15.1 Dragon skin master mould to produce the PVP MNs

To prepare the PVP MN encapsulating model drugs, the silicone moulds were initially filled with the formulation illustrated in Table 15.1. Then, 50 µL of the formulation was pipetted into moulds. These were then placed into a vacuum desiccator to remove any air bubbles and therefore pull the solution into the MN reservoir. After 10 min in the desiccator, the photopolymerisation initiation was obtained by curing the solution using a 100 W lamp for 15 min. The next step was to produce the base structure for the MNA, which was generated using the formulation illustrated in Table 15.1. Then, 800 µL of the base solution was pipetted into the mould and these were cured once again using a 100 W lamp for a further 30 min to ensure photopolymerisation had been carried out successfully. The arrays were gently removed from the moulds and the results are illustrated in Figure 15.2.

Table 15.1 Optimised PVP formulation

MN Structure	Recipe
	50 µL of Vinyl pyrrolidone 1.5 wt% of AIBN 0.347 mg of calcein powder
Base Structure	**Recipe**
	800 µL of vinyl pyrrolidone 1.5 wt% of AIBN

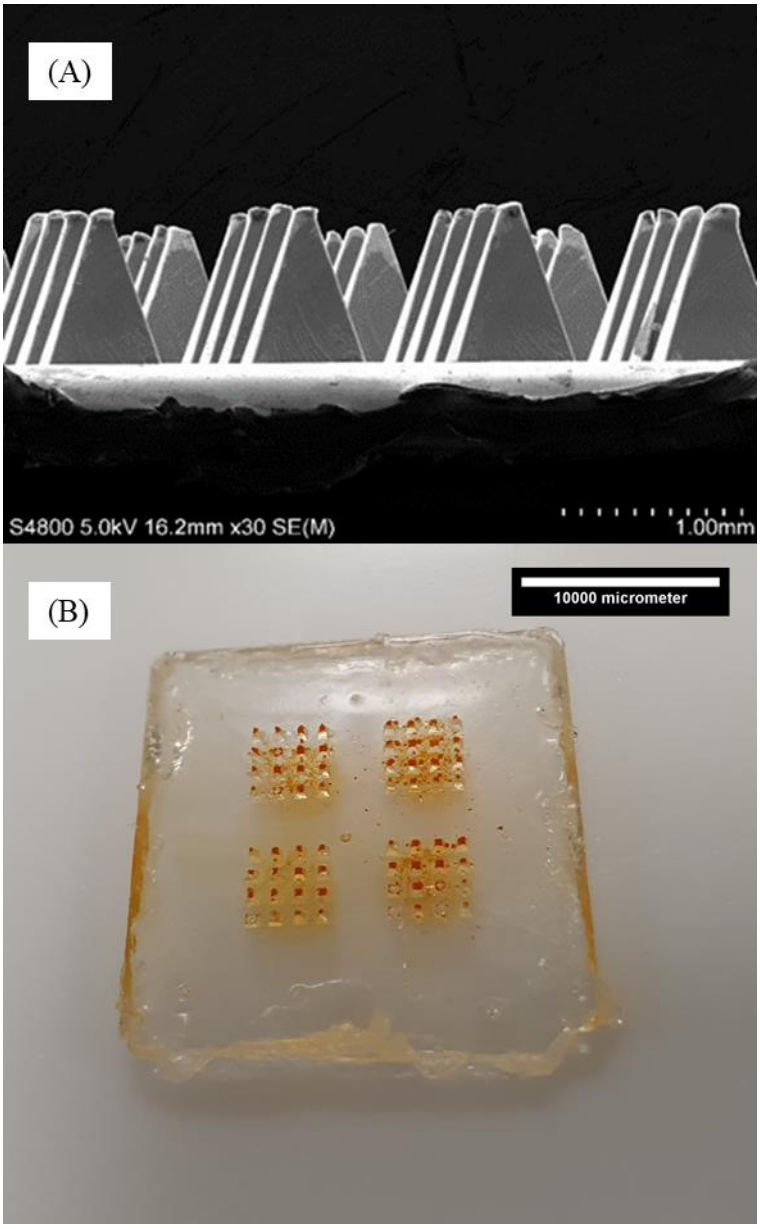

Figure 15.2 (A) SEM image of the demoulded PVP MNAs; (B) Image of an individual PVP MNA

Chapter 16

Characterisation of Self-Dissolvable PVP MNs

16.1 Introduction

As previously described in Chapter 9, characterisation of MNs is a key aspect as it determines the ability of the fabricated MNs to penetrate through the SC and into the epidermis. For the PVP MNs, the moulding technique used may cause the tips to blunt or the encapsulation could lead to an increase in weakness and fragility. An increase in the fragility of the MNs would imply that upon insertion using the applicator the needles may deform on the surface of the skin. As an applicator is being used, force insertion capability tests are necessary to establish the tensile force, which is acceptable.

The aim of this section is to understand whether the PVP MNs are successful in penetrating the skin before drug delivery experiments are carried out.

16.2 Applicator for standardisation of MNA insertion

To control the force and velocity of MNA insertion a MN applicator device was created in collaboration with Joe Wheeler. A 3D printer was used to create the applicator piston, spring holder, and cone. The centralised spring is compressed using a pin locking system to vary the force and velocity of MN application (Figure 16.1).

Figure 16.1 3D Printed applicator used for insertion standardisation.

When the spring is compressed, the magnitude of the force is directly proportional to the decrease in length from the equilibrium length. This relationship is also known as Hooke's law denoted by the following equation (Equation 12):

$$F = -kx \tag{12}$$

where F is the force restoring force on the spring, k is the spring constant, and x is the length change due to compression. The restoring force for this MN applicator device ranges from 4 to 10 N with a velocity variation from 2357 to 2525 mm/sec.

The 3D printed applicator was utilised for the PC MNs and the PVP MNs as the mechanical structure of the arrays are much stronger than that of the silicon MNs. Therefore, thumb pressure was substantial enough for the silicon MNs to be pushed into

porcine skin without breakage, but an applicator for the polymer MNs would not damage the arrays but ensure uniform application.

16.3 Mechanical Deformation Characterisation

Before carrying out penetration of the MNs using an applicator, a mechanical testing is to determine the penetration force is required. To determine this, axial compression tests were utilised using a Hounsfield Olsen compression analyser. A range of different forces were applied using the Hounsfield Olsen compression analyser from 5 to 50 N and this was done by compressing the MNs against a solid polymer surface and measure the compression distance uniformity. If the MNs collapse within the structure during compression this can lead to a kink in the line rather than a uniform exponential decay. Though this technique provides a precise measurement to an accuracy of 1 μm, it does not imitate the skin movement during insertion as the force is intensified at the tip of the MN rather than a distribution of force evenly spread around the needle. Even though porcine skin was used to determine the MNs penetration capabilities, the machine did not have the capability to apply the MNs into the skin accurately enough. Using mechanical testing is still useful enough to validate the insertion limitations and whether they are able to withstand the thumb pressure force of 10 N.

For the PVP MNs, 4×4 arrays from the same composition were subject to various forces to see if there any significant fracturing was observed (Figure 16.2).

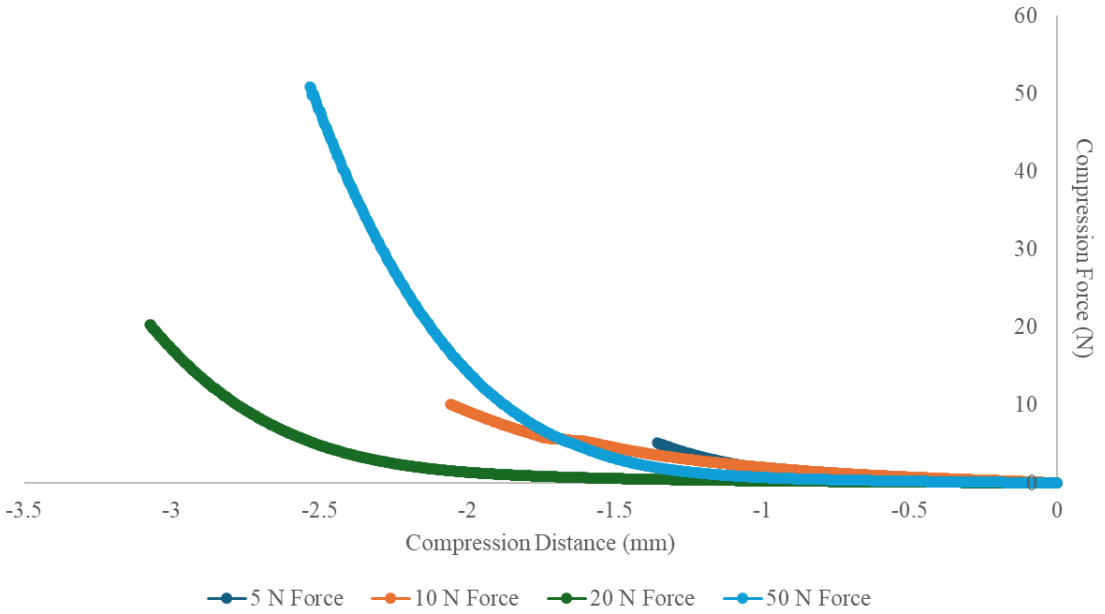

Figure 16.2 Graph of PVP MNs undergoing compression at different forces.

Polymer MNs are fabricated using two or more polymers. Additional materials are also incorporated to improve mechanical strength. Therefore, the fracture force of polymer MNs will be higher than MNs created from other materials such as silicon (57).

The MNAs exhibit no indication of deformation up to 50 N of axial force compression and the results show that these MNs are able to withstand the standard force that is applied by the applicator. As the arrays showed no change graphically, it could be postulated that the tips of each of the MNs would not buckle upon insertion into the skin. The results also show that using the moulding technique for producing the PVP MNs did not show any air pockets within the structure. The presence of air pockets within the structure would cause minor fractures as the force applied at the tip of the needles would cause the pockets to break and crumple the MN structure.

16.4 Dye Staining

As illustrated in Chapter 13 section 13.2, dye staining was utilised to determine whether any microchannels are created after insertion of the MNs into porcine skin (Figure 16.3). As the PVP MNs are mechanically stronger than silicon MNs and an applicator was utilised to apply 10 N of force upon insertion into porcine skin and held for 60 s. This ensured that each insertion force was uniform across the array and there would be no discrepancy in the obtained results.

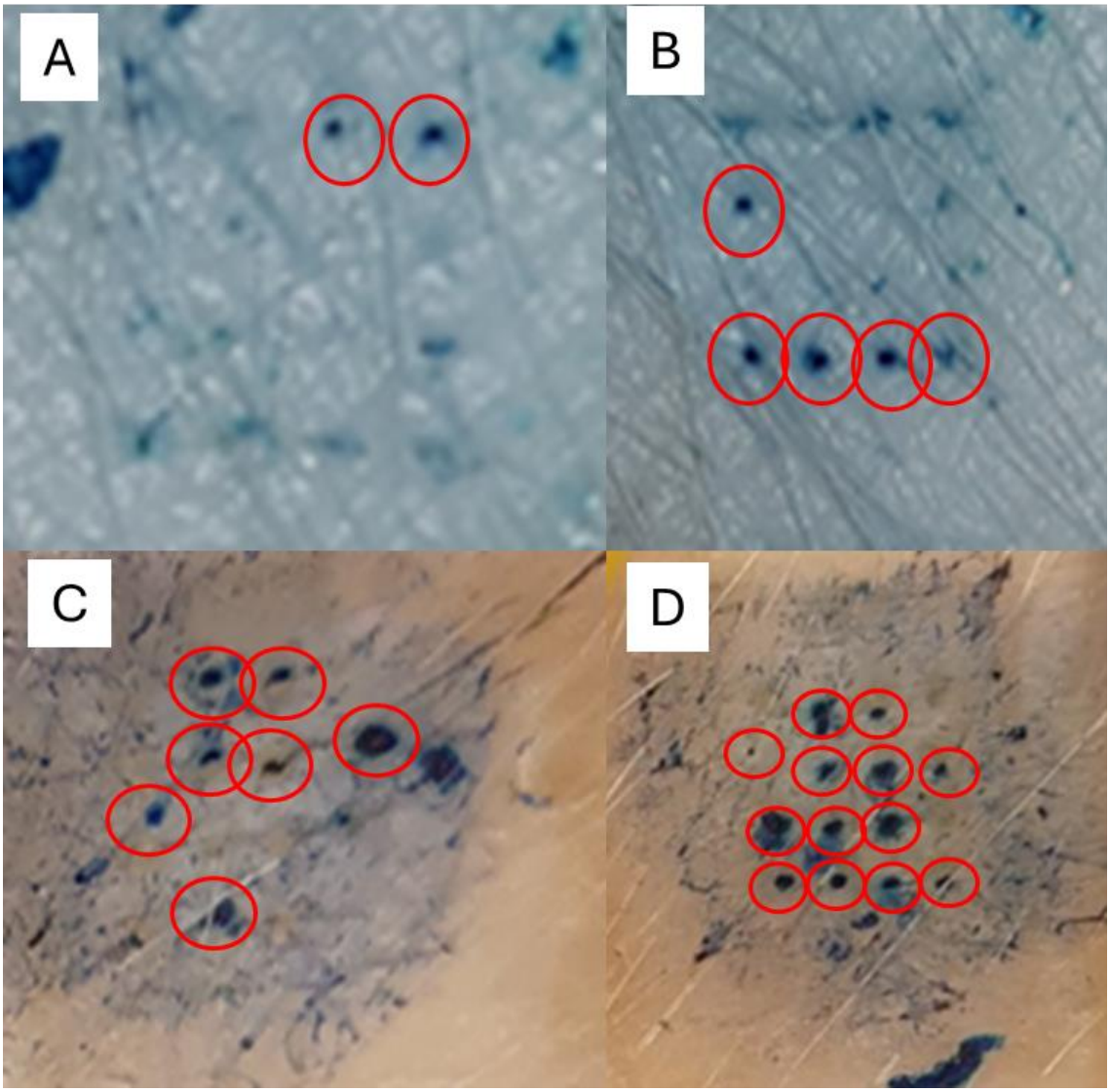

Figure 16.3 Penetration efficiency of PVP MNAs with different applicator forces: (A) 4 x 4 MNA penetrated without an applicator with penetration efficiency of 12.5 ± 0.6 %; (B) 4 x 4 MNA penetrated with an applicator force of 4 N with penetration efficiency of 31.25 ± 0.6 %; (C) 4 x 4 MNA penetrated with an applicator force of 7 N with penetration efficiency of 43.75 ± 0.5 %; (D) 4 x 4 MNA penetrated with an applicator force of 10 N with penetration efficiency of 81.25 ± 0.9 %.

Using the criteria illustrated in Chapter 13 section 13.2, penetration points with deep staining post removal of excess methylene blue (red circles) showed a penetration efficiency of 81.25 ± 0.9 % after a 10 N insertion force was applied compared to 12.5 ± 0.6 % efficiency without an applicator. Therefore, drug delivery capabilities are effective with the use of an applicator.

16.5 Histology

To determine the depth of penetration of the PVP MNs, histological section was utilised. The MNAs penetrated in porcine skin using the applicator at a 9 N insertion force and left in place until the excess skin is cut away. Upon removal from the skin, the sample is immediately placed into a freezer and left to freeze for 24 h.

Once the samples were frozen, they were mounted onto the cryostat chuck ready to be sectioned at 30 μm to obtain optimal slices of the skin to visualise the MN penetration points. After sectioning, the samples are left to dry for 24 before being stained again using the H&E staining process illustrated in chapter 9.3.2.

Post staining, the samples are left to dry before being placed under the microscope to determine the penetration vias present in the sample. The penetration points present in the skin are compared to untreated skin samples to determine the different regions of the skin as seen in Figure 16.3. This will therefore establish the layer in which the MNs sit post penetration.

Histological samples subject to the PVP MNs, had evidently disrupted the SC layer and clear regions were dislodged to a profile similar to the shape of the array containing the encapsulated drug. The microscope images showed in Figure 16.4 were measured using ImageJ to determine a penetration depth of 693 ± 64 μm.

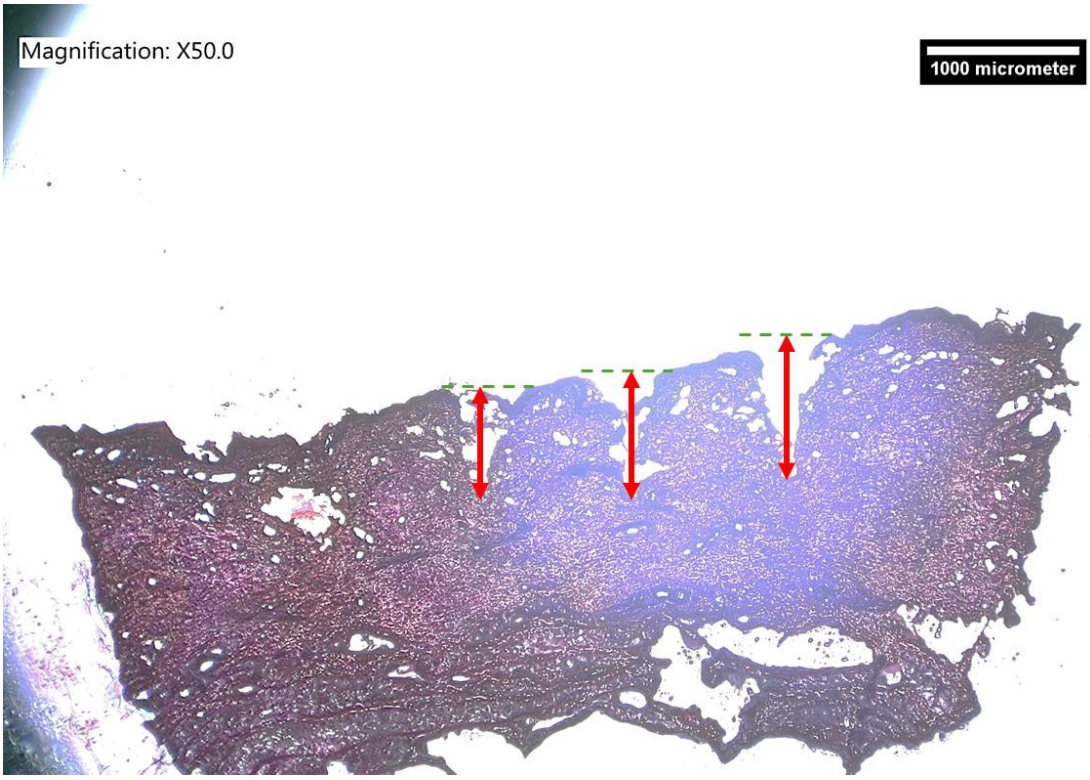

Figure 16.4 Microscope Image showing 3 penetration sites (red arrows) of the PVP MNAs into porcine skin with the green line representing the points of measurement.

Comparative to the 1000 μm height of the PVP MN, the measurements obtained were 30.62 % lower. Although the resulting dimensions from the histological samples were smaller, the limitations from the cryosectioning could be the reason. As well as cryosectioning, as the PVP MNs dissolve upon contact with moisture the vias would begin to close at the tip post penetration. This is because the surface area of the tip is much smaller than the base, so upon the time taken to remove the excess skin prior to freezing the tips would begin to dissolve and in that the penetration points will close due to the skin's elasticity. Therefore, the height in which the MNs are measured would be lower than the actual height of the PVP MN arrays.

Chapter 17

Self-Dissolvable PVP MN for Basal Drug Delivery

17.1 Introduction

Self-dissolving PVP MN can be useful in providing basal drug delivery, which implied that the drug administered will be longer acting. Long acting drug delivery can therefore help to keep levels steady in the body over a long period of time. As the MNs come into contact with the moisture, they will slowly dissolve to diffuse into the system. This mechanism of delivery is similar to sustained drug release tablets where drugs are administered to a patient at a given rate, which aims to maintain a consistent concentration over a specific period of time. Using basal drug delivery, enables a reduced number of doses, as you can encapsulate higher concentrations of drug within the polymer matrix, which lowers expenses and improves patient compliance and decreases side effects. In addition to improving consistency of blood plasma levels to help obtain therapeutic efficacy, basal drug delivery decreases potential toxicity by slowly administering high levels of drug rather than a high dose in a singular injection (194). Examples of potential uses for sustained drug release is illustrated in Table 17.1.

Table 17.1 Examples of potential uses for sustained drug release and pharmaceutical drugs on the market.

Sustained drug release name	Therapeutic use	Maximum Dosage per day
Tegretol	Epilepsy	400 mg
Acebrophylline	COPD and bronchial asthma	200 mg
Lithium carbonate	Manic depressive disorder (Bipolar disorder)	1200 mg
Diclofenac	Anti-inflammatory	150 mg
Acetaminophen	Arthritis Pain	3000 mg
Tramadol	Pain killer	300 mg
Verapamil	High blood pressure and control of angina	120 mg
Mycifor	Lower and upper respiratory tract infections	1000 mg
Insulin	Diabetes	10 mg

17.2 Franz cell results

Post MN characterisation, Franz cell analysis was carried out to determine capability of the PVP MNAs to deliver drugs. Post insertion the MNs would theoretically dissolve and

diffuse through the porcine skin membrane into the receptor cell below. As described in Chapter 10, non-scolded porcine skin, dermatomed to 500 μm thick were tested.

Each of the MNs were inserted into the skin membrane using an applicator before being secured into place on the receptor chamber. During a 24-hour period, 400 μL aliquots were removed at various time intervals to measure the concentration of drugs that permeated from the MNAs to the receptor chamber. To determine the concentration of drug permeated into the receptor chamber a standard curve is created once again as seen in Figure 17.1. To obtain accurate representation of the fluorescent intensity, the standard curve comprised of the polymer and calcein or FITC- insulin to make sure that there is no background fluorescence originating from the polymer. The standard curve will then be able to characterise the values obtained from the aliquots removed from the receptor chamber.

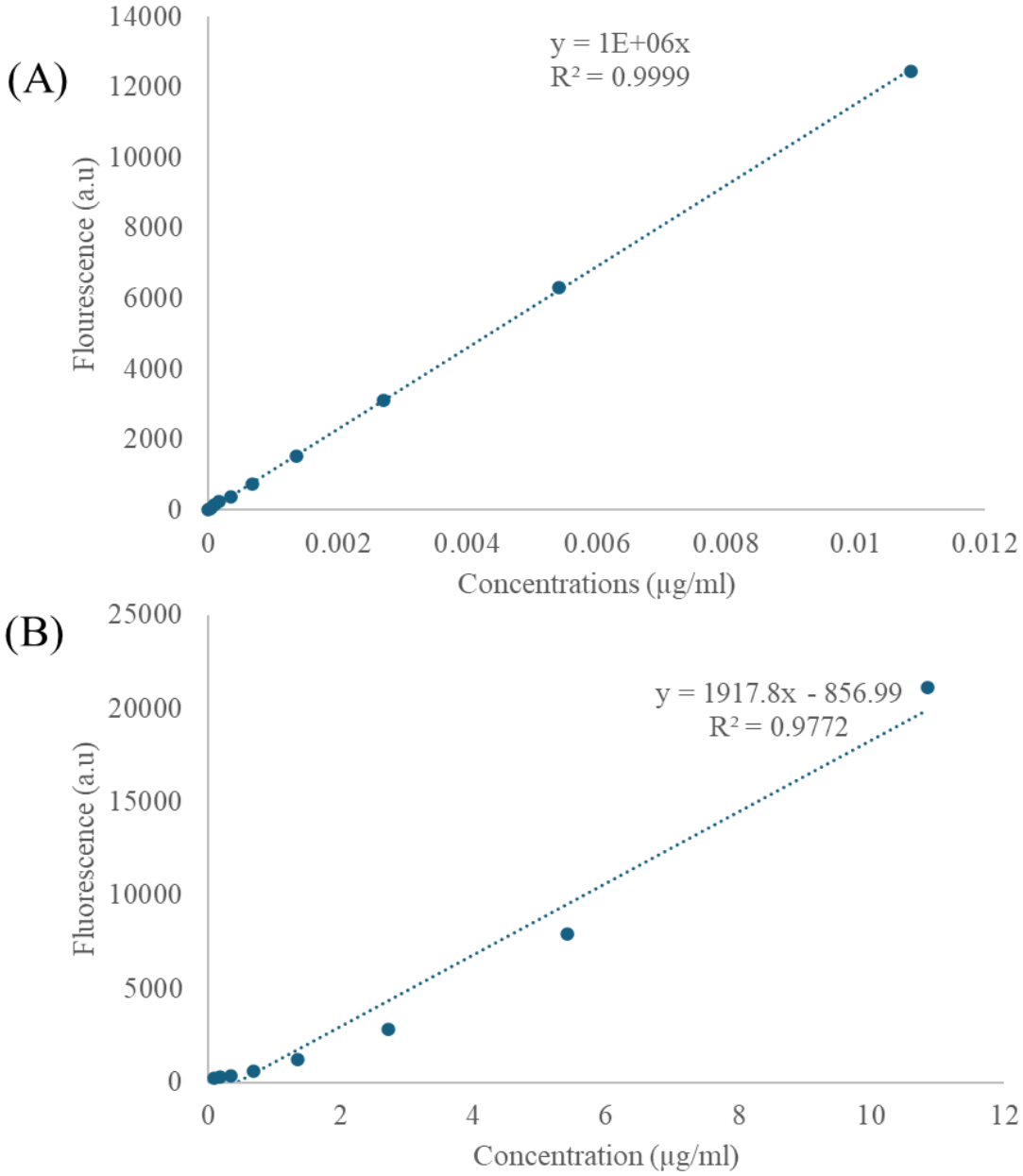

Figure 17.1 Standard curve created for: (A) Calcein with PVP formulation; (B) FITC-Insulin with PVP formulation.

After the 24-h Franz cell experiments, the skin membrane is characterised as described in chapter 10, the location of the remnant encapsulated drug.

17.2.1 Calcein

Over a 24-h period, the flux in the first hour was observed to be at a maximum of 0.00250 µg/cm²/h, which is characteristic of the insertion of the MN into the skin where the moisture within the skin leads to the dissolution of the tip of the MNs. During the

encapsulation, the tip of the MNs possess the highest concentration of calcein, which justifies the high value of flux.

After 1 hour the flux rate across the Franz cell begins to decrease to approximately 0.001 µg/cm^2/h where the rest of the MN gradually dissolves releasing the calcein with the polymer matrix and this will diffuse through the skin membrane into the receptor chamber. After 4 hours the flux rate increases again to approximately 0.00125 µg/cm^2/h, this is due to the central region where a high concentration of calcein is encapsulated comes into contact with the skin moisture therefore increasing the diffusion gradient and this pushes more calcein through the skin membrane into the receptor chamber. After this sudden flux of calcein, the rate plateaus once again to approximately 0.001 µg/cm^2/h where the residual calcein present in the skin membrane diffuses through the system into the Franz cell (Figure 17.2).

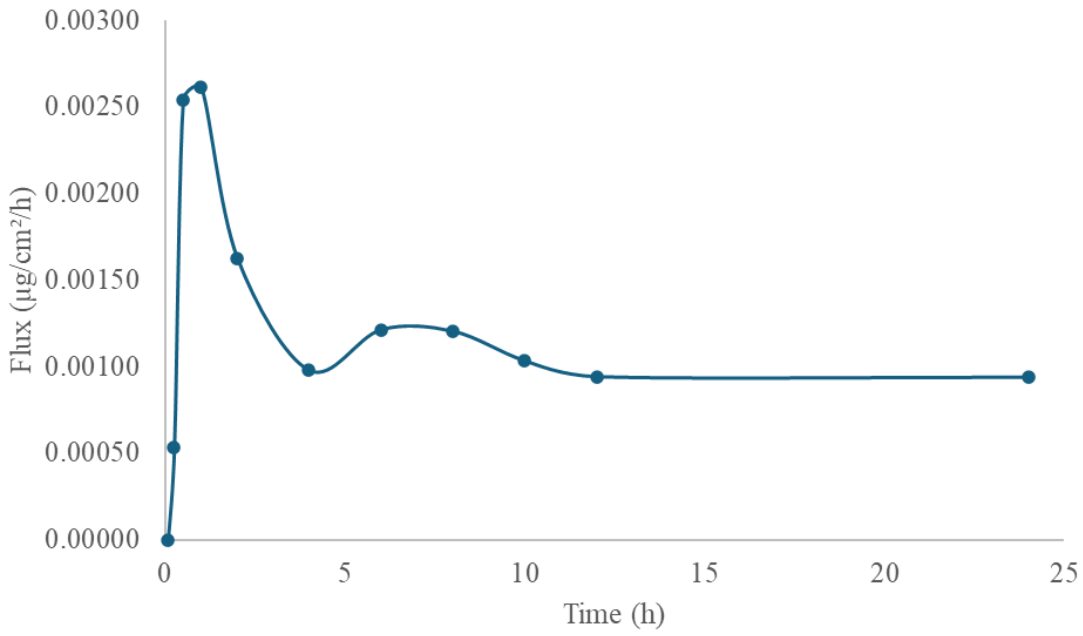

Figure 17.2 Flux change of calcein over 24 h.

When analysing how much calcein was delivered in the first hour it was seen to be 0.00166 µg/ml which represents 8% in the receptor chamber. Although the flux was high in the first hour and the secondary flux peak at 8 hours, the gradual calcein delivered into the receptor chamber at the 24 hour time period was an overall concentration of 0.0125 µg/ml (58.03 %) (Figure 17.3). The dissolution of the MNs takes place from the tip towards the base of the array. As each section dissolves away, the region below will be

exposed to the moisture in the skin membrane and the calcein will slowly begin to diffuse into the receptor chamber.

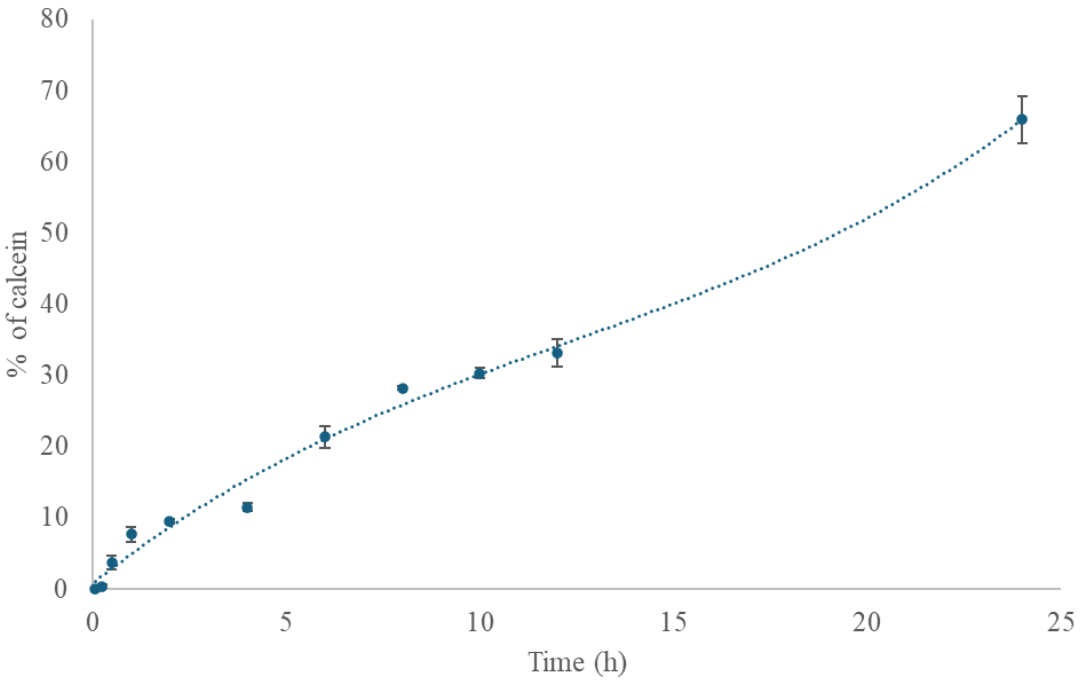

Figure 17.3 Percentage of calcein delivered into the Franz Cell after 24 h.

As not all the calcein had been delivered into the receptor chamber, the next step was to carry out skin homogenisation to determine where the rest of the drug remains as illustrated in Chapter 10. The amount of drug that had not been absorbed totalled to 0.003 µg/ml (14.29%) (Figure 17.4). The non-absorbed drug could have been due to the curing of the tips of the MN, if they haven't fully cured when the base solution is pipetted into the mould it can lead to the solution in the tips mixing with the solution in the base. If the calcein is present in the base structure it means it would take longer to dissolve and diffuse into the skin membrane.

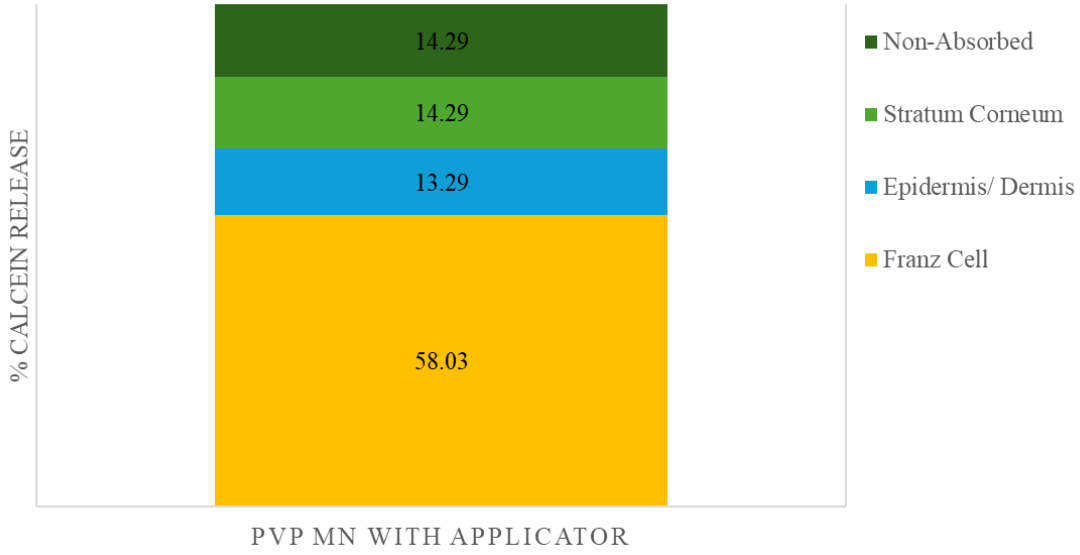

Figure 17.4 Graphical representation of the amount of calcein present in each region of the skin and delivered into the Franz cell after 24 h.

The concentration of calcein present in the SC was 0.003 µg/mL (14.29%). From there, the final region to check is the epidermis/dermis layer which is found through the skin homogenisation. Following skin homogenisation, this revealed that 0.0029 µg/ml (13.29%) was discovered in the epidermis/dermis. Overall drug absorbed into the system from the dissolvable PVP MNs was 0.0186 µg/ml (0.857%).

17.2.2 FITC-Insulin

Similar to delivery of calcein through the PVP MNs, FITC-insulin delivery showed a steady rate over the 24 hour Franz cell. As the polymer MNs are penetrated into the skin, the moisture from the skin membrane causes the MN to dissolve and therefore release the encapsulated FITC-insulin powder with the polymer matrix. Once released, the drug then begins to diffuse through the layers of skin into the receptor chamber of the Franz cell. In the first hour, the flux starts off at a maximum value of 0.00675 µg/cm²/h which then begins to plateau off to 0.0009 µg/cm²/h (Figure 17.5). This is due to the initial contact with the skin leading to the tip of the MNs softening and releasing large proportion of the insulin into the Franz cell system.

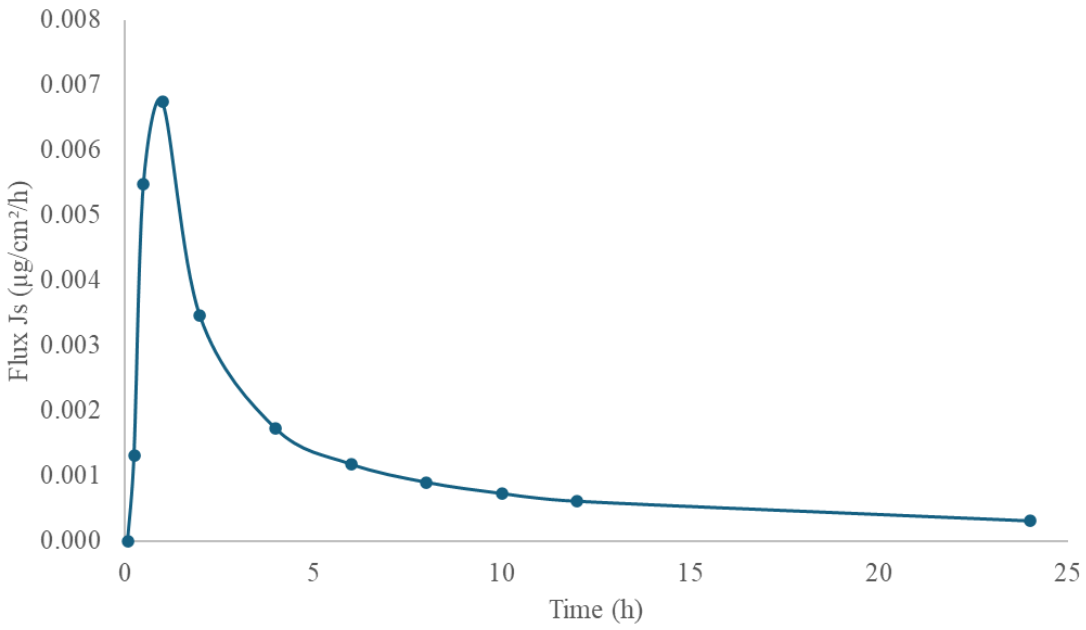

Figure 17.5 Flux change of FITC-insulin over 24 h

Even though the initial flux started off extremely high and the delivery 0.0044 µg/ml, the plateauing off at a substantially lower level meant that the overall concentration of insulin delivered in 24 hours was 0.00466 µg/ml (21.47%) (Figure 17.6).

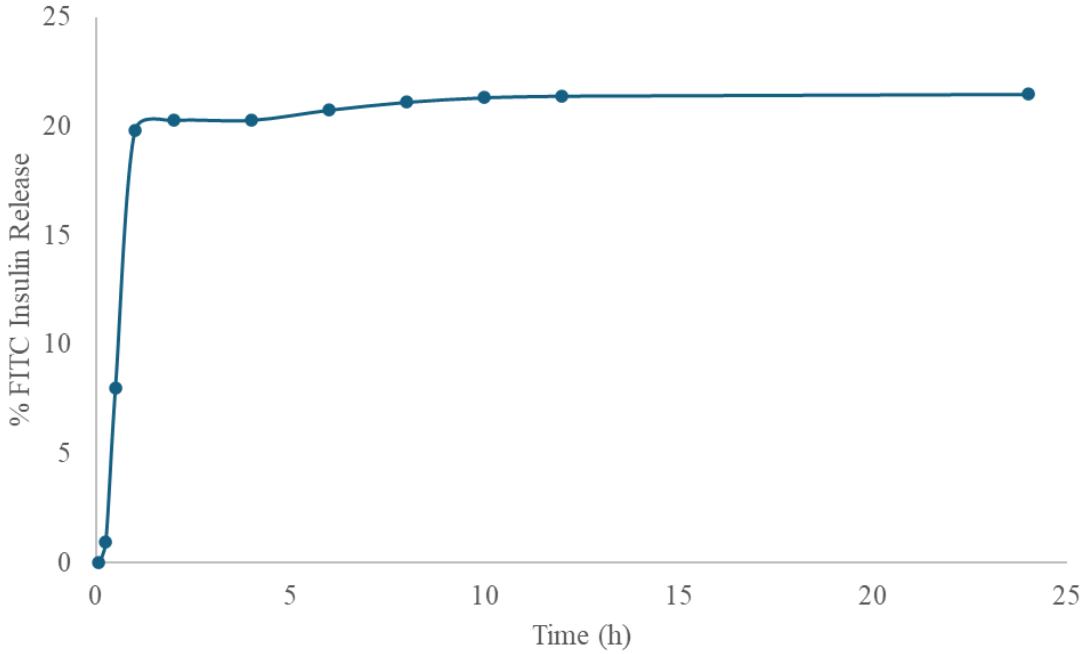

Figure 17.6 Percentage of FITC-Insulin delivered into the Franz Cell after 24 h.

As only a quarter of the insulin encapsulated within the MNA had diffused into the receptor chamber, the next task was to determine where the remainder of the drug remained. Initially, a single tape strip was applied to the surface of the skin membrane to evaluate how much had not been absorbed from the MNA and this was found to be 0.0027 µg/ml (12.68%). The next region that was calculated was the epidermis/ dermis through a further ten tape strips placed consecutively onto the skin membrane, this obtained a volume of 0.0082 µg/ml (37.76%). Finally, the skin membrane is homogenised using collagenase due to insulin being a protein it will be affected by the papain homogenisation. The overall volume extracted from this was 0.0049 µg/ml (22.44%) (Figure 17.7).

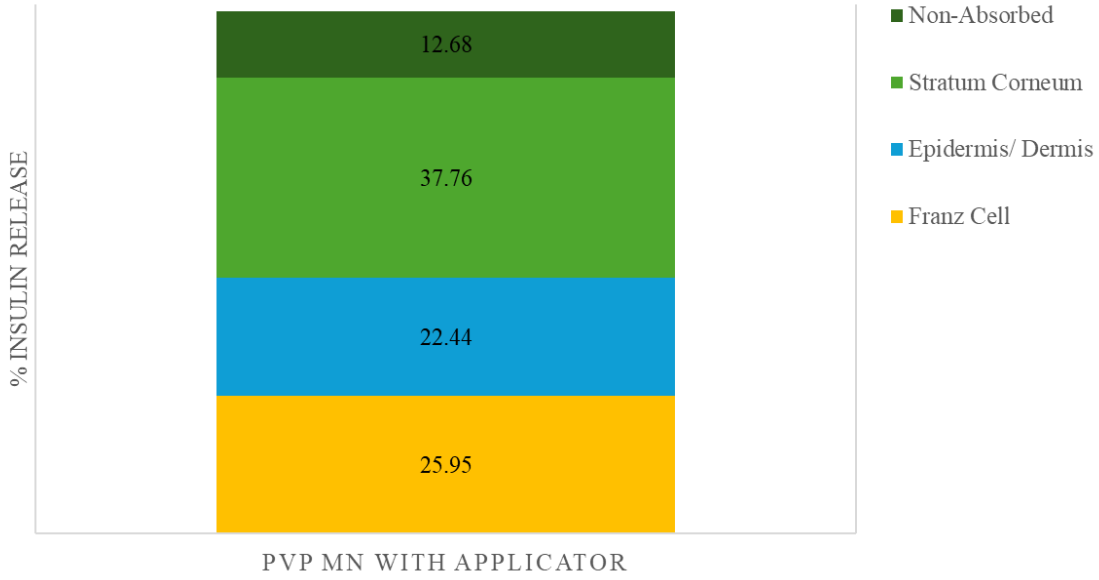

Figure 17.7 Graphical representation of the amount of FITC-Insulin present in each region of the skin and delivered into the Franz cell after 24 h.

Once again, the insulin accumulated within the receptor chamber was significantly lower than calcein. It was found that the majority of the drug was extracted from the epidermis/ dermis and the SC. To overcome the stoppage of movement through the skin membrane, the insulin can be encapsulated within a system such as a nanoparticle as described in section 14.2.3.2.1. After entrapment within this systems, the overall molecule can then be encapsulated within the PVP MN matrix and this can therefore allow the insulin to be diffused through the skin membrane and then upon response to various chemical or physical changes will allow the insulin enclosed to be diffused into the body to maintain the glucose concentration.

17.3 Conclusion

When analysing the drug delivery capabilities of the PVP MNs, it is clear to see that the dissolvability of the array can maintain a constant volume of drug throughout the day. This can therefore mean that drug administration can be reduced and therefore patient compliance will be increased and the cost for administration can be lowered. This is useful for people that suffer throughout the day and have to constantly administer drugs to maintain levels in the body such as pain relief and glucose levels. The maintenance in these concentrations will allow comfort for people and help overcome any side effects that could take place with constant administration and when levels are too low.

Chapter 18

Self-Dissolvable PVP MNs for Controlled Drug Delivery

18.1 Introduction

Controlled drug delivery is effective in providing bolus dosages. Bolus drug delivery is defined as the administration of a single dose over a short period of time and this can be useful in providing on demand drugs such as insulin, anti-inflammatories, or antihistamines when there are high levels of glucose, providing pain relief or relieve symptoms of an allergic reaction. Controlled drug release in the biomedical arena has been employed since 1952 with the first generation of drug delivery focusing on development of oral and transdermal release systems from 1950-1980. Between 1980-2010, the second generations were dedicated to developing zero-order release systems, self-regulated drug delivery systems, long-term depot formulations, and nanotechnology-based delivery systems.

Diffusion controlled drug delivery systems involve entrapment of drugs in an inter water soluble polymeric membrane followed by release. Drug release is governed by Fick's law of diffusion. The equation of the release of drug in the case of controlled delivery is governed as follows (Equation 13):

$$J = -D\frac{\partial \varphi}{\partial x} \tag{13}$$

where J is the energy flux (W/cm^2), D is the diffusivity, φ is the concentration, and x is the position.

For controlled drug delivery, matrix systems are best utilised as the drug is either dissolved or dispersed homogeneously throughout the polymer matrix. The drug is then released when the outer layer is exposed to moisture within the skin or bodily fluids, allowing the drug to diffuse out of the polymer matrix (195).

18.2 Metallisation Optimisation

Metal degradation was utilised to perform on demand-controlled release of drugs. Initially, various biocompatible metals were deposited onto the surface of the MNs at various thicknesses. The deposition of the Pt, Ag, and Au were carried out using PVD as this is a useful tool in providing a uniform coating across a 3D surface. Each MNA is set

onto a chuck and placed into the PVD and the chuck is then programmed to oscillate. The chamber is then pumped down to a pressure of 5.00 E^{-5} before setting the power and Argon gas value for each of the metals as seen in Table 18.1. Each set power and argon will strike a plasma into the system, and this will create a deposition rate for each of the metals. The deposition rate is maintained as low as possible to ensure uniformity on the surface of the MNAs and this is done by varying the power and argon values to ensure the rate is lower than 1. Based on the deposition rate, the samples are exposed to the source for a specific amount of time to achieve the required metal thickness.

Table 18.1 PVD settings for each metal used in coating the PVP MNAs.

Metal	Power (W)	Argon Gas	Deposition Rate (A/s)
Gold	15	60	0.7
Platinum	20	60	0.4
Silver	10	60	0.7

The metallisation deposition range for each metal ranged from 5 nm to 40 nm and these were analysed under SEM to determine the minimal thickness required to provide a uniform coating across the MNA as seen in Figure 18.1. From the SEM, the minimum thickness required for uniformity for each of the metals were 20 nm as there were no clear charge up effects by the non-conductive properties of PVP. Charge up is an undesirable effect where the negative charge of the incident electron beam accumulates on the surface of a non-conductive specimen (196). As the metal is deposited over the surface of the MNA, the conductivity of the coating means that the SEM imaging would no longer have any charge up effects and would lead to a clearer image of the MNAs structure. The images of 5 nm and the 20 nm exhibit distinct differences for each of the metals. As the deposition appears to be uniform at 20 nm the metal thickness was set to this thickness for each array.

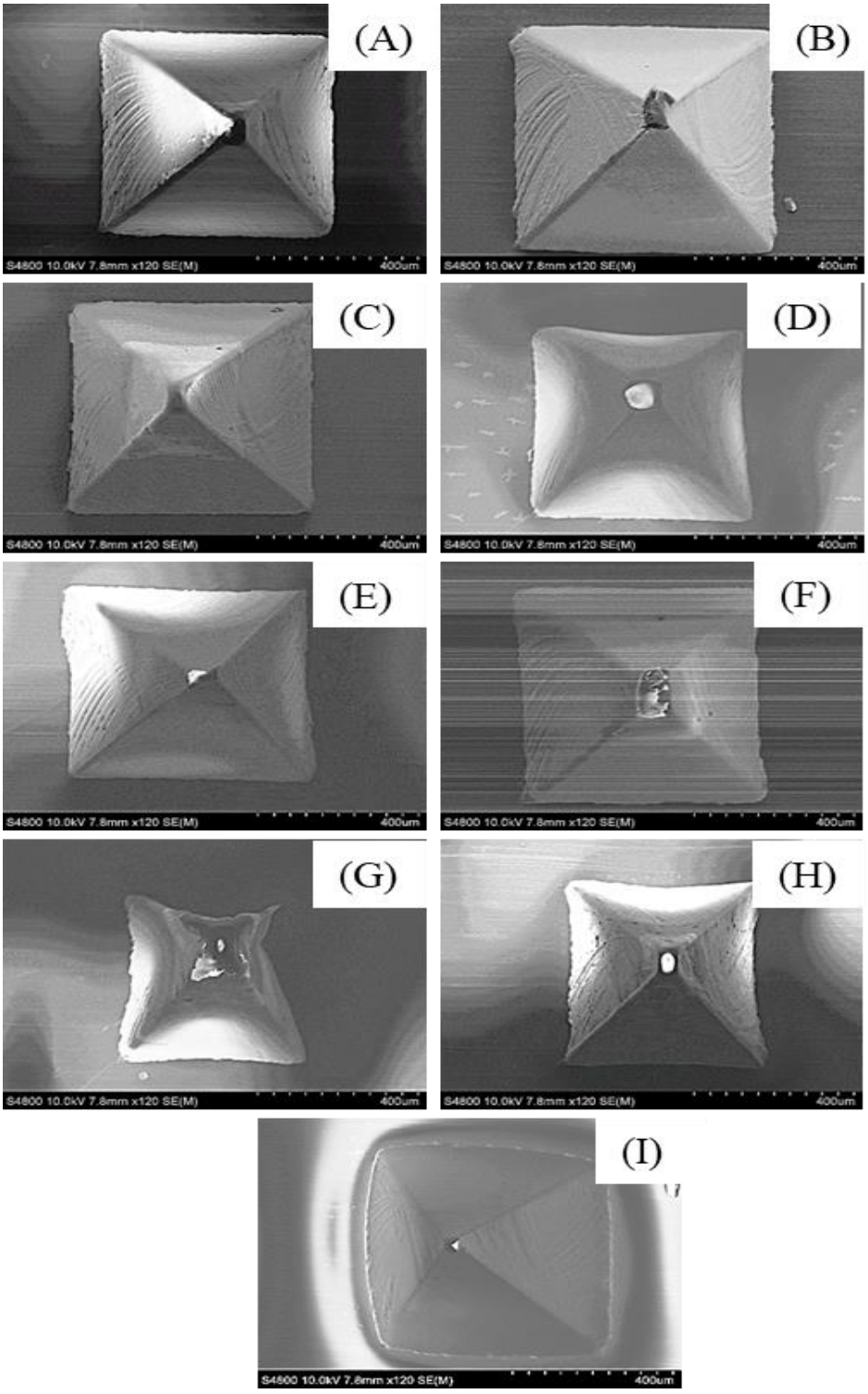

Figure 18.1 SEM images showing various metals and thicknesses to produce a uniform coating across the MN surface: (A) 5 nm Pt; (B) 20 nm Pt; (C) 40 nm Pt; (D) 5 nm Au; (E) 20 nm Au; (F) 40 nm Au; (G) 5 nm Ag; (H) 20 nm Ag; (I) 40 nm Ag.

As the thickness of the metal deposition on the surface of the MNA had been optimised at 20 nm, the next stage was to evaluate their cracking capabilities for controlled drug release. For controlled drug release using a metal coated MNA, 1 V was applied to the surface for 30 s using the set up shown in Figure 18.2. The voltage was set to 1 V as this is seen as the potential for the metal to breakdown and therefore the metal cracking post voltage application can be determined.

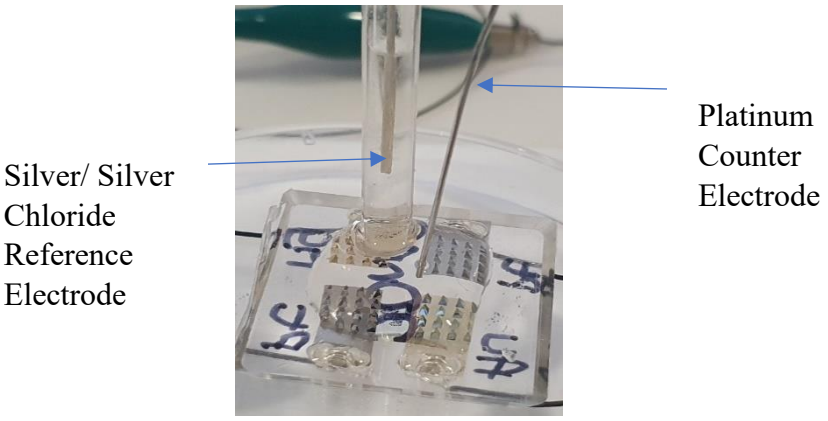

Figure 18.2 External platinum counter electrode and silver/silver chloride reference electrode used to apply 1 V to the MN surface.

Post application of voltage, the MNs are once again examined using an SEM to determine how well each metal has degraded and therefore which metal can be used for controlled drug release (Figure 18.3).

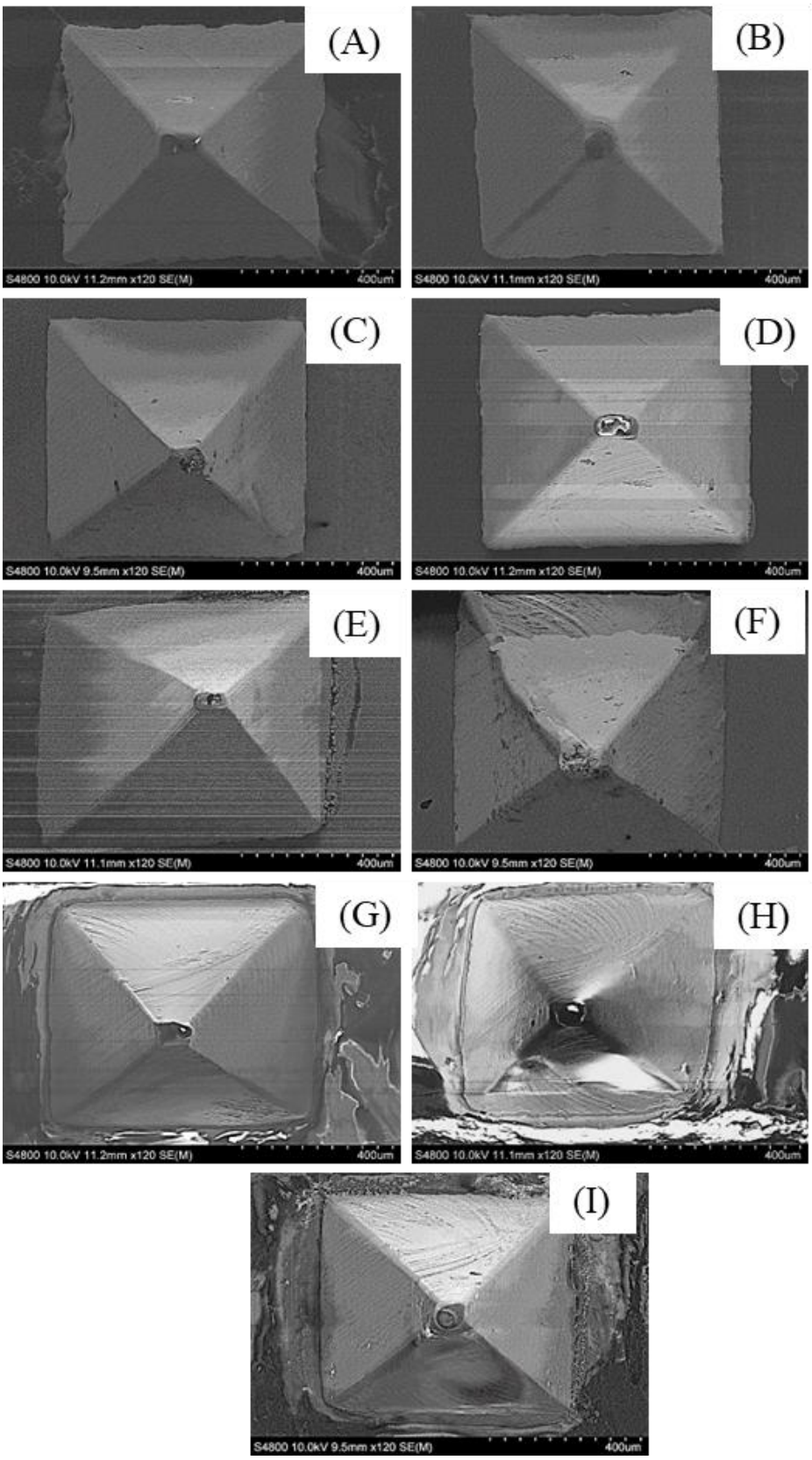

Figure 18.3 SEM images showing various metals and thicknesses coating post voltage application: (A) 5 nm Pt; (B) 20 nm Pt; (C) 40 nm Pt; (D) 5 nm Au; (E) 20 nm Au; (F) 40 nm Au; (G) 5 nm Ag; (H) 20 nm Ag; (I) 40 nm Ag.

Platinum after 30 s of voltage application had not shown any sign of degradation, this may be due to Pt having a breakdown potential greater than 1 V. Gold begins to show slight surface degradation after 30 s of exposure to 1 V but it was not as significant as silver. After 30 s, there is significant breakdown of the silver layer, this may be due to the breakdown potential of silver being 1 V. Silver was therefore used, as the degradation of the metal after voltage application would expose the PVP MNs below. This degradation would consequently lead to the required dissolution for controlled drug release.

18.3 Franz Cell Results

As illustrated in Chapter 10, Franz cells are an essential technique to quantify the drug delivery capabilities of the MNA. The membranes are placed onto the surface of the receptor chamber and firmly secured into place. Each MNA is inserted into the skin sample using the applicator before being connected to a potentiostat in conjunction with a Ag/AgCl reference wire. As seen in section 18.2 metal degradation occurs by applying 1 V for 30 seconds, therefore for the Franz cell the MNA is subject to 1 V for 30 s. The voltage is then switched off and the array is left in the skin for 90 min. A 400 µL aliquot is removed from the receptor chamber at various intervals over the 90 min and the MN is replaced with a new array that is once again subject to 1 V for 30 s. This process is repeated, and the respective drug delivery analysis is carried out.

A standard curve is created for calcein with PVP and silver to determine whether there is any background fluorescence caused from the PVP and silver that can lead to higher concentrations of drug measured (Figure 18.4).

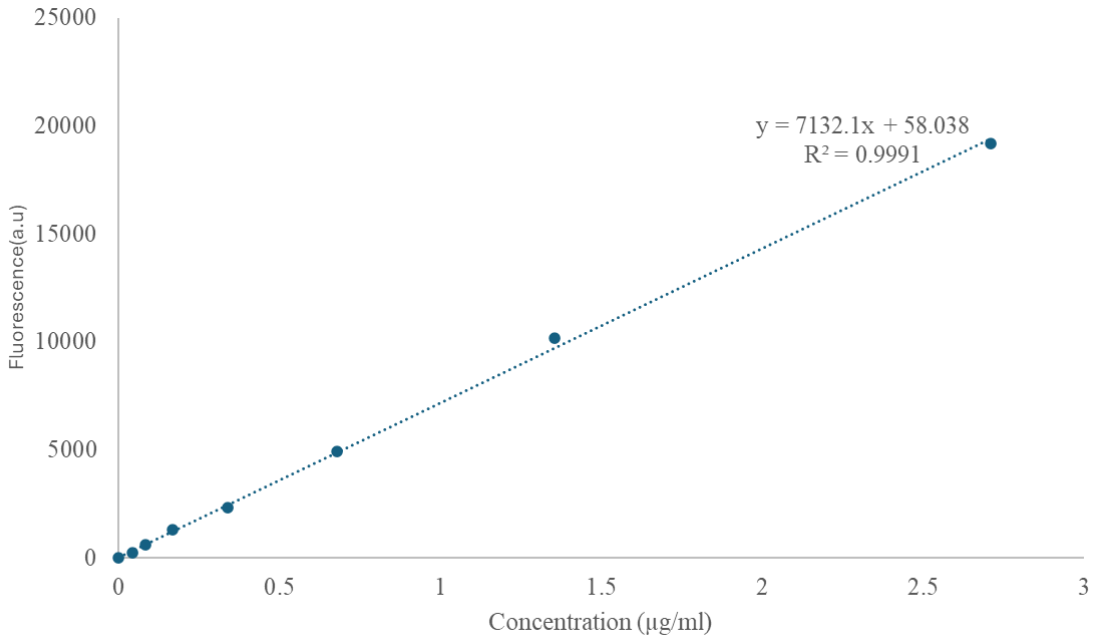

Figure 18.4 Standard curve created for calcein with PVP and silver.

18.3.1 Controlled Release of Calcein

In accordance with Chapter 14.2.3.1, calcein is once again used as a model drug to simulate small molecule drugs (SMD). It can be seen that, there is a high permeation when the voltage is applied to the MNs and the dissolvable polymer beneath the metal comes into contact with the moisture. Once the PVP array is exposed, the calcein encapsulated within the polymer structure is slowly released into the receptor chamber of the Franz cell before plateauing off when the entire volume has been diffused into the system. After each MNA is inserted into the surface of membrane, the concentration of calcein once again increases logarithmically (Figure 18.5).

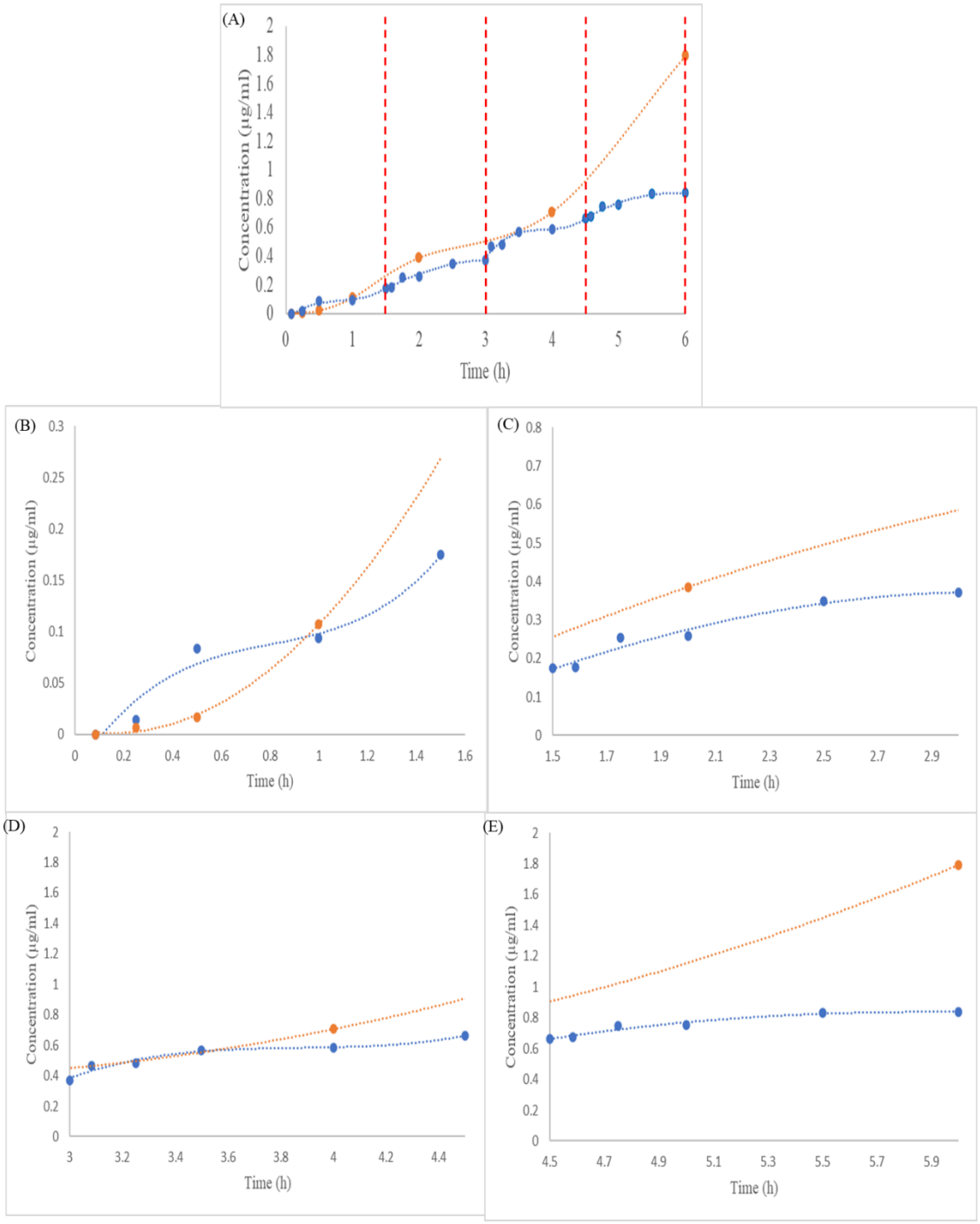

Figure 18.5 (A) Graphical representation of calcein delivered into a Franz cell without metallisation (orange) and 4 metallised MNs changed every 1.5 hours with a voltage applied in the initial 30 seconds; (B) calcein delivered from the first metallised MNA; (C) calcein delivered from the second metallised MNA; (D) calcein delivered from the third metallised MNA; (E) calcein delivered from the fourth metallised MNA.

These results clearly show rapid acting delivery of drug, which can be useful in providing drugs on demand. Comparing with results obtained from the slow release of drug through the MN system, the proportionality was very similar to one another for the first 6 h. The cumulative drug delivered was 0.84 μg/ml for the controlled release compared to 1.79 μg/ml for the slow drug release. Although the value was approximately half it may be due to the lack of time given for the metal coating to degrade and expose the MN below. If the MN isn't exposed, dissolution won't take place releasing the calcein encapsulated within.

As the voltage is applied to the MN, the flux in the system increases to 0.004 μg/cm²/h, which is due to the degradation of the MN. When the 2^{nd}, 3^{rd} and 4^{th} array is applied to the membrane and the voltage is once again applied to the system, the flux clearly shows a further set of logarithmic growth steps. Between the removal of the MNs to the insertion of the next array, followed by the voltage application, the flux shows a sudden burst 0.007 μg/cm²/h. This is indicating the degradation of the metal coating and the further delivery of drug through the membrane into the receptor chamber (Figure 18.6).

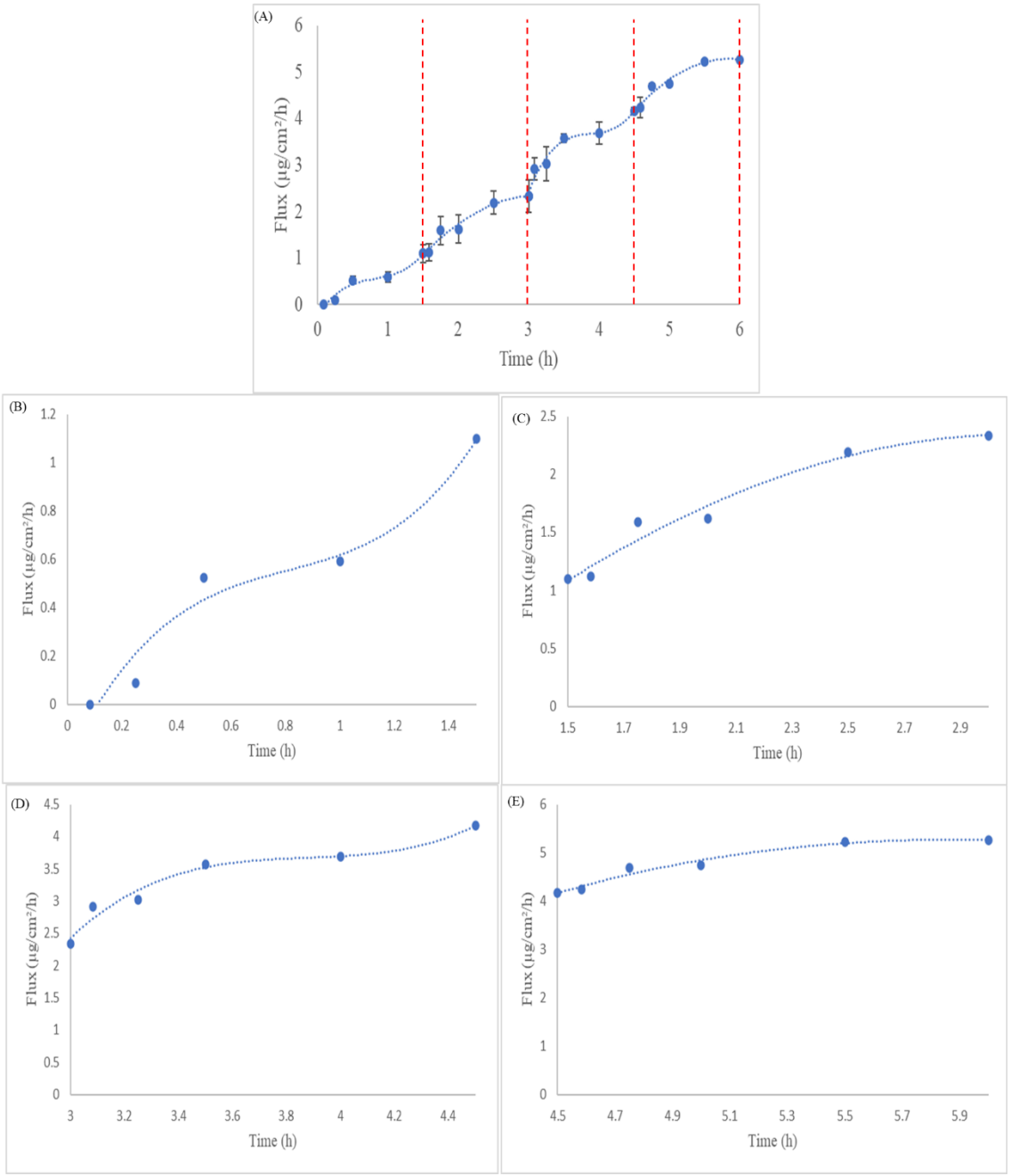

Figure 18.6 (A) Graphical representation of the flux rate for calcein as the 4 metallised MNs are changed every 1.5 hours (B) flux rate for calcein from the first MNA; (C) flux rate for calcein from the second MNA; (D) flux rate for calcein from the third MNA; (E) flux rate for calcein from the fourth MNA.

18.3.2 Controlled Release of FITC-Insulin

Similar to calcein delivery, as the voltage is applied to the MN system, there is high permeation through the skin membrane into the receptor chamber. This is due to the metal degradation once the voltage is applied exposing the polymer MN to the moisture within the skin membrane. Exposure of the MNs moisture leads to dissolution, which releases

the insulin through the skin layers. These begin to plateau off during the 90 min insertion before the MNs are removed and a further array is applied for the concentration of insulin to increase once again. A similar delivery relationship occurs each time a MNA is removed and a new array is applied to the system.

Over the initial 60 minutes, the cumulative drug delivered for controlled drug release was 0.65 µg/ml compared to the 4.47 µg/ml for the slow drug release. This is approximately 85 % greater delivery in the initial 60 minutes from the slow release system (Figure 18.7). When analysing over 6 hours the cumulative drug delivered for both systems vary to result in a percentage difference of 30 % between the slow release system and the controlled release system. This means that the controlled drug release provides the gradual diffusion post insertion of each MNA and the slow drug release provides the high volume of insulin before plateauing off.

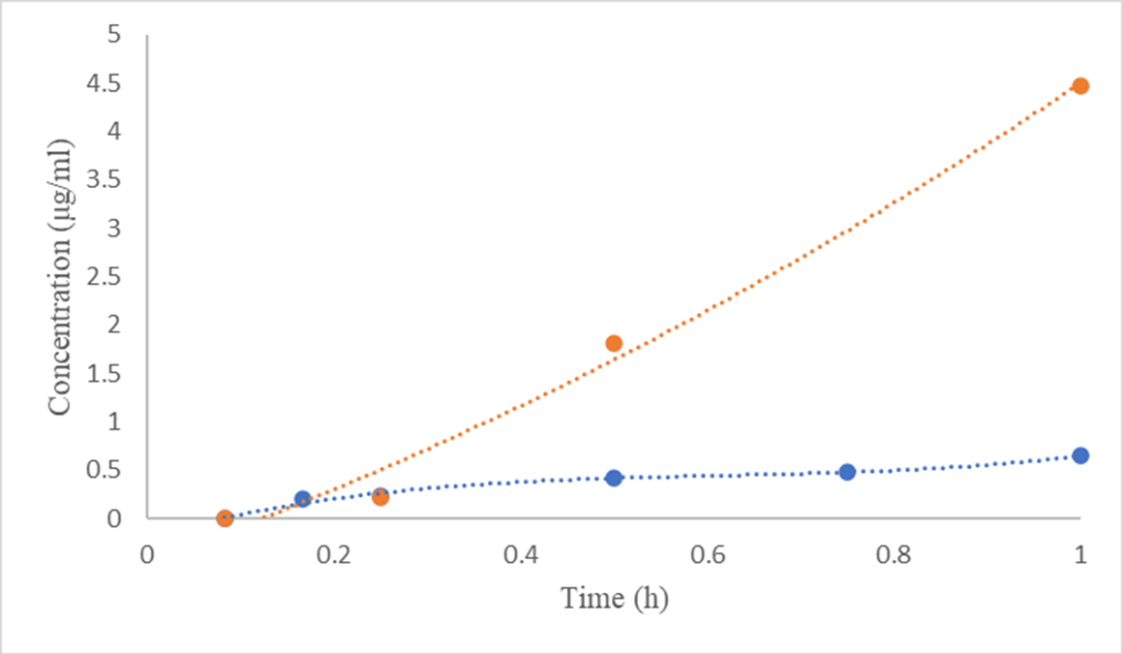

Figure 18.7 Cumulative concentration of FITC-insulin delivered over 60 minutes for controlled drug release (blue line) and slow drug release (orange line).

This experimental set up clearly shows controlled delivery of drug that can therefore provide drug on demand. Relative to the slow release of drug previously described in Chapter 17, the volume of drug delivered is very similar. The cumulative drug delivered over the 6 h for the controlled drug release was 3.28 µg/mL compared to the 4.69 µg/mL for the slow drug release (Figure 18.8). As previously described, the reduction in the amount of drug delivered for the controlled drug release could be due to the lack of time

that was used to allow the metal to degrade and expose the polymer below. Once the MNA has been exposed, the array requires time to come into contact with the skin, dissolve, and release insulin into the system. Therefore, to overcome this, the next stage would be to increase the amount of time the arrays are inserted into the skin and see whether the substantial delivery of insulin increases.

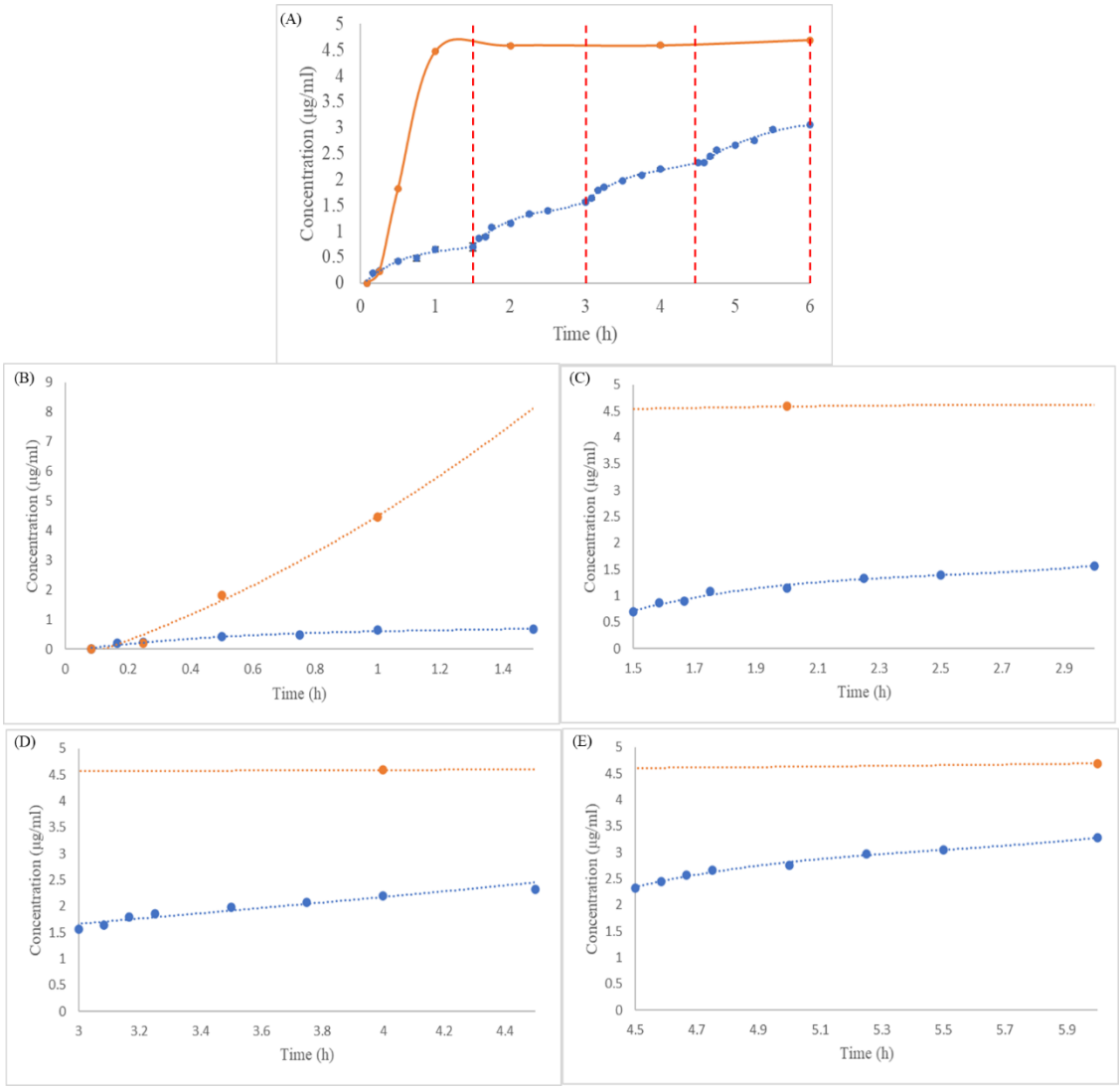

Figure 18.8 (A) Graphical representation of FITC-Insulin delivered into a Franz cell without metallisation (orange) and 4 metallised MNs changed every 1.5 hours with a voltage applied in the initial 30 seconds; (B) FITC-insulin delivered by the first MNA; (C) FITC-insulin delivered by the second MNA; (D) FITC-insulin delivered by the third MNA; (E) FITC-insulin delivered by the fourth MNA.

When analysing the flux within the system, once the MNs are applied to the MNA, it is a sudden increase to 0.03 µg/cm²/h is seen. The sudden increase is due to the degradation of the polymer upon exposure to moisture. As each of the further arrays are applied to the skin surface the flux once again increases at each insertion point. The overall value suddenly increases by 0.002 µg/cm²/h after each array is inserted (Figure 18.9). These once again show the degradation of the metal layer and exposure of the polymer to the skin moisture from each of the MNs.

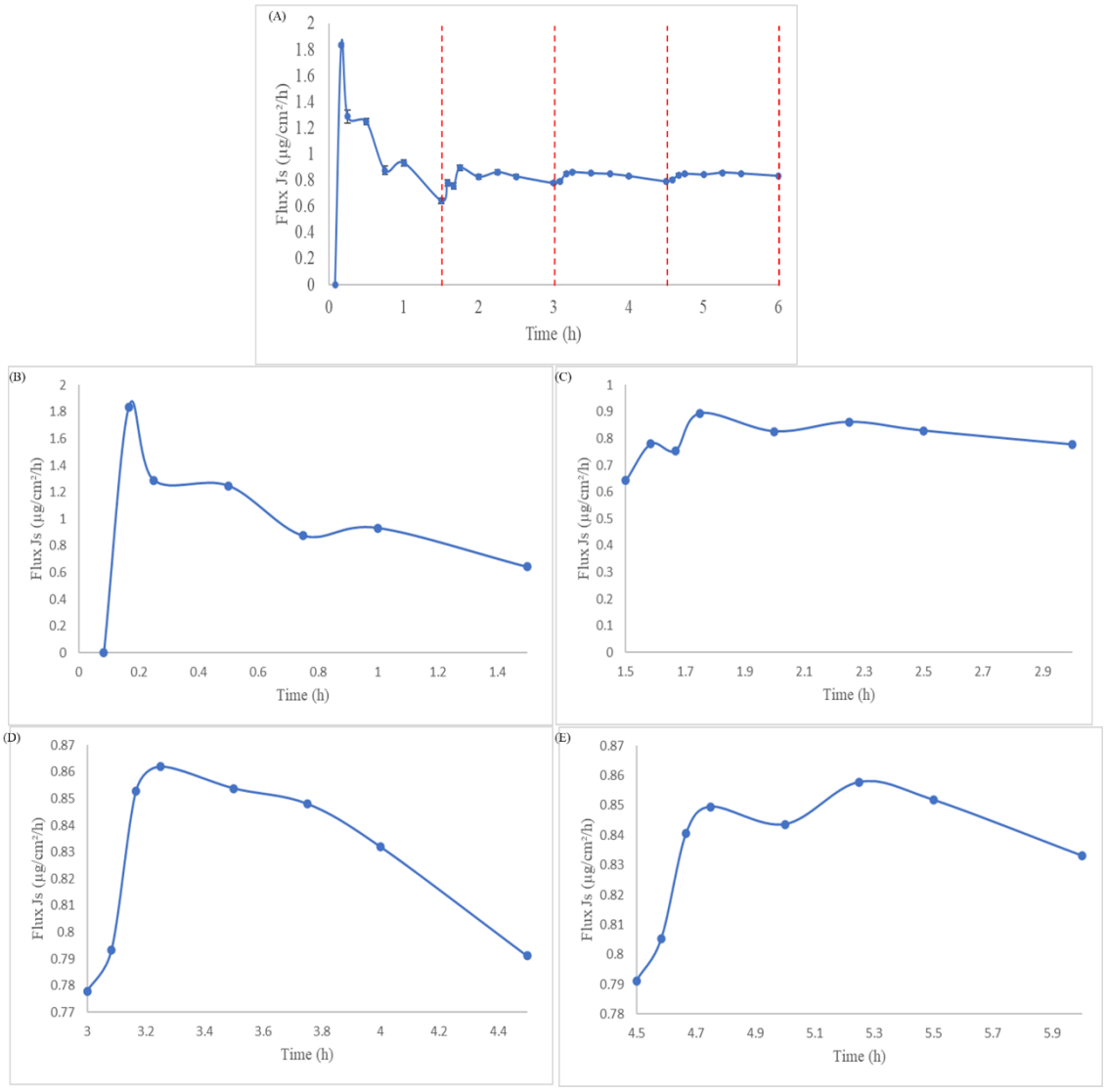

Figure 18.9 (A) Graphical representation of the flux rate for FITC Insulin as the 4 metallised MNs are changed every 1.5 hours; (B) flux rate for FITC insulin from first MNA; (C) flux rate for FITC insulin from the second MNA; (D) flux rate for FITC insulin from the third MNA; (E) flux rate for FITC insulin from the fourth MNA.

18.4 Conclusion

The metallised coating on the surface of the MN can allow for controlled drug release when exposed to a suitable voltage. This can be useful in providing on demand drugs to subjects that require drug delivery. For instance, employing theranostic for MNs to detect glucose and provide insulin on demand in accordance with the concept of artificial pancreas. This will enable patients suffering from diabetes mellitus to monitor their glucose levels and administer insulin to maintain the glucose levels and manage diabetes. It is also showing a new technique using a metallised layer to provide controlled drug delivery that is different to responsive controlled drug release and can be more effective the depending on concentration responsive drug delivery. If the delivery is controlled by concentration levels, it could result in ineffective delivery as the level of analyte of interest needs to reach a certain value before drug is delivered. By using this method, the metal degradation process can be initiated by someone when there is a slight increase in the concentration of the analyte of interest rather than when the concentration reaches a certain concentration in alternative systems. For further understanding of controlled drug delivery, further work would be required to show whether the drug delivered into the system can be targeted and the metal degradation rate can be determined accordingly.

Part 5

Optimisation of Polycarbonate MNs for Diagnostics and Drug Delivery

Chapter 19

Polycarbonate MN Fabrication

19.1 Introduction

In the previous chapter, PVP MNs were fabricated using polycarbonate MNs as its master structure. This means that a device can be produced that utilises polycarbonate MNs for diagnostics and dissolvable PVP MNs for drug delivery applications. Polycarbonate MNs have already demonstrated their ability to diagnose a variety of different biomarkers by modifying the surface with a metal deposition using PVD. The metal deposition can be carried out for gold, silver, or platinum, which uses the same method as the protective coating on the PVP MNs for controlled drug release.

Polycarbonate MNs were produced using an electrical discharge machining technique and is illustrated in Chapter 8, section 8.6. The MN structures created in this format produced a 4 (4 × 4) array (Figure 19.1).

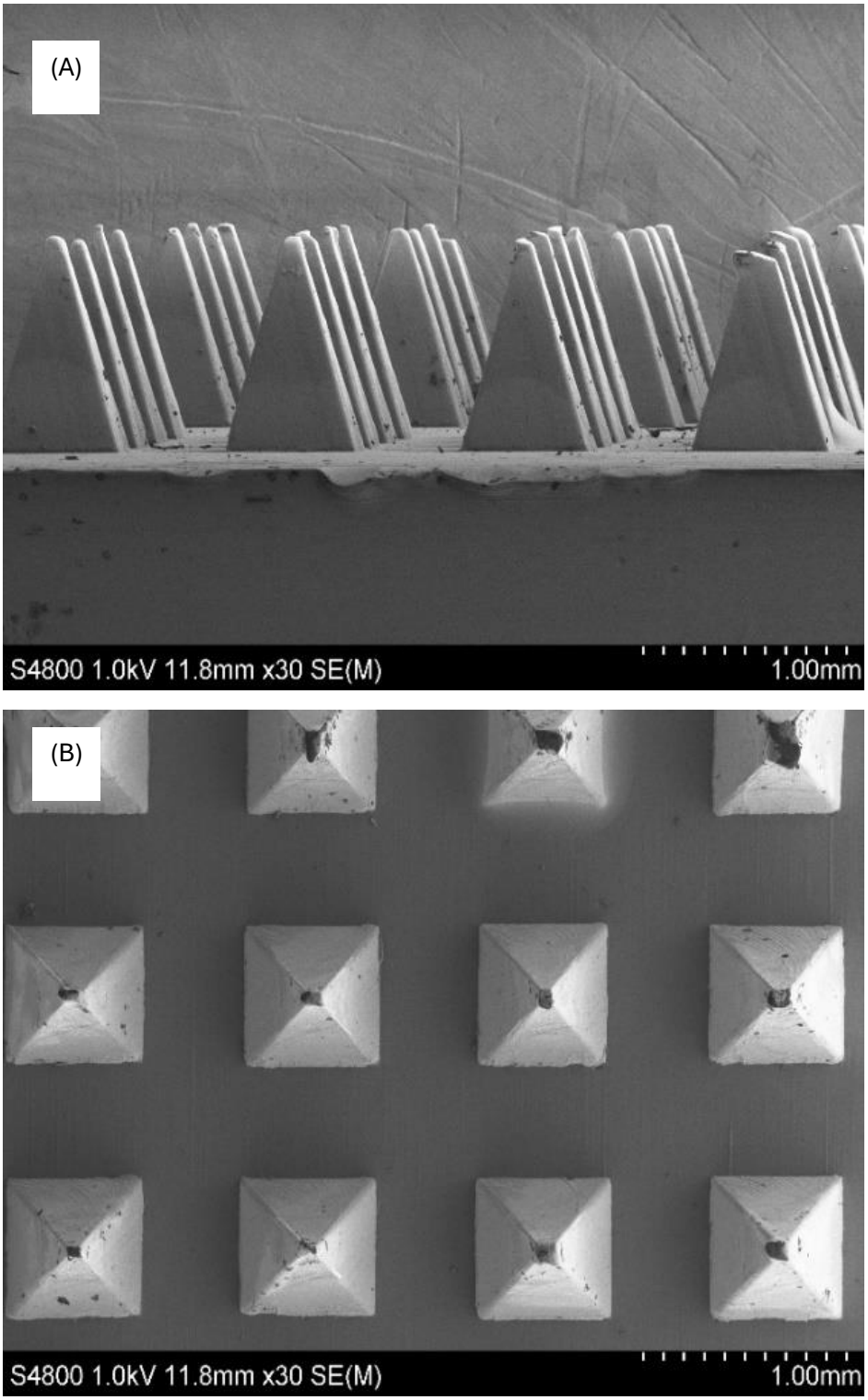

Figure 19.1 SEM images of 4 ×x 4 polycarbonate MNs: (A) Side on view of MNA; (B) Top down view of MNA.

Chapter 20

Polycarbonate MN Characterisation

20.1 Introduction

For diagnostic and drug delivery applications, characterisation for the polycarbonate MNs need to be carried out. This will determine if the MNs break the SC and whether the MNs have the capability to reach the ISF that surrounds viable cells. As the polycarbonate MNs are mechanically stronger than both PVP MNs and silicon MNs, an applicator is used to apply 10 N of force when penetrating the skin to ensure standardised skin insertion.

20.2 Dye Staining

Dye staining protocol has been discussed in Chapter 16.4 for PVP MNs, where 10 N of force is applied to the MNs using an applicator to insert them into porcine skin. The microchannels produced for different applicator forces are seen in Figure 20.1.

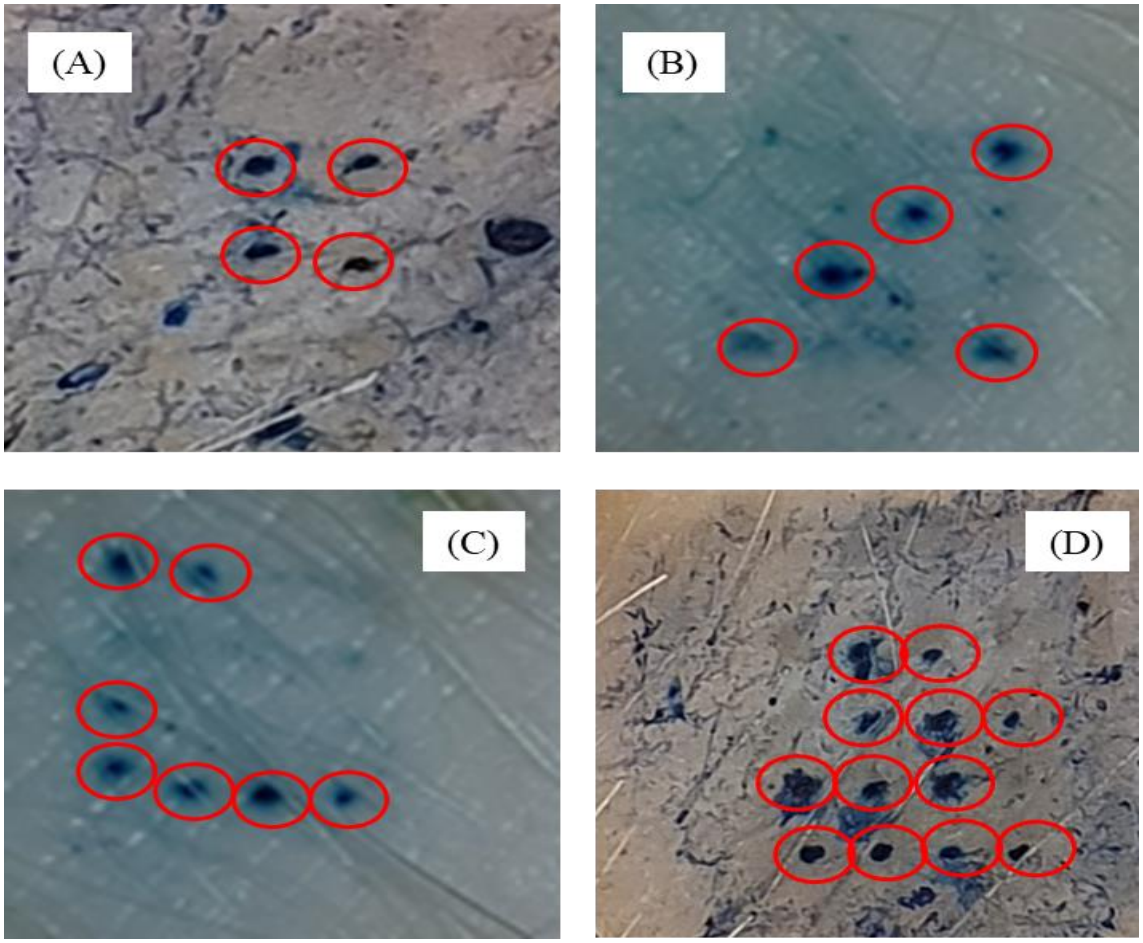

Figure 20.1 Penetration efficiency of PC MNAs with different applicator forces: (A) 4 x 4 MNA penetrated without an applicator with penetration efficiency of 25 ± 0.5 %; (B) 4 x 4 MNA penetrated with an applicator force of 4 N with penetration efficiency of 31.25 ± 0.7 %; (C) 4 x 4 MNA penetrated with an applicator force of 7 N with penetration efficiency of 43.75 ± 0.6 %; (D) 4 x 4 MNA penetrated with an applicator force of 10 N with penetration efficiency of 75 ± 0.9 %.

Using the criteria discussed in Chapter 13, section 13.2, penetration points with deep staining after removal of methylene blue (red circles) showed a penetration efficiency of 75 ± 0.9 % after a 10 N insertion force was applied using the applicator compared to 25 ± 0.5 % without the use of an applicator.

20.3 Histology

As discussed in Chapter 9.3.2, histology was once again utilised to determine whether polycarbonate MNs have broken the SC to reach the ISF between the living cells. The polycarbonate MNs were penetrated into full thickness porcine skin at 10 N insertion force and remain in place while the excess skin is removed. Penetration points produced

post insertion is then analysed under the microscope to determine whether they have the capability to break the SC (Figure 20.2).

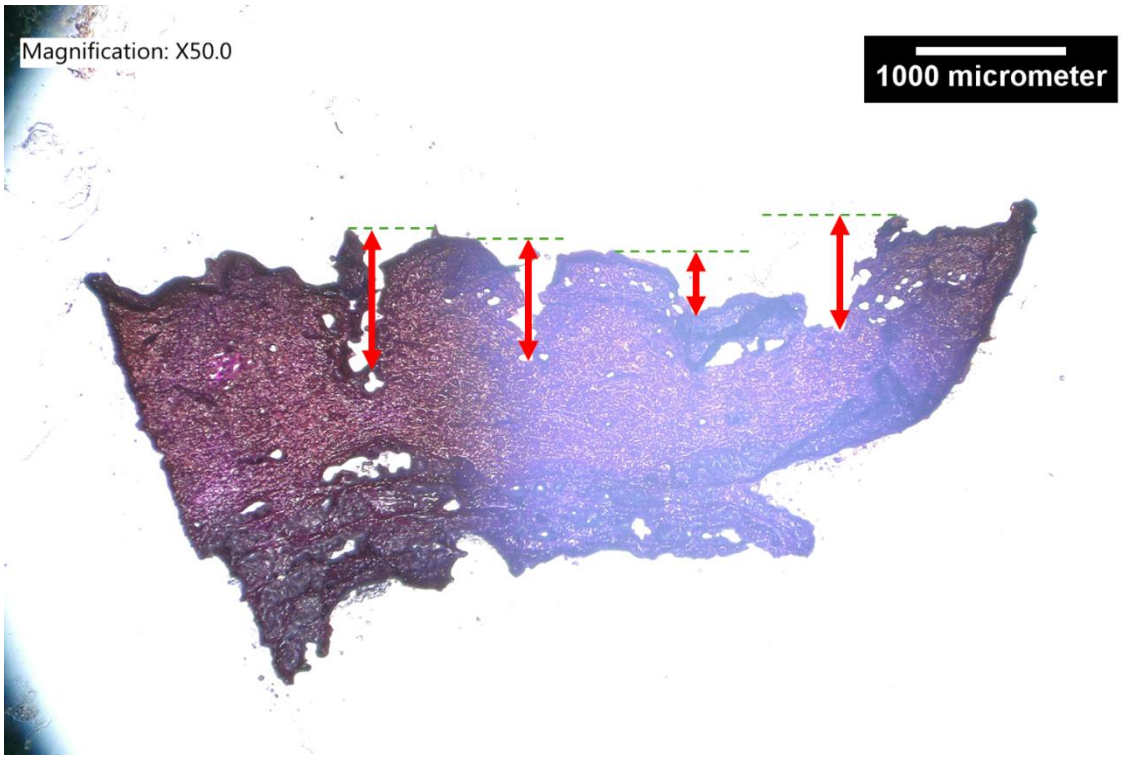

Figure 20.2 Microscope Image showing 4 penetration sites (red arrows) of the PC MNAs into porcine skin with the green line representing the points of measurement.

Polycarbonate MN have evidently penetrated through the SC and there are 4 distinct regions where the skin has been dislodged to a similar shape of the polycarbonate MNs. Compared to the 1000 µm height of the polycarbonate MNs, the insertion points were 892 ± 52 µm (10.8 % lower).

Chapter 21

Polycarbonate MN for Diagnostics

21.1 Introduction

The MNs have the ability to detect biomarkers that are present in the interstitial fluid, as the MN have demonstrated their ability to penetrate the SC and position themselves in the epidermis/dermis layer. Biomarker detection has been most commonly carried out using blood samples, but this is limited by the need for expert training, difficulty in continuous monitoring, and pain associated with drawing blood. For biomarker detection utilising MNs, these can be self-administered using an applicator as seen with commercially available devices and therefore limitations from blood sampling can be overcome. Therefore, the ISF in the skin has been considered as an emerging source for biomarkers that have physiological and medical significance. The ISF surrounds the tissues and cells and acts as a bridge between blood and cells. As ISF is the intermediary link between the circulatory system and cells, it means that the fluid contains rich biological components similar to the blood but also biomarkers unique to the ISF. By modifying the surface of the MNs, continuous monitoring of biomarkers such as glucose or lactic acid can be carried out. Therefore, this chapter describes the application of MNs for continuous glucose monitoring.

21.2 MN Surface Modification

Prior to the enzymatic modification for glucose sensing, the polycarbonate MNs surfaces were metallised to allow surface modification through electrochemistry to be performed. Metallisation of the MNs are carried out using the PVD to deposit a uniform coating of Ti followed by Pt on the surface of the array. Thin layers of Pt do not exhibit adhesive property, which necessitate the use of an adhesive interlayer between the polycarbonate and Pt. Usually, Cr films are used as adhesive films, which becomes ineffective in corrosive environments and high temperatures. In corrosive environments, Cr becomes highly oxidising and has high inter-diffusion rates. To overcome the issues with Cr, Ti films have been utilised as an adhesive interlayer prior to Pt deposition (Figure 21.1).

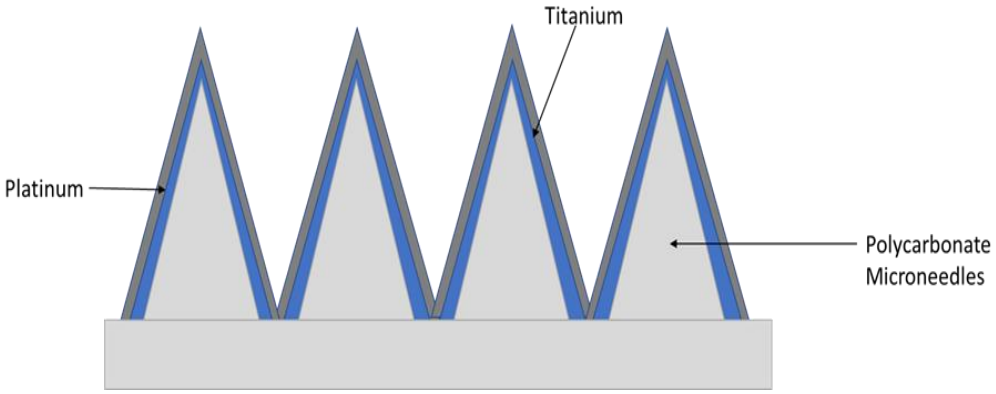

Figure 21.1 Schematic representation of the metallisation onto the surface of the polycarbonate MNs

Using the PVD, 15 nm of Ti is deposited onto the surface of the MNs followed by 150 nm of Pt to ensure that the entire surface of the array is coated without any regions of polycarbonate visible (Table 21.1). Gaps in the metal coating on the surface of the MN, makes it challenging to perform electrochemical measurements.

Table 21.1 Metallisation parameters to create a uniform coating of titanium and platinum across the surface of the MNs.

Metal	Power (W)	Argon	Deposition Rate (A/s)
Titanium	100	60	0.8
Platinum	30	30	2.9

21.3 Cyclic Voltammetry

Post metallisation, 2 holes are drilled at the base of the MNs holes as far from the MN structures as possible. Between the pair of holes, silver conductive paint is coated to provide extra connectivity. Wires measuring at 15 cm long are stripped at either end of their insulating layer and the exposed metal are intertwined through the holes. A resin is then used to cover the exposed metal to protect them from the solutions drop casted onto the surface during the enzymatic modification (Figure 21.2).

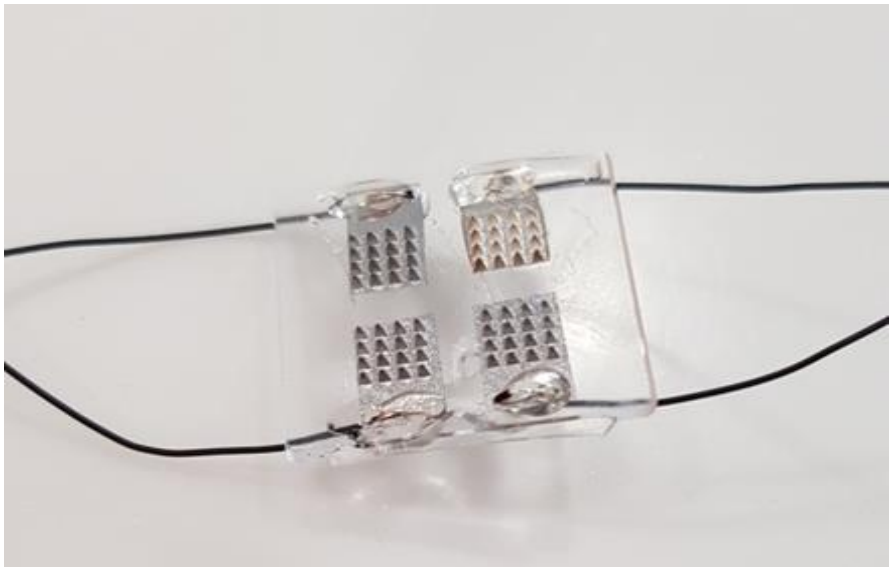

Figure 21.2 Image showing the MN post metallisation and wire bonding ready for electrochemical modification.

As discussed in Chapter 11.2, to assess the electrode surface post wire bonding, cyclic voltammetry using FCA carried out. 200 µL of 5 mM FCA is drop casted onto the surface of the MNA. Once a stable droplet is created, 0.7 V is applied for 120 s and the current is measured (Figure 21.3).

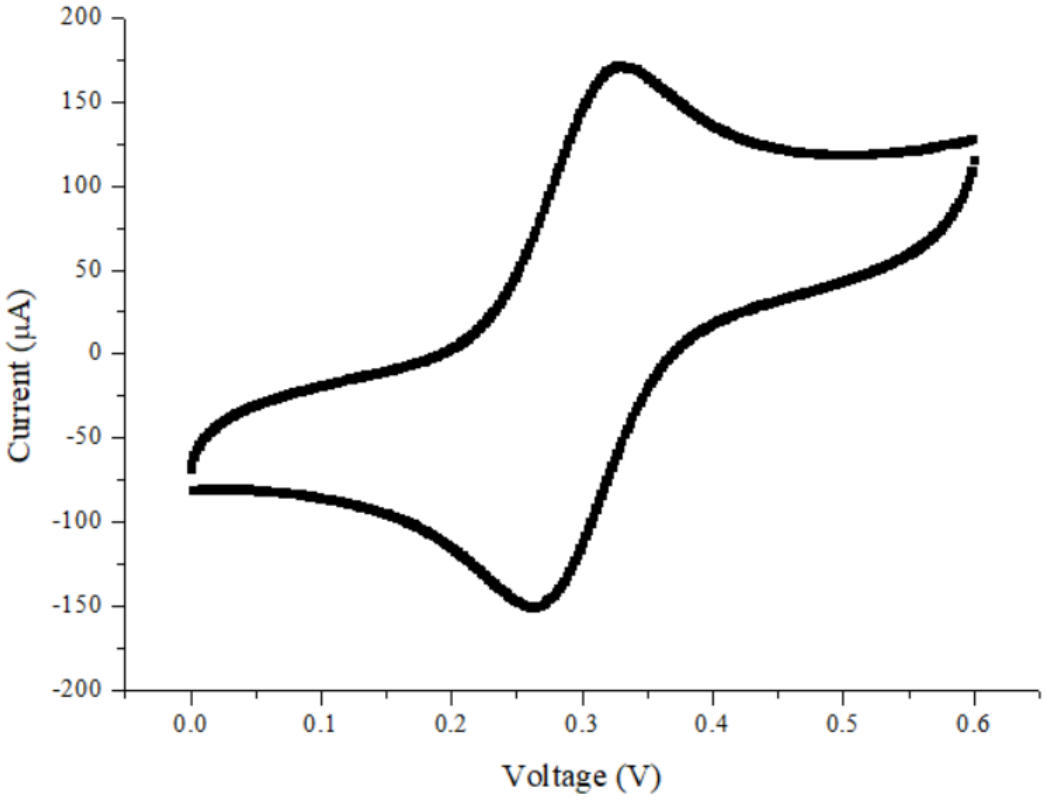

Figure 21.3 Graphical representation of cyclic voltammetry of ferrocene carboxylic acid

An oxidation peak is measured at 0.33 V and a reduction peak is measured at 0.28 V.

21.4 Electropolymerisation

To functionalise the surface of the MNs for glucose sensing, phenol electropolymerisation methods are utilised. Phenol electropolymerisation can be used to modify metal surfaces such as Fe, Au, Pt, and carbon-based electrodes such as glassy carbon and graphite electrodes. The phenol forms a phenoxyl radical during electropolymerisation, which can be oxidised to quinone or an addition reaction in o- and p- positions with the formation of oligomers and polymers. Consequently, a poly(phenylene oxide) film is formed on the surface encapsulating the GOx within the structure (Figure 21.4)(184).

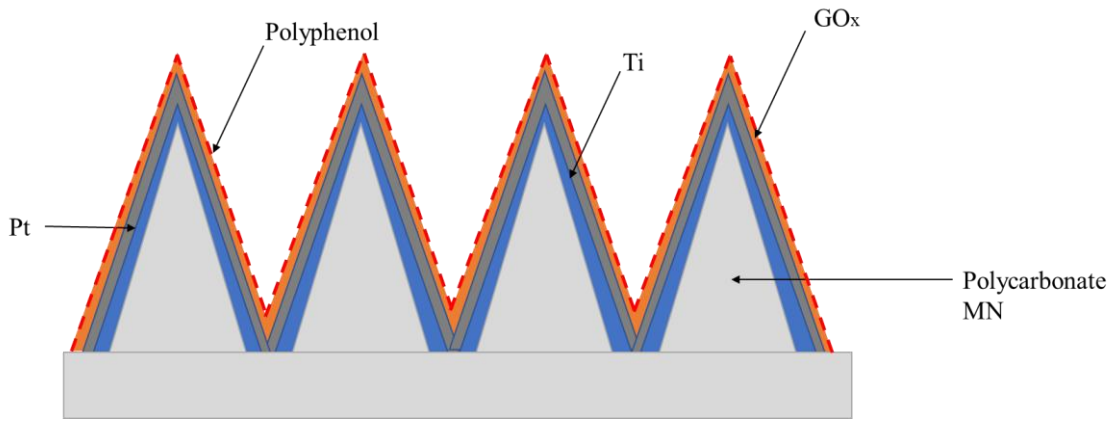

Figure 21.4 Schematic representation of the electropolymerised phenol encapsulating the glucose oxidase.

For the electropolymerisation of the phenol, 50 mM of phenol solution and 10 mg/mL GOx was drop casted onto the surface of the MNs. A cycle comprising of stabilisation at 0 V for 20 s followed by polarising the potential to 0.9 V for 15 min was repeated 6 times (Figure 21.5). This allowed a substantial polyphenol film to form on the surface of the MNs as well as desired GOx loading.

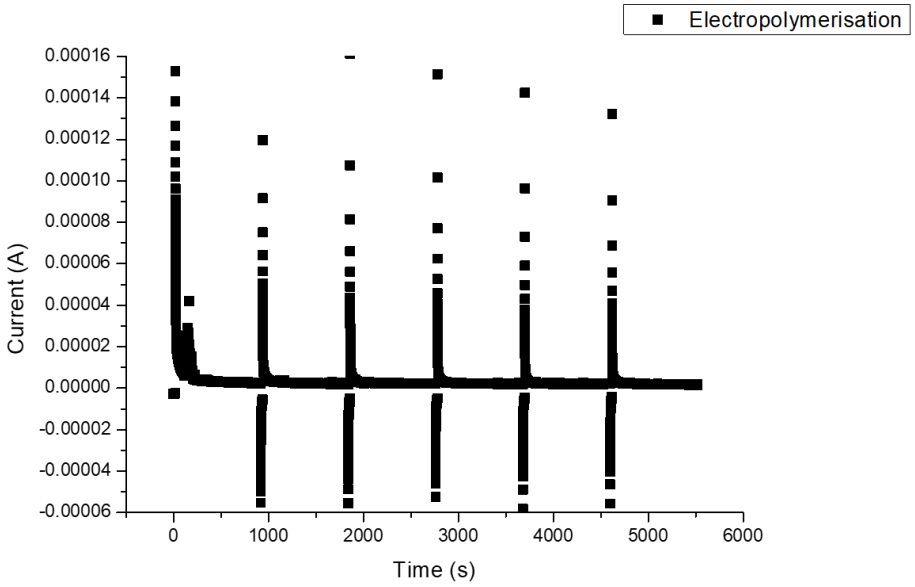

Figure 21.5 Graphical representation of the electropolymerisation process for phenol to encapsulate glucose oxidase.

21.5 Glucose Dose Response

For enzyme kinetics the Michaelis-Menten model is one of the best-known approaches and takes the form of an equation that relates the reaction current to the substrate concentration where a substrate binds to an enzyme. In this case, the substrate is glucose and the enzyme is GOx. The binding between the enzyme and the substrate forms an enzyme complex, which will then react irreversibly to generate a product P and to regenerate the enzyme (197).

The Michaelis-Menten equation is given by (Equation 14):

$$I = I_{max}[S]K_m + [S] \quad (14)$$

where I is the current, S is the glucose concentration and K_m is Michaelis-Menten constant and is the concentration, at which the reaction current is half of the I_{max}.

Aliquots with varying glucose concentrations from 0 to 40 mM were prepared in 100 mM of PBS solution. Each aliquot was drop casted onto the surface of MNs and these are polarised at 0.7 V for 60 s as this provided the current response changes due to the interaction between GO_x and glucose concentration. The steady state current was measured at 60 s as these were interpreted as a function of the correlating glucose concentration.

Each glucose concentration and its corresponding current were plotted against one another to determine the I_{max} and K_{max} from the Michaelis-Menten fitting (Figure 21.6).

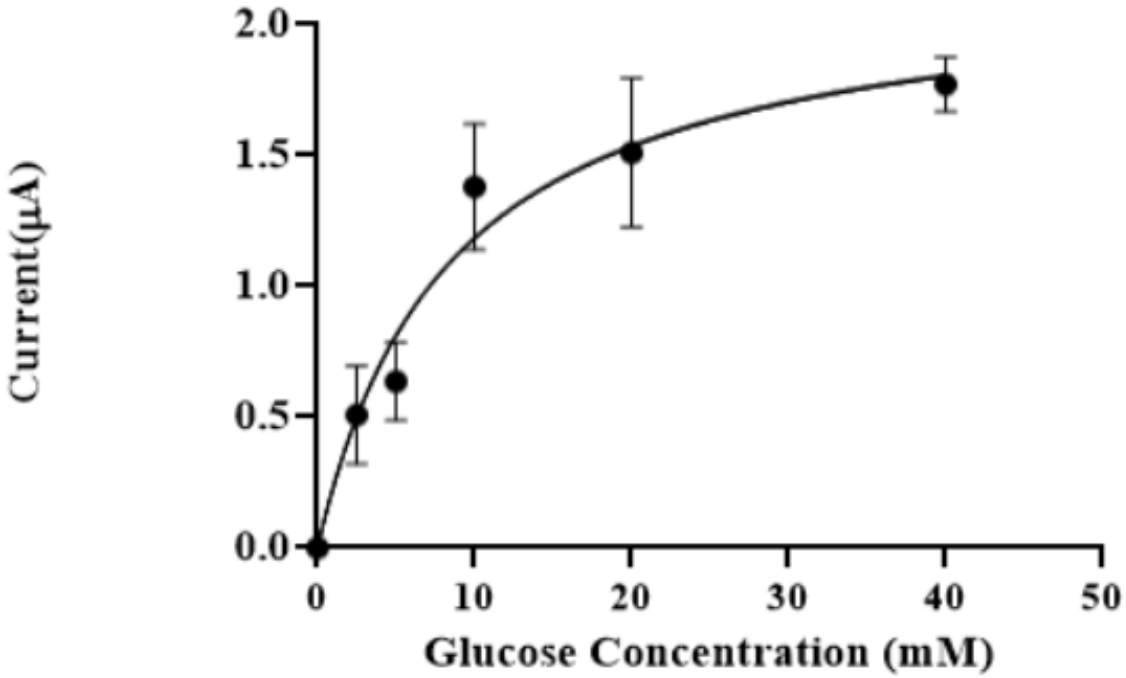

Figure 21.6 Graphical representation of the dose response curve for various glucose concentrations with a Michaelis Menten fit for wire bonded MNs.

From a total of 4 working electrodes the average Michaelis-Menten constant value was determined to be 8.46 mM. Variations in the K_m value could be attributed to the amount of GOx that is loaded within each working electrode during the electropolymerisation as well as the potential drop caused by the distance between the WE and the RE.

21.6 Diagnostics Challenges in Polycarbonate MNs

During the polycarbonate surface modifications to enable glucose sensing, challenges arose during the wire bonding process. The concerns with wire bonding is as follows:

- Inadequate resin application over the wire can interfere with the connectivity.
- Looping the wire through the drilled holes and coating affects the insertion.

These challenges may interfere with *in-vivo* diagnostic applications which need to be addressed in the subsequent section.

21.6.1 Surface Modification Optimisation

To address the wire bonding concerns explained in the earlier section, a new sensor platform was created using a Voltera V-One. The Voltera V-One contains an aligned printing function, which allows alignment and dispensing of conductor 2 ink (silver conductive ink) onto a substrate. Prior to dispensing conductive ink, a sensor platform design was created on AutoDesk Eagle for a 4 × 4 MNA and for a 4(4 x 4) (Figure 21.7).

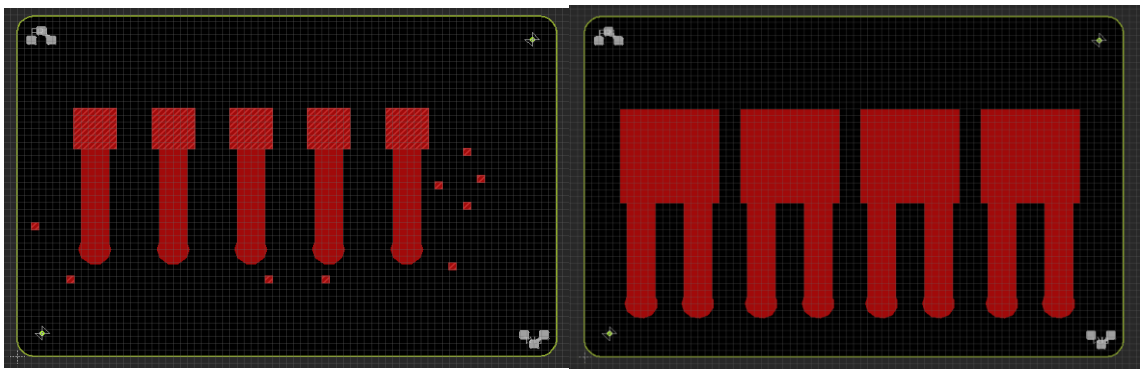

Figure 21.7 Sensor platform design created on Autodesk Eagle for 4 x 4 MNA and 4(4 x 4) MNA.

21.6.2 Conductive Ink Dispensing

Once the sensor platform was designed for the various polycarbonate set-ups, the next stage was to optimise the conductive ink dispensing to optimise the required line thickness for precise printing. To determine the required thickness a design was created on AutoDesk Eagle where the Z-value ranged from 0.2 to 1.4 (Figure 21.8). The Z-value is the pressure button, which is used to adjust the ink flow and can therefore be used to control the thickness of the line.

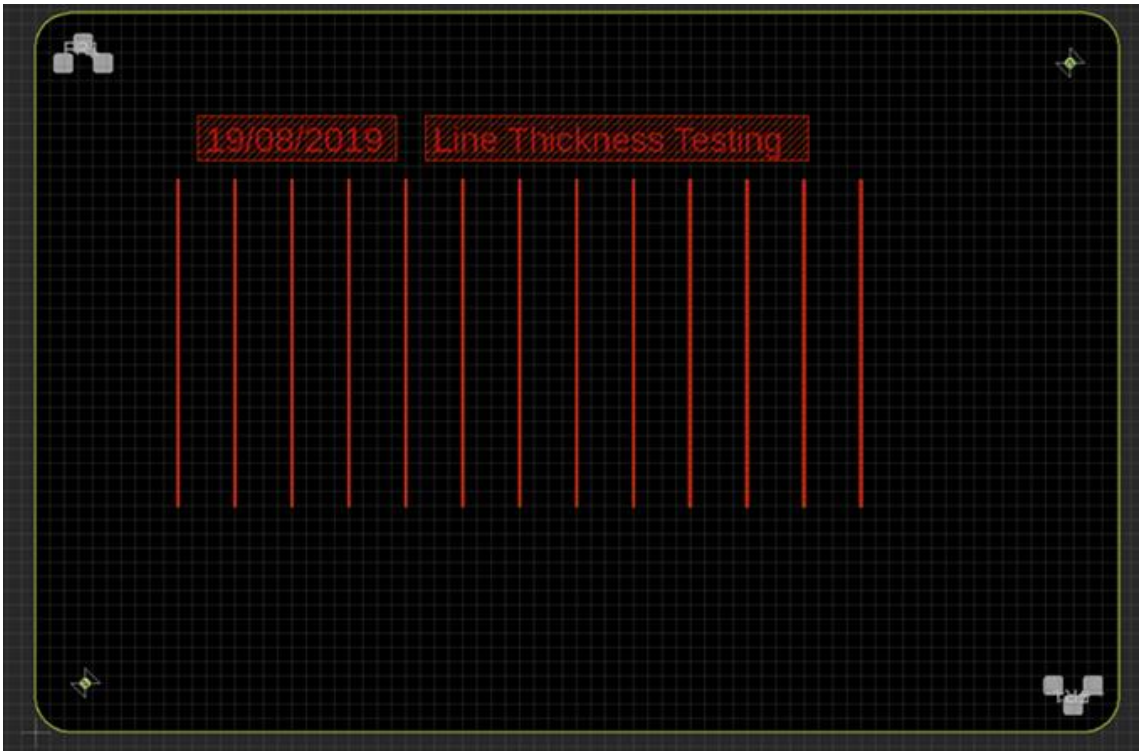

Figure 21.8 Autodesk design created to determine the optimised line thickness with various Z-values.

After optimisation it was found that after a Z value of 0.4 the thickness of the lines had minimal variation and the calibration pattern was also at the correct resolution for the print (Figure 21.9).

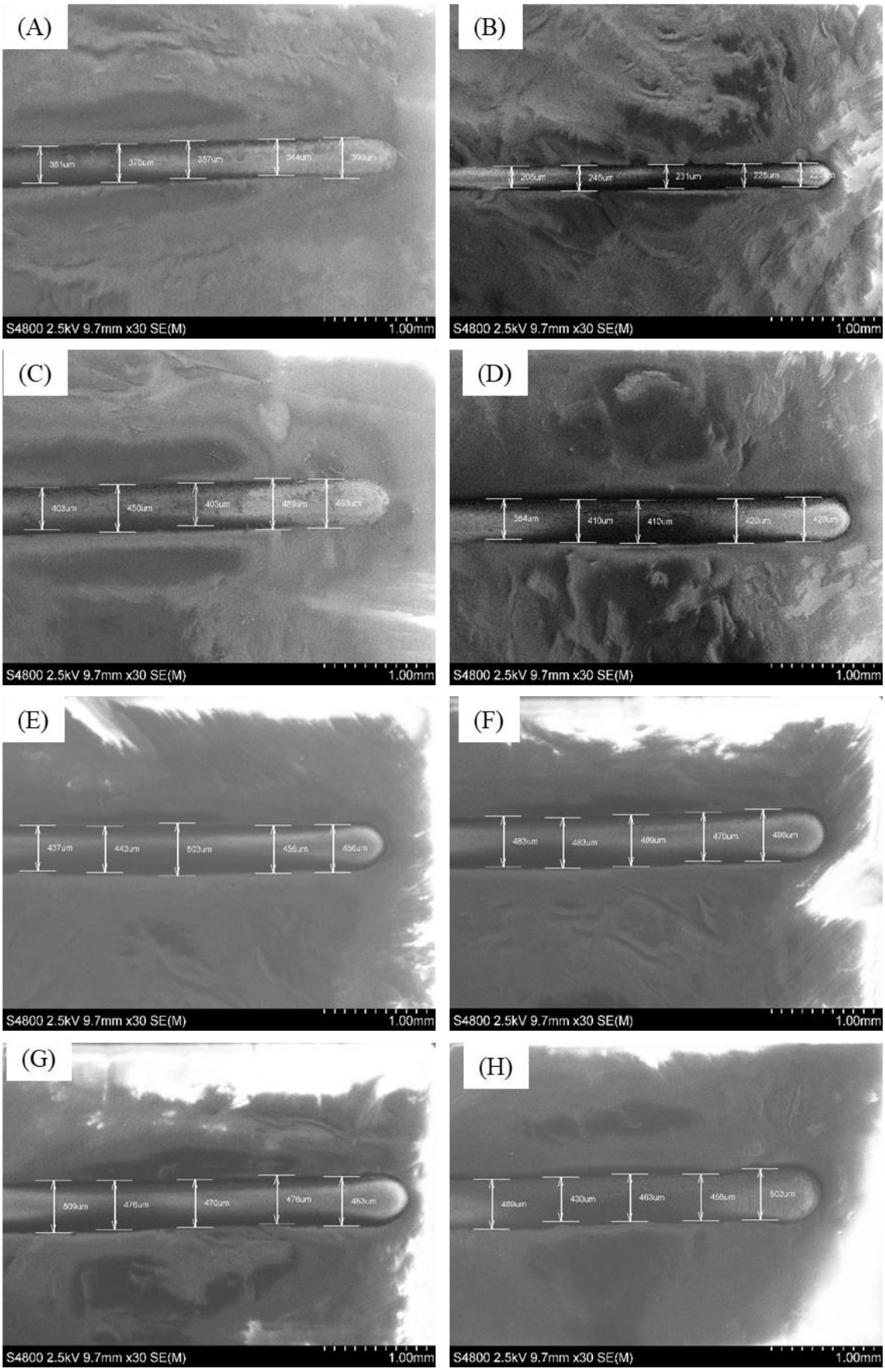
(A)
351um
370um
357um
344um
390um
S4800 2.5kV 9.7mm x30 SE(M)
1.00mm
(B)
205um
245um
231um
225um
S4800 2.5kV 9.7mm x30 SE(M)
1.00mm
(C)
403um
450um
403um
489um
483um
S4800 2.5kV 9.7mm x30 SE(M)
1.00mm
(D)
384um
410um
410um
423um
423um
S4800 2.5kV 9.7mm x30 SE(M)
1.00mm
(E)
437um
443um
503um
456um
456um
S4800 2.5kV 9.7mm x30 SE(M)
1.00mm
(F)
483um
483um
489um
470um
496um
S4800 2.5kV 9.7mm x30 SE(M)
1.00mm
(G)
509um
476um
470um
476um
483um
S4800 2.5kV 9.7mm x30 SE(M)
1.00mm
(H)
489um
430um
463um
456um
503um
S4800 2.5kV 9.7mm x30 SE(M)
1.00mm

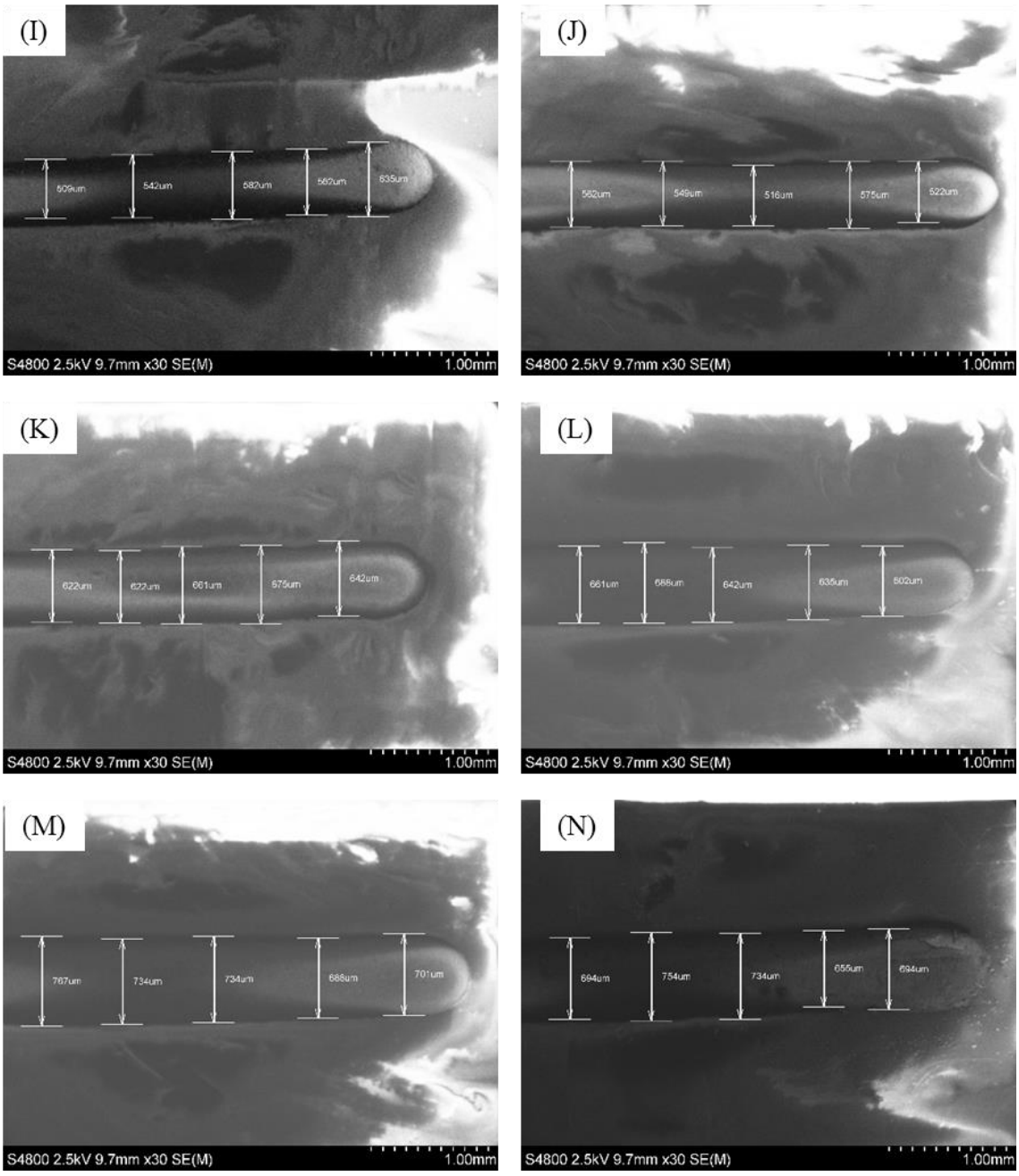

Figure 21.9 SEM images of line thickness variation between 2 identical printed lines: (A) line 1 with Z-value of 0.2; (B) line 2 with Z-value of 0.2; (C) line 1 with Z-value of 0.4; (D) line 2 with Z-value of 0.4; (E) line 1 with Z-value of 0.6; (F) line 2 with Z-value of 0.6; (G) line 1 with Z-value of 0.8; (H) line 2 with Z-value of 0.8; (I) line 1 with Z-value of 1.0; (J) line 2 with Z-value of 1.0; (K) line 1 with Z-value of 1.2; (L) line 2 with Z-value of 1.2; (M) line 1 with Z-value of 1.4; (N) line 2 with Z-value of 1.4.

21.6.3 Sensor Platform Printing

Once the design was loaded onto the Voltera V-One software, the board is clamped into the machine and the machine is set up to print in a certain region of the board. The region was set to an area close to the edge of the board to allow ease for the crocodile clips to clamp the board for diagnostic applications. As the region is set, the Voltera V-One then probes the surface of the board to generate height mapping of the boards surface. By carrying out height mapping, it allows good quality and reproducible printing. The design is then printed onto the surface of the board followed by applying the drilled polycarbonate MNs before baking the surface to dry the conductive ink. To ensure the connection of the array with the printed substrate, the drilled regions through the MNs are filled with silver conductive pain (Figure 21.10).

Figure 21.10 The MN set up to connect the arrays with the potentiostat with an external platinum and silver electrode.

21.6.3.1 Cyclic Voltammetry

As discussed in Chapter 11.2, CV using FCA is performed to determine the connectivity of the polycarbonate MNs post-adhesion to the substrate (Figure 21.11).

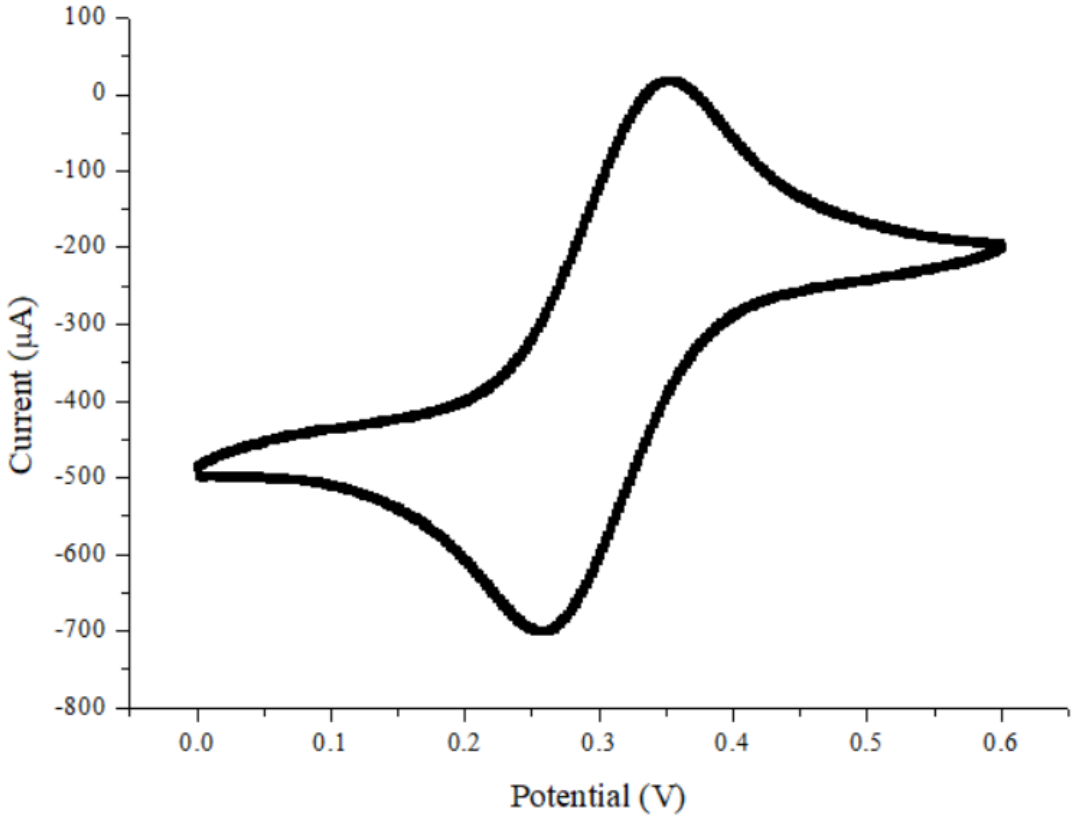

Figure 21.11 Graphical representation of CV of FCA.

21.6.3.2 Glucose Dose Response

In Chapter 11.4, electropolymerisation of the MN surface is utilised to encapsulate GOx with a polyphenol matrix. Post encapsulation, various glucose concentrations ranging from 0 to 40 mM are drop casted onto the surface of the MNs and CA is performed to determine the Michaelis-Menten constant (Figure 21.12).

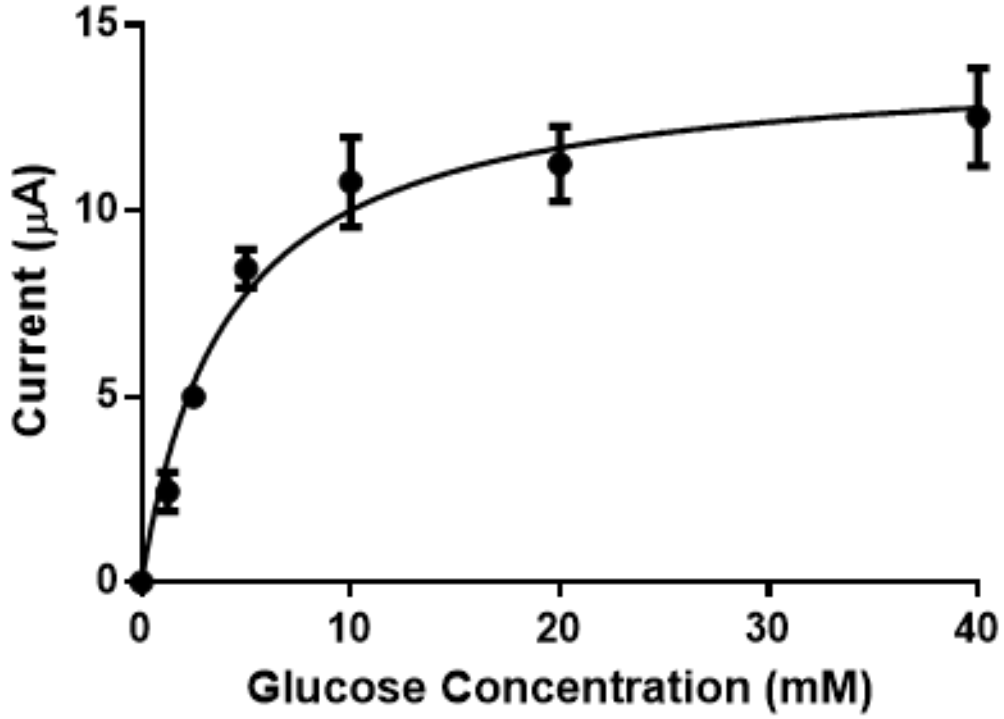

Figure 21.12 Graphical representation of the dose response curve for various glucose concentrations with a Michaelis Menten fit for MNs on a sensor platform.

The Michaelis Menten constant value averaged at 4.052 mM for a total of 4 working electrodes. Variation in the K_m value may be due to the electropolymerisation process performed to encapsulate the GOx within the polymeric metrics. By using this technique, it means that there is a reduction in interference caused by connectivity as there is no insulation coverage required to block interference caused by connections when solution is added. Furthermore, by removing the wires initially used for connections allows the MNAs to be inserted into patients.

21.7 Conclusion

The K_m value was approximately half the value obtained from wire bonded MNs. Compared to the wire bonded MNs, the K_m value variation between each working electrode was relatively lower. The minimal variation between each WE shows that

binding the MNs onto the printed surface produces better connectivity and reproducibility compared to the wire bonding method.

Chapter 22

Polycarbonate MN for Drug Delivery

22.1 Introduction

Polycarbonate MN designs were modified to integrate therapeutic drug delivery and diagnostic application on the same platform. The polycarbonate MN were adapted to have holes between the needles and reservoirs to deliver large quantities of drug upon insertion into the skin using a Computer Numerical Control (CNC) machine. The CNC machine was used due to its ease of fabrication and the cost effectiveness. A CNC machine is usually used for large scale projects but also has the potential to be employed for microscale projects by using smaller scale drills (198). Within this chapter we will discuss optimisation that was carried out to determine the reservoir location and size; damage the needle edges and deforming the MN tip.

22.2 Via Optimisation

To create the vias in the MNA, the following methods were used:

- Measurement of the MN location with the array using a Shadow Starett HE400.
- CAD design of the MN.
- Inputting the CAD designs into the CNC machine.

The blank MN are clamped into the CNC machine and this is projected under the shadowgraph. The shadow graphed image is enlarged on a screen to allow measurements for the distance between the MNAs and the expected bore holes to be visualised (Figure 22.1).

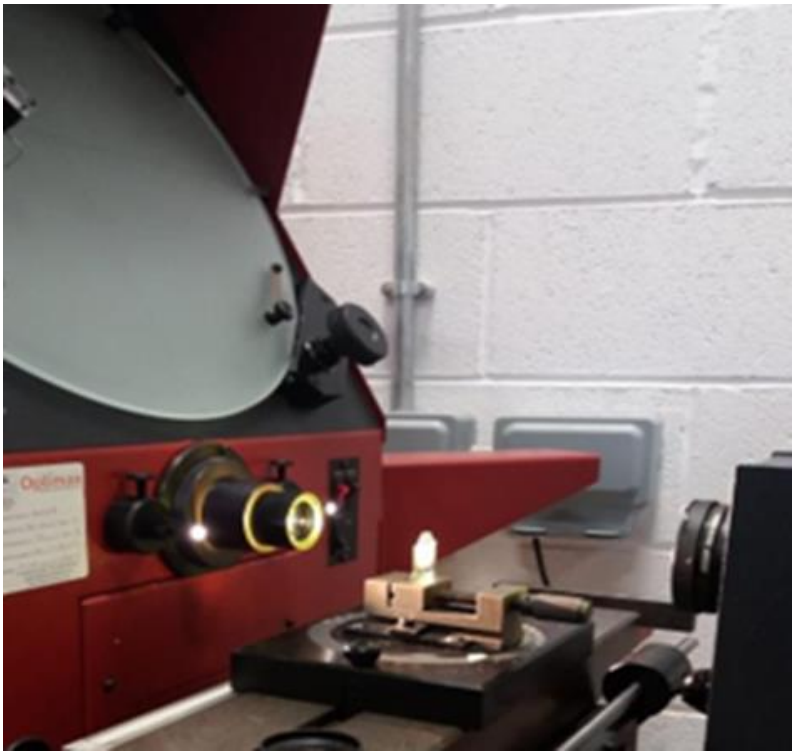

Figure 22.1 MNs clamped into the CNC machine where the arrays are projected under the shadowgraph.

The centre of each MNA is set at (0,0) to ensure that each hole drilled is done precisely and accurately. As each array might have minor discrepancies in distances post-injection moulding, the (0,0) point is set for each MN. Once the positioning was completed, the next action was to draw the new designs on CAD where the drilled holes were indicated with its total radius, break in distance and distance between the holes.

Two designs were established, the first design consisted of two 0.4 mm holes in between each needle and the second of a singular 0.6 mm hole between each needle. The 0.4 mm design would have greater breaking into the MN edge but may lead to damage to the needle tip due to the volume of holes drilled into the array. On the latter, the 0.6 mm design would be less likely to damage the tip but can lead to fewer breaks in the needle edge which can ultimately reduce the volume of drug delivered upon insertion.

As the CNC has a tolerance of 0.2 mm and accuracy of 0.05 mm, there is a possible discrepancy between the measured and actual design (Figure 22.2). Therefore, this discrepancy is considered to ensure the measured and actual design were aligned with one another.

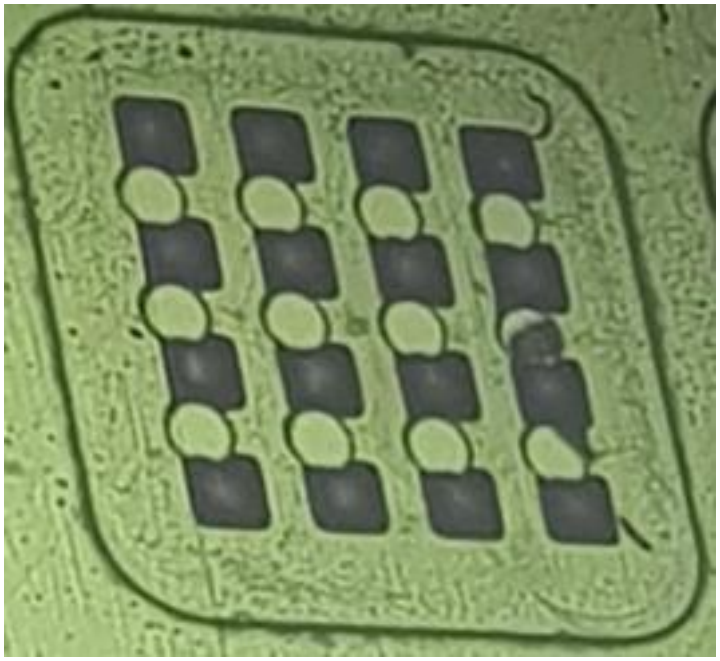

Figure 22.2 Discrepancy between the measured and actual design showing moderate mis-centralisation of the bores to the MNAs.

Post CAD design creating, a set of commands are inputted into the CNC machine. A pecking technique was one of the commands that was set, where the slot drill gradually removes the polycarbonate intermittently. This technique is used when the dimensions of the holes are much smaller than the depth of the component itself (199).

22.3 Via Characterisation

Post-bore optimisation, each design is imaged under an SEM to visualise any significant damage to the MN that can affect drug delivery capabilities. For the 0.4 mm bore design, the tips and the surrounding areas of the MN had been damaged post-drilling. Further to this, a lot of residue is present between the MNs especially at the points where the edge of the array is broken even though they are thoroughly cleaned with a vacuum gun (Figure 22.3).

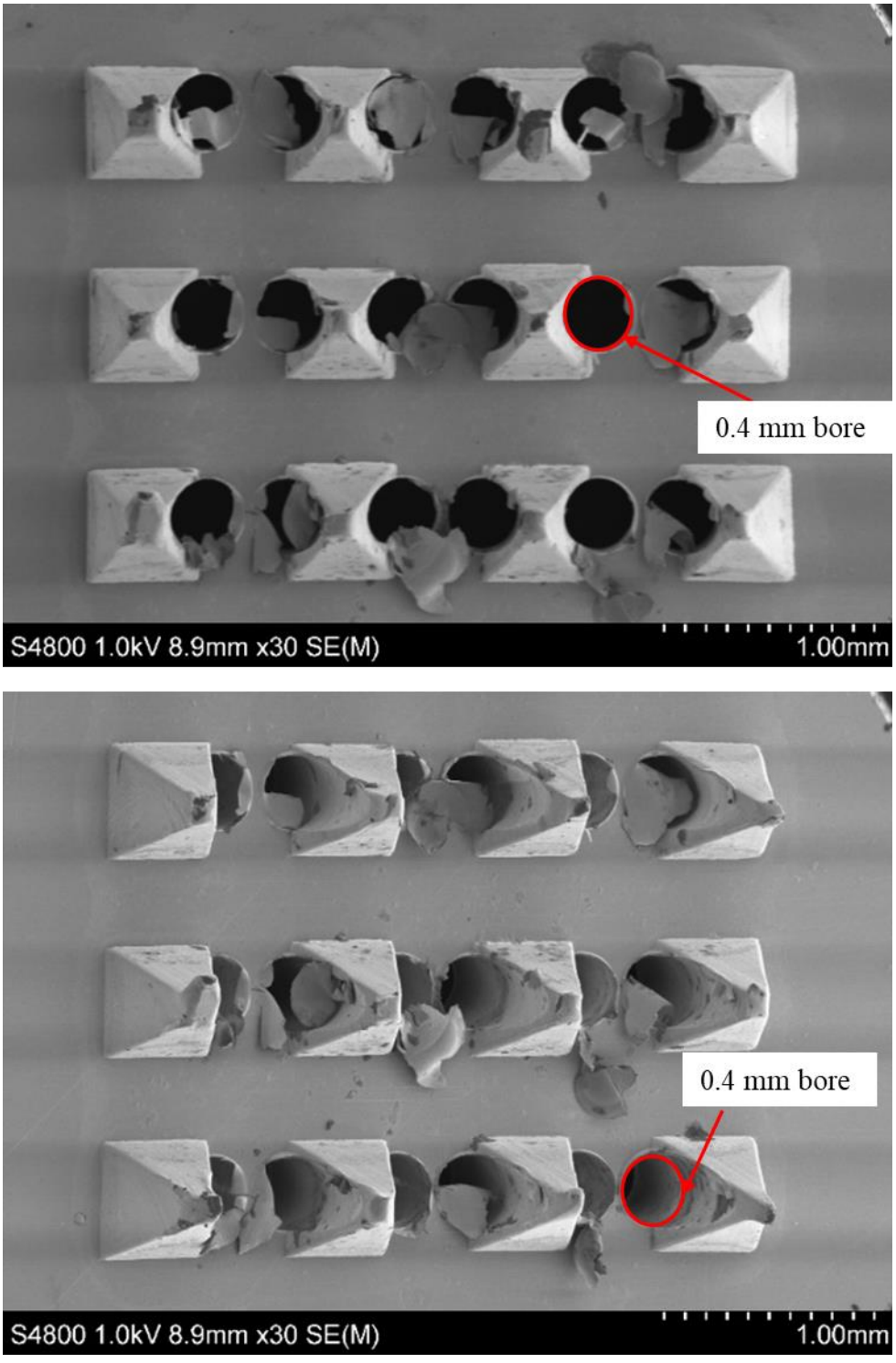

Figure 22.3 SEM image of the 0.4 mm bore design (red circle) post vacuum gun removal of excess residue.

Due to the pressure from drilling the vias, deformation of the MN tip was visualised where they begin to bend over. The placement of the bores shows significant breakage of the base to form a concave shape in the side of the needle.

Comparative to the 0.4 mm drilled holes, the single 0.6 mm holes between the MNs were seen to have less damage sustained to the tip of the MN in addition to exhibiting less residue caused by the drilling (Figure 22.4).

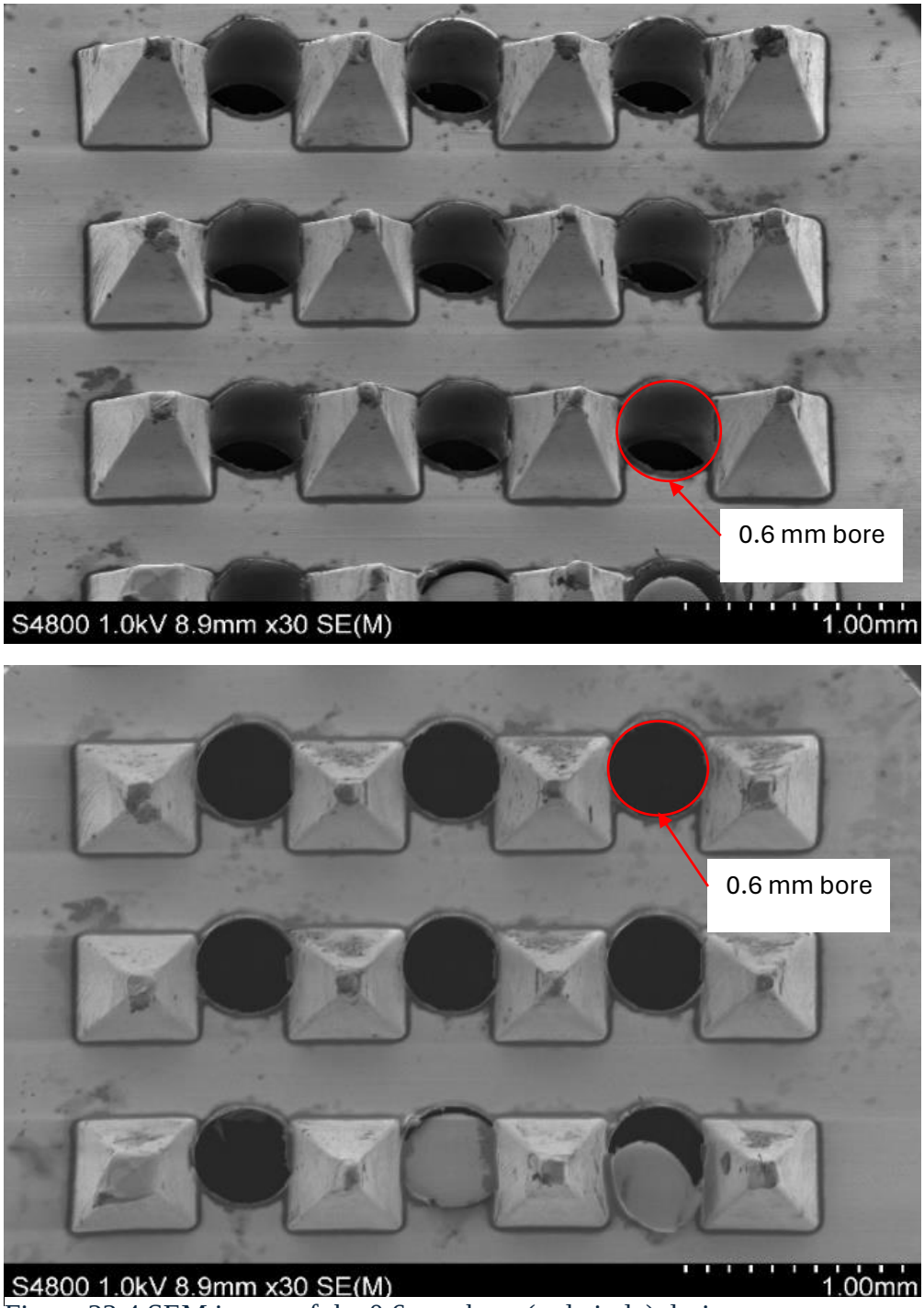

Figure 22.4 SEM image of the 0.6 mm bore (red circle) design post vacuum gun removal of excess residue.

By having slightly larger holes, one singular via was drilled between the MNs leading to less breakage towards the base. Having fewer holes means that the volume of drug injected through the bores may lead to pooling between needles rather than injecting into the skin.

22.4 Via Drug Delivery Capabilities

Post-analysis of the different drilled hole designs, the next stage was to determine their drug delivery capabilities. Each of the MNs were inserted into full thickness porcine skin using an applicator with the 9N force. As the arrays had reservoirs etched at the back, a syringe did not need to be attached to allow injection to occur (Figure 22.5). Instead, the drug is pipetted into the reservoir, and this will flow through the vias.

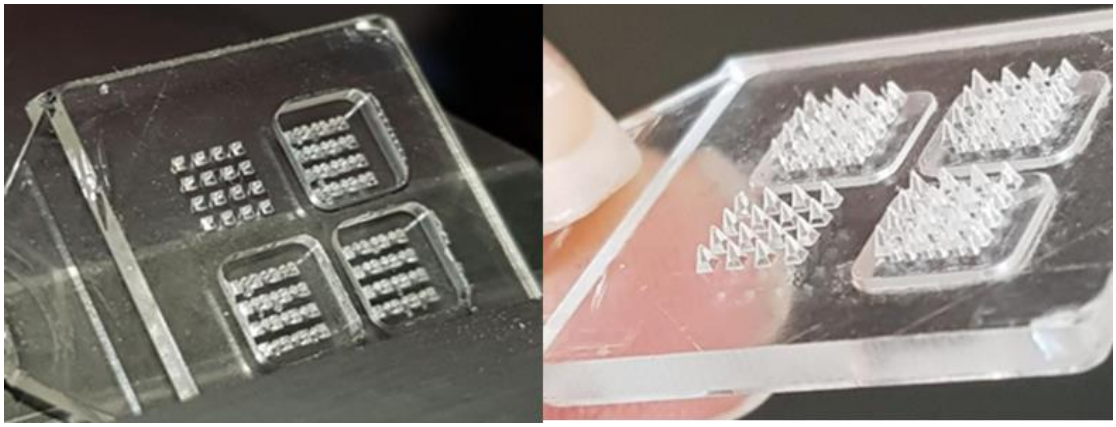

Figure 22.5 Reservoir etching at the back of the polycarbonate MNs to hold large quantities of drugs to be released through the bores.

Initially, a large volume of calcein (200 µL) was pipetted into the reservoir and this led to pooling on the surface of the porcine skin rather than delivery through the skin (Figure 22.6). The pooling is potentially due to the volume of drug pipetted into the reservoir and therefore the high volume injected at one given moment can lead to seepage rather than direct injection into the skin. Alternatively, as the MNs are not sealed in place upon insertion to ensure the arrays are secured and therefore the vias are fully inserted. By not sealing the MNs in place can lead to the volume pipetted leaking out rather than being injected through the skin.

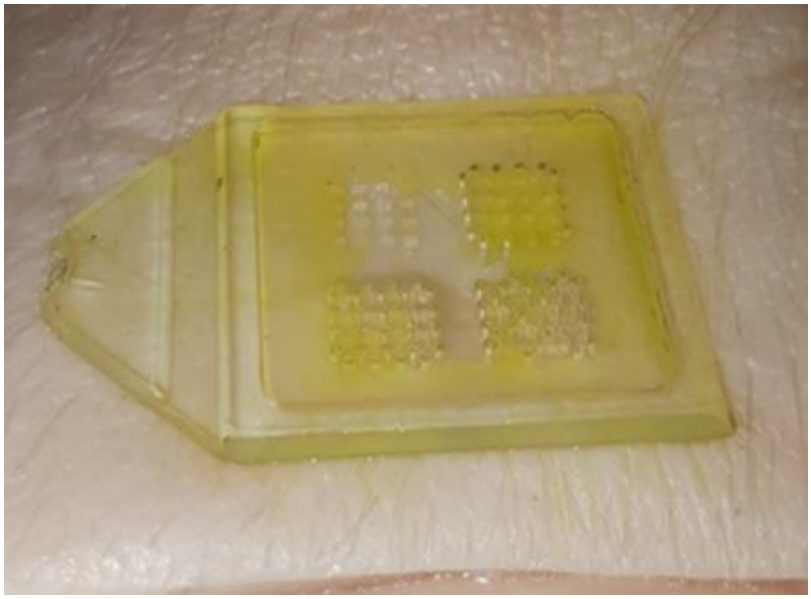

Figure 22.6 Leakage of calcein caused by pipetting 200 µl within the reservoir.

To overcome the pooling on the surface of the skin, a smaller volume of calcein (10 µL) was pipetted into the reservoir. Further to this, the MNs were inserted into dermatomed skin at a thickness of 800 µm rather than full thickness skin. The dermatomed skin was stretched and held in place using pins to form tension before the MNs were inserted using the applicator once again. Upon insertion, the MNs were taped into place to ensure they remained in position and sealed into place while the drug was delivered through the bores (Figure 22.7).

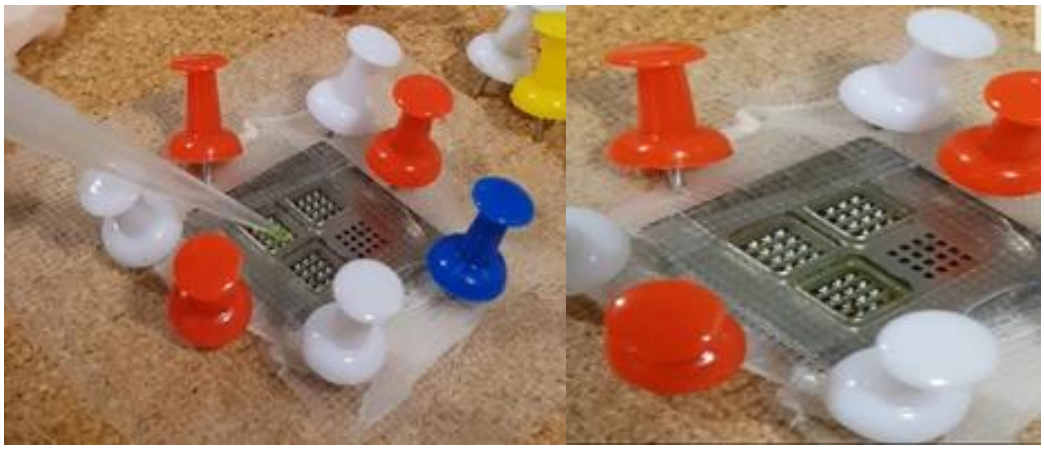

Figure 22.7 Pipetting smaller quantities of calcein into the reservoir led and securing into place to improve drug delivery capabilities through the bores

Although significantly better than applying large volumes to full-thickness porcine skin, some residue was still present on the surface of the MNs (Figure 22.8). This residue on the surface of the skin was significantly smaller than the volume of drug pipetted onto the reservoir and therefore delivery is occurring into the porcine skin.

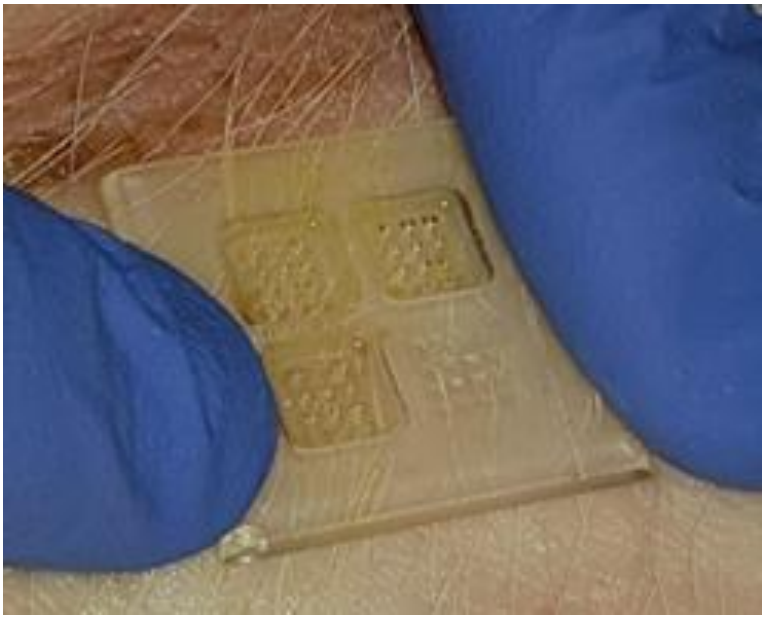

Figure 22.8 Improved drug delivery through the bores by reducing the volume of drug pipetted into the reservoir.

22.5 Conclusion

This same platform can now be modified to deliver drugs transdermally by applying bores within the MNAs. By combining the MN diagnostic and drug delivery capabilities, these polycarbonate MNs can be utilised as a theranostic device for the management of diseases and to monitor the pharmacokinetic responses to transdermal drugs. A potential avenue can be antimicrobial resistance studies or intradermal vaccine delivery (Vaccine smart patch).

Chapter 23

Conclusion

The potential for MNAs to be fabricated from various materials and dimensions provides the advantage of being used as a drug delivery system or a biosensor for point-of-care testing. These platforms can also be incorporated to produce a theranostic MNA that transdermally monitors biomarkers and provides the required dosage of drug to push towards precise and personalised medicine.

In this thesis, MNs have been fabricated from silicon and polymer to have the capabilities to deliver calcein that can be utilised as a proof-of-concept delivery for small molecule drugs and well-known therapies such as insulin for diabetes treatment. As well as providing proof of concept for on demand drug delivery using silicon MNs, the PVP MNAs were adapted to enable basal drug delivery due to its self-dissolving characteristics as well as bolus drug delivery by metallising the surface to provide drug upon voltage application. In order to determine their bolus drug delivery capabilities over a longer time frame, further experiments need to be performed. Initially, the MNs will need to be tested over a 24 hour time frame to analyse how drug delivery efficiency can be improved to administer higher concentrations of drug by allowing the MNAs to dissolve releasing the encapsulated drug within. Secondly, for insulin administration as these favour acidic environments further optimisation of the encapsulation process can be performed. This can be done by loading the insulin onto nanocarriers that are responsive to environmental changes such as temperature or pH to ensure effective delivery.

In addition to drug delivery, MNs have also been utilised for their diagnostic applications in measuring glucose molecules for diabetes management. These were adapted to remove the challenges that the wire bonding process has encountered. By providing a sensor platform allows the challenges with *in-vivo* diagnostic applications to be overcome as well as minimal variation between each electrode enabling better connectivity and reproducibility.

Although future work can be performed for these proof-of-concept MNs, the potential for these MNs to be transformed for theranostic devices is promising. As the MNs have shown proof of concept the next stage would be to incorporate the diagnostic capabilities

of polycarbonate with the self-dissolving drug administration of the PVP MNs to produce an on-demand theranostic device for personalised diabetes management.

References

1. P. Vega-Vasquez NSM, J.Irudayaraj. Nanoscale Drug Delivery Systems: From Medicine to Agriculture. Frontier in Bioengineering and Biotechnology. 2020;8(79).
2. A.D. Mali RB, M.Patil. An updated review on transdermal drug delivery systems. International Journal of Advances in Scientific Research. 2015;1(6):244-54.
3. V. Prasad KDJ, S. Mailankody. The high price of anticancer drugs: origins, implications, barriers, solutions. Nature Review Clinical Oncology. 2017;14(6):381-90.
4. J. Rubbens RM, J. Brouwers, P. Augustijns. Exploring gastric drug absorption in fasted and fed state rats. International Journal of Pharmaceutics. 2018;548(1):636-41.
5. J.A. Thomas FEB, J.L. Stringer, H.P. Rang, I.S. Snyder, J. Scarne, A.W. Cuthbert. Drug 1998 [Available from: https://www.britannica.com/science/drug-chemical-agent.
6. M.R. Prausnitz RL. Transdermal drug delivery. Nature Biotechnology. 2008;26(11):1261-8.
7. T.F. Herman CS. First-Pass Effect: StatPearls; 2023 [Available from: https://www.ncbi.nlm.nih.gov/books/NBK551679/.
8. Le J. Drug Administration 2022 [Available from: https://www.msdmanuals.com/en-gb/home/drugs/administration-and-kinetics-of-drugs/drug-administration.
9. D. Ramadon MTCM, A.J. Courtenay, R.F. Donnelly. Enhancement strategies for transdermal drug delivery systems: current trends and applications. Drug Delivery and Translational Research. 2021;12(4):758-91.
10. P.B. Luppa CM, A. Schlichtiger, H. Schelbusch. Point-of-care testing (POCT): Current techniques and future perspectives. TrAC Trends in Analytical Chemistry. 2011;30(6):887-98.
11. R.V. Dixon ES, W.M. Lau, P. Manning, M.A. Birch-Machin, S.M. Moghimi, K.W. Ng. Microneedle-based devices for point-of-care infectious disease diagnostics. Acta Pharmaceutica Sinica B. 2021;11(8):2344-61.
12. S. Nafisi HIM. Chapter 3 - Skin penetration of nanoparticles. In: Elsevier, editor. Emerging Nanotechnologies in Immunology2018. p. 47-88.
13. H. Yousef MA, S. Sharma. Anatomy, Skin (Integument), Epidermis: StatPearls; 2022 [Available from: https://www.ncbi.nlm.nih.gov/books/NBK470464/.
14. N. Fogh-Andersen BMA, B.T. Altura, O. Siggard-Andersen. Composition of interstitial fluid. Clinical Chemistry. 1995;41(10):1522-5.
15. H. Haslene-Hox EO, K.C. Berg, O. Kolmannskog, K. Woie, H.B. Salvesen, O. Tenstad, H. Wiig. A new method for isolation of interstitial fluid from human solid tumors applied to proteomic analysis of ovarian carcinoma tissue. PLoS. 2011;6(4).
16. P.P. Samant MRP. Mechanisms of sampling interstitial fluid from skin using a microneedle patch. PNAS. 2017;115(18):4583-8.
17. P.P. Samant MMN, N. Raviele, V. Tran, J. Mena-Lapaix, D.I. Walker, E.I. Felner, D.P. Jones, G.W. Miller, M.R. Prausnitz. Sampling interstitial fluid from human skin using a microneedle patch. Science Translational Medicine. 2020;12(571).
18. M. Friedel IAPT, G. Kasting, R. Polsky, D. Cunningham, H.T. Soh, J. Heikenfeld. Opportunities and challenges in the diagnostic utility of dermal interstitial fluid. Nature Biomedical Engineering. 2023;7:1541-55.
19. Debuglies. Dermal interstitial fluid (ISF) could be a new source of biomarkers 2020 [Available from: https://debuglies.com/2020/11/27/dermal-interstitial-fluid-isf-could-be-a-new-source-of-biomarkers/.
20. H.C. Ansel LVA, N.G. Popovich. Pharmaceutical dosage forms and drug delivery system. Americal Journal of Pharmaceutical Education. 2001;65.
21. R. Patel AHB. Formulation and evaluation consideration of transdermal drug delivery systems. International Journal of Pharmaceutical Research. 2011;3:1-9.

22. A.Z. Alkilani MTCM, R.F. Donnelly. Transdermal Drug Delivery: Innovative Pharmaceutical Developments Based on Disruption of the Barrier Properties of the stratum corneum. Pharmaceutics. 2015;7(4):438-70.
23. R.K. Keservani SB, N. Bandyopadhyay, A.K. Sharma. Chapter 4 - Design and fabrication of transdermal/skin drug-delivery system. Advances in Pharmaceutical Product Development and Research2020. p. 131-78.
24. Kramer SN. The sumerians: their history, culture and character: Chicago Press; 1971. 372 p.
25. S. Szunerits RB. Heat: A highly efficient skin enhancer for transdermal drug delivery. Frontier in Bioengineering and Biotechnology. 2018;6.
26. Schwenkenbecker A. Das absorptions verniogen der haut. Arch Anat Physiol. 1904;28:121-65.
27. Annotations. Poisoning by cutaneous absorption of aniline. The Lancet. 1902;159(4094):463-4.
28. Lal N. Insights of transdermal drug delivery: prerequisities and current strategies. Determinations in Nanomedicine and Nanotechnology. 2021;2(3):1-8.
29. Navin E. what is Lipinski rule of 5? 2022 [Available from: https://www.azolifesciences.com/article/What-is-Lipinskis-Rule-of-5.aspx.
30. M.N. Pastore YNK, M. Horstmann, M.S. Roberts. Transdermal patches: history, development and pharmacology. British Journal of Pharmacology. 2015;172(9):2179-209.
31. U. Chadha PB, R. Agarwal, P. Rawat, R. Agarwal, I. Gupta, M. Panjwani, S. Singh, C. Ahuja, S.K. Selvaraj, M. Banavoth, P. Sonar, B. Badoni, A. Chakravorty. Recent progress and growth in biosensors technology: A critical review. Journal of Industrial and Engineering Chemistry. 2022;109:21-51.
32. Prevention CfDCa. National Diabetes Statistics Report 2023 [Available from: https://www.cdc.gov/diabetes/data/statistics-report/index.html.
33. W.R. Rowley CB, Y. Arikan, E. Byrne, S. Krohe. Diabetes 2030: insights from yesterday, today and future trends. Population Health Management. 2017;20(1):6-12.
34. Patton SR. Adherence to glycemic monitoring in diabetes. Journal for Diabetes Science Technology. 2015;9(3):668-75.
35. D.M. Nathan SG, J. Lachin, P. Cleary, O. Crofford, M. Davis, L. Rand, C. Siebert. The effect of intensive treatment of diabetes on the development and progression of long-term complications in insulin-dependent diabetes mellitus. The New England Journal of Medicine. 1993;329(14):977-86.
36. Insights GM. Glucose Biosensors Market Size 2023 [Available from: https://www.gminsights.com/industry-analysis/glucose-biosensors-market.
37. Turner AP. Biosensors-sense and sensitivity. Science. 2000;290(1):1315-7.
38. L.C. Clark CL. Electrode systems for continuous monitoring in cardiovascular surgery. Annals of the New York Academy of Sciences. 1962;102(29):29-45.
39. J.D. Newman APT. Biosensors: principles and practice. Essays in Biochemistry. 1992:147-59.
40. D.R. Thevenot KT, R.A. Durst, G.S. Wilson. Electochemical biosensors: recommended definitions and classification. Biosensors & Bioelectonics. 2001;16:121-31.
41. G.G. Guilbault GJL. An enzyme electrode for the amperometric determination of glucose. Analytical Chemistry. 1973;64:439-55.
42. Pohanka M. Glucose electrochemical biosensors: The past and current trends. International Journal of Electrochemical Science. 2021;16:1-12.
43. C. Lorenz WS, M. Mortellaro. interference assessment of various endogenous and exogenous substances on the performance of the eversense long-term implantable

continuous glucose monitoring system. Diabetes Technology and Therapeutics. 2018;20(5):344-52.
44. D.L. Williams ARD, A. Korosi. Electrochemical-enzymatic analysis of blood glucose and lactate. Analytical Chemistry. 1970;42(1):118-21.
45. J. Liu JW. Improved design for the glucose biosensor. Food technology and biotechnology. 2001;39:55-8.
46. A.P. Turner BC, S.A. Piletsky. In vitro diagnostics in diabetes: meeting the challenge. Clinical Chemistry. 1999;45:1596-601.
47. A. Chaubey BDM. Mediated biosensors. Biosensors & Bioelectonics. 2002;17:441-56.
48. G.F. Khan MO, W. Wernet. Design of a stable charger transfer complex electrode for a third-generation amperometric glucose sensor. Analytical Chemistry. 1996;68:2939-45.
49. F. Palmisano PGZ, D. Centonze, M. Quinto. A disposable reagentless, third-generation glucose biosensor based on overoxidised poly(pyrrole)/tetrathiafulvalene-tetracyanoquinodimethane composite. Analytical Chemistry. 2002;74:5913-8.
50. W. Zhang GL. Third generation biosensors based on the direct electron transfer of proteins. Analytical Sciences. 2004;20:603-9.
51. S.R. Chinnadayyala KDP, S. Cho. In vivo and in vitro microneedle based enzymatic and non-enzymatic continuous glucose monitoring biosensors. Journal of Solid State Science and Technology. 2018;7(7).
52. Gerstel MS, inventorDrug Delivery Device. United States patent US3964482A. 1976.
53. S. Henry DVM, M.G. Allen, M.R. Prausnitz. Microfabricated microneedles: A novel approach to transdermal drug delivery. Journal of Pharmaceutical Sciences. 1998;87(8):922-5.
54. J.A. Matriano MC, J. Johnson, W.A. Young, M. Buttery, K. Nyam, P.E. Daddona. Macroflux microprojection array patch technology: a new and efficient approach for intracutaneous immunization. Pharmaceutical Research. 2002;19(1):63-70.
55. F.K. Aldawood AA, S. Desai. A comprehensive review of microneedles: types, materials, processes, characterizations and applications. Polymers. 2021;13(16):2815.
56. S.R. Karumuri HM, K. Guha, A.K. Puli, A. Einsanwi, G.S. Kondavitee. Design, simulation and analysis of micro electro-mechanical system microneedle for micropump in drug delivery systems. IET Nanobiotechnology. 2021;15(5):484-91.
57. K.A.S. Al-Japairai SM, S.H. Almurisi, J.R. Venugopal, A.R. Hilles, M. Azmana, S. Raman. Current trends in polymer microneedle for transdermal drug delivery. International Journal of Pharmaceutical Research. 2020;587.
58. Gupta J. Kinetics of skin resealing after insertion of microneedles in human subjects. Journal of Controlled Release. 2011;154(2):148-55.
59. Nair KJ. Micro-injection moulded microneedles for drug delivery: University of Bradford; 2016.
60. Ita K. Transdermal Delivery of Drugs with Microneedles—Potential and Challenges. Pharmaceutics. 2015;7(3):90-105.
61. S. Lyu ZD, X. Xu, H.P. Bei, H.Y. Yuen, C.W.J. Cheung, M.S. Wong, Y. He, X. Zhao. Going below and beyond the surface: Microneedle structure, materials, drugs, fabrication, and applications for wound healing and tissue regeneration. Bioactive Materials. 2023;27:303-26.
62. T. Waghule GS, S.K. Dubey, M.M. Pandey, G. Gupta, M. Singh, K. Dua. Microneedles: A smart approach and increasing potential for transdermal drug delivery system. Biomedicine & Pharmacotherapy. 2019;109:1249-58.

63. R. Mishra TKB. Chapter 16: MEMS-based hollow microneedles for transdermal drug delivery. In: Press A, editor. Drug Delivery Devices and Therapeutic Systems2021. p. 325-44.
64. N. Dang TYL, T.W. Prow. Nano- and microtechnology in skin delivery of vaccines. In: Publishing WA, editor. Micro- and Nanotechnology in Vaccine Development2017.
65. W. Martanto JSM, T. Couse, M.R. Prausnitz. Mechanism of fluid infusion during microneedle insertion and retraction. Journal of Controlled Release. 2006;112:357-61.
66. D.V. Mcallister PMW, S.P. Davis, J.H. Park, P.J. Canatella, M.G. Allen, M.R. Prausnitz. Microfabricated needles for transdermal delivery of macromolecules and nanoparticles: fabrication methods and transport studies. Proceedings of the National Academy of Sciences of the United States of America. 2003;100(24):13755-60.
67. J. Li MZ, H. Shan, C. Tong. Microneedle patches as drug and vaccine delivery platform. Current Medicinal Chemistry. 2017;24(22):2413-22.
68. H.S. Gill MRP. Coated microneedles for transdermal delivery. Journal for Controlled Release. 2007;117(2):227-37.
69. H.T. Duong NWK, T. Thambi, V.G. Phan, M.S. Lee, Y. Yin, J.H. Jeong, D.S. Lee. Microneedle arrays coated with charge reversal pH-sensitive copolymers improve antigen presenting cells-homing DNA vaccine delivery and immune responses. Journal for Controlled Release. 2018;269:225-34.
70. K.M. Kwon SML, S. Choi, D.H. Kim, H.E. Jin, G. Jee, K.J. Hong, J.Y. Kim. Microneedles: quick and easy delivery methods of vaccines. Clinical Experimental Vaccine Research. 2017;6:156-9.
71. J. Chen HR, P. Zhou, S. Zheng, B. Du, X. Liu, F. Xiao. Microneedle-mediated drug delivery for cutaneous diseases. Frontier in Bioengineering and Biotechnology. 2022;10.
72. B.M. Lee CL, S.F. Lahiji, U.W. Jung, G. Chung, H. Jung. Dissolving microneedles for rapid and painless local anesthesia. Pharmaceutics. 2020;12(4):366.
73. Ita K. Dissolving microneedles for transdermal drug delivery: advances and challenges. Biomedicine & Pharmacotherapy. 2017;93:1116-27.
74. A.M. Rodgers ASCRFD. Technology update: dissolvable microneedle patches for vaccine delivery. Medical Devices. 2019;12:379-98.
75. L.Y. Chu SOC, M.R. Prausnitz. Fabrication of dissolving polymer microneedles for controlled drug encapsulation and delivery: bubble and pedestal microneedle designs. Journal of Pharmaceutical Sciences. 2010;99(10):4228-38.
76. J.W. Lee JHP, M.R. Prausnitz. Dissolving microneedles for transdermal drug delivery. Biomaterials. 2008;29(13):2113-24.
77. R.F. Donnelly MTM, A.Z. Alkilani, E. Larraneta, E. McAlister, A.J. Courtenay, M.C. Kearney, T.R.R. Singh, H.O. McCarthy, V.L. Kett, E. Caffarel-Salvador, S. Al-Zahrani, D.A. Woolfson. Hydrogel-forming microneedles prepared from 'super swelling' polymers combined with lyophilised wafers for transdermal drug delivery. Plos One. 2014;9(10).
78. R.F. Donnelly DLM, D.A. Woolfson. Hydrogel-forming and dissolving microneedles for enhanced delivery of photosensitizers and precursors. Photochemistry and Photobiology. 2014;90(3):641-7.
79. R.F. Donnelly TRRS, D.A. Woolfson. Hydrogel forming microneedle arrays for enhanced transdermal drug delivery. Advanced Functional Materials. 2012;22(23):4879-90.
80. M. Wang LH, C. Xu. Recent advances in the design of polymeric microneedles for transdermal drug delivery and biosensing. Lab on a chip. 2017;17:1373-87.
81. A.J. Courtenay CTM, J.K. McAvoy, O.H. McCarthy. R.F. Donnelly. Microneedle mediated transdermal delivery of bevacizumab. Molecular Pharmaceutics. 2018;15(8):3545-56.

82. J.G. Turner LRW, P. Estrela, H.S. Leese. Hydrogel-forming microneedles: current advancements and future trends. Macromolecular Bioscience. 2021;21.
83. T.N. Tarbox ABW, Z. Cui, R.O. Williams. An update on coating/manufacturing techniques of microneedles. Drug Delivery and Translational Research. 2017;8:1828-43.
84. J.H. Park MGA, M.R. Prausnitz. Biodegradable polymer microneedles: Fabrication, mechanics and transdermal drug delivery. Journal for Controlled Release. 2005;104(1):51-66.
85. J.D. Zahn NHT, D. Liepmann, A.P. Pisano. Microfabricated polysilicon microneedles for minimally invasive biomedical devices. Biomedical Microdevices. 2000;2:295-303.
86. E. Larraneta REL, D.A. Woolfson, R.F. Donnelly. Microneedle arrays as transdermal and intradermal drug delivery systems: Materials science, manufacture and commercial developments. Materials Science and Engineering. 2016;104:1-32.
87. J.L. Lenhart DAF, S. Sambasivan, E.K. Lin, R.I. Jones, C.L. Soles, W.L. Wu, D.L. Goldfarb, M. Angelopoules. X-ray absorption spectroscopy to probe surface composition and surface deprotection in photoresist films. Langmuir. 2005;21(9):4007-15.
88. Shin-Etsu M. The Difference Between Positive and Negative Photoresist 2013 [Available from: https://www.microsi.com/blog/the-difference-between-positive-and-negative-photoresist/#:~:text=Positive%20photoresists%20are%20able%20to,can%20lead%20to%20pattern%20distortions.
89. J.P. Singh RB, A. Sharma, B. Kaur, S.O. Won, S. Gautam, K.H. Chae. Chapter 2-Fabrication of magnetic tunnel junctions. Advanced Applications in Manufacturing Engineering2019. p. 53-77.
90. W.I. Wu PR, H.H. Hsu, P.R. Selvaganapathy. Materials and methods for the microfabrication of microfluidic biomedical devices. Microfluidic Devices for Biomedical Applications. 2013:3-62.
91. Angely C. Dry etching vs wet etching 2020 [Available from: https://darwin-microfluidics.com/blogs/reviews/dry-etching-vs-wet-etching.
92. S. Franssila LS. Reactive Ion Etching (RIE). In: Springer, editor. Encyclopedia of Microfluidics and Nanofluidics2008. p. 1772-81.
93. S. Duarah MS, J. Wen. Recent advances in microneedle-based drug delivery: special emphasis on its use in paediatric population. European Journal of Pharmaceutics and Biopharmaceutics. 2019:48-69.
94. T. Liu MC, J. Fu, Y. Sun, C. Lu, G. Quan, X. Pan, C. Wu. Recent advances in microneedles-mediated transdermal delivery of protein and peptide drugs. Acta Pharmaceutica Sinica B. 2021;11(8):2326-43.
95. C.M. Lopez-Mendoza AJT-S, L.E. Alcantara-Quintana. Transdermal delivery of drugs for acute and chronic pain 2022 [Available from: https://www.intechopen.com/chapters/83060.
96. I.K. Ramoller IAT, H.O. McCarthy, R.F. Donnelly. Rapidly dissolving bilayer microneedle arrays- a minimally invasive transdermal drug delivery system for vitamin B12. International Journal of Pharmaceutics. 2019;566(1):299-306.
97. S. Kim HY, J. Eum, Y. Ma, S.F. Lahiji, H. Jung. Implantable powder carrying microneedles for transdermal delivery of high-dose insulin with enhanced activity. Biomaterials. 2020;232(1):1-12.
98. Excellence NIfHaC. Antihistamines, allergen immunotherapy and allergic emergencies [Available from: https://bnf.nice.org.uk/treatment-summaries/antihistamines-allergen-immunotherapy-and-allergic-emergencies/.
99. M.S. Arshad SH, A. Hussain, N. Abbas, L. Kucuk, K. Nazari, R. Ali, S. Ramzam, A, Alqahtani, E.G. Andriotis, D.G. Fatouros, M.W. Chang, Z. Ahmed. Improved transdermal

delivery of cetrizine hydrochloride using polymeric microneedles. Journal of Pharmaceutical Sciences. 2019;27(1):673-81.
100. Z. Luo WS, J. Fang, K. Lee, S. Li, Z. Gu, M.R. Dokmeci, A. Khademhosseini. Biodegradable gelatin methacryloyl microneedles for transdermal drug delivery. Advanced Healthcare Materials. 2019;8(3):1-9.
101. D. Kim HK, P.C. Lee, J.B. Lee. Universally applicable RNA membrane-based microneedle system for transdermal drug delivery. Materials Horizons. 2020:1-20.
102. D.H. Shim TTN, P.G. Park, M.J. Kim, B.W. Park, H.R. Jeong, D.S. Kim, H.W. Joo, S.O. Choi, J.H. Park, J.M. Lee. Development of botulinum toxin A-coated microneedle for treating palmar hyperhidrosis. Molecular Pharmaceutics. 2019;16(12):1-38.
103. J. Gupta EIF, M.R. Prausnitz. Minimally invasive insulin delivery in subjects with type 1 diabetes using hollow microneedles. Diabetes Technology and Therapeutics. 2009;11(6):329-37.
104. S.R. Patel ASL, H.F. Edelhauser, M.R. Prausnitz. Suprachoroidal drug delivery to the back of the eye using hollow microneedles. Pharmaceutical Research. 2011;28(1):166-76.
105. J. Yang ZC, R. Ye, J. Li, Y. Lin, J. Gao, L. Ren, B. Liu, L. Jiang. Touch-actuated microneedle array patch for closed loop transdermal drug delivery. Drug Delivery. 2018;25(1):1728-39.
106. L. Wei-Ze HM-R, Z. Jian-Ping, Z. Yong-Qiang, H. Bao-Hua, L. Ting, Z. Yong. Super short solid silicon microneedles for transdermal drug delivery applications. International Journal of Pharmaceutics. 2010;389(1):122-9.
107. N. Bhalla PJ, N. Formisano, P. Estrela. Introduction to biosensors. Essays in Biochemistry. 2016;60(1):1-8.
108. H.O. Fatoyinbo MPH. Biosensors. In: Springer, editor. Encyclopedia of Nanotechnology2012. p. 329-44.
109. Vashist SK. Point-of-care diagnostics: recent advances and trends. Biosensors. 2017;7(4):62.
110. A.S. John CPP. Existing and emerging technologies for point of care testing. Clinical Biochemical Review. 2014;35(3):155-67.
111. J. Li JM. Multiplexed lateral flow biosensors: technology advances for radically improving point of care diagnoses. Biosensors & Bioelectonics. 2016;83(1):177-92.
112. K.M. Koczula AG. Lateral flow assays. Essays in Biochemistry. 2016;60(1):111-20.
113. V. Kavuru TV, L. Karageorge, D. Choudhury, R. Senger, J. Robertson. Dipstick analysis of urine chemistry: benefits and limitations of dry chemistry-based assays. Postgraduate Medicine. 2019:1-9.
114. S. Sakamoto WP, S. Vimolmangkang, W. Phoolcharoen, Y. Shoyama, H. Tanaka, S. Morimoto. Enzyme linked immunosorbent assay for the quantitative/qualitative analysis of plant secondary metabolites. Journal of Natural Medicines. 2018;72(1):32-42.
115. I.H. Cho DHK, S. Park. Electrochemical biosensors: perspective on functional nanomaterials for on-site analysis. Biomaterials Research. 2020;24(6):1-12.
116. N.J. Ronkainen BHH, W.R. Heineman. Electrochemical biosensors. Chemical Society Reviews. 2010;39(1):1747-63.
117. Li D. Single phase electrokinetic flow in microchannels. In: Elsevier, editor. Heat Transfer and Fluid Flow in Minichannels and Microchannels2014. p. 175-219.
118. D. Al Sulaiman JYC, N.R. Bennett, H. Topouzi, C.A. Higgins, D.J. Irvine, S. Ladame. Hydrogel coated microneedle arrays for minimally invasive sampling and sensing of specific circulating nucleic acids from skin interstitial fluid. ACS Nano. 2019;13(1):9620-8.
119. S.A. Gowers DMF, T.M. Rawson, M.L. Rogers, R.C. Wilson, A.H. Holmes, A.E. Cass, D. O'Hare. Development of a minimally invasive microneedle-based sensor for continuous monitoring of B-Lactam antibiotic concentrations in vivo. ACS Sensors. 2019;4(1):1072-80.

120. A. Calio PD, V. Di Palma, M.F. Bevilacqua, A. Di Matteo, H. Iuele, L. De Stefano. Polymeric microneedles based enzymatic electrodes for electrochemical biosensing of glucose and lactic acid. Sensors and Actuators B. 2016;236(1):343-9.
121. Y. Goud CM, R.K. Mishra, C. Yu, R. Narayan, L. Litvan, J. Wang. Wearable electrochemical microneedle sensor for continuous monitoring of levodopa: toward parkinson management. ACS Sensors. 2019;8(4):2196-204.
122. H. Teymourian CM, F. Tehrani, E. Vargas, A. Barfidokht, R. Aghavali, T. Tangkuaram, P.P Mercier, E. Dassau, J. Wang. Microneedle based detection of ketone bodies along with glucose and lactate: toward real-time continuous ISF monitoring of diabetic ketosis/ ketoacidosis. Analytical Chemistry. 2019;92(2):1-32.
123. P.S. Choudhury MG. Differentiated thyroid cancer theranostics: radioiodine and beyond. British Institute of Radiology. 2018;91(1091).
124. J.M. Idee SL, S. Ballet, C. Corot. Theranostics and contrast-agents for medical imaging: a pharmaceutical company viewpoint. Quantitative Imaging in Medicine and Surgery. 2013;3(6):292-7.
125. R. Levine EPK. Clinical history of the theranostic radionuclide approach to neuroendocrine tumors and other types of cancer. The Journal of Nuclear Medicine. 2017;58(1).
126. X. Chen STW. Cancer theranostics: an introduction. In: Press A, editor. Cancer Theranostics2014. p. 3-8.
127. S. Cho OH, I. Lee, G. Lee, D. Yoo, G. Khang, P.M. Kang, D. Lee. Chemiluminescent and antioxidant micelles as theranostic agents for hydrogen peroxide associated inflammatory diseases. Advanced Functional Materials. 2012;22(19):1-6.
128. Lea P. Multiplex planar microarray for disease prognosis, diagnosis and theranosis. Journal of Experimental Medicine. 2015;5(3):188-93.
129. D. Singh FD, S.K. Sahoo. Challenges of moving theranostic nanomedicine into the clinic. Nanomedicine. 2020;15(2):111-4.
130. R.S. Kalash VKL, C.S. Cho, I.K. Park. Theranostics. In: Publishers AAS, editor. Biomaterials Nanoarchitectonics2016. p. 197-215.
131. R.G. Bai KM, S. Manickam. Nanomedicine in theranostics. In: Publishers WAAS, editor. Nanotechnology Applications for Tissue Engineering2015. p. 195-213.
132. S.S. Kelkar TMR. Theranostics: combining imaging and therapy. Bioconjugate Chemistry. 2011;22(10):1879-903.
133. A. Sneider DVD, S. Paliwal, P. Rai. Remotely triggered nano-theranostics for cancer applications. Nanotheranostics. 2017;1(1):1-22.
134. J. Yang JY, X. Gong, Y. Zheng, S. Yi, Y. Cheng, Y. Li, B. Liu, X. Xie, C. Yi, L. Jiang. Recent progress in microneedles-mediated diagnosis, therapy and theranostic systems. Advanced Healthcare Materials. 2022;11(10).
135. P. Dosta NP, A.M. Cryer, A.L. Rodriguez, E. Scott, R. Weissleder, M.A. Miller, N. Artzi. Polymeric microneedles enable simultaneous delivery of cancer immunomodulatory drugs and detection of skin biomarkers. Theranostics. 2023;13(1):1-15.
136. S. Zhu FY, L. Yang, B. Li, R. Xue, W. Yu, Y. Wang, L. Huang, L. Wang, R. Han, Y. Jiang. Low dose x-ray radiodynamic therapy solely based on gold nanoclusters for efficient treatment of deep hypoxic solid tumors combined with enhanced antitumor immune response. Theranostics. 2023;13(3):1042-58.
137. Y. Luo BQ, P. Zhang, C. Yang, J. Cao, X. Yuan, H. Ran, Z. Wang, L. Hao, Y. Cao, J. Ren, Z. Zhou. TME- activatable theranostic nanoplatform with ATP burning capability for tumor sensitization and synergistic therapy. Theranostics. 2020;10(15):6987-7001.

138. V.J. Kelly STW, V. Gottumukkala, R. Coelho, K. Palmer, S. Nair, T. Erick, R. Puri, O. Ilovich, P. Mukherjee. Preclinical evaluation of an 111 In/ 225 Ac theranostic targeting transformed MUC1 for triple negative breast cancer. Theranostics. 2020;10(15):6946-58.
139. Z. Yang JS, W. Tang, W. Fan, Y. Dai, Z. Shen, L. Lin, S. Cheng, Y. Liu, G. Niu, P. Rong, W. Wang, X. Chen. Stimuli-responsive nanotheranostics for real-time monitoring drug release by photoacoustic imaging. Theranostics. 2019;9(2):526-36.
140. C. Li YW, Y. Du, M. Qian, H. Jiang, J. Wang, N. Murthy, R. Huang. Side effects avoided theranostics achieved by biodegradable magnetic silica sealed mesoporous polymer drug with ultralow leakage. Biomaterials. 2018;186(1):1-7.
141. H. Li YM, J. Lu, W. Wei, Y. Wan, S. Liu. Target cell specific fluorescence silica nanoprobes for imaging and theranostics of cancer cells. Analytical Chemistry. 2014;86(1):3602-9.
142. S. Potyl KM, E. O'Neil, J.C. Knight, B. Cornelissen, J.S. Lewis. Zr-PET imaging of DNA double strand breaks for the early monitoring of response following a- and B- particle radioimmunotherapy in a mouse model of pancreatic ductal adenocarcinoma. Theranostics. 2020;10(13):5802-14.
143. C. Zhang YL, P. Liu, Q. Du, Y. Liang, S. Ooi, S. Qin, S. He, S. Yao, W. Wang. FABPS promotes lymph node metastasis in cervical cancer by reprogramming fatty acid metabolism. Theranostics. 2020;10(15):6561-80.
144. B.S. Harrington YH, T. Khan, S. Puttick, P.J. Conroy, T. Kryza, T. Cuda, A. Sokolowski, B.W. Tse, K.K. Robbins, B.J. Arachchige, S.J. Stehbens, P.M. Pollock, S.Reed, J.S. Weroha, P. Haluska, C. Salomon, R. Lourie, L.C. Perrin, R.H. Law, J.C. Whisstock, J.D. Hooper. Anti-CDCP1 immuno-conjugates for detection and inhibition of ovarian cancer. Theranostics. 2020;10(5):2095-114.
145. P. Wang PZ, S. Dong, T. Xu, X. He, M. Chen. An albumin binding polypeptide both targets cytotoxic T lymphocyte vaccines to lymph nodes and boosts vaccine presentation by dendritic cells. Theranostics. 2018;8(1):223-36.
146. M. Giulbudagian GY, S. Honzke, A. Edlich, B. Geisendorfer, B. Kleuser, S. Hedtrich, M. Calderon. Breaking the barrier potent anti-inflammatory activity following efficient topical delivery of etanercept using thermoresponsive nanogels. Theranostics. 2018;8(2):450-63.
147. C. Wang MW, T. Xu, X. Zhang, C. Liu, W. Gao, H. Xu, B. Lei, C. Mao. Engineering bioactive self healing antibacterial exosomes hydrogel for promoting chronic diabetic wound healing and complete skin regeneration. Theranostics. 2019;9(1):65-76.
148. D. Liu WL, X. Jiang, S. Bai, J. Liu, X. Liu, Y. Shi, Z. Kuai, W. Kong, R. Gao, Y. Shan. Using near infrared enhanced thermozyme and scFv dual conjugated Au nanorods for detection and targeted photothermal treatment of Alzheimer's disease. Theranostics. 2019;9(8):2268-81.
149. E. Portnoy NV, A. Bishara, M. Shmuel, S. Magdassi, J. Golenser, S. Eyal. Indocyanine green liposomes for diagnosis and therapeutic monitoring of cerebral malaria. Theranostics. 2016;6(2):167-76.
150. E.Y. Lukianova-Hleb DOL. Malaria theranostics using hemozoin-generated vapor nanobubbles. Theranostics. 2014;4(7):761-9.
151. D. Calle VN, P. Ballesteros, S. Cerdan. Magnetoliposomes loaded with poly-unsaturated fatty acids as novel theranostic anti-inflammatory formulations. Theranostics. 2015;5(5):489-503.
152. C. Cao RJ, H. Wei, Z. Liu, S. Ni, G.J. Liu, H.A. Young, X. Chen, G. Liu. Adaptive in vivo device for theranostics of inflammation: Real-time monitoring of interferon-y and aspirin. Acta Biomaterialia. 2020;101(1):372-83.

153. S.A. Costa Lima SR. Temperature responsive polymeric nanospheres containing methotrexate and gold nanoparticles: A multi-drug system for theranostic rheumatoid arthritis. Colloids and Surface B: Biointerfaces. 2015;133(1):378-87.
154. J.R. McCarthy EK, R. Weissleder, F.A. Jaffer. A light activated theranostic nanoagent for targeted macrophage ablation in inflammatory atherosclerosis. Small. 2010;6(18):2041-9.
155. T. Boltersdorf JA, E.Y. Senchenkova, J. Groeper, D. Pajonczyk, S.A. Vital, G. Kaur, S.J. Alexander, T. Vogl, U. Rescher, N.J. Long, F.N. Gavins. Targeting of formyl peptide receptor 2 for in vivo imaging of acute vascular inflammation. Theranostics. 2020;10(15):6599-614.
156. M. Yang JD, X. Feng, F. Chang, Y. Wang, Z. Gao, X. Zhuang, X. Chen. Scavenger receptor-mediated targeted treatment of collagen-induced arthritis by dextran sulfate-methotrexate prodrug. Theranostics. 2017;7(1):97-105.
157. M. Garnella NG, S. Mailloux, J.M. Pingarron, E. Katz. Antibacterial drug release electrochemically stimulated by the presence of bacterial cells-theranostic approach. Electroanalysts. 2014;26(1):2552-7.
158. A. Kaul SC, A. Attri, M. Kalra, A.K. Mishra. Targeted theranostic liposomes: rifampicin and ofloxacin loaded pegylated liposomes for theranostic application in mycobacterial infections. Royal Society of Chemistry Advances. 2016;6(1):28919-26.
159. Z. Gu TTD, M. Ma, B.C. Tang, H. Cheng, S. Jiang, Y. Dong, Y. Zhang, D.G. Anderson. Glucose-responsive microgels integrated with enzyme nanocapsules for closed loop insulin delivery. ACS Nano. 2013;7(8):6758-66.
160. P. Wang QL, H. Zhao, J.O. Bishop, G. Zhou, K. Olsen, A. Moore. miR-216a-targeting theranostic nanoparticles promote proliferation of insulin secreting cells in type 1 diabetes animal model. Scientific Reports. 2020;10(1):5302.
161. X. Sun WJ, B. Zhang, L. Ma, W. Fu, W. Qian, X. Zhang, L. Jianting, E. Sheng, Y. Tao, D. Zhu. A theranostic microneedle array patch for integrated glycemia sensing and self-regulated release of insulin. Biomaterials Science. 2022;10(5):1209-16.
162. Detloff C. Coating microstructures: understanding the science behind thermal spray coatings 2018 [Available from: https://empoweringpumps.com/tstcoatings-microstructures-science-thermal-spray-coatings/.
163. Instruments O. Inductively coupled plasma – reactive ion etching (ICP-RIE)). [Available from: https://plasma.oxinst.com/technology/icp-etching.
164. A.M. Pinto VBO, D.S. Falcao. Miniaturization of direct alcohol fuel cells: Microfabrication techniques and microfluidic architectures. Direct Alcohol Fuel Cells for Portable Applications. 2018:245-64.
165. S.P. Sullivan DK, M. del Pilar Martin, J.W. Lee, V. Zarnitsyn, N. Murthy, R.W. Compand, I. Skountzou, M.R. Prausnitz. Dissolving polymer microneedle patches for influenza. Nat Med. 2010;16(8):915-20.
166. S. Sharma ZH, M. Rogers, M. Boutelle, A.E.G. Cass. Evaluation of a minimally invasive glucose biosensor for continuous tissue monitoring. Analytical and bioanalytical chemistry. 2016;408(29):8427-35.
167. Coat V. What is an electron microscope? [Available from: https://vaccoat.com/blog/electron-microscope/.
168. K. Gulati TA. Profiling to probing: atomic force microscopy to characterize nano-engineered implants. Acta Biomaterialia. 2023;170:15-38.
169. F.C. Rossetti LVD, M.V. Lopes. Confocal laser scanning microscopy as a tool for the investigation of skin drug delivery systems and diagnosis of skin disorders 2012 [Available from: https://www.intechopen.com/chapters/43810.
170. Keyence. Microscope optical systems [Available from: https://www.keyence.com/products/microscope/digital-microscope/resources/basic/microscope-optical-systems.jsp.

171. B. Srinivasan ARK, J.J. Hickman. TEER measurement techniques for in vitro barrier model systems. Journal of Laboratory Automation. 2015;20(2):107-26.
172. Commission E. Skin PAMPA Permeability System 2012 [Available from: https://tsar.jrc.ec.europa.eu/test-method/tm2012-02#:~:text=The%20Skin%20PAMPA%20is%20a,membrane%20mimicking%20the%20human%20skin.
173. I. Pulsoni ML, M. Aiello, A. Fedi, M. Marzagalli, J. von Hagen, S. Scaglione. Comparison between franz diffusion cell and a novel micro-physiological system for in vitro penetration assay using different skin models. SLAS Technology. 2022;27(3):161-71.
174. F. Jonsdottir BS, S. Gunnarsson, E. Georgsdottir, S. Sigurdsson. Transdermal drug delivery: determining permeation using tape stripping and numerical modelling. Pharmaceutics. 2022;14.
175. C. Surber FPS, E.W. Smith. Tape-stripping technique Journal of Toxicology: Cutaneous and Ocular Toxicology. 2002;20(4):461-74.
176. F. Jonsdottir BS, S. Gunnarsson, E. Georgsdottir, S. Sigurdsson. Transdermal drug delivery: determining permeation parameters using tape stripping and numerical modelling. Pharmaceutics. 2022;14(9):1880.
177. McDermott A. 6 ways to use papain 2018 [Available from: https://www.healthline.com/health/food-nutrition/papain.
178. Aldrich S. Tissue dissociation guide: collagenase, dispase, and liberase enzyme types [Available from: https://www.sigmaaldrich.com/GB/en/technical-documents/technical-article/research-and-disease-areas/cell-signaling/collagenase-guide.
179. Lakowicz JR. Principles of fluorescence spectroscopy. Springer. 2006.
180. M.S. Rafique MR, M.B. Tahir, S. Hajra, T. Nawaz, F. Shafiq. Chapter 3 - Synthesis methods of nanostructures. Nanotechnology and Photocatalysis for Environmental Applications2020. p. 45-56.
181. D. Grieshabar RM, J. Voros, E. Reimhult. Electrochemical biosensors - Sensor principles and architectures. Sensors. 2008;8(3):1400-58.
182. G. Ziyatdinova EG, E. Yakupova. Electrochemical sensors based on the electropolymerized natural phenolic antioxidants and their analytical application. Sensors. 2021;21(24):8385.
183. R.K. Franklin SMM, R.B. Brown. Chemical and biological systems: chemical sensing systems for liquids. Module in Materials Science and Materials Engineering. 2016:433-61.
184. Surti F. Enzyme kinetics 2022 [Available from: https://teachmephysiology.com/biochemistry/molecules-and-signalling/enzyme-kinetics/.
185. C.J.W. Bolton OH, G.J. Blayney, P.F. Eng, J.C. Birchall, B. Gualeni, K. Roberts, H. Ashraf, O.J. Guy. Hollow silicon microneedle fabrication using advanced plasma etch technologies for applications in transdermal drug delivery. Lab on a chip. 2020;20(15):2788-95.
186. Y.A. Gomma LKE-K, V.M. Meidan. Effect of microneedle treatment on the skin permeation of a nanoencapsulated dye. The Journal of Pharmacy and Pharmacology. 2012;64(11):1592-602.
187. Institute NC. Histology [Available from: https://www.cancer.gov/search/results?swKeyword=histology.
188. T. Rosenkranz SK. Enabling stable, high viscosity injectable drug products with new excipient combinations: Pharma's almanac; 2022 [Available from: https://www.pharmasalmanac.com/articles/enabling-stable-high-viscosity-injectable-drug-products-with-new-excipient-combinations.

189. A. Vo MD, G. Rockwell. The biomechanics and optimization of the needle-syringe system for injecting triamcinolone acetonide into keloids. Journal of Med Eng. 2016.
190. H.X. Ngo SG-T. What are the drugs of the future? MedChemComm. 2018;9(5):757-8.
191. S. Govardhanagiri SB, G.P. Nagaraju. Chapter 8 - small molecule and pancreatic cancer trials and troubles. Breaking Tolerance to Pancreatic Cancer Unresponsiveness to Chemotherapy: Academic Press; 2019. p. 117-31.
192. Wick JY. Inhaled Insulin Pros and Cons 2016 [Available from: https://www.pharmacytimes.com/view/inhaled-insulin-pros-and-cons.
193. Kariduraganavar M. Chapter 1 - Polymer synthesis and processing. In: Elsevier, editor. Natural and Synthetic Biomedical Polymers2014. p. 1-31.
194. Pharmaceuticals U. Sustained release capsules manufacturing and handling 2020 [Available from: https://www.upm-inc.com/specialized-handling-capabilities/sustained-release-handling.
195. S. Adepu SR. Controlled drug delivery systems: current status and future direction. Molecules. 2021;26(19):5905.
196. Instruments S. Overcome charge-up effects in scanning electron microscopes (SEMs)]. [Available from: https://www.stinstruments.com/applications/materials-science/overcome-charge-up-effects-in-scanning-electron-microscopes-sems/#:~:text=Charge%2Dup%20effects%20are%20reduced,travel%20through%20the%20gaseous%20environment.
197. M.S. Zafar IF, M. Awais, S. Najeeb, Z. Khurshid, S. Zohaib. Chapter 11 - Bioactive surface coatings for enhancing osseointegration of dental implants. Biomedical Therapeutic and Clinical Applications of Bioactive Glasses: Woodhead Publishing; 2019. p. 313-29.
198. J.S. Mecomber DH, P.A. Limbach. Enhanced machining of micron-scale features in microchip molding masters by CNC milling. International Journal of Machine Tools and Manufacture. 2005;45(12-13):1542-50.
199. D.W. Kim YSL, M.S. Park, C.N. Chu. Tool life improvement by peck drilling and thrust force monitoring during deep-micro-hole drilling of steel. International Journal of Machine Tools and Manufacture. 2009;49(3-4):246-55.